Calibration des algorithmes d'identification des jets issus de quarks b et mesure de la section efficace différentielle de production de paires de quarks top-antitop en fonction de la masse et de la rapidité du système top-antitopdans les collisions p-p à une énergie au centre de masse de 7 TeV auprès de l'expérience ATLAS au LHC.

N. Tannoury

CPPM-T-2012-005

AIX-MARSEILLE UNIVERSITÉ
FACULTÉ DES SCIENCES
163 avenue de Luminy
13288 MARSEILLE Cedex 09

THÈSE DE DOCTORAT

Physique et Sciences de la Matière

Mention : *Physique des Particules et Astroparticules*

présentée par

Nancy TANNOURY

en vue d'obtenir le grade de docteur de l'Université d'Aix-Marseille

Calibration des algorithmes d'identification des jets issus de quarks b et mesure de la section efficace différentielle de production de paires $t\bar{t}$ en fonction de la masse et de la rapidité du système $t\bar{t}$ dans les collisions p-p à $\sqrt{s} = 7$ TeV auprès de l'expérience ATLAS au LHC.

soutenue le 9 Octobre 2012 devant le jury composé de

Dr.	R. Chierici	Examinateur
Prof.	M. Cousinou	Examinateur
Dr.	M. Cristianzini	Examinateur
Dr.	E. Kajfasz	Président du jury
Prof.	J.A. Mueller	Rapporteur
Dr.	D. Pallin	Rapporteur
Prof.	M. Talby	Directeur de thèse

À Salwa, Elias,

Michel, Nadine et Perla.

Remerciements

Je tiens à adresser en premier lieu mes plus chaleureux remerciements à mon directeur de thèse, chef du groupe ATLAS au CPPM, Mossadek Talby, pour son encadrement et son soutien tout au long des années de ma thèse. J'en profite pour lui exprimer ici ma plus profonde gratitude.

Je tiens à remercier sincèrement Eric Kajfasz, directeur du CPPM, pour m'avoir acceuillie au sein du laboratoire et pour la bonne ambiance qu'il a su distillée parmis les membres du laboratoire.

Je remercie les membres de jury: James Mueller et Dominique Pallin, mes rapporteurs, ainsi que Roberto Chierici, Marie-Claude Cousinou, Markus Cristianzini et Eric Kajfasz.

Je remercie tous les membres du groupe ATLAS au CPPM et au CERN pour leur aide et soutien pendant les trois années de thèse. Je tiens à remercier plus spécifiquement Joe Boudreau, James Mueller et Frank Filthaut pour leur aide sur *System*8, la première partie de ma thèse. Je remercie également Jörgen Sjölin, Francesco Spano, Venkatesh Kaushik, Jiri Kvita et Lorenzo Bellagamba pour leurs conseils et aides pour la partie section efficace différentielle $t\bar{t}$.

Je remercie tous mes collègues de travail, dont la plupart sont devenus de très bons amis, pour avoir faciliter le chemin et le rendre plus agréable.

Je tiens à remercier chaleureusement tous les membres de ma famille, ma mère Salwa, mon père Elias, mon frère Michel et mes deux soeurs Nadine et Perla. Sans vous, tout celà n'aurait jamais été possible.

Contents

Resumé

Le Modèle Standard (MS) de la physique des particules est le cadre théorique des travaux réalisés au cours de mes années de thèse, présentés dans ce manuscrit. Il décrit les particules élémentaires et leurs interactions électromagnétiques, faibles et fortes avec une grande précision. Le MS fournit aussi une description unifiée et précise des interactions électrofaibles jusqu'à des échelles d'énergie qui ont été étudiés dans les expériences de physique de haute énergie. Les interactions ainsi que les désintegrations d'un grand nombre de particules élémentaires ou non, découvertes et observées dans différentes expériences au cours des 50 dernières années sont également décrites avec une très bonne précision.

Le premier chapitre de cette thèse introduit le MS et décrit, selon leur spin, les particules élémentaires (bosons et fermions). Les bosons, de spin 1, sont les médiateurs des intéractions faibles, fortes et électromagnétiques. Les fermions, particules de spin 1/2, constituent les briques élémentaires de la matière. Les fermions comportent six leptons et six quarks. Les leptons sont divisés en trois particules éléctriquement chargées sensibles aux interactions électromagnétique et faible, et en trois particules éléctriquement neutres sensibles à l'interaction faible seulement. Les quarks sont des particules qui possèdent, en plus de la charge éléctrique, une charge de couleur. À ce jour, il y a six quarks connus: *up*, *down*, *charm*, *strange*, *top* et *bottom*. Les quarks sont des particules confinées dans des états liés appelés hadrons, mésons (formés d'un quark et d'un anti-quark) ou baryons (formés de trois quarks), à l'exception du quark top. Occupant le sujet du deuxième chapitre de cette thèse, le quark top est le dernier quark qui a été découvert en 1995 au TeVatron. Le quark top est la particule la plus massive observée à ce jour. Sa masse ésr de l'ordre de 41 fois la masse du quark b, le deuxième quark massif. Grâce à sa masse élevée, le quark top possède une petite durée de vie de l'ordre de 10^{-25} s, plus petite que le temps caractéristique d'hadronisation des quarks. De ce fait, ses propriétés peuvent alors être étudiées directement, contrairement à tous les autres quarks. Le deuxième chapitre passe en revue les différentes propriétés du quark top, ses modes de production par interaction forte (pair $t\bar{t}$) et par interaction faible (single top) dans les collisionneurs hadroniques et leurs sections efficaces, ses canaux de désintégration ainsi que les dernières

mesures effectuées sur ses propriétés tel que sa masse, charge et spin. Le quark *top* dans des scénarios au-delà du MS et dans la recherche de nouvelle physique est aussi discuté dans ce chapitre de cette thèse.

En dépit de son succès, le Modèle Standard est loin d'être une théorie complète des interactions fondamentales car il ne décrit pas l'interaction gravitationnelle et n'apporte pas de réponses à plusieurs questions fondamentales telles que la hierarchie de masse entre particules élémentaires, le nombre de génération de particules de matières, ...etc. Le MS ne permet pas non plus de rendre compte de l'expansion accélérée de notre univers ni de son contenu hors matière baryonique (matière noire et énergie noire) dont l'existance est attestée par les obseravtions cosmologiques. Également, il ne prend pas compte des oscillations de neutrinos (et leurs masses non nulles). On pense que le MS est une très bonne approximation à basse énergie d'une théorie plus générale qui reste à découvrir à haute énergie. Cette dérnière devrait apporter des réponses aux questions fondamentales non encore élucidées et pourrait mettre en évidence une nouvelle physique à haute énergie. L'échelle à laquelle cette nouvelle physique devrait apparaître n'est pas bien connue, cependant plusieurs arguments soulignent l'échelle du TeV qui a motivé la construction du collisionneur hadronique LHC au CERN.

Le Large Hadron Collider (LHC) est le plus grand accélérateur et collisionneur de particules construit à jour. Il est concu pour fournir des collisions proton-proton avec une énegie au centre de masse de l'ordre de $\sqrt{s} = 14$ TeV, avec une luminosité instantanée de $10^{34}\text{cm}^{-2}\text{s}^{-1}$. Le LHC a fourni des collisions proton-proton avec une énegie au centre de masse de $\sqrt{s} = 7$ TeV en 2010 et 2011. En 2012, le LHC a fonctionné avec une énergie au centre de masse de 8 TeV et il est prévu de fournir des collisions avec la valeur nominale ou proche de la nominale début de 2015. Deux expériences généralistes, ATLAS et CMS, sont installées sur l'anneau du LHC pour analyser les collisions.

L'expérience ATLAS au LHC est concue pour analyser un large spectre de particules issues des collisions fournies par le LHC à des énergies jamais explorées à ce jour. Ce fait pourrait mettre en évidence un large pavel de nouvelle physique prédite par des modèles théoriques au delà du MS. Les physiciens des particules utilisent les données enregistrées par le détecteur ATLAS afin d'identifier et d'identifier les différentes particules connues ainsi que pour rechercher de nouvelles signatures et éventuellement découvrir de nouvelles particules.

Le troisième chapitre de cette thèse porte sur le LHC et le détecteur ATLAS. Le détecteur ATLAS est constitué de plusieurs sous-détecteurs avec différentes technologies. Il est constitué de trois sous-détecteurs:

- Un détecteur interne ou trajectographe, composé d'un détecteur à Pixels de

Scilicium, d'un détecteur a micropistes de Scilicium et d'un détecteur à rayonnement de transition. Le détecteur interne baigne dans un champ magnétique de 2 Tesla fourni par un aimant solenoïdale supraconducteur. Le détecteur interne permet de determiner la trajectoire des particules chargées comme les électrons et les muons, et d'en mesurer ensuite leurs impulsions. Grâce a sa grande résolution, il permet aussi de reconstruire non seulement les vertex primaires d'interaction entre pacquets de proton mais aussi les vertex secondaires issus de la désintégration de particules de très courtes durée de vie au voisinage du point d'intéraction.

- Un calorimètre, formé d'un calorimètre électromagnétique et d'un calorimètre hadronique. Le calorimètre électromagnétique utilise l'Argon liquide comme milieu actif et le plomb comme absorbeur. Il permet la mesure des énergies des électrons et des photons à partir de leurs gerbes électromagntétiques. Le calorimètre hadronique est formé de tuiles scintillantes et d'absorbeurs en fer. Il permet de mesurer les énergies des particules hadroniques à partir de leurs gerbes hadroniques. Le calorimètre permet aussi de mesurer l'énergie transverse manquante.

- Un spectromètre à muons constitué de grandes chambres à muons composées de tubes à dérive qui baignent dans un champ magnétique de 1 Tesla fournit par un aimant toroïdal supraconducteur. Le spectromètre à muons permet de mesurer les traces des muons ainsi que leurs impulsions avec une très bonne précision et une grande efficacité.

Les différents algorithmes d'identification et de reconstructions des objets physiques dans ATLAS sont détaillés dans le quatrième chapitre. Tout d'abord, la reconstruction des traces chargées dans le détecteur interne est présentée. L'identification et la reconstruction des électrons dans le calorimètre électromagnétique avec l'association d'une trace chargée identifiée dans le trajectographe est ensuite détaillée. Dans ATLAS, il existe trois types d'identification des électrons: "Loose", "medium" et "tight" qui diffèrent suivant la sévérité des coupures appliquées sur des variables reconstruites à partir des informations issues du trajectographe et du calorimètre électromagnétique. L'identification et la reconstruction des muons dans le spectromètre à muons et dans le trajectographe est ensuite présentée. La reconstruction des jets dans le calorimètre hadronique en utilisant un algorithme qui cherche les dépôts d'énergies dans un cône fixe, ainsi que la calibration de leurs énergies sont décrites par la suite. La dernière partie du chapitre est dédiée à l'algorithme de

reconstruction de l'énergie transverse manquante et sa calibration.

La première analyse que j'ai effectué, présentée dans le chapitre 5, a été réalisée avec les données enregistrées par le détecteur ATLAS en 2010 avec une énergie au centre de masse de $\sqrt{s} = 7$ TeV. Cette analyse porte sur la mesure de l'efficacité de l'étiquetage des jets issus de quarks b sur un ensemble de données correspondant à 35 pb^{-1}. L'étiquetage des jets issus de quarks b est la capacité d'identifier les jets qui sont issus de la hadronisation de quarks b. Cette identification est très importante car plusieurs analyses de physiques, en particulier les canaux impliquant le quark top, le boson de Higgs ainsi que des canaux de recherche de nouvelle physique, présentent dans leurs états finals des jets issus de la hadronisation de quarks b. Plusieurs algorithmes d'identification des jets issus de quarks b sont utilisés dans ATLAS. Ils reposent essentiellement sur les propriétés des hadrons b. Leur fragmentation est dure, ce qui fait qu'une grande partie de l'énergie initiale du quark b est transmise au hadron b final, contraitrement aux quarks plus légers (u, d, c et s) qui ont une fragmentation plus souple. Les hadrons b ont une durée de vie relativement longue en raison de leur désintégration par intéraction faible. Par conséquent, ils ont, avant de se désintégrer, une longueur de vol importante dans le détecteur. La distance parcourue dans le détecteur dépend de l'impulsion du hadron b. Un quark b avec, par exemple, une impulsion de 50 GeV parcourera environ 3mm, une distance qui est mesurable dans le détecteur, avant de se désintégrer ce qui résulte en un vertex secondaire déplacé par rapport au vertex primaire. Cette propriété est largement exploitée par les algorithmes d'étiquetage des jets issus de quarks b soit en reconstruisant directement le vertex secondaire, ou en mesurant le grand paramètre d'impact transverse des traces issues de la désintégration des hadrons b. Le paramètre d'impact transverse correspond à la distance d'approche minimale entre la trace projetée dans le plan transverse et la projection dans ce même plan du vertex primaire. Les traces provenant de la désintégration du hadron b ont un paramètre d'impact transverse relativement grand ce qui permet de les distinguer des traces provenant directement du vertex primaire. Une autre propriété très importante des hadrons b est leur désintégration semi-leptonique qui permet d'identifier les jets b en identifiant des leptons dans les jets.

La mesure de l'efficacité d'étiquetage des jets issus de quarks b est d'une grande importance pour toute analyse de physique qui présente au moins un quark b dans son état final et qui utilise des algorithmes d'identifications des jets b. Dans ATLAS, l'efficacité d'étiquetage des jets issus de quarks b est effectué soit en selectionnant des événements top-antitop soit des événements avec des jets b contenant un muon. Pour ces derniers, deux méthodes sont utilisées dans ATLAS: p_T^{rel} et $System8$. La méthode sur laquelle j'ai travaillé est la méthode $System8$. Cette méthode, comme son nom l'indique, consiste en 8 equations non-linéaires

avec 8 inconnus dont l'efficacité d'étiquetage des jets issus d'un quark b. Deux échantillons sont sélectionnés pour pouvoir mesurer l'efficacité des algorithmes d'étiquetage des jets b. Le premier échantillon est sélectionné en exigeant la présence d'au moins un jet contenant un muon, en appliquant des coupures de qualités sur le muon et le jet. Le deuxième échantillon est un sous-ensemble du premier, formé en exigeant que le jet contenant un muon ait un jet opposé, étiqueté comme jet issu d'un quark b. Ceci permet de disposer de deux échantillons d'événements avec une fraction de jets b différente. Une fois ces deux échantillons sont formés, on applique deux algorithmes d'étiquetage non correlés ce qui permet d'obtenir un système de 8 equations (voir Eq. 5.8) avec 8 inconnus ainsi que 8 facteurs de correlations qui tiennent compte de la correlations des deux algorithmes d'étiquetage des jets issus de quarks b. Les facteurs de correlation sont en partie mesurés en utilisant la simulation, et c'est la seule information que *System*8 utilise à partir de la simulation Monte Carlo. Pour résoudre ce système de 8 equations à 8 inconnus, j'utilise la méthode de minimisation de χ^2 (voir Eq. 5.10) à partir d'un ajustement utilisant le programme MINUIT. La matrice de covariance des 8 facteurs de correlation est aussi incluse dans le fit pour pouvoir estimer l'incertitude sur ces facteurs. J'ai utilisé cette approche pour mesurer l'efficacité de deux algorithmes qui ont été concus pour les premières données issues des collisions proton-proton au LHC: `JetProb` et `SV0`. Les résultats obtenus avec la méthode *System*8 sont en très bon accord avec ceux obtenus avec la méthode p_T^{rel} comme le montre les Figures 5.29 et 5.30. Les résultats obtenus avec la méthode *System*8 ont d'abord servi pour vérifier les résultats obtenus avec la méthode p_T^{rel} qui était la méthode standard utilisé par les groupes de physiques dans ATLAS. La méthode *System*8 bien que plus compliquée que la méthode p_T^{rel}, s'appuie moins sur la simulation ce qui présente l'avantage d'être moins sensible aux effets systématiques résultants de la simulation Monte Carlo. Depuis la mise en service de *System*8 en 2010, ses résultats sont combinés avec ceux de la méthode p_T^{rel}. Le résultat de cette combinaison est communiqué aux groupes de physiques dans ATLAS ce qui a réduit largement l'erreur systématique résultante de l'utilisation de l'étiquetage des jets issus de quarks b dans les analyses de physiques.

La deuxième partie de cette thèse décrit la mesure de la section efficace différentielle de la production des paires de quarks top-antitop en utilisant 4.7 fb^{-1} de données enregistrées par le détecteur ATLAS en 2011 à une énergie au centre de masse de 7 TeV. Le quark top a été découvert en 1995 au TeVatron. C'est la particule élémentaires la plus massive jamais observée et ses propriétés ne sont pas encore connues avec précision. Le LHC est une usine à top vue la grande section efficace de production de ce quark aux énergies fournies par le LHC. Il est produit essentiellement en paires top-antitop. Deux grands secteurs de recherche sur l'étude des propriétés de ce quark sont ouverts au LHC: les mesures de pré-

cision de ses propriétés dans le cadre du Modèle Standard, et la recherche de signe d'une nouvelle physique au-delà du Modèle Standard. Grâce à sa masse très élevée, le quark top pourrait être lié à la présence de nouvelles particules ou de nouveaux couplages non décrit par le Modèle Standard. La mesure de la section efficace de production des paires top-antitop est une mesure importante car elle permet de tester et valider les modes de production du quark top dans le cadre du Modèle Standard. La mesure de la section efficace différentielle de la production des paires top-antitop en fonction de sa masse et de sa rapidité permet de son côté d'ouvrir une nouvelle fenêtre sur la recherche de signe d'une physique au-delà du Modèle Standard. En effet, si une particule massive se couple avec le quark top, celà apparaîtra comme soit une résonnance soit une distortion dans le spectre de la section efficace différentielle en fonction de la masse du système $t\bar{t}$ ou de sa rapidité.

Le quark top se désintègre presque à 99% des cas en un quark b et un boson W. Le boson W se désintègre leptoniquement dans $\approx 33\%$ des cas en un lepton (électron, muon ou tau) et son neutrino correspondant et dans le reste des cas, il désintègre hadroniquement en une paire de quark-antiquark. Selon la désintégration du boson W, on peut distinguer trois canaux de désintégration des paires top-antitop: le canal dileptonique où les deux bosons W se désintègrent leptoniquement, le canal tout hadronique où les deux bosons W se désintègrent hadroniquement et le canal semi-leptonique où un boson W se desintègre leptoniquement et le deuxième se désintègre hadroniquement. J'ai effectué la mesure de la section efficace différentielle des paires top-antitop dans le canal semi-leptonique qui est un bon compromis entre les deux autres canaux: il ne souffre pas du grand bruit de fond combinatoire que présente le canal tout hadronique qui a six jets dans son état final, ni de la grande énergie transverse manquante due à la présence de deux neutrinos dans le canal dileptonique, le neutrino n'étant pas directement détécté dans le détecteur à cause de sa très faible interaction avec la matière. Pour la sélection des événements candidats top-antitop, je demande que les événements passent un système de déclenchement qui exige que l'événement ait un lepton avec une grande impulsion transverse. J'applique ensuite une série de coupures sur les différents objets reconstruits pour garder à la fin les événements qui ont exactement un lepton (électron ou muon) de grande énergie bien identifié et reconstruit, au moins quatres jets de grandes énergies bien identifiés dont au moins un jet qui est étiqueté comme étant un jet issu d'un quark b et une grande énergie transverse manquante qui représente le neutrino issu de la désintégration leptonique du boson W. Une fois les évenements candidats top-antitop identifiés, la reconstruction du système top-anitop est ensuite effectuée en passant les objets physiques reconstruits dans un ajustement de vraissemblance qui teste toutes les combinaisons possibles pour reconstruire le quark top, l'antiquark top et ensuite le système top-antitop. La combinaison avec des jets, un lepton et une énergie

transverse manquante possédant la plus grande probabilité de vraissemblance au système top-antitop est retenue.
Les bruits de fond des événements top-antitop se divisent en deux parties: bruit de fond de physique et bruit de fond instrumental. Les bruits de fond de physique sont dominés par les événements $W + jets$ qui présentent la même signature que les événements top-antitop et qui peuvent ainsi passer la préselection. Ce bruit de fond est éstimé à partir des données. Les autres bruits de fond de physique sont moins dominants et sont de nature électrofaible: les événements $Z + jets$, la production du top singlet et la production associée de deux bosons (WW, WZ et ZZ). Ces bruits de fond sont éstimés à partir de la simulation Monte Carlo. Le bruit de fond intrumental essentiel, estimé à partir des données, est la production d'événements multi-jets où il y a au moins un jet qui est mal identifié et reconstruit comme un lepton. Une partie de ces événements a la même signature qu'un événement top-anitop et passe donc les critères de sélection . Une fois les bruits de fond éstimés, la section efficace est mesurée dans 5 bins de masse du système top-antitop et 6 bins de sa rapidité après avoir corriger ces spectres par une fonction qui tient compte de la résolution du détecteur ATLAS, pour pouvoir comparer les résultats obtenus avec les prédictions théoriques. Les résultats sont comparés avec les prédictions du $2^{\text{ème}}$ ordre (NLO) et l'approximation NNLO. Aucune distortion visible n'est observée dans les spectres de la section efficace différentielle en fonction de la masse et de la rapidité du système top-antitop. Les distributions sont tout à fait compatibles avec les prédictions du Modèle Standard.

Introduction

The Standard Model of particle physics is very successful in describing elementary particles and their interactions with a great precision. It describes three of the four known fundamental interactions between elementary particles: the weak, the strong and the electromagnetic interactions. The Standard Model also provides an accurate description of the electroweak interactions up to energy scales that have been explored in high energy physics experiments. The interaction and decay of a large number of particles discovered and observed throughout different experiments in the last 50 years are also described.

Despite its great success, the Standard Model falls short of being a complete theory of fundamental interactions because it does not incorporate the full theory of gravitation as described by general relativity, or predict the accelerating expansion of the universe (as possibly described by dark energy). The theory does not contain any viable dark matter particle that possesses all of the required properties deduced from observational cosmology. It also does not account for neutrino oscillations (and their non-zero masses). It is thought that new physics should exist leading to new particles and phenomena. The scale at which this new physics should appear is not well known, though several arguments point to the TeV scale and require a very high energy and powerful hadron collider.

The Large Hadron Collider (LHC) is the biggest existing particle accelerator and collider. It is designed to provide proton-proton collisions with an unprecedented center-of-mass energy of $\sqrt{s} = 14$ TeV, with instantaneous luminosities up to 10^{34} cm^{-2}s^{-1}. The LHC has provided proton-proton collisions with center-of-mass energy of $\sqrt{s} = 7$ TeV during 2010 and 2011. In 2012, the LHC is providing collisions with 8 TeV center-of-mass energy and it is expected to provide collisions with the nominal or close to nominal center-of-mass energy at the beginning of 2015. Two multipurpose experiments, ATLAS and CMS, are installed on the LHC ring to analyze the collisions.

The ATLAS detector is formed by several sub-detectors with different technologies. The ATLAS experiment is designed to take advantage of the unprecedented energy provided by the LHC and observe phenomena that involve highly

massive particles which were not observable using earlier lower-energy accelerators. It might shed light on new theories of particle physics beyond the Standard Model. Particle physicists use the data recorded by the ATLAS detector in order to identify different known particles as well as to search for new signatures and eventually discover new particles.

This thesis describes two analysis that involve the 2010 and the 2011 data recorded by the ATLAS detector with a center-of-mass energy of $\sqrt{s} = 7$ TeV. The first analysis is the measurement of the b-tagging efficiency on a data set of 35 pb^{-1} recorded by ATLAS in 2010. b-tagging is the ability to identify the jets that are stemming from the hadronization of b-hadrons. It is of big importance for many physics analysis that involve the signature of b-jets in the final state. The second part of this thesis describes the measurement of the $t\bar{t}$ differential cross section using the 4.7 fb^{-1} of the 2011 ATLAS data. The top quark is still a not very well known particle, and the study of its properties is of a big importance especially since it is the most massive known particle till these days. This dissertation is organized as follows:

- Chapter 1 is an introduction to the Standard Model of particle physics.

- Chapter 2 describes the role of the top quark within the Standard Model and beyond it, with the motivation behind the measurement of the $t\bar{t}$ differential cross section.

- Chapter 3 describes the LHC collider and the ATLAS detector.

- Chapter 4 describes the different algorithms used in ATLAS for the identification and the reconstruction of the physics objects, especially the algorithms that are used later for the b-tagging efficiency measurement as well as the ones used for the $t\bar{t}$ differential cross section measurement.

- Chapter 5 presents an overview of the different b-tagging algorithms used in ATLAS, the data driven method used for the measurement of the b-tagging efficiency, as well as the results on the full 2010 ATLAS data.

- Chapter 6 presents the measurement of the $t\bar{t}$ differential cross section as function of the $t\bar{t}$ mass and its rapidity, using the full 2011 ATLAS data.

Chapter 1

Introduction to the Standard Model

Developed in the 1960s and 1970s, the Standard Model [1, 2, 3] (SM) of particle physics is the theoretical framework which describes the elementary particles and their interactions. It is a relativistic quantum fields theory built on the principles of gauge invariance under the symmetry group $SU(3)_C \otimes SU(2)_L \otimes U(1)_Y$, and spontaneous breaking of the electroweak $SU(2)_L \otimes U(1)_Y$ to the electromagnetic local phase symmetry $U(1)_{em}$. The ability of the SM model to accurately describe all measurements carried out to date with particle accelerators makes it a well established model, and a reference model for all studies of the particles, their production and their interactions and decays. Many experiments were carried out in the course of the 20^{th} century to study and understand the composition of matter. These experiments have led to the observation and the discovery of different elementary particles described by the SM, except the "Higgs boson", which was until July 2012, the main missing piece of the SM. Refined techniques and more powerful experiments, like those carried out at the Large Hadron Collider (LHC), are required to solve the remaining open questions of the SM and maybe discover predicted or unpredicted new physics beyond it. The LHC, described in details in Chapter 3 Section 3.1 collides two proton beams at world-record center-of-mass energies. The LHC has led recently, by ATLAS and CMS experiments, to the observation of a new "Higgs-like" particle, in the mass region around 126.5 GeV [4, 5], at the level of 5 sigma, where the expected significance of the presence of a SM Higgs boson with the same mass is 4.6 sigma. The SM and its elementary particles as well as the fundamental interactions are described in Section 1.1.

1.1 The Standard Model

The Standard Model has been remarkably successful in describing all known and observed particles as well as three of the four known fundamental interactions:

the strong, the weak and the electromagnetic interactions. The gravitational interaction, described by the General Relativity which is not a quantum theory, is not included in the SM, because to date there is no rigorous quantum mechanical description of the force of gravity. On the other hand, the standard[1] gravitational interaction is at energy scales probed by particle colliders, extremely weak compared to other fundamental interactions. In the SM, the elementary particles are divided into two categories according to their spin:

- The fermions, particles with a spin 1/2. They are the building block of matter. The fermions are divided into two categories:

  - six leptons: they hold a leptonic number. They are divided into three electrically charged fermions sensitive to the weak and the electromagnetic interactions, and three electrically neutral fermions sensitive to the weak interaction only.

  - six quarks: they are electrically charged, hold a color charge and are sensitive to the weak, the electromagnetic and the strong interactions. They hold a baryonic number.

  Both leptons and quarks are divided into three families/generations. The first family of leptons is formed by the electron and its associated neutrino, and the first quark family contains the up and down quarks. The two other families are replicas of the first family, their particles having different mass and flavor. The second family of leptons is composed of the muon and its associated neutrino, the third and last one is formed by the tau and its associated neutrino. The second family of quarks is formed by the charm and the strange quarks, and the third one is formed by the bottom and the top quarks. Each fermion has its anti-particle with the same mass and spin but with opposite charges (electric charge, color charge etc.). Table 1.1 and Table 1.2 show the three generations of the leptons and the quarks respectively with their leptonic and baryonic numbers, their electric charge and their mass.

[1] Alternative models to standard gravitational interaction like extra dimension models predicts gravitational effects to show up at TeV scale.

- The bosons, particles with a spin equal to unity. SM fundamental interactions are described in terms of spin 1 boson exchanges between fermions. There are three kinds of bosons:

  - the photon (γ) which is the particle of light, is the mediator of the electromagnetic interaction. The photon is massless[2] and stable therefore the electromagnetic interaction has an infinite range. The photon can interact with all the particles carrying an electric charge.

  - The gluons are the mediators of the strong interactions. There are eight gluons that differ by their color charge. They are massless, but due to the confinement[3] property of the strong interaction, its range is finite. The gluons can, contrary to the photon, interact among themselves and interact with all particles carrying a color charge.

  - The $W^{\pm}$ and Z bosons are the mediators of the weak interactions between particles of all flavors carrying a weak isospin and a weak hypercharge quantum numbers. The W boson has a mass of 80.385 $\pm$ 0.015 GeV [6] and Z boson has a mass of 91.187 $\pm$ 0.002 GeV [6]. They both have a finite lifetime, therefore, the range of the weak force is finite too.

  The gravitational interaction is, at energy scales relevant for experimental particle physics, many orders of magnitude weaker than the other three fundamental interactions and can be totally neglected. Table 1.3 shows the four fundamental interactions and their properties.

1.1.1 Quantum Electrodynamics

The Quantum Electrodynamics (QED) is the part of the SM that describes the electromagnetic interaction between fermions. It is an abelian gauge theory with the local symmetry group $U(1)$. The QED Lagrangian for a spin 1/2 particles interacting with the electromagnetic field is given by the real part of:

$$\mathscr{L} = \overline{\psi}(i\gamma^{\mu}D_{\mu} - m)\psi - \frac{1}{4}F_{\mu\nu}F^{\mu\nu} \tag{1.1}$$

[2]Experimental measurements show that its mass is less than 1×10^{-18} eV [6].

[3]One of the most important properties of QCD is the confinement [7] which forbids the presence of free colored particles.

Family	Particle	Charge	Mass
1^{st}	e	-1	0.511 MeV
	ν_e	0	< 2 eV
2^{nd}	μ	-1	105.66 MeV
	ν_μ	0	< 0.19 MeV
3^{rd}	τ	-1	1.78 GeV
	ν_τ	0	< 18.2 MeV

Table 1.1: Leptons classification showing the electric charge and the particle mass, taken from [6].

Family	Particle	Charge	Mass
1^{st}	u	+2/3	$2.3^{+0.7}_{-0.5}$ MeV
	d	-1/3	$4.8^{+0.7}_{-0.3}$ MeV
2^{nd}	c	+2/3	1.275 ± 0.025 GeV
	s	-1/3	95 ± 5 MeV
3^{rd}	t	+2/3	$173.5 \pm 0.6 \pm 0.8$ GeV
	b	-1/3	4.18 ± 0.03 GeV

Table 1.2: Quarks classification showing the electric charge and the particle mass, taken from [6].

Interaction	Charge	Boson Vector	Range[m]
Strong	Color	gluons	10^{-15}
Electromagnetic	electric charge	photon	∞
Weak	weak isospin	$W^{\pm}, Z$	10^{-18}
Gravitational	mass	graviton ?	∞

Table 1.3: Fundamental interactions and some of their properties. The gravitational interaction is not described by the SM but, it is added for completeness.

where γ^μ are the Dirac matrices, ψ a bispinor field of spin 1/2 particles (e.g. electron or positron fields), $\overline{\psi} \equiv \psi^\dagger \gamma_0$ is referred to as Dirac adjoint, $D_\mu \equiv \partial_\mu + ieA_\mu$ is the gauge covariant derivative where e is the electromagnetic coupling coefficient equal to the electric charge of the bispinor field, A_μ is the covariant four-potential of the electromagnetic field generated by the electron itself. The electromagnetic field tensor $F_{\mu\nu}$ is given by:

$$F_{\mu\nu} = \partial_\mu A_\nu - \partial_\nu A_\mu \tag{1.2}$$

The QED Lagrangian, shown in Eq. 1.1, is invariant under local $U(1)$ transformations:

$$\psi \rightarrow e^{i\alpha(x)}\psi \tag{1.3}$$

and

$$A_\mu \rightarrow A_\mu - \frac{1}{g_e}\partial_\mu \alpha(x) \tag{1.4}$$

where g_e is the electromagnetic coupling constant of the elementary unit of charge $e = \sqrt{4\pi\alpha}$. A mass term for the photon field of the form $\frac{1}{2}MA^\mu A_\mu$ is forbidden by the gauge symmetry, consistent with the massless photons observed experimentally.

1.1.2 Quantum Chromodynamics

The current theoretical picture of the strong interaction begins with the identification of the elementary partons. As the properties of these partons became better understood, the nature of their interactions became tightly constrained, in a way that led eventually to a unique candidate theory. In 1963, M. Gell-Mann and G. Zweig proposed a model [8, 9] known as the quark model that explained the spectrum of strongly interacting particles in terms of elementary constituents, what we call today the quarks. In 1969, Richard Feynman introduced the parton model as a way to analyze high-energy hadron collisions [10]. In this model, a hadron like a proton for example is composed of a number of point-like constituents, named "partons", what are referred now to as quarks and gluons. In 1972, M. Gell-Mann and H. Fritzsch introduced the conserved quantum number "color charge", and later along with H. Leutwyler, they introduced quantum chromodynamics (QCD) as the gauge theory of the strong interaction [11]. Color was introduced to explain the observation of, for example, the Δ^{++} baryon, a *uuu* state. Such state, with all three *u* quarks having the same quantum numbers violates the Pauli exclusion principal, with the three fermions occupying the same state. The introduction of three colors - red, blue and green - allows the fermions to each carry an additional quantum number and occupy the same state. Quarks are found in colorless confined states of baryons or mesons, but never free. The baryons are three quark states with equal mixtures of red, green and blue, while mesons are two quark states of a color and its anti-color.

The gauge theory of QCD is invariant under transformations of the non-Abelian

$SU(3)$ Yang-Mills [12] group. The QCD Lagrangian is given by:

$$\mathscr{L}_{\mathrm{QCD}} = \overline{\psi}_i \left(i\gamma^\mu (D_\mu)_{ij} - m\,\delta_{ij} \right) \psi_j - \frac{1}{4} G^a_{\mu\nu} G^{\mu\nu}_a \tag{1.5}$$

where $\psi_i(x)$ is the quark field, a dynamical function of space-time, in the fundamental representation of the $SU(3)$ gauge group, indexed by i,j. $G^a_\mu(x)$ are the gluon fields, also a dynamical function of space-time, in the adjoint representation of the $SU(3)$ gauge group, indexed by a, b. The γ^μ are Dirac matrices connecting the spinor representation to the vector representation of the Lorentz group. The symbol $G^a_{\mu\nu}$ represents the gauge invariant gluonic field strength tensor, analogous to the electromagnetic field strength tensor, $F^{\mu,\nu}$, in QED. It is given by

$$G^a_{\mu\nu} = \partial_\mu G^a_\nu - \partial_\nu G^a_\mu - g f^{abc} G^b_\mu G^c_\nu \tag{1.6}$$

where f^{abc} are the structure constants of $SU(3)$.

The gluon-gluon interaction term in Eq. 1.6 is responsible for the increase in the strength of the QCD coupling at large distances. At small length scales (large energies) the quarks and gluons behave as quasi-free particles because the strong coupling is small[4]. In the high energy regime, QCD can be described perturbatively. At large separations (low energies), the strong coupling is large and quarks and gluons form bound states. The global $SU(3)$ symmetry of QCD leads to conservation of color, where only colorless bound states are observed.

1.1.3 The Weak Interactions

The weak interaction differs[5] quite a lot from the strong and the electromagnetic interactions, and it is responsible for the radioactive decay of subatomic particles and initiates the process known as hydrogen fusion in stars. The weak charged current interaction couples only to left handed particles. The field Ψ is decomposed into a left handed field and a right handed one: $\Psi_L = \frac{1}{2}(1-\gamma_5)\Psi$ and $\Psi_R = \frac{1}{2}(1+\gamma_5)\Psi$. The $(1-\gamma_5)$ structure is known as the $V-A$ form of the charged weak current. The weak isospin is a quantum number which governs how particles interact weakly. The weak isospin is to the weak interaction what electric charge is to the electromagnetism, and what color charge is to strong interaction. The fermions have weak isospin values of $\pm\frac{1}{2}$. The up-type quarks (u,c,t) have a weak isospin of $+\frac{1}{2}$ and always transform via weak charge current interaction

[4]The scale of QCD is set by $\Lambda_{QCD} = 217^{+25}_{-23}$ MeV . "Small" and "large" energies are small or large with respect to Λ_{QCD}.

[5]Weak interaction proceeds via two fundamental processes: weak charge current interaction with $W^\pm$ bosons as mediators and weak neutral current interaction with Z^0 boson as mediator.

into down-type quarks (d,s,b), which have an opposite weak isospin of $-\frac{1}{2}$, and vice-versa. On the other hand, at a first order, a quark never decays weakly into a quark of the same weak isospin. Bosons have weak isospin of ± 1, or 0. Weak isospin is conserved: the sum of the weak isospin numbers of the particles exiting a reaction equals the sum of the weak isospin numbers of the particles entering that reaction. For example, a π^+, with a weak isospin of 1 normally decays into a ν_μ with a weak isospin of $+\frac{1}{2}$ and a μ^+ with a $+\frac{1}{2}$ weak isospin. Table 1.4 shows the left handed fermions with their weak isospin. The right handed particles have 0 weak isospin. The weak interaction couples quarks of different flavors. For ex-

Family	Fermion	Weak Isospin
1^{st}	e^-	$-\frac{1}{2}$
	ν_e	$+\frac{1}{2}$
	u	$+\frac{1}{2}$
	d	$-\frac{1}{2}$
2^{nd}	μ^-	$-\frac{1}{2}$
	ν_μ	$+\frac{1}{2}$
	c	$+\frac{1}{2}$
	s	$-\frac{1}{2}$
3^{rd}	τ^-	$-\frac{1}{2}$
	ν_τ	$+\frac{1}{2}$
	t	$+\frac{1}{2}$
	b	$-\frac{1}{2}$

Table 1.4: Left-handed fermions in the Standard Model with their weak isospin.

ample, in the decay of a pion, $\pi^+ \to \mu^+ \nu_\mu$ shown in Fig. 1.1, the weak interaction couples the u to the $\overline{d}$ quark. The weak interaction is the only interaction capable of changing the flavor of quarks (i.e., of changing one type of quark into another). A neutron, for example, is heavier than a proton, but it cannot decay into a proton without changing the flavor of one of its two down quarks to up. Flavor changing is not possible with electromagnetic and strong interactions.

In terms of strength, the weak interaction is weaker than the electromagnetic and the strong interaction at energy scales probed by the SM.

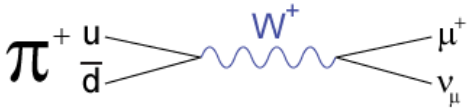

Figure 1.1: The Feynman diagram for the decay of π^+.

The W and Z bosons of the weak interaction are massive and have a short lifetime of the order of 10^{-24} s [13]. In the case of QED or QCD, the gauge symmetry of the Lagrangian requires the photon and the gluons to be massless. Massive gauge bosons suggest that the symmetry of the weak interaction is inexact: i.e. the Lagrangian and the physical vacuum do not obey the same symmetry. This is the case for a spontaneously broken symmetry [14]. Furthermore, the interference of the electromagnetic and neutral current processes suggest a unification of the electromagnetic and weak interactions, the "electroweak" interaction. To introduce gauge bosons (W and Z) masses in a way which preserves the original gauge invariance of the Lagrangian, P. Higgs, R. Brout, F. Englert [15, 16] suggested in 1964 a spontaneous symmetry breaking mechanism which could lead to massive bosons in a non-Abelian Yang-Mills theory. This is the so-called "Higgs mechanism", giving rise to a scalar particle, the Higgs boson. The fermionic masses are generated by adding ad-hoc interaction terms of the fermions with this Higgs field.

1.1.3.1 The Yukawa Coupling and the Cabibbo Kobayashi Maskawa (CKM) Mixing Matrix

The fermion mass terms of the form $m\overline{\Psi}\Psi = m(\overline{\Psi}_L\Psi_R + \overline{\Psi}_R\Psi_L)$ are forbidden under the electroweak gauge symmetry as the left and right components does not transform the same way under $SU(2)$, therefore they are not allowed in the Lagrangian. The fermions are as we know massive, with the top quark being by far the heaviest state among them, so the electroweak gauge theory must incorporate massive fermions in some way. This is done by adding the following Yukawa term for fermions, where the Higgs field couples the left and right handed fermions according to:

$$\mathscr{L}_{\text{Yukawa}} = -\frac{1}{\sqrt{2}}\lambda_f(H(x)+\upsilon)(\overline{F}_R F_L + \overline{F}_L F_R) \tag{1.7}$$

where $H(x)$ is the Higgs field, υ is vacuum expectation value (vev) which is equal to 246 GeV [17], F is the fermion (lepton or quark) field and λ_f is known as the Yukawa coupling of the fermions to the Higgs boson. The mass of each fermion

is given by:

$$m_f = \frac{1}{\sqrt{2}}\lambda_f \upsilon \tag{1.8}$$

Given the high mass of the top quark, its coupling λ_t to the Higgs boson is expected to be of the order of one. The reason behind this is an open question in the Standard Model.

The Yukawa Lagrangian in equation 1.7 is gauge invariant under the electroweak gauge transformation but it does not follow from any gauge principle. It is possible to write a Yukawa interaction that is gauge invariant and mixes the generations:

$$\mathscr{L}^{quark}_{\text{Yukawa}} = -\frac{1}{\sqrt{2}}\Lambda^u_{ij}(H(x)+\upsilon)(\overline{u}^i_R u^i_L + \overline{u}^i_L u^i_R) - \frac{1}{\sqrt{2}}\Lambda^d_{ij}(H(x)+\upsilon)(\overline{d}^i_R d^i_L + \overline{d}^i_L d^i_R) \tag{1.9}$$

where u^i and d^i are an up-type and a down-type quark respectively. Under the assumption of zero neutrino mass, there is no such Lagrangian for the lepton sector. The eigen-fields of the Yukawa Lagrangian are fields with definite mass and diagonal mass matrices. These fields are related to the fields of equation 1.7 by bi-unitary transformations. In other words, there is a change of basis from the eigen-fields of definite mass to the eigen-fields of the weak interaction. The neutral-current interactions remain unchanged by the change of basis. However, now the charged-current interaction couples quarks of different generations, as in the decay $D^0 \to K^+\pi^-$. The mixing is conventionally ascribed to the down-type quarks such that:

$$\begin{pmatrix} d' \\ s' \\ b' \end{pmatrix} = \begin{pmatrix} V_{ud} & V_{us} & V_{ub} \\ V_{cd} & V_{cs} & V_{cb} \\ V_{td} & V_{ts} & V_{tb} \end{pmatrix} \begin{pmatrix} d \\ s \\ b \end{pmatrix} \tag{1.10}$$

where the $d^{i'}$ quarks are the weak interaction eigen-fields. The 3×3 unitary mixing matrix is known as the Cabibbo Kobayashi Maskawa (CKM) matrix [18, 19]. Not all elements of the CKM matrix have been directly probed by experiment. However, the unitarity of the matrix puts constraints on the unmeasured elements. The matrix is approximately diagonal, as expected by the dominance of same generation charged- current decays over different generation charged-current decays.

Chapter 2

Top Quark Physics

The Top quark was discovered in 1995 [20, 21] by the CDF and DØ experiments at the TeVatron proton-antiproton collider. It is the heaviest known elementary particle, ≈ 40 times larger than the mass of the next heavy quark, and is close to the electroweak symmetry breaking scale. This unique property raises a number of interesting questions. For example, is the top quark mass generated by the Higgs mechanism as the Standard Model predicts? Does it couple strongly with the fields responsible for the electroweak symmetry breaking? Or does it play an even more fundamental role in the electroweak symmetry breaking mechanism? Produced predominantly in hadron-hadron collisions, through strong interactions, the top quark, contrary to the other quarks, decays without forming a hadron state. This has important consequences. Above all, it offers the possibility to explore the interactions of a bare quark at energies of a few hundred GeV to several TeV. Furthermore, it is an important asset of top quark physics as not only the effects of the electroweak interactions, but also of the strong interactions of these particles can, in most situations, be reliably predicted and compared to measurements.
The LHC is a top factory: for a top mass of 172 GeV, the top pair production cross section with a center-of-mass energy of 14 TeV is 854^{+105}_{-104} pb [22] at NLO and at $\approx$ NNLO it's 919^{+75}_{-55} pb [22], while at the TeVatron, the top pair production cross section with a center-of-mass energy of 1.96 TeV is $7.01^{+0.58}_{-0.84}$ pb [22] at NLO and at exact NNLO it's 7.0056 pb [23]. This opens the possibility to explore the quark top with an unprecedented precision at the LHC. The Top quark production modes at the LHC are detailed in Section 2.1 and its decay is detailed in Section 2.2 and the profile of the top quark is presented in Section 2.3,

2.1 The Top Quark Production at the LHC

2.1.1 Single Top Production

The production of the single top in the SM is an electroweak process which happens via three different channels:

- the t-channel, shown in Fig. 2.1 (a). The single top quark has been discovered in the t-channel in 2009 by the DØ and the CDF collaborations at the TeVatron [24, 25]. This channel has been also observed at the LHC by the ATLAS and the CMS collaborations [26, 27]. The single top production cross section, in the t-channel, at NLO for a top mass of 172 GeV at the LHC with a center-of-mass energy of 7 TeV is $42.2^{+1.2}_{-0.7}$ pb [28] while with a center-of-mass energy of 14 TeV, it is expected to be $156.9^{+1.8}_{-3.6}$ pb [28].

- the Wt-channel, shown in Fig. 2.1 (b), is an associated production of a top quark and a W boson. The ATLAS and CMS collaborations have found evidence for this channel published in 2012 [29, 30]. The Wt production cross section at NLO for a top mass of 172 GeV at the LHC with a center-of-mass energy of 14 TeV is expected to be 60 pb [31].

- the s-channel, shown in Fig. 2.1 (c). The s-channel has not been observed yet at the LHC and also many searches are being carried out to observe the single top in this channel [32]. The s-channel production cross section at NLO for a top mass of 172 GeV at the LHC with a center-of-mass energy of 14 TeV is expected to be around 10 pb [31].

However, in a hadron collider, the dominant process for the production of the top quark is the production of pair top-antitop ($t\bar{t}$) via the strong interaction.

2.1.2 Top-Quark Pair Production

At the LHC, the top pair quark production happens through both gluon-gluon and quark-antiquark scattering. The top pair production at leading order is shown in Fig. 2.2. Since the LHC is a p-p collider with a high center of mass energy[1] of the collision, the dominant production process is the gluon-gluon fusion, almost

[1] 7 TeV during 2011 data taking, 8 TeV during 2012 and expected to reach the nominal design value of 14 TeV in 2015.

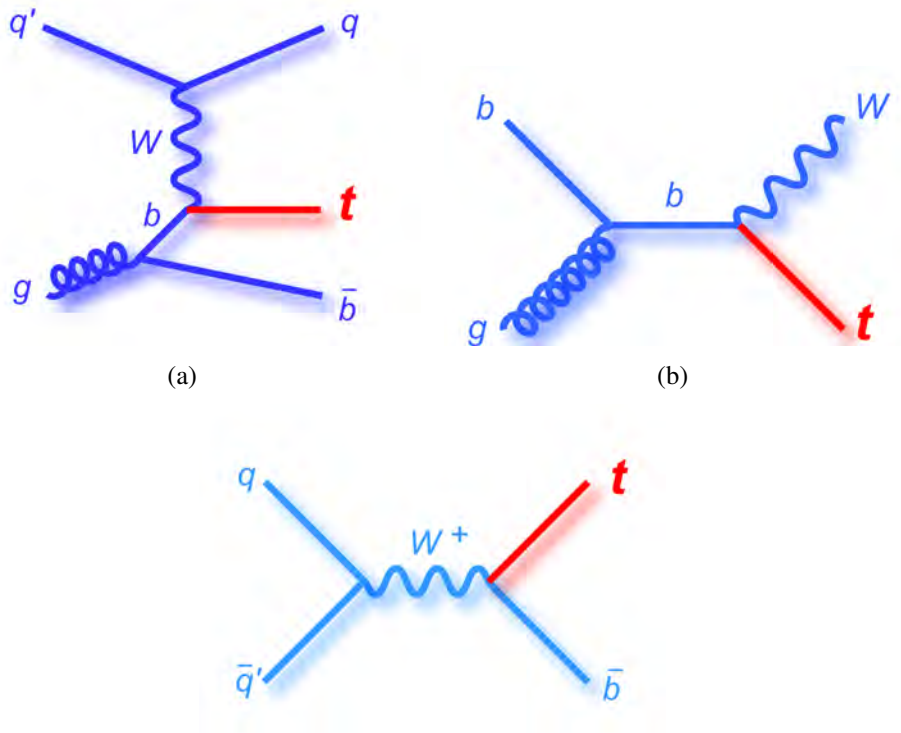

Figure 2.1: Main Feynman diagrams corresponding to the three production mechanisms of single-top quark events: the t-channel (a), the Wt associated production (b) and the s-channel (c).

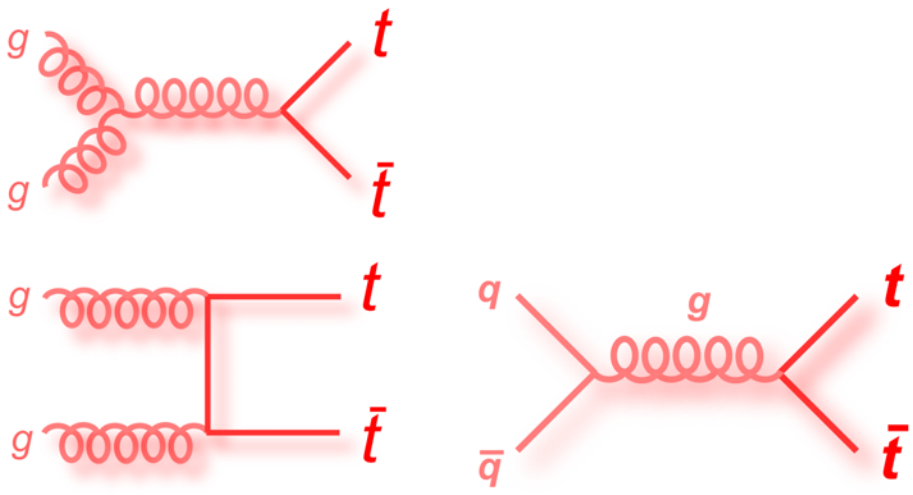

(a) (b)

Figure 2.2: Top pair production processes at lowest order: gluon-gluon scattering diagrams (a) and quark-quark scattering diagram (b).

90% [31] of the total while the production via quark-antiquark is about 10% [31]. At the TeVatron, which is a proton-antiproton collider with 1.96 TeV energy at the center-of-mass of the collision, the quark-antiquark annihilation is the dominant process. To quantify the production of single top quark or $t\bar{t}$, a quantity that has a sound theoretical interpretation should be measured : the cross section which will be described in Section 2.1.3.

2.1.3 The Cross Section

The LHC is a p-p collider which is fundamentally a scattering experiment: the two proton beams are brought into collision and scatter. The resulting elastic scattering of the protons and diffractive events will mostly not be seen in the detector, only the inelastic scattering, that gives rise to particles at sufficient high angles with respect to the beam axis, will be detected.
In p-p collisions, the cross section [2] is not trivial. In a high energy environment such as the LHC the protons can scatter inelastically, producing new particles as in $pp \rightarrow t\bar{t}$, in addition to the elastic scattering $pp \rightarrow pp$. The total inclusive cross

[2]The cross section (σ), which has units of area, measures the "size" of the target. In other words, the cross section is the effective area which governs the probability of the scattering event. For example, in the hard scattering of two billiard balls with a radius R, the cross section is πR^2, the entire cross sectional area of the balls interact in the collision - nothing happens outside of a radius of R.

section is the sum of all the possible elastic and inelastic scattering processes. The exclusive cross section for a process such as $pp \rightarrow t\bar{t}$ can be thought of as the probability per unit area for a $t\bar{t}$ pair to be produced in a p-p collision. In Fig. 2.3, different cross sections measured by the ATLAS experiment for several exclusive processes of interest at the LHC are shown. One can notice that the production of

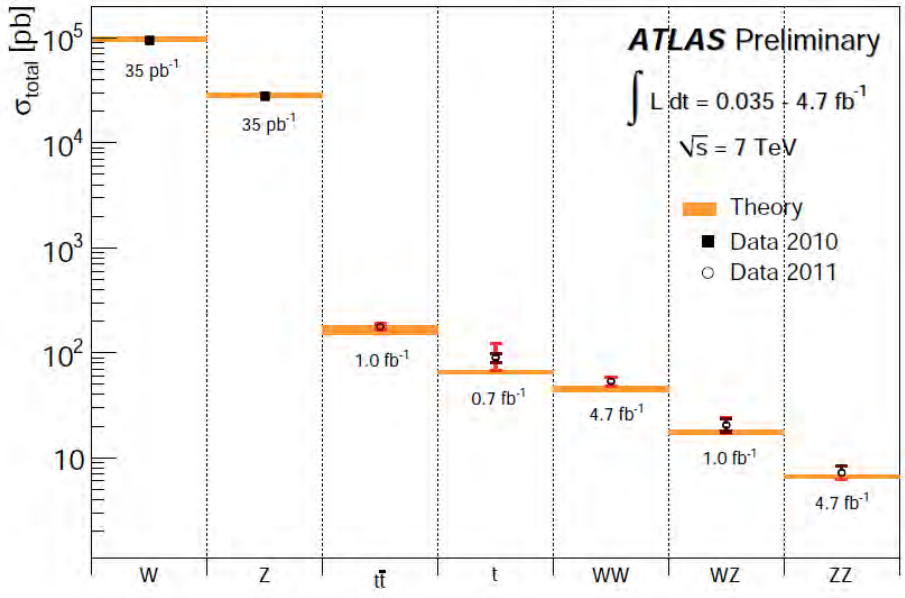

Figure 2.3: The theoretical and measured cross sections for various processes of interest at the LHC, taken from [33].

a W or a Z boson are much more important than the production of a $t\bar{t}$ pair. The cross section of a physics process is related to the number of events of that process by:

$$\sigma = \frac{N}{\int Ldt} \tag{2.1}$$

where $\int Ldt$ is the integrated luminosity of the experiment. The luminosity is a collider parameter which represents the number of particles provided by the beams per unit area and per unit time, and it will be discussed in detail in Chapter 3 Section 3.1. In practice, detectors do not usually offer complete coverage and certain selection cuts are made to reduce the background so the equation 2.1 is modified to:

$$\sigma = \frac{N}{\varepsilon \int Ldt} \tag{2.2}$$

where ε gives the efficiency of the detector and the particle selection cuts that are made. The event selection will be detailed in Chapter 6. The cross section is usually expressed in barn (b)[3].

At a hadron collider, it is not possible to collide single proton with another single proton. At the LHC, there are $\approx$ 600 millions of collisions per second. Because the center of mass energy of the LHC is in the regime where the quarks and gluons behave as quasi-free particles, the cross section is factored into the contribution from $q\bar{q}'$ and gg. These cross sections are convoluted with the parton distribution function (PDF) of the protons. The PDF gives the distribution of the proton's momenta among its constituent particles - the quarks, the gluons which hold them together and the $q\bar{q}$ pairs which pop in and out of the vacuum (the "sea" quarks). PDFs are calculated from the combination of vast amounts of high energy physics data.
The total cross section of $pp \rightarrow t\bar{t}$ is then given by:

$$\sigma_{t\bar{t}} = \sum_{i,j} \int dx_i dx_j f_{i,p}(x_i, Q^2) f_{j,p}(x_j, Q^2) \hat{\sigma}_{i,j}(i, j \rightarrow t\bar{t}) \tag{2.3}$$

where x_i and x_j are the fraction of momenta carried out by the two colliding partons, $f_{i(j),p}(x_{i(j)}, Q^2)$ represent the parton distribution functions of the colliding partons and the hat notation refers to the underlying partonic process. The total exclusive cross section for $t\bar{t}$ pair production depends on the mass of the top quarks. The reason for this is simple - a heavier top is harder to produce. Figure. 2.4 shows a summary of measurements by the ATLAS experiment of the top-pair production cross-section at $\sqrt{s} = 7$ TeV compared to the corresponding theoretical expectation for a top mass of 172.5 GeV.

A differential cross section, as a function of the mass of the $t\bar{t}$ system $(d\sigma/dM_{t\bar{t}})$, contains additional important information. In this case, the experimental interpretation of equation 2.2 is modified to:

$$\frac{d\sigma_i}{dM_{t\bar{t}}} = \frac{N_i}{\varepsilon_i \Delta_i^{M_{t\bar{t}}} \int L dt} \tag{2.4}$$

where the superscript i indicates a bin of the $M_{t\bar{t}}$ distribution and $\Delta_i^{M_{t\bar{t}}}$ refers to the $t\bar{t}$ mass range where the cross section is being measured. If there was a massive particle X that strongly couples to the top quark it would be seen as a resonance or distortion in $d\sigma/dM_{t\bar{t}}$ in the region of M_X. The exact nature of the resonance or

[3] A barn is equal to 10^{-24}cm^2, a unit which is much too large for $t\bar{t}$ production, where the cross section is of the order of picobarns (1pb $= 10^{-12}$b).

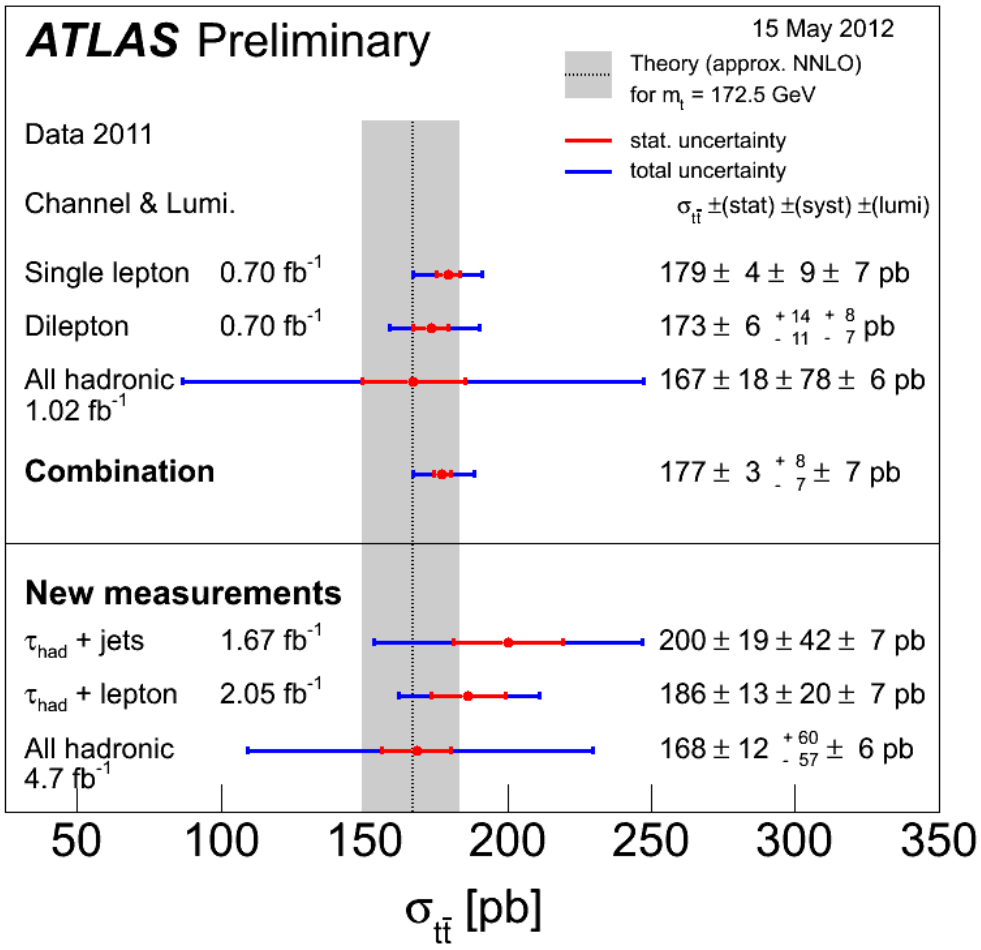

Figure 2.4: Summary of measurements of the top-pair production cross-section compared to the corresponding theoretical expectation. The upper part of the figure shows measurements that are averaged to give the combined value shown. The lower part shows additional newer measurements not included in the combination.

distortion would depend on the mass of the particle, its width, coupling to the top, and any interference with the SM. It is possible to imagine a scenario where such a process would not change the integrated cross section to an appreciable degree, but only the differential cross section. In this way differential distributions provide a unique window to non-Standard Model physics.

2.2 The Top Quark Decay

The top quark has a very short lifetime, of about 5.10^{-25} s, which is short enough that it decays before it hadronizes, therefore only its decay products can be detected by the experiments. The top quark is unique in this respect as it provides the only probe of the behavior of a bare quark. The top quark decay is dominated by the decay $t \rightarrow Wb$ as the CKM element V_{tb} is nearly 1 (0.9990 to 0.9992 [6]) which is determined using the ratio of branching fractions $R = B(t \rightarrow Wb)/B(t \rightarrow Wq)$ where $q = b, s, d$. The b quark will then hadronize to a B meson or baryon. The B hadrons will subsequently decay via a $b \rightarrow Xc$ or $b \rightarrow X\mu$ processes. The former decay is more probable than the latter, according to CKM matrix. However, V_{cb} is not a diagonal element so the b decay is somewhat suppressed. This contributes to the relatively long lifetimes of the B hadrons, most are approximately 1.5 ps. This characteristic of the B hadrons is exploited to identify them, as it will be discussed in Chapter 5. The W boson decays in about 1/3 of times into a lepton and its associated neutrino. All three lepton flavors are produced at approximately equal rate. The rest 2/3 of the times, the W boson decays into a quark-antiquark and the abundance of a given pair is determined by the magnitude of the relevant CKM matrix elements. As a result, the W boson has a branching ration (BR) of 10.8% [34] for its leptonic decay (i.e. for each lepton flavor) and 67.6% [34] for its hadronic one.

Given the decay of the W boson, three decay channels can be identified for the top pair quarks:

- *the dilepton channel*: the two W bosons decay into a lepton and its associated neutrino. This decay channel represents about 1/9 of the $t\bar{t}$ decays. the resulting $t\bar{t}$ event signature is characterized by the presence of two high energy leptons, two neutrinos and two b quarks. In particle physics detectors, such as ATLAS at the LHC, these events represent a clean sample of top quarks because of the two leptons signature. However, the dilepton sample has limited use in probing the top quark reconstruction, due to the two neutrinos escaping detection since the neutrino doesn't interact with the detector matter, and its identification is performed via the missing energy in

the transverse plane of the detector, as it will be discussed in Chapter 4 Section 4.5.

- *the full hadronic channel*: the two W bosons decay into quarks, which gives rise to at least six quarks in the event: four light quarks coming from the W decays and two b quarks. This channel represents about 4/9 of the $t\bar{t}$ decays. The $t\bar{t}$ signal in this channel is not easily distinguished from the SM QCD multi-jets events, which are expected to be orders of magnitude larger than the signal. Another challenging point of this signature is the presence of a high combinatorial background when reconstructing the top quark mass.

- *the lepton+jets channel*: one W boson decays into a lepton and its associated neutrino, and the other one decays into a pair of quark-antiquark. This channel is called the "golden channel" and it represents about 4/9 of the $t\bar{t}$ decays. It is considered as a good compromise between the dileptonic channel and the full hadronic one. The presence of a single high energy lepton allows to suppress the SM W+jets and QCD backgrounds. The neutrino can be reconstructed as it is the only source of the missing transverse energy for signal events.

2.3 The Profile of the Top Quark

The top quark couples to all known fundamental interactions. It is expected to couple strongly to the scalar fields that break the electroweak gauge symmetry because of its large mass. While the interactions of the top quark have not been explored in great detail so far, its mass has been experimentally determined very precisely. In this section, what is known about the top quark properties, in term of mass, spin and charge is presented and discussed.

2.3.1 The Top Quark Mass

The top quark mass is an important parameter of the SM. As the top quark does not hadronize, it seems natural to exploit the picture of the top quark being a highly unstable bare fermion. This suggests to use the concept of on-shell or pole mass, which is defined to be the real part of the complex valued pole of the quark propagator $S_t(p)$. This is a purely perturbative concept. A quark is unobservable due to color confinement, so its full propagator has no pole. In finite order perturbation theory, the propagator of the top quark has a pole p at the complex value $\sqrt{p^2} = m_t - i\Gamma_t/2$, where m_t is the pole or on-shell mass and Γ_t is the decay width

of the top quark. However, the all-order resummation of a class of diagrams, associated with so called infrared renormalons, implies that the pole mass has an intrinsic, non-perturbative ambiguity of order $\Lambda_{QCD} \approx 217^{+25}_{-23}$ MeV. The present experimental determinations of the top mass at the TeVatron is a combination of the results between the CDF and the DØ Collaborations. Their average value of the top quark mass amounts: $m_{top} = 173.2 \pm 0.9$ GeV [35]. Recently, measurements of the top quark mass from the LHC have become available, and it is also a combination between the ATLAS and the CMS Collaborations results. Fig. 2.5 shows the different measurements of the top quark mass performed by the ATLAS and the CMS Collaborations separately as well as the combination which results in a top mass of: $m_{top} = 173.3 \pm 1.4$ GeV [36].

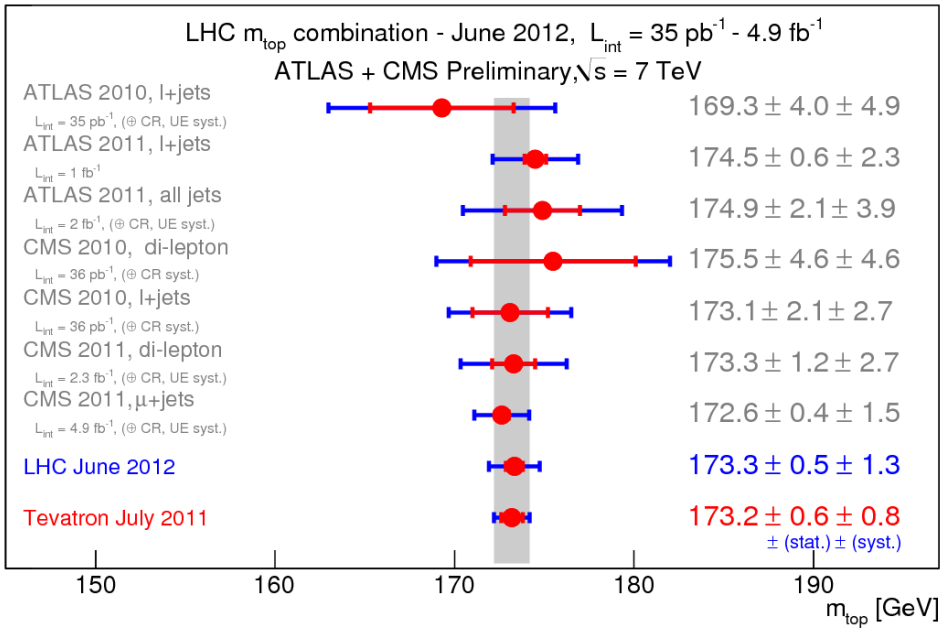

Figure 2.5: Top mass measurements in ATLAS and CMS at the LHC with different $t\bar{t}$ decay channels, and the result of their combination giving $m_{top} = 173.3 \pm 0.5(\text{stat}) \pm 1.3(\text{syst})$, while the measurement at the TeVatron is $m_{top} = 173.2 \pm 0.6(\text{stat}) \pm 0.8(\text{syst})$. Taken from [36].

2.3.2 The Top Quark Spin

The top quark, as observed at the TeVatron, is a fermion with a spin 1/2. However, a dedicated experimental verification for this property has so far not been

made fully. The observed decay $t \to Wb$, the known spins of W and b, and the conservation of total angular momentum imply that the top quark is a fermion. If the spin of the top quark was 3/2, the $t\bar{t}$ cross section at the TeVatron would be much larger than the measured one. A direct experimental evidence for the top quark having spin 1/2 would be the observation of the resulting polarization and spin-correlation effects. Another possibility is the measurement of the differential cross section $d\sigma/dM_{t\bar{t}}$ near the $t\bar{t}$ production threshold. The ATLAS and CMS collaborations have measured the spin correlation using 7 TeV proton-proton collisions [37, 38]. As is well-known the behavior of the near-threshold cross section as a function of the particle velocity is characteristic of the spin of the produced particle and antiparticle.

2.3.3 The Top Quark Electric Charge

Top quark, like the other quarks, carry color charge. It transforms as a color triplet under the $SU(3)_c$ gauge group of the strong interactions. Color-confinement precludes the direct measurement of this quantum number; but indeed, measurements of the $t\bar{t}$ production cross section are consistent with the SM predictions for a color-triplet and anti-triplet quark-antiquark pair. The top quark is the +1/2 weak-isospin partner of the b quark, assuring the consistency of the SM at the quantum level. The electric charge of the top quark, which is therefore $Q = 2/3e$ according to the SM, has so far not been measured. The observed channel $t\bar{t} \to b\bar{b}W^+W^-$ does a priori not preclude the possibility that the observed top resonance is an exotic heavy quark with charge $Q = -4/3e$ decaying into bW^- [39]. However, this has been excluded in the meantime by the DØ and CDF experiments at the TeVatron [40, 41] and by the ATLAS experiment at the LHC at more than five standard deviations [42]. The top-quark charge can be directly determined by measuring the production rate of $t\bar{t}$ plus a hard photon and taking the ratio $\sigma(t\bar{t}\gamma)/\sigma(t\bar{t})$. At the LHC this ratio is approximately proportional to Q^2 because $t\bar{t}$ and $t\bar{t}\gamma$ production is dominated by gluon fusion.

2.4 The Top Quark Beyond the SM

The existence of physics beyond the standard model (BSM) could affect $t\bar{t}$ production in several ways. New particles which strongly couple to top quarks could show up as resonance bumps in the $t\bar{t}$ invariant-mass spectrum, or may be produced in association with $t\bar{t}$ pairs. Virtual new particle exchanges may significantly modify the total cross section and/or kinematic distributions.The effects of virtual new particle exchanges on the $t\bar{t}$ cross section and distributions has been extensively studied in the literature for a number of SM extensions. If resonance

effects are absent, one expects significant deviations from SM predictions only if the new particles X that couple to top quarks are not too heavy, $m_X \approx$ a few hundred GeV.
Many BSM physics scenarios predict heavy, electrically neutral bosons X^0, with masses m_{X^0} up to a few TeV, that strongly couple to $t\bar{t}$ pairs. Thus these resonances would show up as bumps in the $M_{t\bar{t}}$ invariant mass distribution. Supersymmetric extensions for example, predicts a spectrum of neutral Higgs bosons, some of which can be heavy enough to decay into a pair $t\bar{t}$. Models that aim to explain the mechanism of electroweak gauge symmetry breaking "dynamically" by a new strong force, like technicolor models and their descendants [43], contain new spin-zero and spin-one states. In top-color [44] and Little Higgs models [45], the top quark plays a special role. New vector resonances appear in these models with reasonably strong couplings to top quarks. Models with extra dimensions [46, 47] have massive spin-one and spin-two Kaluza-Klein (KK) excitations. In some of these models the couplings of the new states to light quarks and gluons is suppressed [48, 49], and their decay into $t\bar{t}$ is expected to be their main discovery channel.

In summary, a large class of BSM models predict distortions to the $t\bar{t}$ invariant mass spectrum. The goal of the $t\bar{t}$ analysis in this thesis is to remain as model-independent as possible when analyzing the $M_{t\bar{t}}$ spectrum. In this way, it maintains sensitivity to the many BSM effects which are possible.

Chapter 3

The ATLAS Experiment

This chapter describes briefly the Large Hadron Collider (LHC) which is located at CERN at the French-Swiss border, and more specifically one of its main experiments, ATLAS, one of the biggest particle detectors ever built.

3.1 The LHC

The LHC [50] presents a new era in high energy physics. It is the biggest hadron accelerator and collider nowadays. It lies in the existing LEP (Large Electron Positron) tunnel at CERN, a circular underground tunnel of 27 km circumference. Being a particle-particle collider, rather than a particle-antiparticle collider, the LHC consists of two rings with counter-rotating beams. Due to the limited size of the LEP tunnel, a two-in-one design was chosen for the supra-conducting magnets needed to keep the accelerated particles along the curved trajectory, so that the magnets provide a magnetic field in opposite direction for the two nearby lying accelerated particle beams.
The maximum beam energy that the LHC can deliver to the experiments depends on the maximum magnetic field of the dipole magnets needed to keep the particles along the trajectories. The nominal field being 8.33 T, this corresponds to a beam energy of 7 TeV and a center of mass energy for collisions of 14 TeV. This allows to significantly extend the physics reach in terms of sensitivity to new physics phenomena with respect to previous experiments.
The LHC has a design instantaneous luminosity L of $10^{34}\text{cm}^{-2}\text{s}^{-1}$. The luminosity is a collider parameter which represents the number of particles provided by the beams per unit area and per unit time. It is defined as follows:

$$L = \frac{N_1 N_2}{4\pi\sigma_x\sigma_y} f N_b \tag{3.1}$$

where N_1 and N_2 are the number of protons per bunch in the first and second beam respectively, N_b is the number of bunches per beam, f is the bunch crossing frequency and σ_x and σ_y are the x and y components of the transverse beam size at the interaction point, in the plane perpendicular to the beam axis. The LHC is also a heavy (Pb) ions collider with a design energy of 2.8 TeV per nucleon and a design luminosity of $10^{27}\text{cm}^{-2}\text{s}^{-1}$. The first beams circulated successfully in the LHC rings in September 2008, but a magnet quench occurred which caused the loss of almost six tons of liquid helium and the vacuum conditions in the beam pipe. It's only after a year when the next successful beams with an energy of 450 GeV circulated and the first proton-proton collisions occurred with an energy at the center of mass of 900 GeV on November 2009. The first collisions with an energy at the center of mass of 7 TeV happened on March 2010, which allowed the LHC to set the world record for high-energy collisions. The LHC collided proton beams with an energy of 3.5 TeV in 2011 and it is still colliding proton beams in 2012 with an energy of 4 TeV, and the first collisions with the nominal designed energy are expected to be in early 2015. Figure 3.1 shows the total integrated delivered luminosity by the LHC in 2010 and 2011 and recorded by the ATLAS experiment for the collisions with a center of mass energy of 7 TeV. Table 3.1 shows the main LHC parameters for the nominal functioning.

	Injection	Collision
Energy	450 GeV	7000 GeV
Instantaneous luminosity	$10^{34}\text{cm}^{-2}\text{s}^{-1}$	
Number of bunches	2080	
Bunch spacing	25 ns	
Number of particles per bunch	$1.15\ 10^{11}$	
Beam current	0.58 A	
Main dipole field	8.33 Tesla	
Main dipole operation temperature	1.9 K	

Table 3.1: Main parameters of the LHC collider in the proton-proton collisions mode.

Before injecting the proton beams in the LHC, the protons, extracted from the hydrogen atoms, cross through a complex of accelerators. The chain of the beam injection is shown in Figure 3.2 and it is composed of:

- Linac : it is a linear accelerator. It is the first element of the acceleration and it provides a proton beam with an energy of 50 MeV.

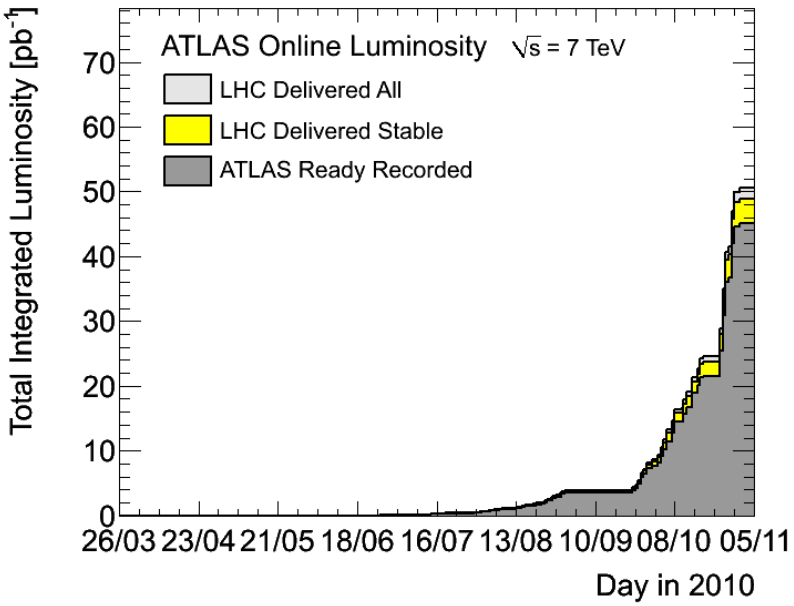

(a)

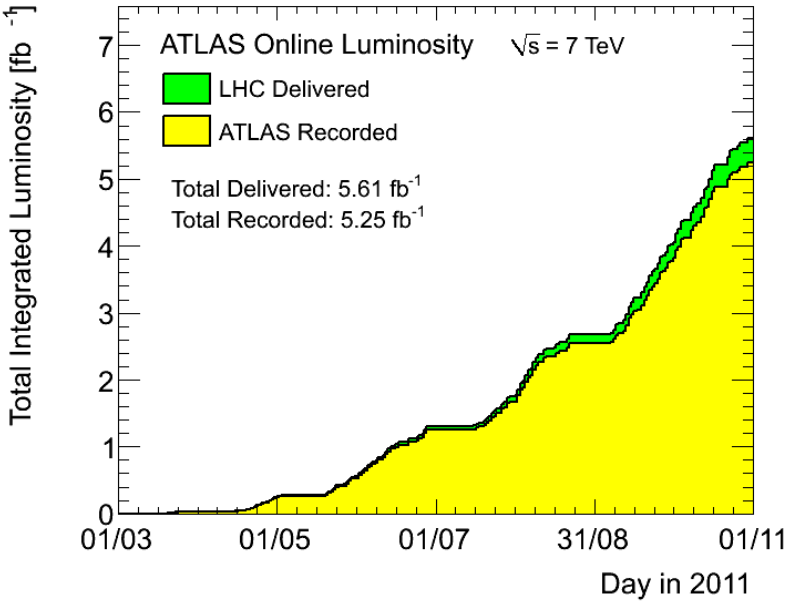

(b)

Figure 3.1: The integrated luminosity delivered by the LHC and the one recorded by the ATLAS experiment, with a center of mass energy of collisions of 7 TeV, for 2010 (a) and 2011 (b).

- PSB (Proton Synchrotron Booster) : it is a proton synchrotron that accelerate the protons coming from the Linac up to an energy of 1.4 GeV.

- PS (Proton Synchrotron) : it accelerates the protons to an energy of 25 GeV. It also defines the length of the proton bunches as well as their spacing.

- SPS (Super Proton Synchrotron) : it constitutes the last element of the accelerating chain before injecting the proton beams into the LHC. In the SPS, the beams are accelerated up to an energy of 450 GeV. Then the SPS injects the proton beams to the LHC through two points (Point 2 and Point 8 shown in Figure 3.2 and Figure 3.3) providing the LHC with two proton beams circulating in opposite directions.

Once at the LHC, the proton beams are accelerated up to an energy of 3.5 TeV for example (7 TeV during the nominal functioning). The LHC ensures the beam crossing at each one of the four collisions points where highly sophisticated detectors are installed. The four main experiments at the LHC are described in the following section.

3.1.1 The Experiments at the LHC and their Physics Goals

The LEP tunnel had eight crossing points of the beam, however, only four of them were equipped with particle detectors for the LHC. The LHC ring and its four major experiments are shown in Figure 3.3.

The four experiments are:

- ALICE [51] (A Large Ion Collider Experiment) is an experiment dedicated to heavy ion collisions. It is located at Point 2 (see Figure 3.3) of the LHC ring and focuses on studying the strongly interacting matter and the quark-gluon plasma at extreme values of energy density and temperature in nucleus-nucleus collisions.

- ATLAS [52] (A Toroidal LHC ApparatuS) and CMS [53] (Compact Muon Solenoid) are two general purpose experiments at the LHC. Both of the experiments are designed to operate with a nominal luminosity of $10^{34}\text{cm}^{-2}\text{s}^{-1}$ and they are located respectively at Point 1 and Point 5 (see Figure 3.3) of the LHC ring. ATLAS and CMS have a wide physics program dedicated to perform Standard Model precision measurements, such as the study of

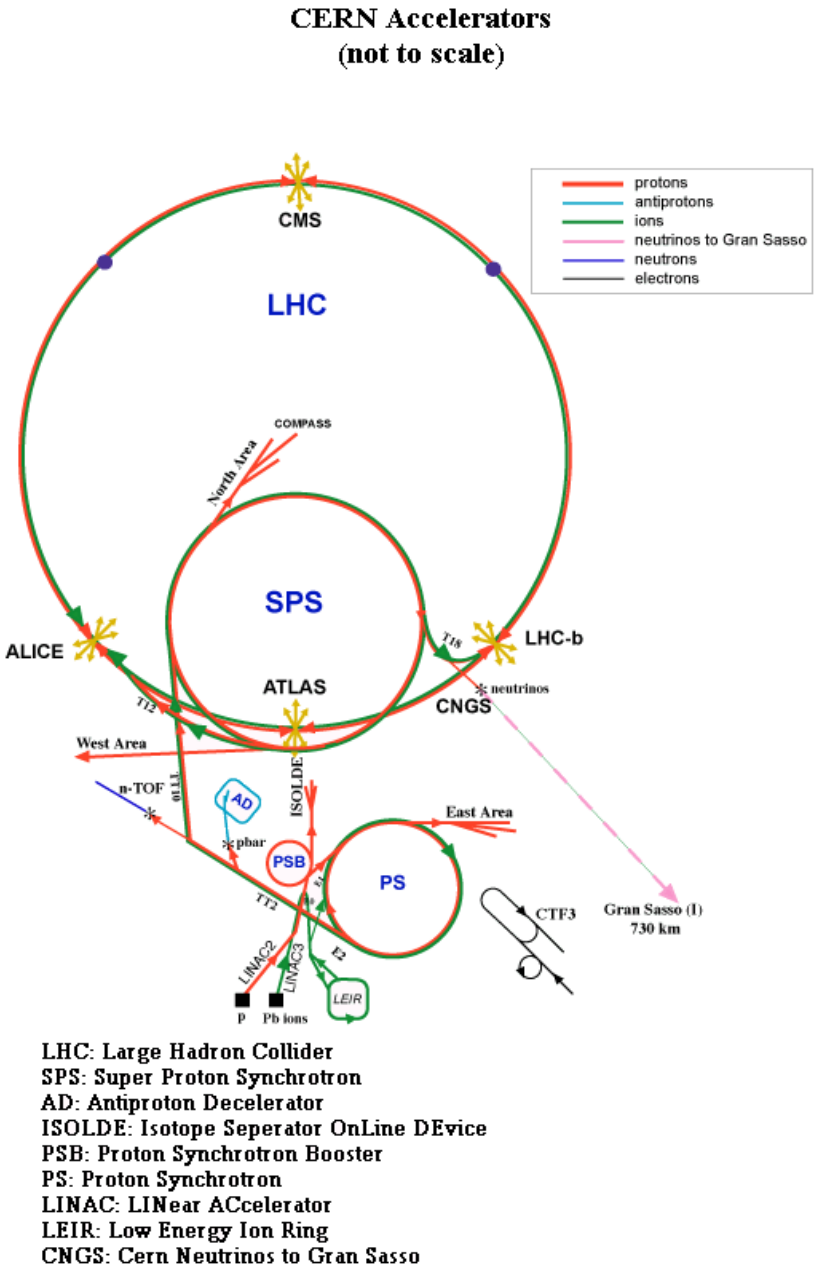

Figure 3.2: The layout of the LHC indicating the chain of acceleration of the beams, and their four points of intersection.

top quark production and decays, vector boson production, heavy flavor physics, electroweak physics, QCD, ...etc. They also have dedicated physics

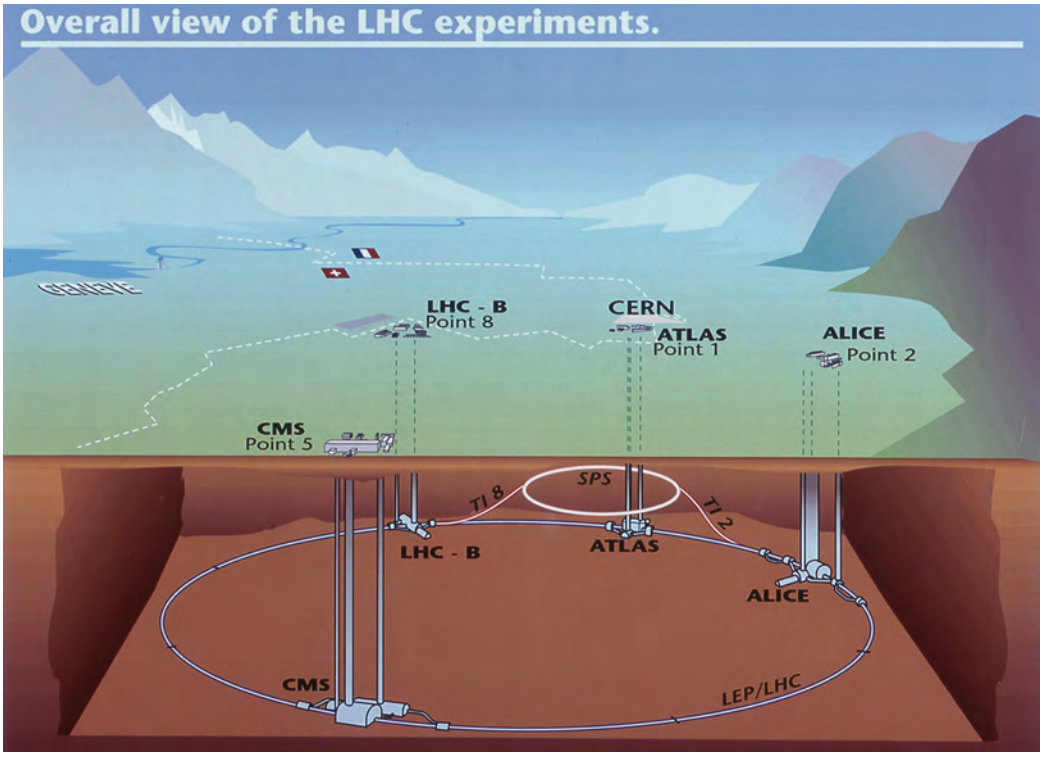

Figure 3.3: The layout of the LHC underground ring and its four major experiments.

programs for the search and the study of the Higgs boson, SUSY, and beyond SM searches.

- LHCb [54] (Large Hadron Collider beauty experiment) is dedicated to t he study of heavy flavor physics. It studies the rare decays of the b-hadron and make precision measurements of CP violation as well as the search for indirect evidence of new physics in these processes. It is located at Point 8 of the LHC ring, and it is designed to operate with a nominal luminosity of $10^{32}\text{cm}^{-2}\text{s}^{-1}$.

3.2 The ATLAS Detector

The ATLAS detector is, as mentioned in the previous section, one of the two general purpose experiments at the LHC. In size, it is the biggest detector ever built with a 44 m long and 24 m height. The overall weight of the detector is

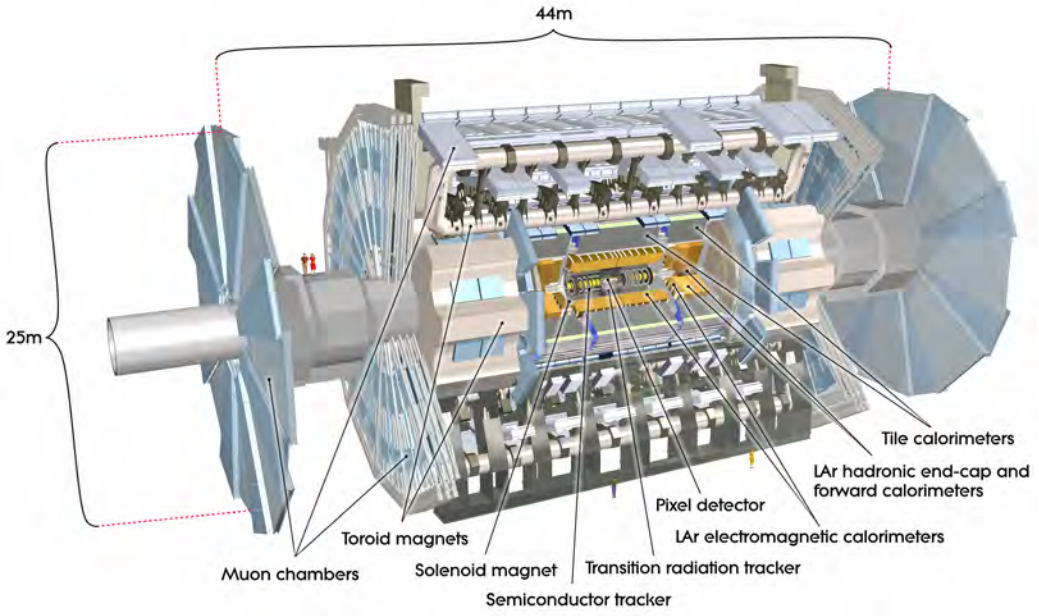

Figure 3.4: Cut-away view of the ATLAS detector.

approximately 7000 tons. An overview of the detector is shown in Figure 3.4

3.2.1 The ATLAS Coordinate System

Defining the ATLAS coordinate system, shown in Figure 3.5, is important since it will be brought out several times. The beam direction defines the z-axis. Consequently, the x-y transverse plane is perpendicular to the beam direction. The positive x-axis points from the interaction point towards the center of the LHC ring. The positive y-axis points upwards. ϕ is the azimuthal angle with respect to the x-axis in the transverse plane, θ is the polar angle with respect to the z-axis. The pseudorapidity η is defined as:

$$\eta = -\ln(\tan\frac{\theta}{2}). \tag{3.2}$$

The rapidity is used instead of the pseudorapidity whenever there are massive objects like jets and it is defined as :

$$y = \frac{1}{2}\ln\left[\frac{(E+p_z)}{(E-p_z)}\right] \tag{3.3}$$

where E is the energy of the reconstructed object and p_z denotes the z-component of the momentum along the beam axis. The distance ΔR between two directions

pointing towards the collision point of the detector in the η-ϕ plane is given by:

$$\Delta R = \sqrt{\Delta\eta^2 + \Delta\phi^2}. \tag{3.4}$$

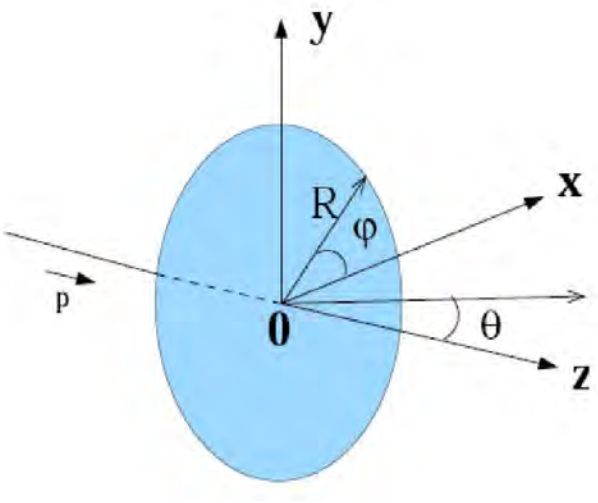

Figure 3.5: The ATLAS coordinate system.

3.2.2 The ATLAS Sub-detectors

ATLAS is a cylindrical detector composed of three main sub-detectors with different technologies and purposes:

- The inner detector or the tracker surrounded by a solenoidal magnet.
- The calorimeters composed by an electromagnetic calorimeter and a hadronic one.
- The muon spectrometer embedded in an air-cone toroid magnet.

Each one of the sub-detectors is described in the following.

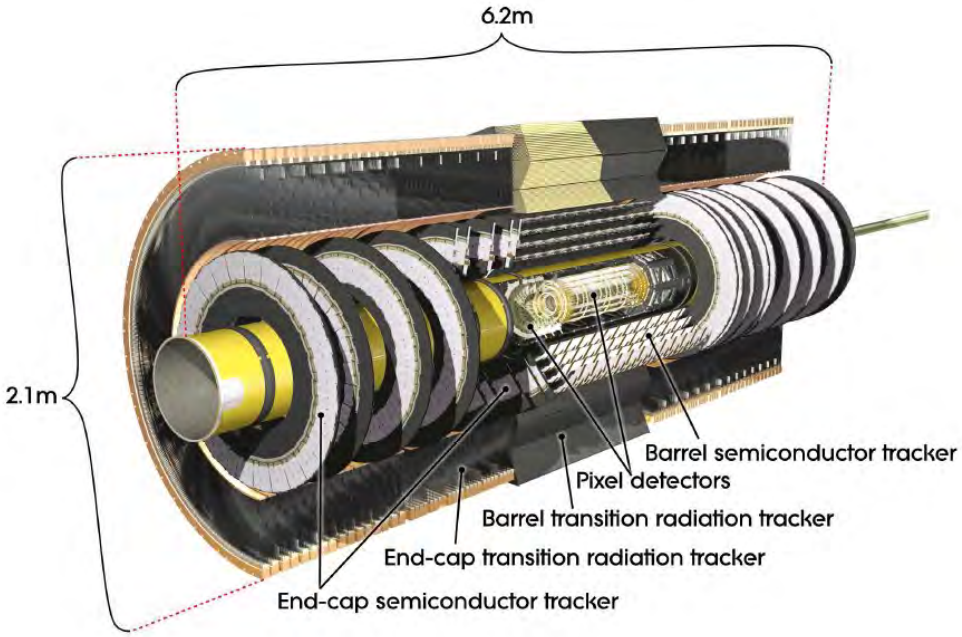

Figure 3.6: Cut-away view of the ATLAS inner detector.

3.2.2.1 The Inner Detector

The ATLAS inner detector [55] (ID) is the inner tracking system of the detector. Its general aim is to reconstruct the trajectories of charged particles. It is designed with a high granularity in order to provide an accurate and robust pattern recognition. It also provides excellent primary and secondary vertex measurements with a high momentum resolution for all charged tracks above a transverse momentum (p_T) threshold and within a pseudorapidity range of $|\eta|$ <2.5. Nominally, the p_T threshold is 0.5 GeV, but it can be lower (0.1 GeV) for some studies dedicated for initial measurements with minimum bias events. The full ID is immersed in a 2T solenoidal magnetic field. Three independent sub-detectors with complementary technologies form the ID. Silicon-based detectors are the closest in position to the interaction point. They have different granularities and provide high precision measurements for the hits on tracks in the z direction and the R-ϕ plane. Straw-tube detector surrounds the silicon detectors and provides many measurements, in the R-ϕ plan, to obtain good momentum resolution. The ID is shown in a cut-away view in Figure 3.6. It is composed of the pixel detector that contributes to measure vertices accurately, the semi-conductor tracker (SCT) also known as the silicon microstrip tracker that contributes to measure precisely the particle momentum and the transition-radiation tracker (TRT) that eases the

pattern recognition and contributes to the electron identification.

The Pixel Detector The pixel detector [56] is the innermost ATLAS sub-detector and it is a critical component in the ID tracker. It is designed with the most advanced technology among silicon detectors to sustain the high level of radiation around the interaction point. It has a coverage of the pseudorapidity range $|\eta|$ <2.5. It has a good resolution in the longitudinal z-coordinate which allows excellent primary vertex reconstruction of charged tracks with $\sigma(z)$ <1 mm. The amount of material in terms of radiation length (X_0) composing the pixel detector is minimal in order to reduce secondary interactions and multiple scattering. It is also designed to work with a very high efficiency, low noise and low occupancy. It allows three-dimensional-vertexing capabilities and the measurement of the transverse impact parameter[1] with a resolution better than about 15 microns. The pixel detector plays a major role in the identification of jets stemming from the hadronization of the b-hadrons (b-tagging presented in Chapter 5) and the identification of τ leptons as well.
All these performances are led by the design choice of the pixel detector. The pixel detector is a semi-conductor that operates as a diode in reverse polarization mode. It is formed of high-granularity n^+n implants connected by bump-bonding to the read-out electronics. A crossing particle ionizes the sensor and the charges drift in the electric field and are collected on the n^+ side.

The pixel detector is composed of three barrel layers, Layer 0 (also known as the b-layer) which is 5 cm away from the beam pipe, Layer 1 and Layer 2 at radius 8.85 cm and 12.25 cm respectively, and two identical end-cap regions with three disks each, as shown in Figure 3.7. It contains almost 80.4 million pixels spread over 1744 modules. A module is a basic building block that is composed of silicon sensors, front-end electronics and flex-hybrids with control circuits. All modules function identically at the sensor/integrated circuit level, but differently in the interconnection schemes for barrel modules and disk modules. The barrel region has 1456 modules and the disks have 288 ones leading to 67 million pixels in the barrel and 13 million in the endcaps. The pixel size is small, with 50 μm in the ϕ direction and 400 μm in z (barrel region, along the beam axis) or r (disk region), limited by electronics design. A few special pixels (11.1% of the pixels) in the region between integrated circuits on a module have larger dimensions 50μm x 600μm. In the barrel region, modules are mounted on mechanical/cooling supports, called staves. A stave contains thirteen modules and its layout is identical for all layers. The staves are mounted in half-shells manufactured from a carbon-fiber composite material. Two half-shells are joined to form each barrel layer. The

[1]The transverse impact parameter (d_0) is the distance of the closest approach between the track to the interaction point.

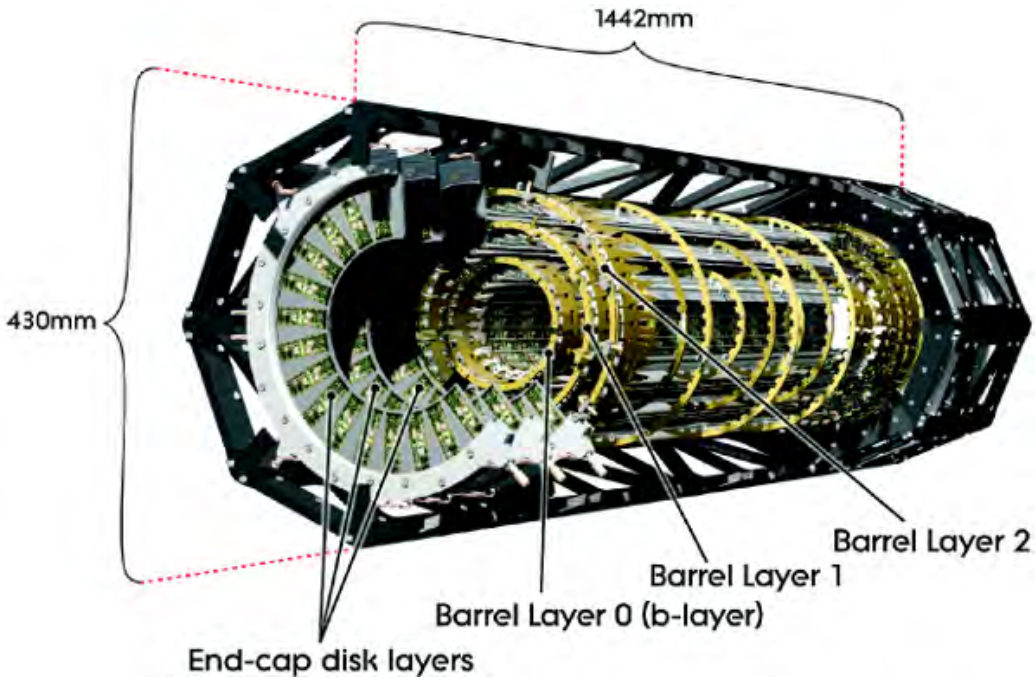

Figure 3.7: Layout of the ATLAS pixel detector.

two endcap regions are identical. Each is composed of three disk layers, and each disk layer is identical. The disk modules are mounted on mechanical/cooling supports, called disk sectors. There are eight identical sectors in each disk.

The pixel detector was commissioned using cosmic rays in Autumn 2008 and first collisions in late 2009. At the time being, about 96.4% of the pixel modules are fully operational and the noise level is very low. Most of the non-operational modules are in the b-layer, the closest to the interaction point. However, an upgrade for the pixel detector is envisioned for 2013-2014 LHC shutdown period, where a new pixel layer, called the Insertable B-Layer (IBL) will be inserted at a radius of about 3.2 cm between the existing pixel b-layer and a new (smaller radius) beam-pipe.

The Semiconductor Tracker The SCT [57] is a semiconductor *p*-in-*n* silicon-microstrip sensor based detector that has a similar working principle as the pixel detector. It is designed, like the pixel detector, to ensure adequate radiation resistance. It has an active silicon area of almost 63 m^2. The choice of silicon was made because of its fast signal speed and excellent spatial segmentation, and the silicon sensors can survive high luminosity operation for a long-term. The SCT detector is designed to allow acceptable fluency levels in order to maintain

a satisfactory signal-to-noise ratio. It has low-noise and low-power on detector components which have been developed in hard radiation technologies. The SCT provides fast signal processing that helps separating signals from successive bunch crossings, and it also has a fast recovery time that minimizes the loss of signals in subsequent bunches.

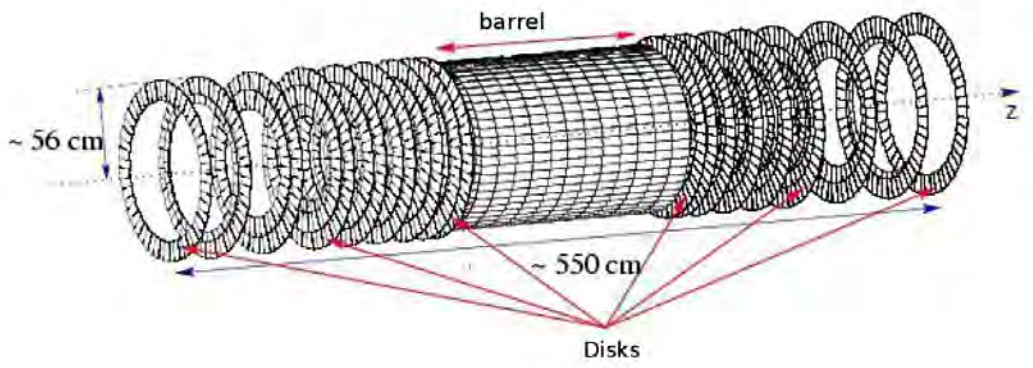

Figure 3.8: Layout of the ATLAS SCT detector.

In order to identify and reconstruct isolated leptons with p_T >5 GeV with a 95% efficiency within a pseudorapidity range of $|\eta|$ <2.5 and a fake track rate lower than 1%, the SCT combined with the pixel must have at least six tracking layers able to provide space point information. Therefore, the SCT detector is composed of four barrel layers and nine disks on each side, as shown in the Figure 3.8. The barrel consists of 8448 identical rectangular single-sided *p*-in-*n* sensors mounted on 2112 silicon strip modules resulting in 3,244,032 channels. The 18 disks consists of 6944 single-sided *p*-in-*n* sensors of five different shape geometries, mounted on 1976 modules resulting in 3,035,136 channels. The modules are mounted on light support structure composed of carbon fibers. Each module contains two sensors on each side rotated by 40 mrad with respect to each others. This design allows reading out a position in two dimensions using the intersection of the activated strip from both sides. It also allows robust measurements in the R-ϕ direction even if one of the two sensors is damaged. In the barrel region, every twelve modules are staggered in radius by $\pm$ 1mm shift from the cylinder nominal radius to give an overlap in the z-direction and an overlap of 1% in the ϕ direction which makes the detector hermetic for p_T >1 GeV and decreases significantly the dead region (a dead space does remain between the daisy-chained detectors).

The SCT detector was successfully commissioned using the 2008 cosmic ray data and the first collision data too. About 99.2% of the modules are fully operational and they allow intrinsic accuracy of pseudo-3D measurements of 17 μm in R-ϕ and 580 μm in the z-direction.

The Transition-Radiation Tracker The TRT [58] is the outermost part of the ATLAS ID. It is based on drift tubes of 4 mm diameter commonly called straw-tubes. The choice of 4 mm is a reasonable compromise between speed of response, mechanical and operational stability and the number of ionization clusters. Straws guarantee a high modularity for the overall detector and they are

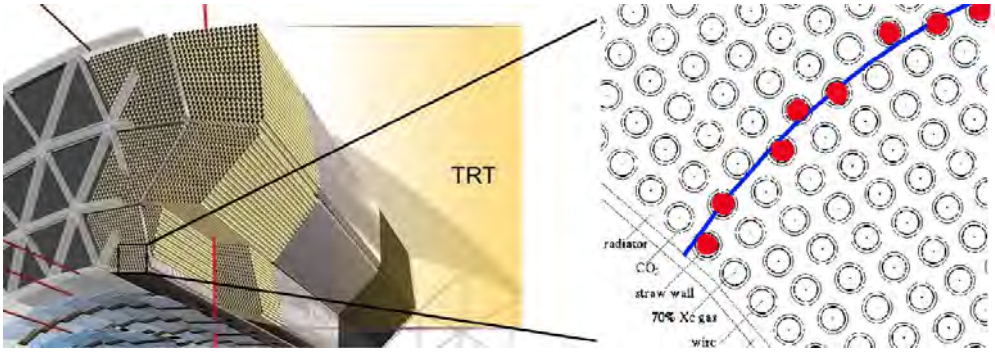

Figure 3.9: The TRT detector of the ATLAS experiment.

integrated into a medium producing transition radiation without compromising the continuous tracking concept. The straw tubes are filled with a gas mixture, of 70% Xe, 27% CO_2 and 3% O_2, which has good counting characteristics and high X-ray absorption. The straw surface forms the cathode and the anode is a 31 μm-diameter tungsten wire plated with gold localized in the center of the straw. When a particle passes, it ionizes the gas mixture inside the tube and the charges drift and are collected at the end of the wire. The drift time is computed and gives a spatial accuracy of about 130 μm. The TRT plays a major role in identifying the electrons. Electrons deposit more energy in the gas mixture than pions. Figure 3.9 shows the TRT detector and a schematic view of a passing particle through the straw tubes. Typically, 36 hits per crossing particle are collected from the TRT.

The TRT is composed of a barrel and two endcaps. The barrel consists of three cylindrical rings, each containing 32 identical and independent modules. There are three types of barrel modules. The first type contains 329 axial straws positioned in 19 layers in the innermost radius. The second type of module contains 520 axial straws positioned in 24 layers at an intermediate radius, and the third type contains 793 axial straws positioned in 30 layers at the outermost radius.

All the straws are embedded in stacks of polypropylene/polyethylene fibers which produce the transition radiation X-rays used for the electron identification. Each of the two endcaps of the TRT consists of three sets of identical and independent wheels. Each wheel is divided into identical sub-wheels. There are three types of wheels. The first type contains 12,888 radial straws positioned in 16 successive layers spaced by 8 mm along the z-axis. Each layer is formed from 768 straws in the R-ϕ plane, and the free space between the layers is filled with polypropylene. There are six wheels from this type standing side by side at 803 mm $< z <$ 1684 mm. The second type of wheels contains 6144 radial straws positioned exactly as the first type but with a spacing of 16 mm instead of 8 mm along the z-axis. There are eight wheels from the second type and they are placed at 1687 mm $< z <$ 2774 mm. The last type of wheels contains 9216 radial straws positioned in 16 successive layers also spaced by 8 mm along the z-axis. There are four wheels side by side from the last type, and they are placed at 2818 mm $< z <$ 3363 mm. Nowadays, 97.5% of the straws are fully operational.

The ID cooling system The front-end (FE) chips and the modules of the pixel and SCT detectors constitutes a major heat source : The pixel FE chips dissipate more than 15 kW [59] into the detector volume and the SCT modules dissipate a significant amount of heat, more than 25 kW [59]. To prevent reverse annealing of the silicon detectors, an evaporative cooling system for the SCT and the pixel detectors is in place. It is sufficient to remove the heat from the detector modules and maintain the silicon temperature at or below -7 °C for the SCT and 0 °C for the pixel. The pixel and the SCT systems are inside a thermal enclosure flushed with dry Nitrogen (N_2). The system is thermally neutral with respect to the rest of the ATLAS sub-detectors. The fluid used in the cooling system are non-corrosive, non-toxic, radiation hard and non-flammable. The C_3F_8 fluid is chosen as a refrigerant for the ID because of its highest heat coefficient among all the C_nF_{2n+2}, and it gives lower pressure drops in the vapor phase, thus allowing for a reduced return tube size, which is critical for the ID services.

The TRT detector is operated at the ambient room temperature. C_6F_{14} is used as a coolant to remove the heat and all the TRT volume is filled with CO_2 to reduce the contamination of the mixture gas inside the straw tubes with other molecules.

3.2.2.2 The Calorimeters

The ATLAS calorimeters [52] cover a wider range of pseudorapidity of $|\eta| < 4.9$ than the ID. They are made of different and complementary technologies and optimized to meet the requirements in terms of good energy resolution, good position accuracy and the radiation environment.

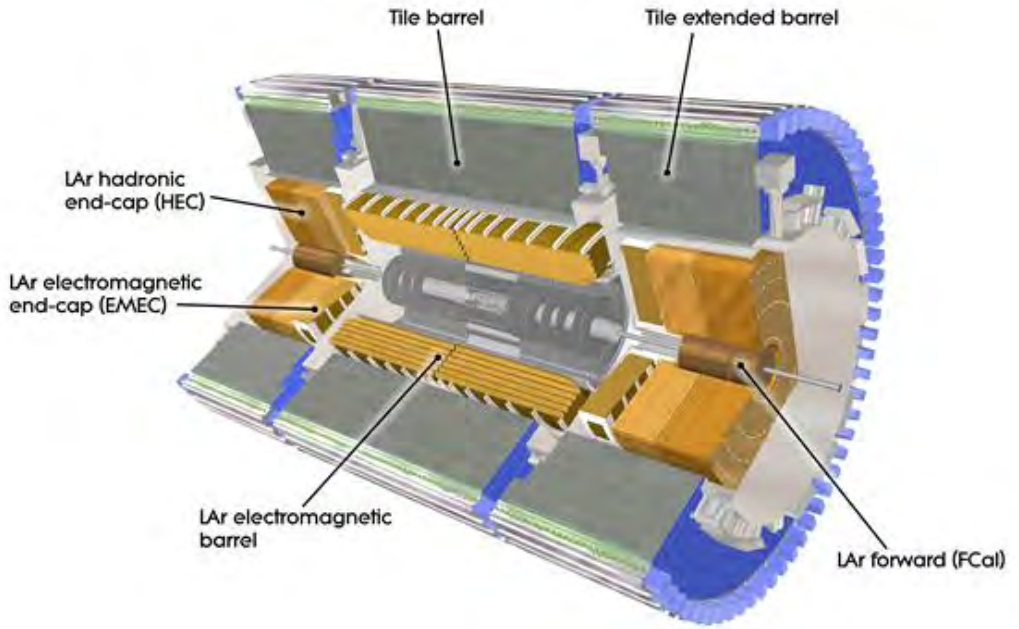

Figure 3.10: A schematic view of the ATLAS calorimeter system and its three components.

Figure 3.10 shows a cut-away view of the calorimeter system of the ATLAS detector. It is composed of three different sub-calorimeters:

- The electromagnetic calorimeter (EM) which is suited for precision measurements for electrons and photons.

- The hadronic calorimeter which is suited for the jet reconstruction and the missing transverse energy measurements.

- The forward calorimeter (FCal) is integrated into the endcap cryostats. It allows a measurement of the forward jets and improves the transverse missing energy measurement.

The calorimeter system provides good containment of the electromagnetic and hadronic showers, and helps limiting the punch-through (particles other than muons)

into the muon system. The installation of the calorimeters was completed in 2006 into the ATLAS cavern.

The Electromagnetic Calorimeter The EM calorimeter has a pseudorapidity coverage range of $|\eta|$ <3.2. It has a high granularity and presents excellent performance in terms of energy and position resolutions for electrons and photons as well as for the electromagnetic component of the jets. It is composed of kapton electrodes and lead absorbers immersed in a liquid argon active material. It has a geometry of an accordion for the electrodes which lead to ensure a full coverage in ϕ without azimuthal cracks. The electromagnetic calorimeter is divided into a

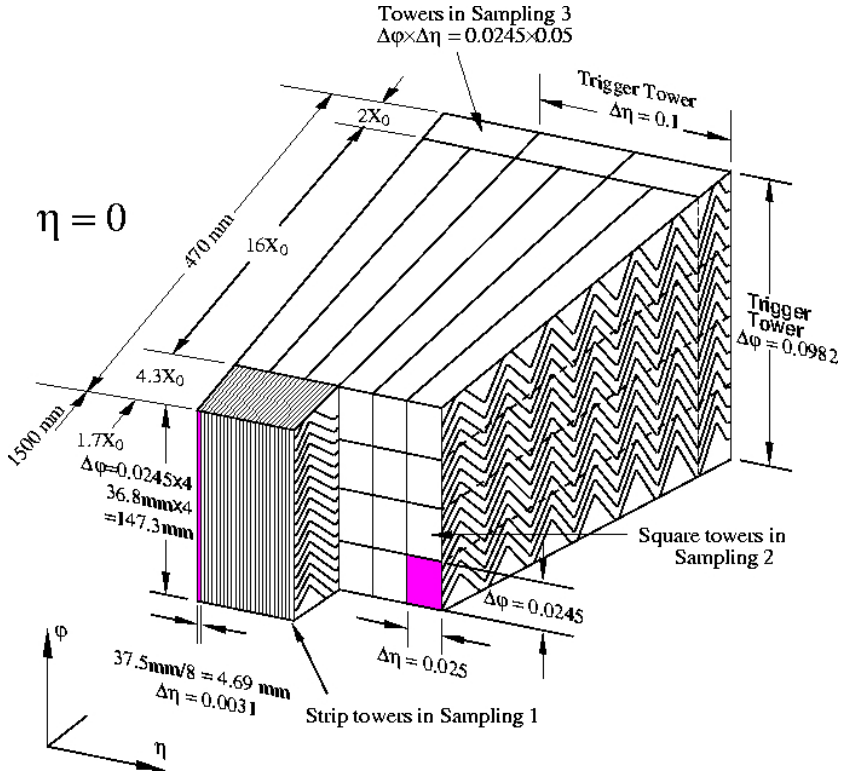

Figure 3.11: A schematic view of the three samplings of the ATLAS barrel electromagnetic calorimeter system.

barrel with a pseudorapidity coverage of $|\eta| < 1.457$ and two endcap components with a coverage of $1.375 < |\eta| < 3.2$, each housed in their own cryostat. The barrel is composed of two identical parts separated by a small gap of 4 mm at z=0. Each end-cap calorimeter has two coaxial wheels: an outer wheel covering the region $1.375 < |\eta| < 2.5$, and an inner wheel covering the region $2.5 < |\eta| <$ 3.2. The barrel EM calorimeter is segmented into three layers or samplings, as

shown in Figure 3.11, which ensures the best precise measurements for the ID pseudorapidity coverage ($|\eta|$ <2.5). The first sampling, the closest to the ID, has a fine granularity in η which provides a good spatial resolution for identifying electrons and photons. The second and third samplings have a less granularity in η but a finer one in ϕ and this is where the electrons and photons deposit most of their energies. A typical electromagnetic shower begins in the first sampling, has its essential energy deposited in the second sampling and if it continues, it dies in the last one. The endcaps outer wheels are divided into two layers with a coarser granularity in both directions. The pseudorapidity region with $|\eta|$ <1.8 is covered by a presampler located in front of the EM. This presampler helps estimating the energy loss due to the material in front of the calorimeter. The EM is at 99.8% fully operational.

The Hadronic Calorimeter The hadronic calorimeter, which measures hadronic jets, has a coverage in pseudorapisidty of $|\eta| < 3.2$. It is divided into a barrel and two endcaps. The barrel also called Tile calorimeter is composed of steel as the absorber and scintillating tiles as the active material. It is divided into 64 modules distributed among a large barrel and two smaller extended barrel cylinders. the large barrel has a pseudorapidity coverage of $|\eta| < 1.0$ and the two barrel cylinders $0.8 < |\eta| < 1.7$. 96.2% of modules are fully operational.

For the hadronic endcaps (HEC), a copper/liquid-argon technology, similar to the electromagnetic one, is used. They cover the range $1.5 < |\eta|$ <3.2 of the pseudorapidity and they use the same cryostat as the electromagnetic calorimeter endcaps. Each endcap consists of two independent wheels located directly behind the EM endcaps. Each wheel is built from 32 identical wedge-shaped modules, assembled with fixtures at the periphery and at the central bore. It is divided into two segments in depth, for a total of four layers per endcap. The HEC have the ability to detect muons and to measure any radiative energy loss. 99.6% of the endcaps modules are fully operational.

Forward calorimeter Two forward calorimeters (FCal) are positioned on each side of the ATLAS detector to allow the measurements of the forward jets as well as better estimation of the missing transverse energy. They provide both electromagnetic and hadronic measurements and they extend the pseudorapidity range to $|\eta| < 4.9$. Their hermetic design minimizes the energy loss in the cracks between the calorimeter systems and also limits the backgrounds which reach the muon spectrometer. Each FCal module is formed by three sub-modules: one electromagnetic module and two hadronic ones. For the electromagnetic one, which is the closest to the interaction point, cooper is used as the absorber in order to optimize the resolution and the heat removal. For the two hadronic modules, tungsten

is used to provide containment and minimize the lateral spread of hadronic showers. The forward calorimeters are almost fully operational with only 0.2% of the modules not working correctly.

3.2.2.3 The Muon Spectrometer

The muon spectrometer [60] is the outermost part of the ATLAS detector and it defines the overall dimensions of the detector. Figure 3.12 shows the layout of the muon spectrometer with its components.

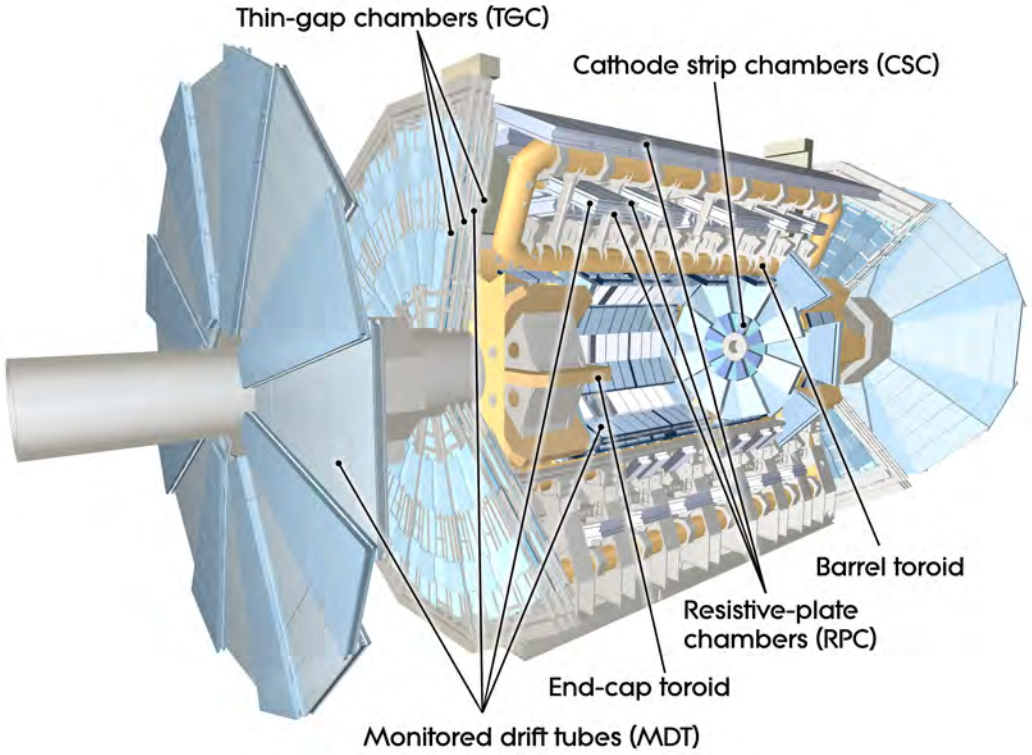

Figure 3.12: An overview of the ATLAS muon spectrometer.

It is designed to detect and measure the momentum of the particles that excites from the barrel and the endcap of the calorimeters within pseudorapidity range $|\eta|$ <2.7, and trigger on them within $|\eta|$ <2.4. The muon spectrometer consists of four different types of muon chambers with different technologies and purposes: the Monitored Drift Tubes (MDT), the Cathode Strip Chambers (CSC), the Resistive Plate Chambers (RPC) and the Thin Gap Chambers (TGC).

The MDT consist of a barrel and two endcaps. The chambers in the barrel are rectangular and in the endcaps trapezoidal. The MDT consists of three to eight layers of 29.970 mm (in diameter) drift tubes, operated at an absolute pressure of 3 bar, which achieve a resolution of 80 μm per tube. The drift tubes contain a mixture gas of 93% Ar and and 7% CO_2. After the ionization, the electrons are collected at the center on a 50 μm tungsten-rhenium wire. The wire is held in position at the tube ends by a cylindrical end-plug which guarantees the concentricity of the wire with respect to the tube. The MDT allows high precision momentum measurement with a high accuracy, a predictability in mechanical deformations and simplicity in construction. The MDT covers the range up to $|\eta|$ <2.7, but in the region 2.0 < $|\eta|$ <2.7 which represents the innermost layer of the endcap region where the rate is high, the MDT are replaced by the CSC. The CSC combine high spatial, time and double track resolution with high-rate capability and low neutron sensitivity. They consist of two disks with multiwire proportional chambers. The wires are oriented in the radial direction with both cathodes segmented in perpendicular directions, which allows measurements in both direction.

The RPC and the TGC are used as the trigger system of the muon spectrometer. The RPC is in barrel region while the TGC is in the endcaps. They are used for triggering with timing resolution of the order of 1.5-4 ns and bunch crossing identification. They provide acceptance over $|\eta|$ <2.4 and over the full ϕ region. They allow fast but less precise measurements. An air-core toroid system generates strong bending field in a large volume within a light and open structure. Two toroids form the endcaps and are inserted in a larger one that covers the barrel region.

3.2.3 The Trigger System and Data Acquisition

At nominal functioning, with 40 MHz bunch crossing frequency and of about 23 inelastic collisions per bunch crossing on average, it is impossible to save and analyze all the collision data produced by the LHC. Therefore, ATLAS has a trigger system [61] that is designed to reject the largest possible rate of background but still selects efficiently potential interesting events. It consists of three levels, as shown in Figure 3.13: a Level-1 trigger (L1), a Level-2 trigger (L2) and an event filter trigger (EF). The L2 and the EF form the High Level Trigger (HLT).
The L1 trigger is hardware-based, it is implemented in the electronics and it is responsible of the first selection of the events. It uses reduced-granularity information from the RPC and the TGC of the muon spectrometer to search for high p_T muons, and all the calorimeter sub-systems for to search for the electromagnetic clusters, electrons, jets and missing transverse energy. It reduces the initial event rate to less than 75 kHz and the L1 decision reaches the front-end electronics

within 2.5 μs after its bunch crossing.

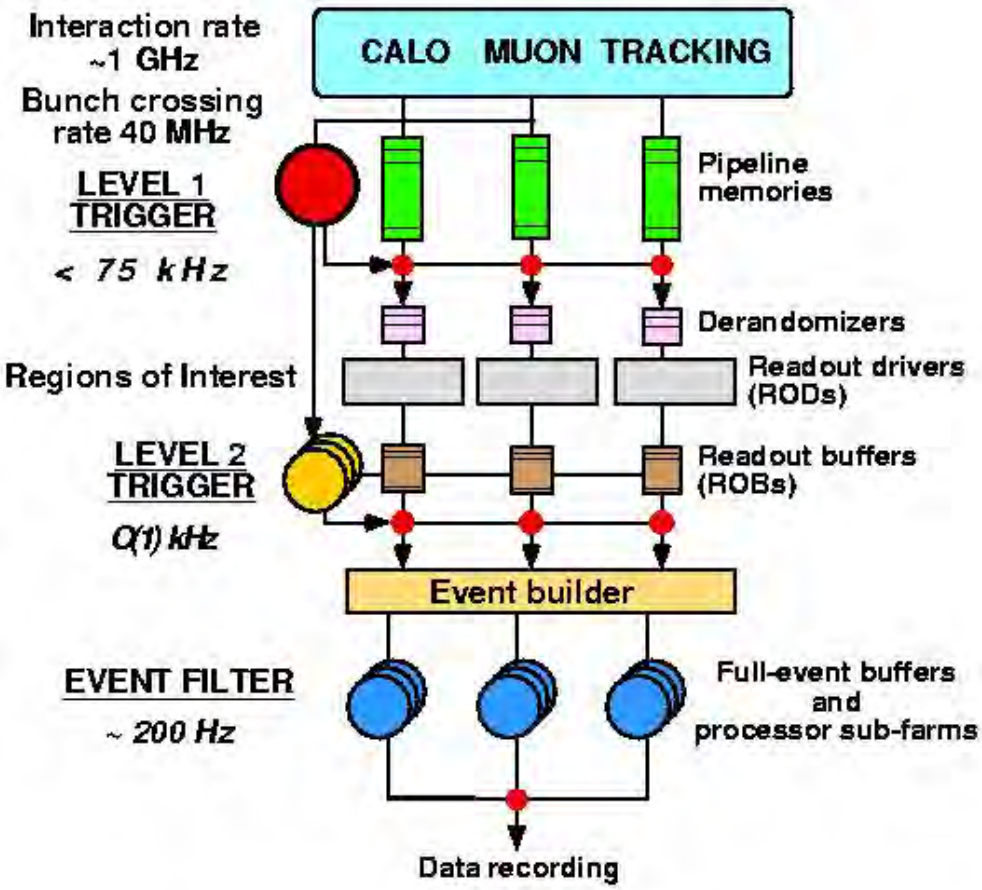

Figure 3.13: Diagram of the ATLAS trigger/DAQ system showing its three levels.

The L2 is a software-based trigger. It relies on the regions of interest of the detector where the L1 has already identified possible objects in the event. This helps reducing the L2 trigger decision time since the amount of data is already reduced by the L1. The L2 trigger reduces the event rate to less than 3.5 kHz, with an average event processing time of almost less than 40 ms.
The EF is the last level of the trigger system and it is also a software-based system. It uses offline analysis procedures on fully-built events to further select events down to a rate which can be recorded for subsequent offline analysis. It reduces the event rate to approximately 200 Hz, with an average event processing time of the order of four seconds.

3.2.4 Offline Data Processing and Analysis

The Grid paradigm and a high level of decentralization and sharing of computing resources are embraced in the ATLAS computing system [62]. This, of course, requires off-site facilities with computing resources for the operation of ATLAS. The first type of data before any processing is called RAW data. RAW data are events stored for reconstruction after the Event Filter step of the trigger system. Events are in byte-stream format as delivered by the detector systems and need to be transformed into object-oriented representations during the reconstruction. The first event processing occurs at CERN facility called Tier-0. The processed data as well as the RAW data are archived at CERN and copied to other facilities around the world called Tier-1. The Tier-1 facilities archive the RAW data and they provide the re-processing capacity as well as the access to the various processed versions. They allow scheduled analysis of the processed data by physics analysis groups. The derived datasets produced by the physics groups are copied to Tier-2 facilities for further analysis. The Tier-2 facilities provide the simulation capacity for the experiment, with the simulated data housed at Tier-1 facilities. In addition, Tier-2 centers provide analysis facilities and some of them provide the capacity to produce calibrations based on processing RAW data.

The ESD, Event Summary Data, are the object-oriented representations of the RAW data. They refer to the data written as the output of the reconstruction process and they contain reconstructed physics object in order to limit the use of RAW data as much as possible. The AOD, Analysis Object Data, are derived from the ESD and they are a reduced representation of them with a less disk size. The AOD contain all the reconstructed physics objects and are ready to be used for the physics analysis. The DPD, Derived Physics Data, are N-tuple representation with a smaller disk size than the AOD. The DPD are easily customized by the physics groups and they contain reduced information than the AOD with the physics objects that are needed by the analysis. They are the final type of data format that is used directly in the analyses.

After the data acquisition, the identification of good runs for the physics analyses is based on the quality of the recorded data. The data quality assessment takes into account each sub-detector individually and its performance during the data taking, but also the performance of the object reconstruction of particle trajectories, jets, electrons or muons. The results of the data quality assessments is stored as data quality flags and they are used to compile a list of good runs and luminosity blocks, referred to as good runs list (GRL). The GRL is created by applying data quality flags selection criteria, and possibly other criteria like the beam energy, to a list of physics runs. The GRL is created before the physics

analysis, and contains run numbers and, for each run, luminosity block ranges. The GRL is subsequently used during the physics analysis to select these good runs and luminosity blocks.

Chapter 4

Object Identification and Reconstruction

The offline event reconstruction in ATLAS starts from RAW data recorded from various ATLAS sub-detectors. These are mainly hits and energy deposits, and proceeds through different algorithms and stages to reconstruct physics objects like charged tracks, vertices, photons, electrons, muons, jets and all other necessary information for physics analyses. This task is not trivial and a special software framework, ATHENA, has been implemented for this purposes as well as an enormous effort to try to improve the reconstruction and identification algorithms in the different detectors and physics domains.
In this chapter, an overview of different ATLAS algorithms is described for different physics objects, and especially the ones that are used later in the b-tagging and $t\bar{t}$ differential cross section analysis.

4.1 Charged Tracks Reconstruction

At the design luminosity functioning of $10^{34} cm^{-2} s^{-1}$, there will be in ATLAS more than 1000 particles emerging from the collision point every 25 ns within $|\eta| < 2.5$ which leads to a very large track density in the detector. High precision measurements are made in the Inner Detector (ID), in order to achieve the resolution requirements imposed by the physics processes. The pixel, SCT and the TRT detectors, described in Chapter 3 Section 3.2.2.1, are the key detectors for the track reconstruction and high granularity track measurements. The inner detector track reconstruction software [63] has a modular and flexible design, which includes features covering the requirements of both the ID and the muon spectrometer [52] reconstruction. These features comprise a common Event Data Model (EDM) [63] and detector description [64], which allow for standard-

ized interfaces to all reconstruction tools, such as track extrapolation, track fitting including material corrections and vertex fitting. The extrapolation package combines propagation tools with an accurate and optimized description of the active and passive material of the full detector [65] to allow for material corrections in the reconstruction process. The track-fitting tools includes global-χ^2 and Kalman-filter techniques, and also more specialized fitters.

The tracking reconstruction can be divided into three stages:

- A pre-processing stage: it consists mainly of transforming the RAW data from the three ID sub-detectors into readable information. The RAW data from the pixel and SCT detectors are converted into clusters and the TRT RAW timing information is translated into calibrated drift circles. The pixel and the SCT clusters are transformed into space-points, using a combination of the cluster information from opposite sides of a pixel or SCT module.

- A track-finding stage: it uses different tracking algorithms and strategies, in order to find the pattern recognition. At this stage, the high granularity of the pixel and SCT detectors is exploited to find prompt tracks originating from the vicinity of the interaction region. The track candidate stems from a combination of space-points in the three pixel layers and the first SCT layer. Then, the track candidates are fitted which allows to resolve the ambiguities in the cluster-to-track association. Subsequently, quality cuts are applied in order to reject fake tracks. The quality cuts, for example, can be applied on the number of associated clusters, with explicit limits set on the number of clusters shared between several tracks and the number of holes[1] per track. The selected tracks are then extended into the TRT to associate drift-circle information in a road around the extrapolation (which cover up to $|\eta| = 2$) and to resolve the left-right ambiguities in the association of the tracks to the drift circles. Finally, the extended tracks are refitted with the full information of the three ID sub-detectors. The quality of the refitted tracks is compared to the silicon-only track candidates and hits on track extensions resulting in bad fits are labelled as outliers (they are kept as part of the track but are not included in the fit).

  A complementary track-finding strategy, called back-tracking, searches for unused track segments in the TRT. Such segments are extended into the SCT and pixel detectors to improve the tracking efficiency for secondary tracks

[1] A hole is defined as a silicon sensor crossed by a track without generating any associated cluster.

from conversions or decays of long-lived particles. This recovers tracks for which the first pixel hits are missing because they originated from secondary vertices for example.

- A post-processing stage, in which a dedicated vertex finder is used to reconstruct primary vertices [2]. This is followed by algorithms dedicated to the reconstruction of photon conversions and of secondary vertices.

For the track reconstruction, generally only prompt tracks originating from a primary vertex with transverse momentum $p_T > 1$ GeV and $|\eta| < 2.5$ are considered. Also, a set of quality cuts is applied on the tracks. These cuts require the reconstructed track to have at least seven hits in the silicon detector (Pixel and SCT). In addition, two cuts are applied on the transverse and longitudinal track impact parameters. The transverse impact parameter d_0, is the distance of the closest approach of the track to the primary vertex in the $r-\Phi$ plane. The longitudinal impact parameter, z_0, is the z coordinate of the track at the point of closest approach in $r-\Phi$ plane. The transverse and longitudinal impact parameters must fulfil respectively the following requirements: $d_0 < 2$mm and $|z_0 - z_v| \times \sin\theta <$ 10 mm, where z_v is the position of the primary vertex along the beam and θ is the polar angle of the track. More tighter cuts, called b-tagging cuts, can be applied on the selected tracks. They will be discussed more in details in Chapter 5.
Figure 4.1 shows the tracks reconstruction efficiency, for different cuts on the transverse momentum of the track, as a function of the pseudorapidity for muons in Figure 4.1 (a), pions in Figure 4.1 (b) and electrons in Figure 4.1 (c). Figure 4.2 shows the track reconstruction efficiency also as a function of the pseudorapidity for muons, pions and electrons for the same cut on the transverse momentum of the track, $p_T > 5$ GeV. While the muons can be reconstructed with a very high efficiency, the reconstruction inefficiency for electrons and pions is due mainly to the hadronic interactions like spallation processes in the detector material, which is present in higher amounts at higher pseudorapidity.

4.2 Electron Identification

The measurement of the electrons is essential for many physics analysis in ATLAS over the full detector acceptance. The electromagnetic calorimeter, described in

[2] In proton-proton collisions, at high luminosity, an event may contain many reconstructed primary vertices. This is a result of multiple proton-proton interactions per bunch crossing, the so-called pile-up.

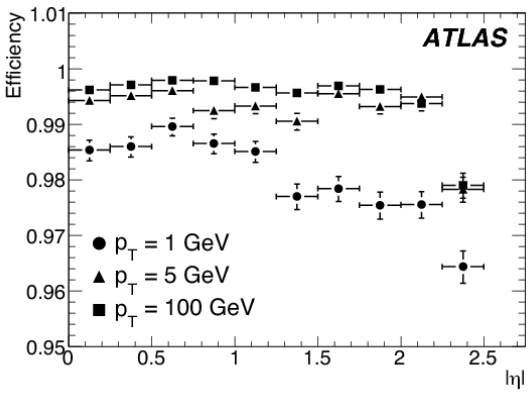

(a)

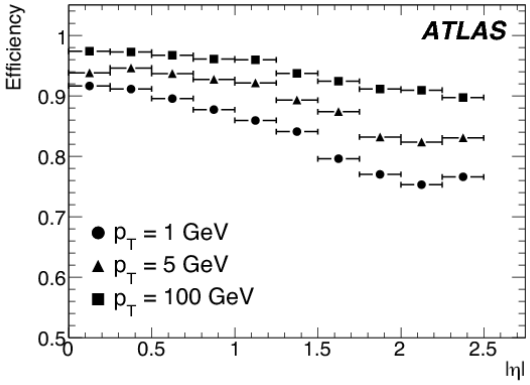

(b)

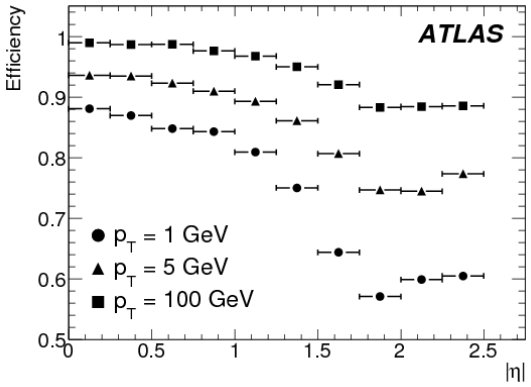

(c)

Figure 4.1: Track reconstruction efficiency for different track transverse momentum cuts (p_T =1, 5 and 100 GeV) as a function of $|\eta|$ for muons in Figure (a), for pions in Figure (b) and for electrons in Figure (c). Taken from [31].

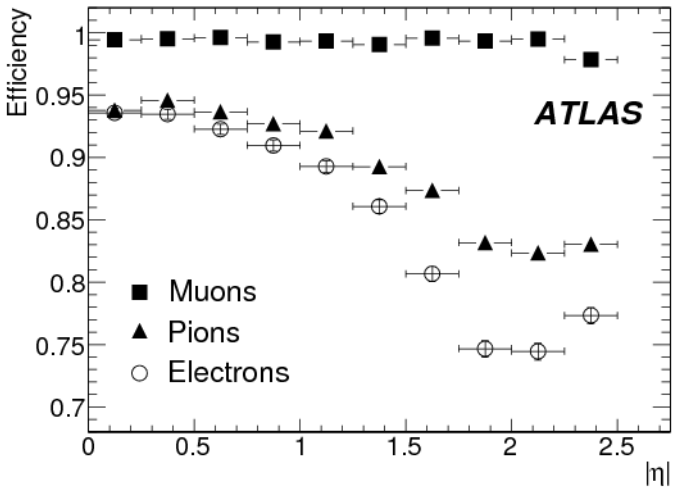

Figure 4.2: Track reconstruction efficiency as a function of $|\eta|$ for muons, pions and electrons with $p_T > 5$ GeV. The inefficiencies for pions and electrons reflect the shape of the amount of material in the inner detector as a function of $|\eta|$. Taken from [31].

Chapter. 3 Section 3.2.2.2, is able to identify and reconstruct electrons in a wide range of energies, going from 5 GeV up to 5 TeV. In order to isolate real electrons, it is crucial to be able to reject the very large background which consists mainly of jets faking electrons, or electrons coming from heavy flavour or from Dalitz decays or photon conversion originating from neutral pion decays, with a rejection factor up to 10^5 while keeping a uniform and high identification efficiency over the full p_T and η range.

The electron reconstruction algorithm [66] uses the reconstructed energy clusters in the electromagnetic (EM) calorimeter and matches them to a reconstructed track in the ID. Information is used from the electromagnetic calorimeter and the inner detector to give a maximum identification efficiency for the electrons with the highest possible rejection of the background. The EM calorimeter has a fine segmentation in the lateral ($\eta \times \phi$ space) and the longitudinal directions of the EM shower. Most of the EM shower energy is collected in the second layer of the EM calorimeter which has a lateral granularity of 0.025.025 in $\eta \times \phi$ space.

The identification of electrons starts by selecting seed clusters with energies above 2.5 GeV [67] in the EM calorimeter that must fulfil 3×5 in η/ϕ in the middle layer cell unit. Duplicated clusters with seed clusters are then removed after an energy comparison. If the final seed cluster lies in the region of the

tracker ($|\eta|$ <2.5), it is then matched to one or more reconstructed tracks and thus the electron is defined. The matching between the tracks and the EM clusters is performed by extrapolating them from their last measured point in the ID to the second layer of the calorimeter. The impact point η and ϕ coordinates are compared to the corresponding seed cluster η and ϕ coordinates in that layer. If their difference is below a certain threshold then the track is considered matched to the cluster. Special tracking algorithms, like Guassian Sum Filter [68] or Dynamic Noise Adjustement [69], are applied in order to account for Bremsstrahlung losses in the detector material.

If the final seed cluster lies in the forward region (2.5< $|\eta|$ <4.9), the identification of the electrons doesn't use any information from the tracker, and it is no more possible to distinguish between electrons and photons. In the forward calorimeters, an electron candidate is identified if there is an EM cluster with transverse energy $E_T > 5$ GeV. The direction of the electron is defined from the barycenter of the cells belonging to the cluster in the calorimeter, and the sum of the energies of the cluster cells determines the energy of the electron. In order to distinguish electrons from hadrons, the difference in the electromagnetic showers induced by the electrons and the hadronic showers induced by the hadron (eg. pion) is exploited. These differences appear in the energy deposition and the shower shape of the two types of particles.

4.2.1 Electron Preselection Cuts

The standard electron identification algorithm for high p_T electrons (E_T >20 GeV and $|\eta|$ <2.5) is based on a combination of cuts using variables that provide good separation between isolated electrons and jets (faking electrons), with three reference sets of cuts, *loose*, *medium* and *tight* providing different electron efficiency vs jet rejection working points. To allow for robustness, various changes are made based on the expected level of understanding of the detector performance.

Loose Electron Identification

The loose electron cuts uses a limited number of discriminating variables from the calorimeter. This selection provides high identification efficiency (94.32% [67]) but a low background rejection. The cuts are applied on the hadronic leakage which is the ratio between the E_T of the first sampling of the hadronic calorimeter and the E_T of the EM cluster. Also some cuts on the shower shape in the EM calorimeter are applied. The different discriminating variables as well as their cut values are presented in Table 4.1.

Type	Description	Name
Loose selection		
Acceptance	$\|\eta\| < 2.47$	
Hadronic leakage	Ratio of E_T in the first layer of the hadronic calorimeter to E_T of the EM cluster (used over the range $\|\eta\| < 0.8$ and $\|\eta\| > 1.37$)	R_{had1}
	Ratio of E_T in the hadronic calorimeter to E_T of the EM cluster (used over the range $\|\eta\| > 0.8$ and $\|\eta\| < 1.37$)	R_{had}
Middle layer of EM calorimeter	Ratio of the energy in 3×7 cells over the energy in 7×7 cells centered at the electron cluster position	R_η
	Lateral width of the shower	$w_{\eta 2}$
Medium selection (includes loose selection cuts)		
Strip layer of EM calorimeter	Total shower width	w_{stot}
	Ratio of the energy difference between the largest and second largest energy deposits in the cluster over the sum of these energies	E_{ratio}
Track quality	Number of hits in the pixel detector (≥ 1)	n_{pixel}
	Number of total hits in the pixel and SCT detectors (≥ 7)	n_{Si}
	Transverse impact parameter ($\|d_0\|$ <5 mm)	d_0
Track–cluster matching	$\Delta\eta$ between the cluster position in the strip layer and the extrapolated track ($\|\Delta\eta\| < 0.01$)	$\Delta\eta$
Tight selection (includes medium selection cuts)		
Track–cluster matching	$\Delta\phi$ between the cluster position in the middle layer and the extrapolated track ($\|\Delta\phi\| < 0.02$)	$\Delta\phi$
	Ratio of the cluster energy to the track momentum	E/p
	Tighter $\Delta\eta$ requirement ($\|\Delta\eta\| < 0.005$)	$\Delta\eta$
Track quality	Tighter transverse impact parameter requirement ($\|d_0\|$ <1 mm)	d_0
TRT	Total number of hits in the TRT	n_{TRT}
	Ratio of the number of high-threshold hits to the total number of hits in the TRT	f_{HT}
Conversions	Number of hits in the b-layer (≥ 1)	n_{BL}
	Veto electron candidates matched to reconstructed photon conversions	

Table 4.1: Definition of the discriminating variables used for loose, medium and tight electron identification cuts for the central region of the detector with $|\eta| < 2.47$.

Medium Electron Identification
The medium selection includes the loose cuts and adds more cuts on the shower width as well as the ratio of the energy difference associated with the largest and second largest energy deposit over the sum of these energies. The medium cuts also include cuts on the tracks, for the number of hits in the pixel detector, the number of hits in the silicon detector, the track transverse impact parameter and a cut on the $\Delta\eta$ between the track and the cluster. The details of the cuts and the variable names is also given in Table 4.1. The medium electron identification has an efficiency of $\approx 90\%$ [67], less than the loose identification efficiency as expected, but it increases the jet rejection by a factor 5-6 with respect to the loose identification.

Tight Electron Identification
The tight electron identification includes the medium selection cuts and it is foreseen to achieve high rejection background. Additional cuts are applied on the silicon hits to reject electrons from conversion, and the tight selection is adapted to take into account disabled *b*-layer modules. The tight candidate electron crossing a disabled *b*-layer module is kept. Cuts on the hits in the TRT as well as on the fraction of high threshold hits [3] in the TRT are applied. The electrons that match reconstructed conversion photons are rejected. More cuts are applied on the $\Delta\phi$ between the cluster position in the second layer of the calorimeter and the extrapolated track as well as the cluster energy over track momentum (E/p). In addition, the tight selection has stricter $\Delta\eta$ and impact parameter cuts than the medium selection. All the variables used and the cut values for the tight selection are shown in Table 4.1. The tight selection identification has an efficiency of $\approx 73\%$. The jet rejection improves by a factor of ≈ 100 with respect to the medium electron identification.

Isolated Electron Identification
The loose, medium and tight sets of cuts don't include any requirement on the electron isolation. This cut is applied on top of these because it is analysis dependant and various analyses may require different isolation criteria of different tightness. The reconstructed energy in a cone of half opening angle R_0 around the electron candidate direction, excluding the energy of the electron itself, is used to compute the calorimetric isolation. While a larger cone will contain more energy in case of misidentified jets, a smaller cone is more robust against energy depositions from pile-up events. A cone with $R_0 = 0.3$ has been found to give the best trade-off with high discrimination power and robustness against pile-up

[3] The threshold hits in the TRT corresponds to the transition radiation, and therefore applying a cut on it gives a higher probability of having electrons than charged pions.

Cuts	Efficiency(%)	Jet rejection
Reco	96.25±0.03	87.3±0.1
Loose	94.68±0.03	614.3±1.5
Medium	89.61±0.03	4435±30
+isol. 99%	88.49±0.03	6280±50
+isol. 98%	87.57±0.03	8330±80
+isol. 95%	84.99±0.03	13000±160
+isol. 90%	81.26±0.03	17700±250
Tight	72.77±0.03	$(4.9\pm0.1).10^5$
+isol. 99%	71.95±0.03	$(7.1\pm0.2).10^5$
+isol. 98%	71.27±0.03	$(9.4\pm0.3).10^5$
+isol. 95%	69.33±0.03	$(1.52\pm0.06).10^5$
+isol. 90%	66.50±0.03	$(2.10\pm0.10).10^5$

Table 4.2: Expected jet rejections, isolated electron efficiencies and non-isolated electron efficiencies for the three standard sets of identification cuts with $E_T > 20$ GeV and η <2.5. The total jet rejection includes hadron fakes and background electrons from photon conversions and Dalitz decays. The efficiencies are computed on a $Z \rightarrow ee$ sample and rejections are computed on a filtered dijet sample. The quoted errors are statistical. Taken from [66].

at the same time. The summed scalar p_T of tracks in a cone of $R_0 = 0.3$ around the electron is used and other track quality criteria are applied in order to reject tracks from secondary vertices. The tracks with $p_T > 1$ GeV are considered with a hit in the *b*-layer, at least 7 hits in silicon detectors and transverse and longitudinal impact parameter less than 1 mm. For tracks within $\Delta R < 0.1$ with respect to the electron it is also required that they are not matched to a conversion vertex. The cuts are optimized for different region of p_T and η. The electrons which are used for the cut optimization are required to pass the medium electron identification criteria. The optimization is performed in such a way that the efficiency for isolated electrons, with respect to the pre-selection, is constant in all ranges of p_T and η. Three sets of cuts that exploit calorimetric and tracking isolation variables are part of the recent software releases. Each of them allow to retain 99%, 98%, 95% or 90% efficiency for isolated electrons.

The identification efficiency and the expected jet rejection, for isolated and non-isolated high energy electrons, for the three standard sets of identification cuts are given in Table 4.2. The efficiencies are computed on a $Z \rightarrow ee$ sample and the rejection is computed using a filtered dijet sample. The Table 4.3 shows the expected efficiencies for the three sets of identification on simulated $t\bar{t}$ events.

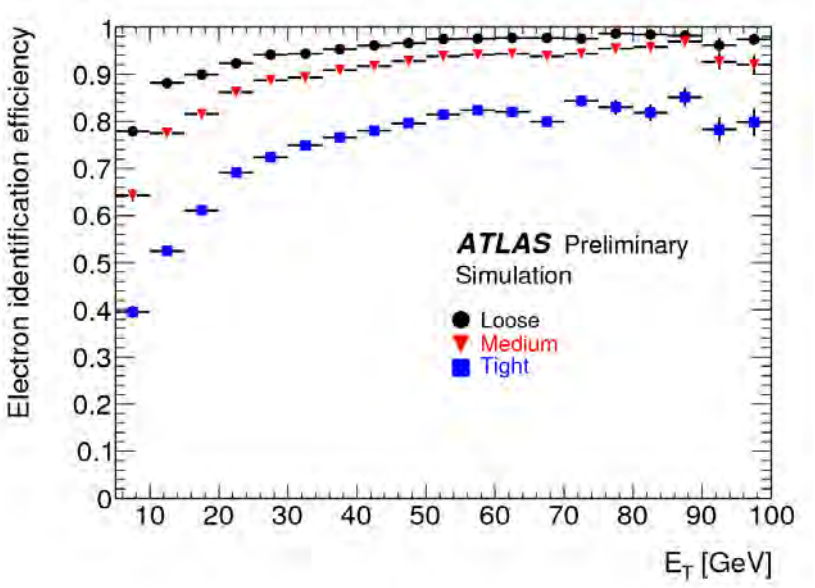

(a)

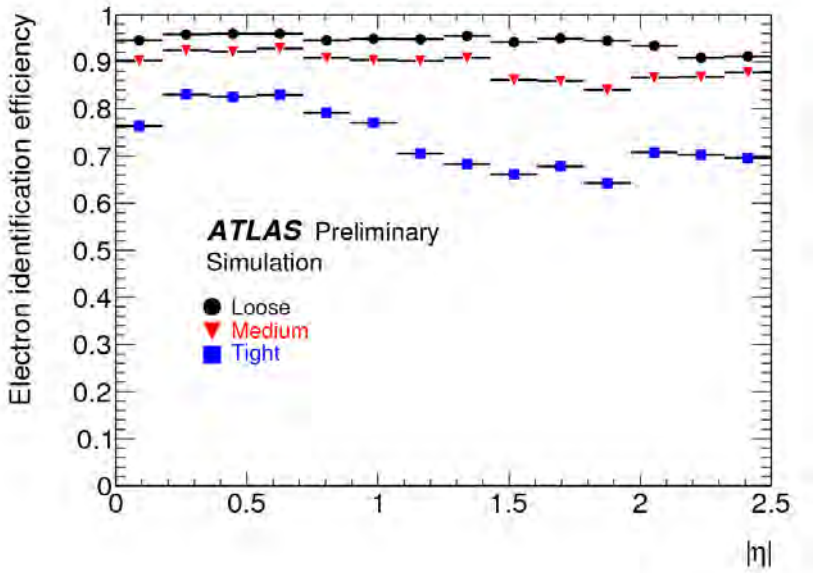

(b)

Figure 4.3: Electron identification efficiency for loose, medium and tight selection cuts normalized to all reconstructed electron candidates as a function of E_T (a) and $|\eta|$ (b) in $Z \rightarrow ee$ events. Taken from [66].

Cuts	Efficiency(%)
Loose	89.73±0.04
Medium	87.20±0.05
Tight	75.26±0.06

Table 4.3: Electron identification efficiency for non-isolated electron for the three standard sets of identification cuts with $E_T > 17$ GeV and $\eta < 2.5$ derived from simulated $t\bar{t}$ events. The quoted errors are statistical. Taken from [66].

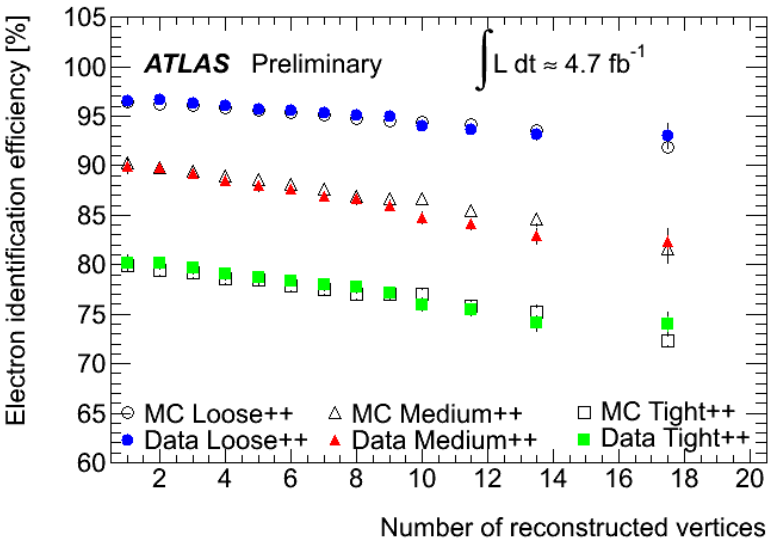

Figure 4.4: Electron identification efficiency dependence on pileup for loose, medium and tight selection cuts derived from the whole 2011 data.

Figure 4.3 shows the loose, medium and tight electron identification efficiencies as a function of the transverse energy E_T (Figure 4.3 (a)) and as a function of the pseudorapidity (Figure 4.3 (b)). Figure 4.4 shows the loose, medium and tight electron identification efficiencies as a function of the pileup, using the full 2011 data. These efficiencies can be applied to any physics process in forms of data to MC scale factors which are defined as the ratios of the data to MC efficiencies in any specific bin which are applied multiplicatively to the MC prediction in the same bin.

4.3 Muon Identification

There are three different approaches to reconstruct muons in ATLAS. The first one, the *standalone* reconstruction, starts by identifying track segments in the muon spectrometer (MS). These track segments are subsequently linked together and the resulted track is extrapolated towards the interaction point through the ID. For the extrapolation, the energy loss and the multiple scattering based on the material crossed in the ID and the calorimeters are taken into account. The second approach, *combined* muons, the one that will be further described since it's the one recommended for the physics analyses and the one used in this thesis, matches the standalone muons in the MS to tracks in the inner detector and then combines the measurement from the two systems. This combination improves the track parameter resolution. *Combined* muons significantly reduce the rate of fake prompt muons, originating from π and K decays in flight. The third muon reconstruction approach, called *tagged* muons, reconstructs the muons by extrapolating inner detector tracks to the muon spectrometer detectors by searching for nearby hits.

4.3.1 *Combined* Muons

The *combined* muon reconstruction matches the reconstructed tracks in the MS to reconstructed tracks in the ID. It uses a χ^2_{macth} to determine the quality of the match. The χ^2_{macth} is defined as the difference between outer (in the MS) and inner (in the ID) track vectors ($\vec{T}$) weighted by their combined covariance matrix ($\vec{C}$):

$$\chi^2_{macth} = (\vec{T}_{MS} - \vec{T}_{ID})^T (\vec{C}_{ID} + \vec{C}_{MS})^{-1} (\vec{T}_{MS} - \vec{T}_{ID}) \tag{4.1}$$

where $\vec{T}$ denotes the vector of five track parameters, expressed at the point of closest approach to the beam line and $\vec{C}$ its covariance matrix.
There are two muon combination algorithms in ATLAS, STACO and MuId, and they are both used in this thesis. STACO algorithm uses χ^2_{macth} to decide which

pair (ID-MS) to keep. It performs a statistical combination of the inner and outer track vectors weighted by their co-variance matrices, to obtain the combined track vector:

$$\vec{T} = (\vec{C}_{ID}^{-1} + \vec{C}_{MS}^{-1})^{-1}(\vec{C}_{ID}^{-1}\vec{T}_{ID} + \vec{C}_{MS}^{-1}\vec{T}_{MS}) \quad (4.2)$$

MuId algorithm performs a partial fit. It starts from the ID track vector and its covariance matrix, and it adds the measurements from the track in the MS. The fit takes into account the material (multiple scattering and energy loss) and magnetic field in the calorimeter and muon spectrometer.

Combined muons are the highest purity muon candidates. Their reconstruction efficiency is determined mainly by the ability to form the independently reconstructed MS track, which varies with pseudorapidity and the azimuthal angle. This is most apparent in two regions:

- ⋆ At $\eta \sim 0$, the MS is only partially equipped with muon chambers to provide space for services of the ID and the calorimeters.
- ⋆ At $|\eta| \sim 1.2$, in the region between the barel and the endcaps, the muon crosses only one muon chamber in the muon spectrometer due to staged end-cap chambers. So no stand-alone momentum measurement is available and the combined muon efficiency is lower in this region.

4.3.2 Reconstruction Efficiency for Combined Muons

Figure 4.5 and Figure 4.6 show the efficiency for combined muons as a function of the muon transverse momentum and detector region for data and simulation, respectively for the STACO and MuId algorithms. The simulation includes all considered backgrounds. The scale factor, defined as the ratio between data and Monte Carlo, is displayed in the lower panel of each plot. The scale factor is on average equal to 0.9806 ± 0.0024 for the STACO algorithm and 0.9918 ± 0.0020 for the MuId, where the errors are statistical only. The largest deviation is found to be in the Transition region with a scale factor of 0.902 for STACO and 0.971 for MuId. The efficiency drop in the Transition region is attributed to the limited accuracy of the magnetic field map used in the first-pass reconstruction of the ATLAS data in this region which leads to a small mismeasurement of the stand-alone muon momentum.

4.4 Jet Reconstruction

The EM and hadronic calorimeters play a major role in the reconstruction of the jets since they provide an effective way to reconstruct the four momentum of both

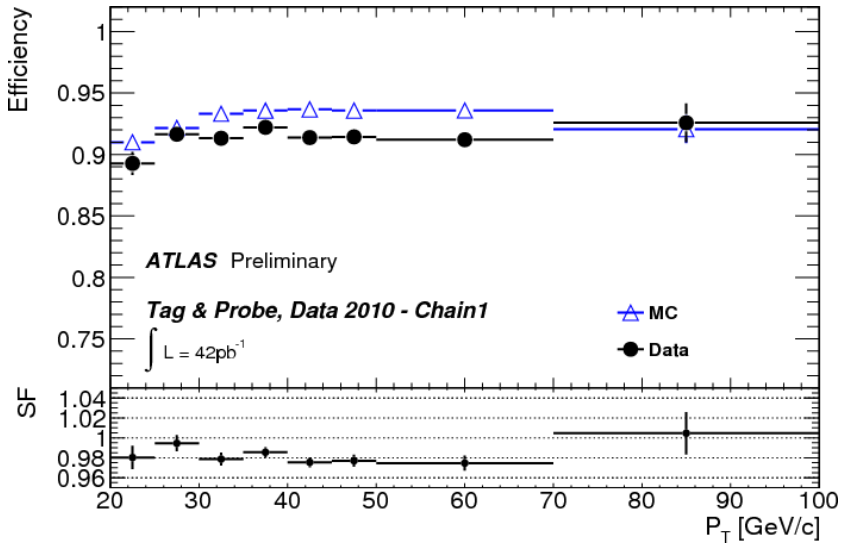

(a)

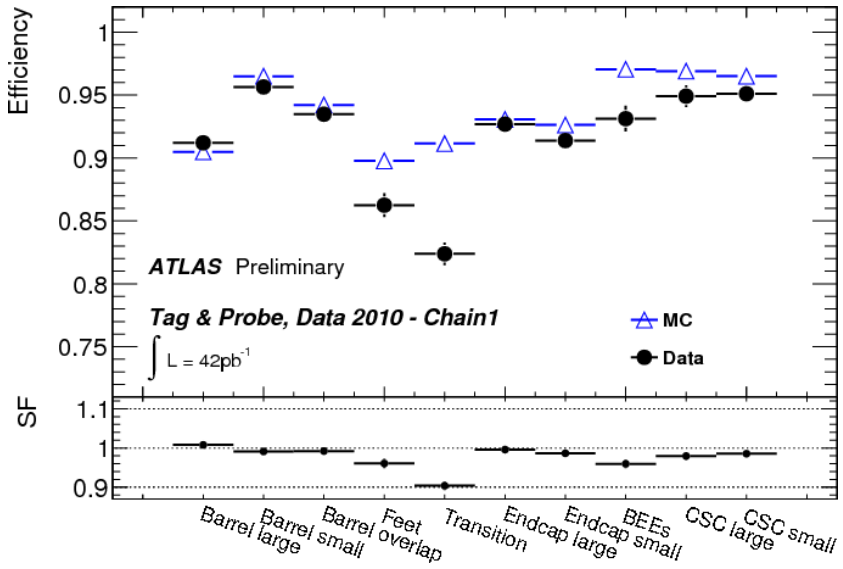

(b)

Figure 4.5: Muon reconstruction efficiency and scale factors for combined muons using the STACO algorithm. The efficiency obtained from data (dots) and Monte Carlo simulation (open triangles) including backgrounds, is shown in the upper part of each figure, in (a) as a function of the muon p_T and in (b) as a function of different regions of the detector. The corresponding scale factors are shown in the lower part. Taken from [70].

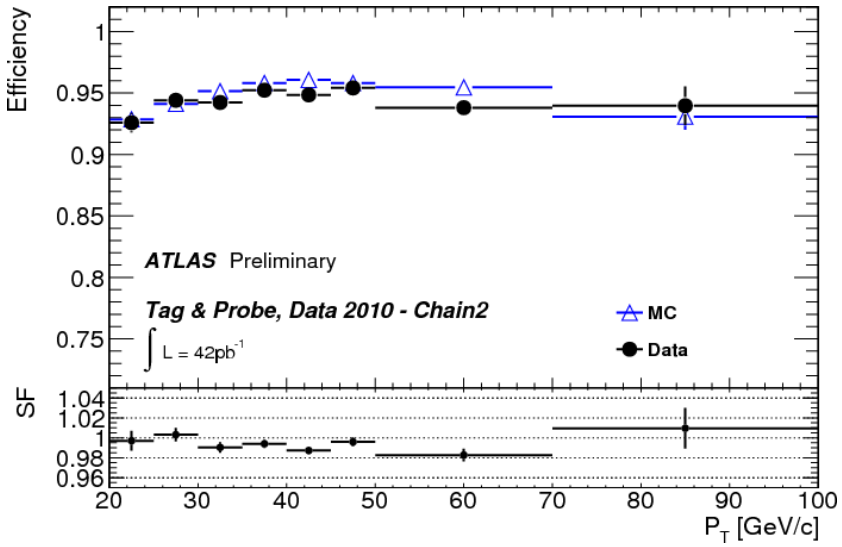

(a)

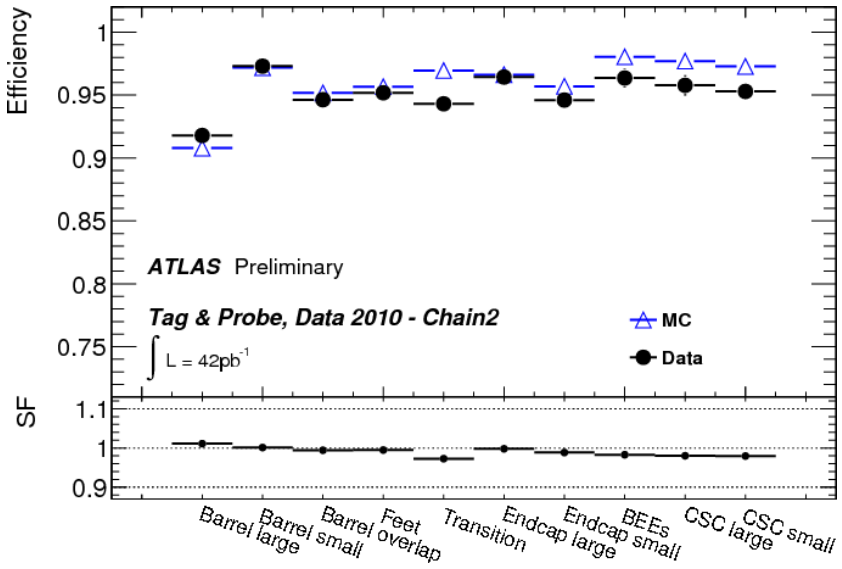

(b)

Figure 4.6: Muon reconstruction efficiency and scale factors for combined muons using the MuId algorithm. The efficiency obtained from data (dots) and Monte Carlo simulation (open triangles) including backgrounds, is shown in the upper part of each figure, in (a) as a function of the muon p_T and in (b) as a function of different regions of the detector. The corresponding scale factors are shown in the lower part. Taken from [70].

charged and neutral particles. They consists of ≈ 200000 individual cells of various sizes with lateral and longitudinal segmentations and provide nearby hermetic coverage in pseudorapidity: $-4.9 < |\eta| < 4.9$. The technology choices of the calorimeters, detailed in Chapter. 3 Section 3.2.2.2, are well suited for high quality jet reconstruction in the challenging environment of the proton-proton collisions at the LHC.

Many features should be thought about for the jet reconstruction algorithm, like for example the presence of additional soft particles between two particles belonging to the same jet should not affect the recombination of these two particles into a jet. And the correct reconstruction of the jet should not be affected by the absence of additional particles between these two. Generally, any soft particles not coming from the fragmentation of a hard scattered parton should not affect the number of jets produced. A jet should be reconstructed independently from the amount of transverse momentum carried by one particle, or if a particle is split into two collinear particles. The same hard scattering process should be reconstructed independently at parton-, particle- or detector level. Since the detector has a finite spacial and energy resolution, the jet and its kinematic must be calibrated or corrected from these effects and inefficiencies.

4.4.1 Jet Finding Algorithm

For the jet finding, the individual calorimeter cells are combined into larger signal objects with physically meaningful four-momenta, these objects are called topological cell clusters [31]. The inputs to the jet finding algorithm are usually the sum of the energy deposits in the calorimeter towers (the EM and the hadronic connected calorimeter cell layers) of 0.1×0.1 in $\Delta\phi \times \Delta\eta$ or, more sophisticatedly, a complex three-dimensional clusters energy without geometric constraints, the *topoclusters*. *Topoclusters* are the ones used in ATLAS. A *topocluster* starts with a seed cell with a signal significance $\Gamma = |E_{cell}|/\sigma_{noise,cell} > 4$. The direct neighbours in three dimensions to the seed are added to the cluster if they have a signal significance $\Gamma > 2$. The cells at the boundaries are required to have minimum energy deposit. The cells that constitute the *topoclusters* are hence called *topocells*. This set of thresholds, referred to as 4/2/0, is optimized to suppress electronics noise as well as pile-up from minimum bias events, while keeping the single pion efficiency as high as possible. Once the *topocells* are found, the initial three-dimensional clusters are analyzed for local signal maxima. If multiple local signal maxima are found, the clusters are split between those maxima by a splitting algorithm. These clusters are formed using the basic electromagnetic scale cell signals and are directly used as input for the jet reconstruction. The calibration of the jets to the final energy scale is done on a jet-by-jet basis. This procedure is described in Section 4.4.4.

4.4.2 Jet Reconstruction Algorithm

Fixed Cone Jet Finder in ATLAS

An iterative fixed cone-jet finder [31] is the standard jet finding algorithm in ATLAS. First, all input clusters are ordered in decreasing order in transverse momentum p_T. If the leading object is above the seed threshold, which is set to 1 GeV, all objects within a cone of $\Delta R = \sqrt{\Delta\eta^2 + \Delta\phi^2} < R_{cone}$, where R_{cone} is a fixed cone radius, are combined with the seed. From the four momentum inside the initial cone, a new direction is calculated and a new cone is centered around it. Once this new cone is fixed, objects are then recollected in it, and a new direction is recalculated. Many iterations are performed until the direction of the cone does not change anymore after recombination. At this stage, the cone is considered stable and is called a jet. The same iterative procedure is applied to the next seed and so on, until no further seeds are available. This technique is not completely safe from jets sharing constituents. This is partially recovered by a split or merge step after the jet formation. The jets that share constituents corresponding to a fraction $f_{sm} = 0.5$ of the transverse momentum p_T of the less energetic jet are merged, while they are splitted in the opposite case. This algorithm is well defined only up to a leading order of perturbation theory but the splitting and the merging procedure makes it partially infrared safe.

The Anti-k_t Jet Clustering Algorithm

The default jet reconstruction algorithm in ATLAS is the anti-k_t [71] jet clustering algorithm. It is a simple jet reconstruction algorithm that introduces distances d_{ij} between pseudo-jets i and j and d_{iB} between pseudo-jet i and the beam B. The distance d_{ij} is defined as:

$$d_{ij} = min(p_{T,i}^2, p_{T,j}^2)\frac{\Delta R_{ij}^2}{R^2}, \text{ with } \Delta R_{ij}^2 = \Delta\eta_{ij}^2 + \Delta\phi_{ij}^2 \tag{4.3}$$

where R represents the cone radius parameter which determines the size of the jet. In this thesis, only jets with $R = 0.4$ are considered which is the narrower in ATLAS. The distance to the beam is defines as follows:

$$d_{iB} = p_{T,i}^2 \tag{4.4}$$

where $p_{T,i}$ is the transverse momentum of the jet i. The algorithm searches for the minimum d_{min} of all d_{ij} and d_{iB}. If d_{min} is a d_{ij}, the corresponding objects i and j are combined into a new object k using four-momentum recombination. Both objects i and j are removed from the list, and the new object k is added to it. If d_{min} is one of the d_{iB}, the object i is considered to be a jet by itself and thus removed from the list. This procedure is repeated with many iterations, each time

with the new d_{ij} and d_{iB}, until all objects are removed from the list. This algorithm is infrared safe because no objects are shared between the jets, and it is collinear safe as it does not start with seeds.

4.4.3 Truth jets

In simulated data, the so-called truth jets are formed by clustering stable truth particles originating from the fragmentation and decay of short lived particles ($\tau <$ 10 ps) in the Monte Carlo physics generator. Jet finding with generated particles uses the same code as calorimeter reconstruction. In ATLAS, stable truth particles are those with a lifetime $\tau > 10$ ps, thus typically including electrons, muons, photons, charged pions, kaons, protons, neutrons, neutrinos, and their corresponding antiparticles. These particles represent the truth reference of a hard scattering process for performance studies and simulation based calibration approaches.

4.4.4 Jet Energy Scale Calibration

The jet should be corrected or calibrated to compensate for the energy loss in the crack region ($1.37 < |\eta| < 1.52$) due to particles escaping the calorimeters or out-of-cone contributions, or for the e/π energy response ratio of the non-compensating calorimeter[4]. The standard calibration procedure adopted in ATLAS is based on cell energy weighting, denoted Local Hadronic Calibration (LCW), applied to the calorimeter cells of the three-dimensional topoclusters in the jet. Low energy densities in calorimeter cells indicate a hadronic energy in a non-compensating calorimeter and thus need an energy weight for compensation of the order of the e/π energy ratio , while high energy densities are more likely generated by electromagnetic showers and therefore do not need additional energy weighting. The energy in each cell i is weighted by a function depending on its location $\vec{X}_i$ and the cell energy density $\rho = E_i/V_i$ where E_i is the electromagnetic energy and V_i is the cell volume. The weighting functions are universal in that they do not depend on any jet feature or variable. The calibrated jet four-momentum $(E_{jet,calo}, \vec{p}_{reco})$ is then recalculated from the weighted cell energies, which are treated as massless four-momenta $(E_i, \vec{p}_i)$ with fixed directions:

$$(E_{jet,calo}, \vec{p}_{reco}) = (\sum_{i}^{N_{cells}} w(\rho_i \vec{X}_i) E_i, \sum_{i}^{N_{cells}} w(\rho_i \vec{X}_i) \vec{p}_i) \tag{4.5}$$

The energy weighting functions have been determined using seeded fixed size cone jets ($R_{cone} = 0.6$) in fully simulated QCD dijet events by fits of reconstructed

[4]The basic energy scale for the ATLAS calorimeters is the electromagnetic scale [72]

calorimeter tower jet energies to match Monte Carlo truth particle jet energies. The calibration has been determined using the ideal, non-distorted detector geometries. At present, ATLAS uses a calibration scheme referred to as EM+JES that applies jet-by-jet corrections to the jets reconstructed at the electromagnetic scale. These corrections depend on the jet energy and pseudorapidity of the jet. The calibration restores the jet energy scale within 2% for the full kinematic range. Figure 4.7 shows the average jet energy scale correction as a function of the calibrated jet transverse momentum p_T for three different ranges of the pseudorapidity.
The identification and reconstruction as well as the calibration of b-jets is described in Chapter 5.

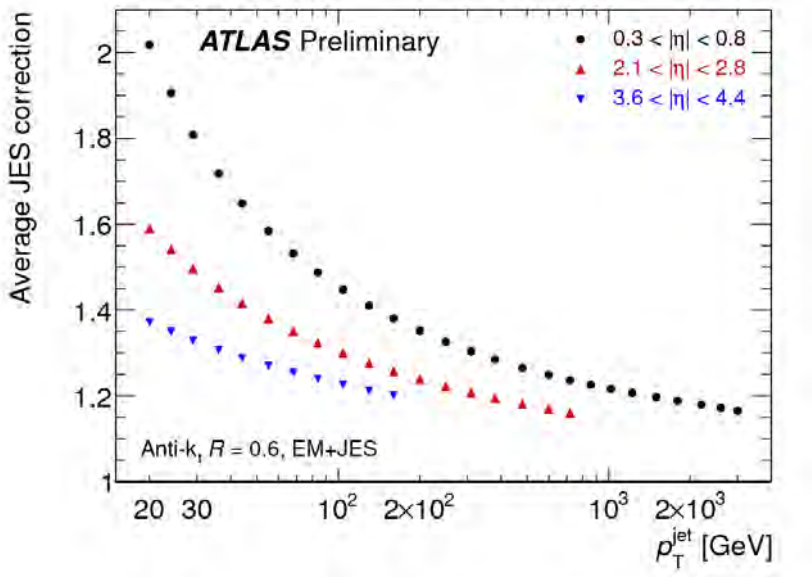

Figure 4.7: Average jet energy scale correction as a function of calibrated jet transverse momentum for three pseudorapidity η intervals, $0.3 < |\eta| < 0.8$, $2.1 < |\eta| < 2.8$ and $3.6 < |\eta| < 4.4$. The correction is only shown over the accessible kinematic range, i.e. values for jets above the kinematic limit are not shown. Taken from [72].

4.5 Missing Transverse Energy

Measuring the transverse missing energy E_T^{miss} in ATLAS is of a great importance. It is expected to be one of the key signature of new physics signals like SUSY or extra dimensions. A good E_T^{miss} measurement in terms of resolution and precision

is very important for new physics search, but also for reconstructing $t\bar{t}$ events with one top decaying semi-leptonically as it will be discussed in Chapter 6. It is crucial as well for the efficient and accurate reconstruction of the Higgs boson mass when the Higgs boson decays to a pair of τ-leptons for instance. The measurement of E_T^{miss} is mainly based on energy deposit in the calorimeters and on the reconstructed muon tracks that escape the calorimeters. The missing energy can only be measured in the transverse plane since the LHC is a hadron collider and after the hard scattering occurs, an unknown fraction of the longitudinal momentum of the incoming protons is taken away from the proton remnants leaving the detector outside its acceptance. The E_T^{miss} reconstruction includes contributions from transverse energy deposits in the calorimeters, corrections for energy loss in the cryostat and measured muons:

$$E_{x(y)}^{miss} = E_{x(y)}^{miss,Calo} + E_{x(y)}^{miss,muon} \tag{4.6}$$

The transverse missing energy E_T^{miss} and its azimuthal position (ϕ_{miss}) are then calculated as:

$$E_T^{miss} = \sqrt{(E_x^{miss})^2 + (E_y^{miss})^2} \text{ and } \Phi^{miss} = a\tan\left(\frac{E_y^{miss}}{E_x^{miss}}\right) \tag{4.7}$$

$E_{x(y)}^{miss,Calo}$ in Eq. 4.6 refers to the calorimeter term of the E_T^{miss}. To minimize the impact of the noise, the calorimeter cells belonging to the topoclusters are selected, and from the transverse energies measured in the topoclusters, the x and y components are calculated:

$$E_x^{miss,Calo} = -\sum_i^{N_{topocells}} E_i sin\theta_i cos\phi_i \ , \ E_y^{miss,Calo} = -\sum_i^{N_{topocells}} E_i sin\theta_i sin\phi_i \tag{4.8}$$

where E_i, θ_i and ϕ_i are respectively the energy, the polar and the azimuthal angles of the topocluster in $|\eta| < 4.5$. All the topocells are then calibrated on the basis of the reconstructed physics object to which they belong. The calorimeter cells are associated with a reconstructed and identified high-p_T parent object: electrons, photons, hadronically decaying τ-leptons, jets and muons. Cells belonging to topoclusters not associated with any such objects are also taken into account in the E_T^{miss} calculation. Once the cells are associated with a category of object as described above and calibrated accordingly, $E_T^{miss,calo}$ is calculated as follows:

$$E_T^{miss,Calo} = E_T^{miss,e} + E_T^{miss,\gamma} + E_T^{miss,\tau} + E_T^{miss,jets} + E_T^{miss,softjets} + E_T^{miss,Calo,\mu} + E_T^{miss,CellOut} \tag{4.9}$$

where $E_T^{miss,jets}$ is reconstructed from topocells in jets with $p_T > 20$ GeV and $E_T^{miss,softjets}$ is reconstructed from topocells in jets with $7 < p_T < 20$ GeV.

$E_T^{miss,Calo,\mu}$ is the contribution from energy lost by muons in the calorimeter and $E_T^{miss,CellOut}$ is calculated from the topoclusters which are not included in the reconstructed objects.

$E_{x(y)}^{miss,muon}$ in Eq. 4.6 represents the muon term and it is calculated from the momenta of muons measured in a range of pseudorapidity, defined by $|\eta| < 2.7$:

$$E_{x(y)}^{muon} = -\sum_{RecMuons} E_{x(y)} \tag{4.10}$$

Apart from the loss of muons outside the acceptance of the muon spectrometer ($|\eta| > 2.7$), there is a loss of muons in other regions due to limited coverage of the muon spectrometer. The muons reconstructed from the inner detector and calorimeter energy deposits could be used to recover these events. Only well-reconstructed muons in the muon spectrometer with a matched track in the inner detector are considered. The matching requirement considerably reduces contributions from fake muons.

4.5.1 E_T^{miss} Calibration

The standard calibration of the E_T^{miss} in ATLAS is referred as $RefFinal$ and is the one used in this thesis. Its different components are calculated as follows:

- $E_T^{miss,e}$ is calculated from medium electrons with p_T >10 GeV and calibrated with the default electron calibration at EM scale.
- $E_T^{miss,\gamma}$ is calculated from tight photons with p_T >10 GeV at EM scale.
- $E_T^{miss,\tau}$ is calculated from tight τs with p_T >10 GeV and calibrated with LCW.
- $E_T^{miss,jets}$ is calculated from jets with p_T >20 GeV and calibrated with LCW and with the JES correction applied. The jets are reconstructed using the anti-k_t algorithm with $R = 0.6$.
- $E_T^{miss,softjets}$ is calculated from jets with 7 < p_T <20 GeV and calibrated with LCW and with the JES correction applied. The jets are reconstructed using the anti-k_t algorithm with $R = 0.6$.

- $E_T^{miss,CellOut}$ is calculated with the LCW calibration.

The E_T^{miss} used in the following analyses is always the $RefFinal$ version with EM-based configuration, which means that all topoclusters are taken at the EM-scale, except those associated to electrons which are calibrated with the default electron calibration. Additionally, the JES correction factor is applied to cells associated to jets with p_T >20 GeV. It should be mentioned that, in ATLAS, object selection and calibration are fully configurable and thus they can be chosen according to specific analysis criteria, if needed.

Figure 4.8 shows the E_x^{miss} and E_y^{miss} resolution in $Z \rightarrow e^+e^-$ and $Z \rightarrow \mu^+\mu^-$ events compared with the resolution in minimum bias events from ATLAS data at $\sqrt{s} = 7$ TeV. The same E_T^{miss} is used for the different samples. In Figure 4.8 (a), the total hadronic transverse energy in calorimeters is used, calculated by subtracting the contribution of electrons and photons from the $\sum E_T$, while the total transverse energy in the event, calculated by summing the p_T of muons and the total $\sum E_T$ is presented in Figure 4.8 (b). There is a reasonable agreement in the E_T^{miss} resolution in the different physics channels, as can be seen from the fit parameters reported in the figure 4.8. The E_T^{miss} resolution as a function of the total transverse energy in the event is slightly improved in $Z \rightarrow ll$ events, due to the presence of the leptons which are measured with a better precision. The fit to resolution in MC minimum bias and in $Z \rightarrow ee$ MC events is overlayed showing that the agreement between data and MC simulation is reasonably good in Z events. The resolution in MC minimum bias events is worse than in data due to imperfections of the modelling of soft particles in MC.

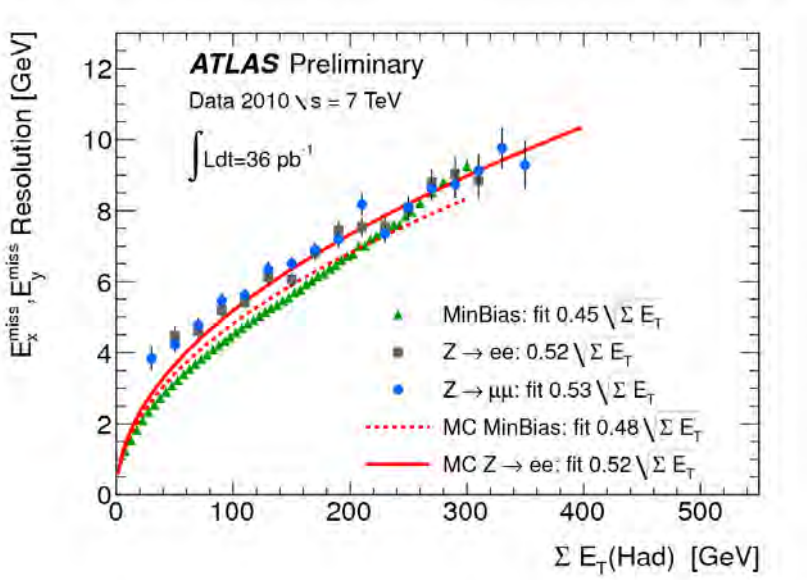

(a)

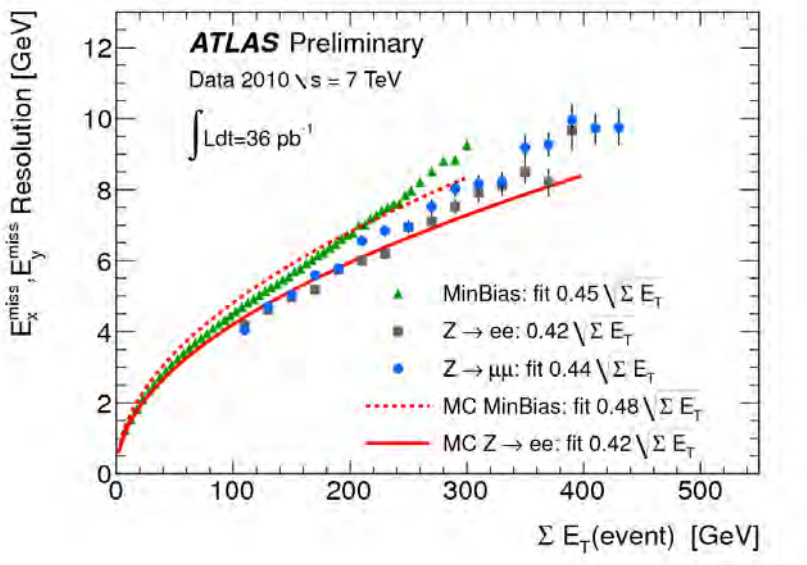

(b)

Figure 4.8: E_x^{miss} and E_y^{miss} resolution as a function of the total hadronic transverse energy in calorimeters calculated by subtracting the contribution of electrons and photons from the total $\sum E_T$ in (a) and of the total transverse energy in the event calculated by summing the p_T of muons and the total $\sum E_T$ in (b). The resolution in $Z \rightarrow ee$ and $Z \rightarrow \mu\mu$ events is compared with the resolution in minimum bias for data taken at $\sqrt{s} = 7$ TeV. The fit to resolution in MC minimum bias and in MC $Z \rightarrow ee$ events is superposed. Taken from [73].

Chapter 5

B-Tagging

The *b*-tagging is the procedure for identifying jets originating from the hadronization and the fragmentation of *b*-quarks, the so-called *b*-jets[1]. This identification is very important for several physics analyses since many interesting physics processes contain *b*-jets in their final states. This is particularly true for physics channels involving *top*-quark and also in the search for the Higgs boson as well as many other research channels for physics beyond the SM[2].

The goal of *b*-tagging is to detect the *b*-jets with a high efficiency and to reject most of the background contamination coming from jets originating from the fragmentation of *light*-quarks, gluons and also *c*-quarks.

In ATLAS, different *b*-tagging algorithms are used to identify b-jets and the majority of the physics analysis that makes use of the *b*-tagging require good *b*-tagging performance. In this chapter, an overview of the *b*-tagging algorithms used in ATLAS is presented in Section 5.1, as well as the measurement of their efficiency with the *System8* method in Section 5.2.2.

5.1 Overview of Tagging Algorithms in ATLAS

The *b*-tagging algorithms take advantage of *b*-hadron properties that have high discriminating power against jets that contain *c* or *light*-quarks. The mass of the *b*-hadrons is higher than that of other hadrons, so for the same momentum their decay products have a larger transverse momentum with respect to the jet axis. Their fragmentation is hard, therefore most of the original *b*-quark energy is transmitted

[1] In Monte Carlo, *b*-jets originating from *b*-quarks are defined as jets (either truth or calorimeter jets) within $\Delta R = \sqrt{\Delta\eta^2 + \Delta\phi^2} < 0.3$ of a generated *b*-quark.

[2] Top quark decays quasi-exclusively to *b*-quark and *W* boson. Low mass Higgs decays predominately to $b\bar{b}$ and many SUSY processes involving third generation *s*-quarks contain *b*-jets in their final states.

to the final b-hadron; the average fraction of energy transmitted from a b-quark to a b-hadron is about 70% [31]. This property of b-quarks can be exploited in b-tagging since the lighter (u,d,s and c) quarks have a softer fragmentation function into light (u,d,s and c) hadrons. Most importantly, the b-hadrons have a relatively long lifetime of the order of 1.5 ps [31] due to their decay through weak interactions. Therefore they have a significant flight length in the detector before decaying. The distance traveled in the detector depends on the b-hadron momentum. A b-quark, for example, with a momentum of ≈ 50 GeV will travel about 3 mm in the detector before decaying, a distance which is visible in the detector[3]. Due to its relatively high mass ($m_B \approx 5.28$ GeV) and its relatively long lifetime, the charged particles produced at the decay vertex will be significantly displaced with respect to the primary vertex, most likely giving a reconstructed secondary vertex (SV). The *lifetime* b-tagging algorithms take advantage of this feature by either reconstructing the displaced SV, called the secondary vertex based b-tagging algorithms (*SV* algorithms), or by measuring the large impact parameter of the tracks from the b-hadron decay products, called the impact parameter based tagging algorithms (*IP* algorithms). The transverse impact parameter d_0 shown in Figure 5.1, is defined as the distance of the closest approach of the track to the primary vertex in the $r-\Phi$ projection. The longitudinal impact parameter, z_0, is the z coordinate of the track at the point of closest approach in $r-\Phi$ projection. The tracks from the b-hadron decay have a relatively larger impact parameters which allow them to be distinguished from the tracks coming directly from the primary vertex.

Another important property of the b-hadrons is their semi-leptonic decay which can be exploited to identify b-jets by tagging the lepton in the jet. A lepton coming from the semi-leptonic decay of the b-hadron ($b \to l$) or from the subsequent decay of the c-hadron ($b \to c \to l$) is produced in $\approx 21\%$ of the cases: the fraction of $b \to l$ decay is $\approx 11\%$ and the fraction of $b \to c \to l$ decay is $\approx 10\%$. Due to the hard fragmentation and the b and c-hadron masses, the lepton will be emitted with a relatively large transverse momentum with respect to the jet axis. The algorithms that make use of this property are called the soft-lepton[4] tagging algorithms. While these algorithms are intrinsically limited by the branching ratios to leptons, they exhibit a very high purity and a low correlation with the *lifetime* based algorithms. In Section 5.1.1, the *lifetime* b-tagging algorithms are described in detail since they are the ones that are being calibrated for the use of the physics analyses.

[3]The ID has a spatial resolution of 10 μm in the R,Φ plane and ≈ 100 μm in the z direction.

[4]Leptons from b semileptonic decay are softer than those originating from W and Z decays. They are also non isolated compared to the latter.

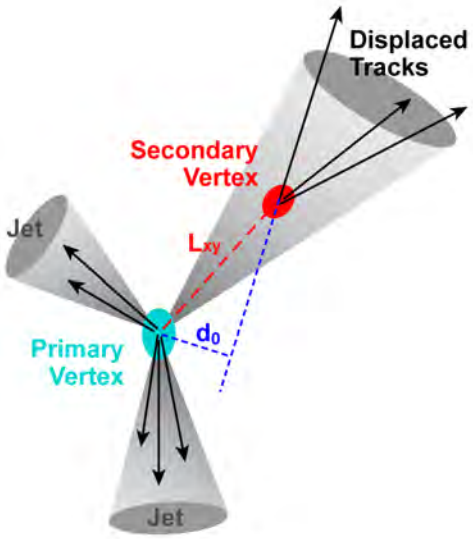

Figure 5.1: Definition of the impact parameter d_0 of a displaced track.

5.1.1 Tagging Algorithms

Two *lifetime* b-tagging algorithms were commissioned and calibrated for the 2010 ATLAS data physics analyses: `JetProb` and `SV0`, so-called *early*-taggers. These two taggers were calibrated using the *System*8 method as well as another muon-based b-tagging calibration method, the so called p_T^{rel} method which will be described briefly later.

A more sophisticated tagging algorithm, MV1, was calibrated for the 2011 data analyses. The MV1 tagger improves greatly the performance with respect to the *early*-taggers. It provides higher *light*-jet rejection for the same b-tagging efficiency as the *early*-taggers. The MV1 tagger consist on combining three powerful and advanced b-tagging algorithms, `IP3D`, `SV1` and `JetFitterCombNN`, using a neural network. All of the listed taggers above are described in this section. This chapter presents the calibration of the *early*-taggers with the *System*8 method for the 2010 data. this represents the work I have performed during the first year of my thesis. For the $t\bar{t}$ differential cross sections analysis which is presented in Chapter 6, I have used the MV1 tagger which was also calibrated using the *System*8 and the p_T^{rel} methods.

5.1.1.1 `JetProb`

The `JetProb` [74] tagging algorithm uses only the transverse impact parameter of charged tracks associated to calorimeter jets with a spatial matching in ΔR(jet,

track)[5]. This algorithm is not powerful compared to other more advanced taggers, but its simplicity allows its use in early data. It was commissioned [74] using ≈ 1 nb^{-1} of early 2009 ATLAS data at $\sqrt{s}$ = 900 GeV, and was calibrated [75] using the *System*8 and p_T^{rel} methods on the whole 35 pb^{-1} collected in 2010 at $\sqrt{s}$ = 7 TeV, as well as on the 2011 data.

The impact parameters of tracks are computed with respect to the primary vertex. They are signed to further discriminate the tracks originating from *b*-hadron decays from tracks originating from the primary vertex. The sign is defined using the jet direction $\vec{P}_j$ as measured by the calorimeters, the direction $\vec{P}_t$ and the position $\vec{X}_t$ of the track at the point of closest approach to the primary vertex and the position $\vec{X}_{pv}$ of the primary vertex:

$$\text{sign}(d_0) = \left(\vec{P}_j \times \vec{P}_t\right) \cdot \left(\vec{P}_t \times (\vec{X}_{pv} - \vec{X}_t)\right) \tag{5.1}$$

The experimental resolution generates a random sign for the tracks originating from the primary vertex, while tracks from *c*- or *b*-hadron decays tend to have a positive d_0 sign. The sign of the longitudinal impact parameter z_0 is given by the sign of $(\eta_j - \eta_t) \times z_{0t}$ where again the t subscript refers to quantities defined at the point of closest approach to the primary vertex.

The distribution of the signed transverse impact parameter significance $S_{d_0} = \frac{d_0}{\sigma_{d_0}}$, where σ_{d_0} is the error on d_0, is illustrated in Figure 5.2, for tracks coming from *b*-jets, *c*-jets and *light*-jets in $t\bar{t}$ simulated events at $\sqrt{s} = 14$ TeV [31].

`JetProb` uses the signed impact parameter significance S_{d_0} of each selected track, shown in Figure 5.2, and compares it to a resolution function of prompt tracks in order to measure the probability that a track i is originating from the primary vertex. The resolution function $\mathscr{R}$ can be determined from collision data using the negative side of the signed impact parameter distribution , assuming there is no contribution from heavy-flavor particles. The probability of a track i to originate from the primary vertex is:

$$\mathscr{P}_{\text{trk}\,i} = \int_{-\infty}^{-|d_0^i/\sigma_{d_0}^i|} \mathscr{R}(x)dx\,. \tag{5.2}$$

There are several ways to combine the individual probabilities of each of the N tracks associated to the jet to obtain a jet probability, $\mathscr{P}_{\text{jet}}$, which discriminates between *b*-jets and *light*-jets. In the calculation of the jet probability $\mathscr{P}_{\text{jet}}$, only

[5]The association cut varies as a function of the jet p_T according to $R = 0.239 + e^{(-1.22-1.64\cdot10^{-5}\cdot p_T^{jet})}$, in order to have a smaller cone for jets at high p_T which are more collimated. For the average jet p_T of 26 GeV, the ΔR cut is 0.43. At 20 GeV, it is 0.45 while for a jet with a p_T around 150 GeV the ΔR cut is 0.26.

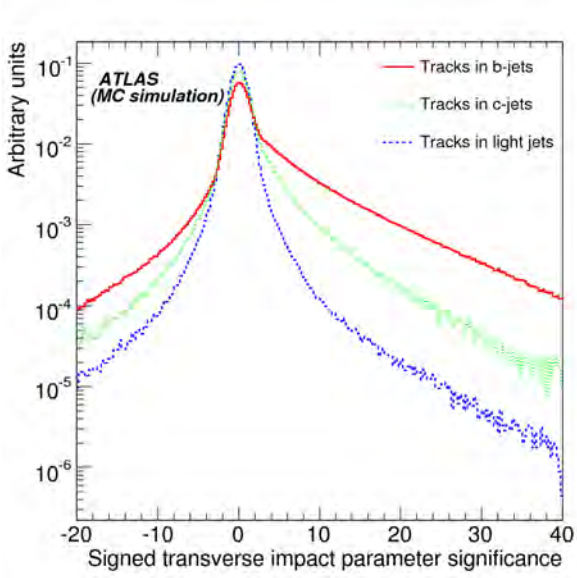

Figure 5.2: Distribution of the impact parameter significance d_0/σ_{d_0}, signed with respect to the jet axis, for *b*-jets, *c*-jets and *light*-jets from simulated $t\bar{t}$ events at $\sqrt{s}$ = 14 TeV data (from Ref. [31]).

tracks with positive impact parameter are used and their individual probabilities $\mathscr{P}_{\text{trk}}$ are combined as follows:

$$\mathscr{P}_{\text{jet}} = \mathscr{P}_0 \sum_{j=0}^{N-1} \frac{(-ln\mathscr{P}_0)^j}{j!}, \tag{5.3}$$

where

$$\mathscr{P}_0 = \prod_{i=1}^{N} \mathscr{P}_{\text{trk}i}\,. \tag{5.4}$$

The jet probability $\mathscr{P}_{\text{jet}}$ is simply the product $\mathscr{P}_0$ of all the individual track probabilities, with a weighting factor depending on the track multiplicity. For light jets, the distribution of $\mathscr{P}_{\text{jet}}$ should be flat, while it should peak around zero for *b*-jets. The distribution of $\mathscr{P}_{\text{jet}}$ is shown in Figure 5.3 in a $-\log_{10}$ scale for 15 nb^{-1} of 2010 ATLAS data and for simulation for *b*-jets, *c*-jets and *light*-jets.

5.1.1.2 SV0

The `SV0` [76] tagging algorithm explicitly reconstructs secondary vertices from tracks associated with a jet. This is also a simple tagging algorithm that was used in early data. It was commissioned [76] using 0.4 nb^{-1} of 2010 data at $\sqrt{s}$ = 7

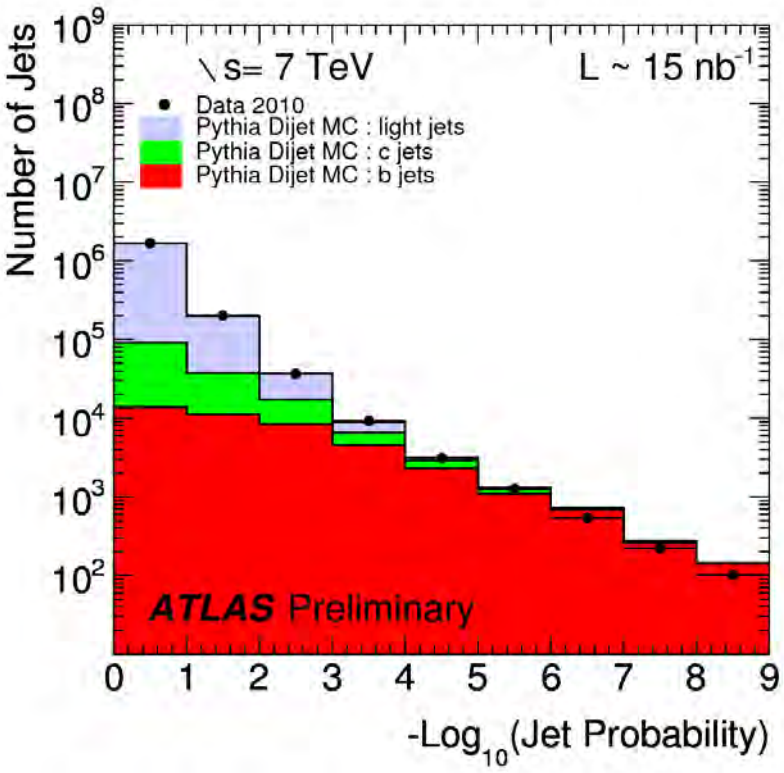

Figure 5.3: Distribution of the probability $\mathscr{P}_{\text{jet}}$ for a jet to be compatible with a light jet, for real data (solid black points) and for simulation (histograms), as a function of $-\log_{10}(\mathscr{P}_{\text{jet}})$. Taken from [74].

TeV, and was calibrated [75] on the whole 35 pb^{-1} collected in 2010 at $\sqrt{s}$ = 7 TeV, as well as on the 2011 data.

It places a cut on the signed decay length significance of the reconstructed secondary vertex. The sign of the decay length significance is given by the sign of the projection of the decay length vector on the jet axis.

As input, the tagging algorithm uses a list of tracks associated to the calorimeter jet. The track-to-jet association is done using a ΔR matching between the tracks and the jet axis. A track is not allowed to be associated to multiple jets, but only to the closest one. The jet matching cone normally has $\Delta R = 0.4$, but R varies with the jet p_T according to $R = 0.239 + e^{(-1.22-1.64\cdot 10^{-5}\cdot p_T^{jet})}$. A jet with $p_T^{jet} = 7$ GeV will thus have an association cone size of 0.50, while for a jet with $p_T^{jet} = 30$ GeV, the association cone size is decreased to 0.42.

The SV0 algorithm starts by reconstructing two-track vertices significantly displaced (in three dimensions) from the primary vertex. Tracks are considered for the two-track vertices if $d_{3D}/\sigma(d_{3D}) > 2.3$, where $d_{3D}/\sigma(d_{3D})$ is the impact parameter significance of the track in three dimensions with respect to the primary vertex. Furthermore, the sum of the impact parameter significance S_{d_0} of the two tracks has to be greater than 6.6. Two-track vertices must have a $\chi^2_{pv} < 4.5$ and be incompatible with the primary vertex by requiring the χ^2 of the distance between the primary and secondary vertex, computed in three dimensions, to be greater than 6.25.

The standard version of the algorithm then removes two-track vertices with a mass consistent with a K^0_s meson, a Λ^0 baryon or a photon conversion. In addition, two-track vertices at a radius consistent with the radius of one of the three Pixel detector layers are removed, as these vertices are likely to originate from material interactions. In the present loose version of the tagging algorithm the vetoes against vertices from long-lived particles and material interactions are not applied.

Tracks from surviving two-track vertices after the above cuts are used by the SV0 algorithm to fit an inclusive secondary vertex. In an iterative process it removes the track with the largest χ^2 contribution to the common vertex until the fit probability of the vertex is greater than 0.001, the vertex mass is less than 6 GeV and the largest χ^2 contribution from any one track is $\leqslant 7$. Finally, the algorithm tries to re-incorporate the tracks failing the selections made during the two-track vertices reconstruction into the vertex fit. Figure 5.4 shows the distribution of the signed decay length significance of the SV0 b-tagging algorithm using 2.9 pb^{-1} of 2010 data. The different flavor jets are shown using simulation, in yellow for b-jets, blue for c-jets and red for *light*-jets.

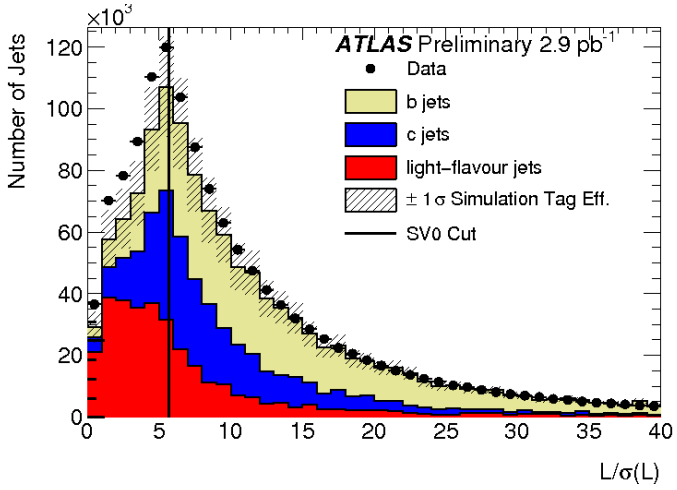

Figure 5.4: The signed decay length significance $L/\sigma(L)$ for the SV0 b-tagging algorithm in data (points) and simulation (stacked histogram) for an inclusive jet sample. The vertical line indicated the cut weight that was calibrated corresponding to 50% b-tagging efficiency. The contributions of the different flavors in simulation have been scaled by the b-tag efficiency and mistag rate scale factors as measured in [76] . Taken from Ref. [76].

5.1.1.3 SV1

The SV1 [77] is also a secondary vertex based algorithm. As the SV0 algorithm, it uses the three-dimensional signed decay length significance $L/\sigma(L)$ as a discriminator. To increase the discriminating power, SV1 takes advantage of three of the vertex properties: the invariant mass of all tracks associated to the vertex, the ratio of the sum of the energies of the tracks in the vertex to the sum of the energies of all tracks in the jet, and the number of two-track vertices. These variables are combined using a likelihood ratio technique. SV1 relies on a 2D-distribution of the two first variables, and a 1D-distribution of the number of two-track vertices. In addition the distance ΔR between the jet axis and the line joining the primary vertex to the secondary one is used. Figure 5.5 shows the distribution of the secondary vertex mass as used by the SV1 tagging algorithm, using 330 $text pb^{-1}$ of the 2011 ATLAS data.

5.1.1.4 IP3D

The IP3D [77] is an impact parameter based algorithm. It is a more advanced version of the JetProb. It combines the impact parameter significances of all the tracks in the jet. And to increase the tagging performance, it uses a likelihood ra-

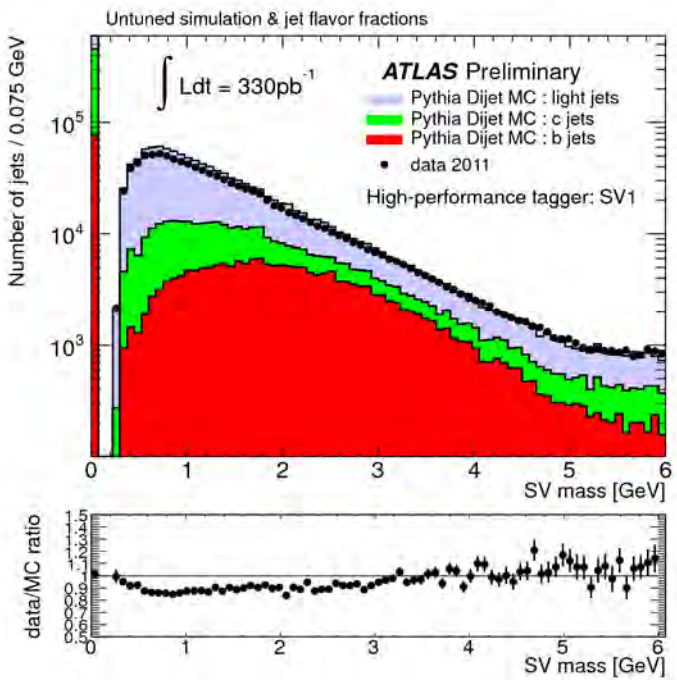

Figure 5.5: Distribution of the invariant mass of all tracks associated to the inclusive secondary vertex found by the `SV1` tagging algorithm for data (solid black points) and for simulated data (filled histograms for the various flavors). The ratio data/simulation is shown at the bottom of the plot. Taken from [77].

tio technique in which the input variables are compared to pre-defined smoothed and normalized distributions for both the *b*- and *light*-jet hypotheses, obtained from Monte Carlo simulation. The distributions in this case are two-dimensional histograms of the signed transverse impact parameter significance d_0/σ_{d_0} and longitudinal impact parameter significance z_0/s_{σ_0} of tracks, taking advantage of the correlations between the two variables.
A more advanced tagger, `IP3D+SV1`, can be easily obtained by summing the weights of the `IP3D` and `SV1` taggers since they both are derived from the likelihood ratio method.

5.1.1.5 `JetFitterCombNN`

The `JetFitterCombNN` [77] is a decay chain reconstruction based algorithm. It exploits the topology of weak *b*- and *c*-hadron decays inside the jet. A Kalman filter is used to find a common line on which the primary vertex and the *b*- and *c*-vertices lie, as well as their position on this line, giving an approximated flight path for the *b*-hadron. The *b*- and *c*-hadron vertices are not necessarily merged in this approach, even when only a single track is attached to each of them. The discrimination between *b*-, *c*- and *light*-jets is based on a likelihood using similar variables as in the `SV1` tagging algorithm above, and additional variables such as the flight length significances of the vertices.
The `JetFitterCombNN` can also be combined with the `IP3D` to give a more powerful tagger, `IP3D+JetFitterCombNN`. The combination done here is more sophisticated. It uses an artificial neural network technique with Monte Carlo simulated training samples and additional variables describing the topology of the decay chain used by `JetFitterCombNN`. A more sophisticated algorithm, `MV1`, can be obtained by combining the three advanced taggers using a neural network: `SV1`, `IP3D` and `JetFitterCombNN`.

Figure 5.6 shows the expected performance of the different *b*-tagging algorithms in ATLAS. It shows the *light*-jet rejection as a function of the *b*-tagging efficiency measured on a simulated $t\bar{t}$ events, for jets with $P_T^{jet} > 15$ GeV and $|\eta^{jet}| < 2.5$. One can easily notice that for the same *b*-tagging efficiency, the advanced taggers have a higher *light*-jet rejection.

5.2 B-Tagging Calibration Using Muon-Jets

The *b*-tagging efficiency is defined as the fraction of reconstructed jets originating from *b*-quarks that are tagged by the *b*-tagging algorithm. In order to measure the *b*-tagging efficiency in data, the number of *b*-jets before and after applying the b-tagging requirement needs to be known. Several methods are being used in

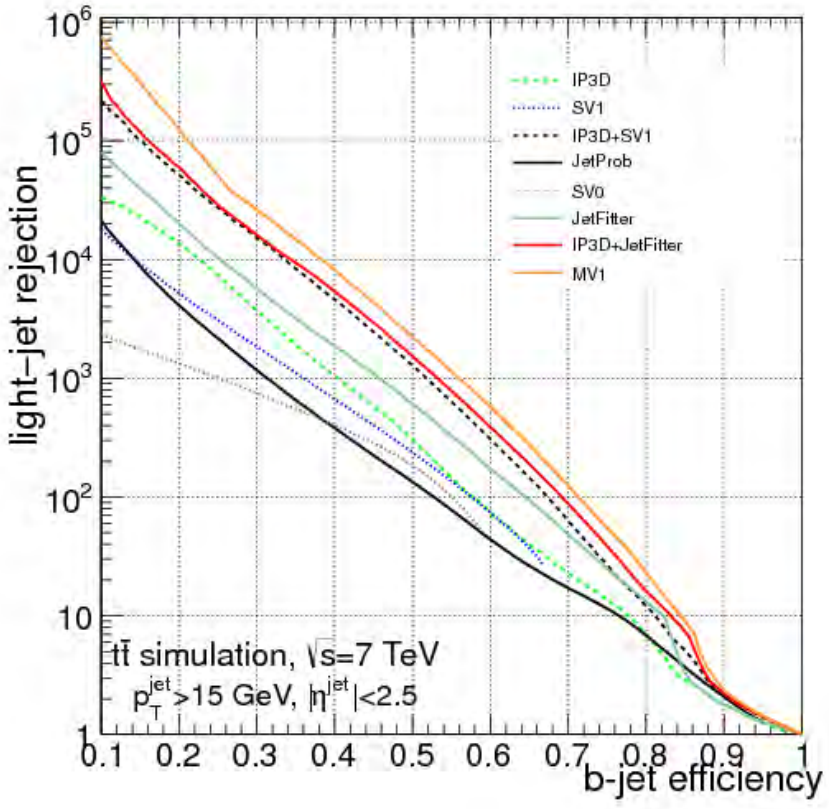

Figure 5.6: Light-jet rejection as a function of the *b*-jet tagging efficiency for the early tagging algorithms (`JetProb` and `SV0`) and for the advanced algorithms, `IP3D`, `SV1`, `IP3D+SV1`, `JetFitterCombNN`, `IP3D+JetFitterCombNN` and `MV1`, based on simulated $t\bar{t}$ events for jets with $P_T^{jet} > 15$ GeV and $|\eta^{jet}| < 2.5$. Taken from [77].

ATLAS to measure the b-tagging efficiency in data. Methods based on $t\bar{t}$ events are not described in this thesis. They need high statistics in order to derive the b-tagging efficiency in multiple bins of jet p_T and they were not used for the 2010 nor the 2011 data analyses. Three methods based on muon-jets events are used in ATLAS: $p_{\mathrm{T}}^{\mathrm{rel}}$, *System*8 and $D^*\mu$. The $D^*\mu$ method measures the b-tag efficiency in a specific final state, namely b-decays with an exclusively reconstructed D^{*+} meson and an identified muon. The decay in which the D^{*+} meson has been reconstructed, $D^{*+} \rightarrow D^0\pi^+$, means that at least four tracks from the b-hadron decay have been reconstructed in the jet, leading to a bias in the measurement of the b-tag efficiency. The $p_{\mathrm{T}}^{\mathrm{rel}}$ method is briefly described in Section 5.2.1 and the *System*8 method in Section 5.2.2.

5.2.1 $p_{\mathrm{T}}^{\mathrm{rel}}$

$p_{\mathrm{T}}^{\mathrm{rel}}$, sketched in Figure 5.7, is a variable computed from the muon momentum $\vec{p}_\mu$ and the jet momentum $\vec{p}_{jet}$.

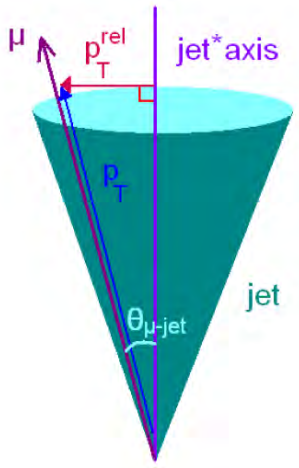

Figure 5.7: The $p_{\mathrm{T}}^{\mathrm{rel}}$ variable.

The b-quark direction is estimated from the vector $\vec{p}_\mu + \vec{p}_{jet}$, and the component of the muon momentum $\vec{p}_\mu$ transverse to the combined muon plus jet axis is defined as :

$$p_{\mathrm{T}}^{\mathrm{rel}} = \frac{|\vec{p}_\mu \times (\vec{p}_\mu + \vec{p}_{jet})|}{|\vec{p}_\mu + \vec{p}_{jet}|} = \frac{|(\vec{p}_\mu \times \vec{p}_{jet})|}{|\vec{p}_\mu + \vec{p}_{jet}|} \tag{5.5}$$

where $\times$ is the vectorial product of $\vec{p}_\mu$ and $\vec{p}_{jet}$. Muons from b-hadron decays have a harder $p_{\mathrm{T}}^{\mathrm{rel}}$ spectrum than the muons in c- and *light*-flavor jets as shown

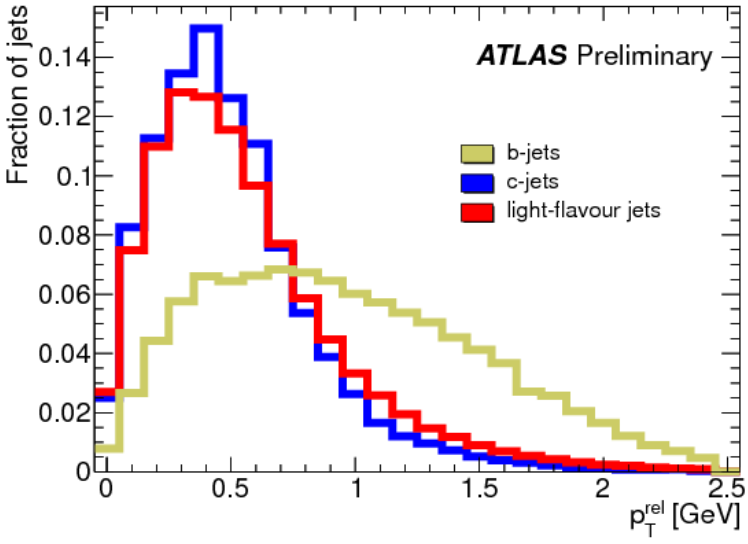

Figure 5.8: Examples of $p_{\mathrm{T}}^{\mathrm{rel}}$ templates for *b*-, *c*- and *light*-flavor jets. One can directly notice the discrimination between *b* and *cl*-jets.

in Figure 5.8. Templates are constructed separately for *b*-, *c*- and *light*-quark jets and are fitted to the corresponding inclusive distribution in data, using a binned maximum likelihood technique. Each bin is treated as an independent Poisson variable, to obtain the fraction of *b*-jets before and after requiring a jet to be *b*-tagged. Statistical fluctuations of the $p_{\mathrm{T}}^{\mathrm{rel}}$ templates are not considered during the fit, but are taken into account as a systematic uncertainty. Once the flavor composition of jets containing muons from the $p_{\mathrm{T}}^{\mathrm{rel}}$ fits is obtained, the *b*-tagging efficiency is defined as:

$$\varepsilon_b^{data} = \frac{f_b^{tag} \dot{N}^{tag}}{f_b \dot{N}} \tag{5.6}$$

where f_b and f_b^{tag} are respectively the fractions of *b*-jets in the pretagged (before applying any *b*-tagging requirement) and the tagged (after applying the *b*-tagging requirement) samples of jets containing muons, and N and N^{tag} are the total number of events in these two samples. The *b*-tagging efficiency measured in data using the muon-jets is also measured in simulated events to derive data to MC scale factors defined as :

$$K_{\varepsilon_b}^{data/MC} = \frac{\varepsilon_b^{data}}{\varepsilon_b^{MC}} \tag{5.7}$$

This scale factor is used to correct the simulation in physics analyses to account for possible discrepancies between data and Monte Carlo while applying the *b*-

tagging requirement. The scale factor $K_{\varepsilon_b}^{data/MC}$ calculated for b-jets from semi-leptonic decays is assumed to be valid for all types of b-jets, including those originating from hadronic decays.

The $p_{\mathrm{T}}^{\mathrm{rel}}$ method is a rather simple method used to measure the b-tagging efficiency in data, but it can only be used up to a certain range of jet transverse momentum. As shown in Figure 5.9, for high jet p_T, the momentum of the muon begins to be collimated with the one of the jet, and the $p_{\mathrm{T}}^{\mathrm{rel}}$ spectrum for b-jets can not be further discriminated from the c- and *light*-jets. The $p_{\mathrm{T}}^{\mathrm{rel}}$ provides the b-tagging efficiency measurement up to a 140 GeV jet p_T range, and this method provided the full calibration for the 2010 LHC data for the physics analysis. The *System*8 method came later as cross check for the $p_{\mathrm{T}}^{\mathrm{rel}}$ results, but for the 2011 data, the $p_{\mathrm{T}}^{\mathrm{rel}}$ and the *System*8 results were combined and used in all physics analysis. In Section 5.2.2, the *System*8 method is described in detailed as well as the results of the b-tagging efficiency and the data-to-MC scale factors for the 2010 LHC data.

5.2.2 *System8*

The *System8* method provides a calibration of the b-tagging efficiency for lifetime tagging algorithms. It was developed within the DØ experiment [78] for the same purpose, and was designed to involve a minimal input from simulation. The *System8* method is based on the use of two (nearly) uncorrelated b-taggers and two muon-jet samples, denoted the n and p-samples. The p-sample is a subset of the n-sample where an away-jet from the probed jet is tagged as a b-jet. The correlations between the two samples and between the two b-taggers are estimated from simulation. The flavor contributions are written for each combination of sample and tagger producing a system of eight equations with eight unknowns. The results of the system-of-equations are the b-tagging efficiencies and charm+light (cl) quark and gluon mistagging for the two taggers applied on the samples. As with the result obtained by the $p_{\mathrm{T}}^{\mathrm{rel}}$ method described in Section 5.2.1, a correction factor needs to be applied to convert this to a result for generic b-jets; alternatively, a data-to-MC scale factor is obtained by comparing the b-jet tagging efficiency in data with the one from simulated b-jets in comparable final states. Two taggers, `SV0` and `JetProb` (described in Section 5.1.1, are calibrated using the *System*8 method on the 2010 data. Several working points[6] for both algorithms are calibrated, however only three benchmark points were chosen to be communicated to the physics analyses groups, one working point for `SV0`, a cut on its weight

[6]The working points are to be understood as cuts on the tagging weights, e.g. for the `SV0` 5.85 working point, only jets with $w > 5.85$ are considered as tagged.

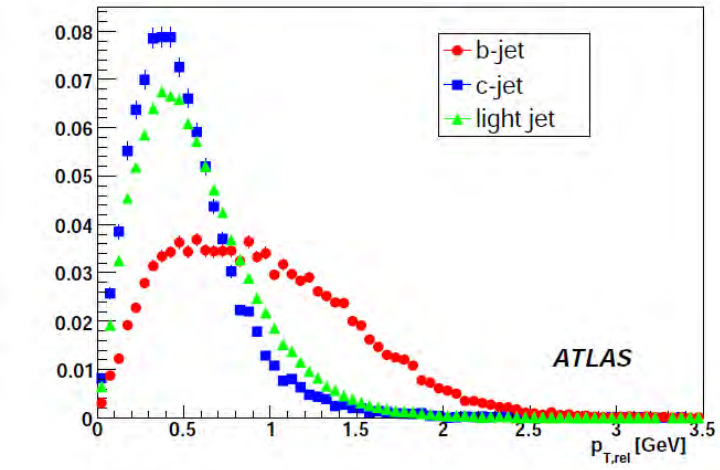

(a)

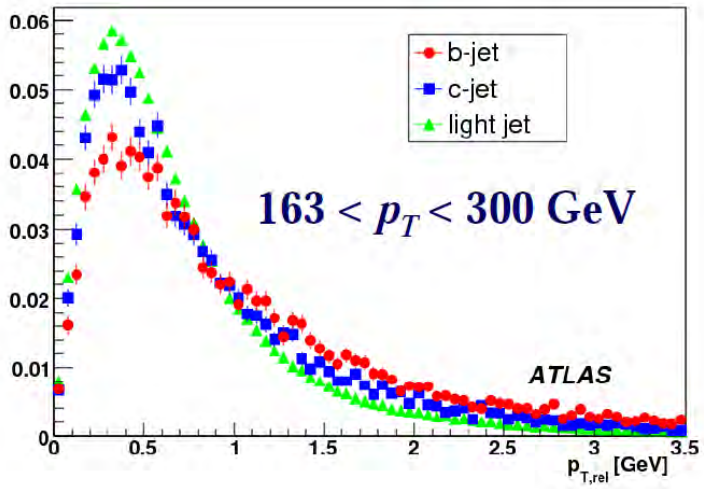

(b)

Figure 5.9: Distribution of $p_{\mathrm{T}}^{\mathrm{rel}}$ templates for *b*-, *c*- and *light*-flavor jets with transverse momentum between 15 GeV and 28 GeV (a), and another distribution where the jet transverse momentum is between 163 GeV and 300 GeV (b). One can directly notice the shape of the distribution is similar for all the three flavor jets for high p_T jets.

at 5.85 corresponding to 50% b-tagging efficiency (as measured on simulated $t\bar{t}$ events), and two working points for `JetProb`, a cut on its weight at 3.25 corresponding to 50% b-tagging efficiency and another one at 2.05 corresponding to a 70% b-tagging efficiency. Table 5.1 shows the different working points for `SV0` and `JetProb` calibrated using the *System*8 method.

Tagging algorithm	working points
`SV0`	10.05, 7,85, 5.85, 3.3
`JetProb`	3.95, 3.25, 2.65, 2.05, 1.4

Table 5.1: Lifetime tagging algorithms and corresponding working points calibrated using *System*8.

5.3 *System*8: The Method

The *System8* method is based on the notion that the application of all combinations of n uncorrelated selection criteria on a given sample leads to 2^n observables which are the numbers of events surviving any given subset of cuts. This sets of observables can be used to determine some of the unknown quantities, like sample compositions and/or cut efficiencies, without having to rely on detailed input from simulation. The practical implementation of *System*8 uses $n = 3$, resulting in 8 constraints. These are exactly sufficient to solve a system of equations with 8 unknowns, namely: the efficiencies ε_b for b and ε_{cl} cl (c and $light$) jets to pass each of the three selection criteria, and the number of b and cl-jets (n_b, p_b, n_{cl} and p_{cl}) originally present in the sample. It is clear that this does not leave sufficient degrees of freedom to make a complete separation into (c, s, d, u, g) jet flavors; instead, these are lumped together and denoted cl. This reflects the fact that the tagging efficiency for c-jets may differ substantially from that for the other jet flavors. A consequence of lumping together all non-b backgrounds is that the method does not allow to obtain calibration results for individual flavors other than b-jets. Note that the $p_{\mathrm{T}}^{\mathrm{rel}}$ variable, shown in Figure 5.8, used for the calibration of the lifetime taggers isn't the best discriminator between c and $light$-jets.

The three selection criteria chosen are:

- The lifetime tagging criterion under study.

- A muon requirement : a simple cut on the $p_{\mathrm{T}}^{\mathrm{rel}}$ variable which is shown in Figure 5.8. The $p_{\mathrm{T}}^{\mathrm{rel}}$ cut used is equal to 700 MeV, where one observes good

discrimination between the b- and cl-jets.

- An *opposite-jet* tagging, requiring the presence of another jet which is b-tagged and satisfies $\pi - |\Delta\phi_{jj}| < 1$

The primary motivation for these criteria is that inherently, little correlation between them is expected. In addition, the muon requirement facilitates efficient triggering and selection of calibration events. However, even if tagger correlations are small in practice, they should be accounted for. As it is impossible to isolate independent corresponding samples in data, these correlations are measured from simulated samples, and therefore, this is the *only* information inferred from simulated data. The resulting system of equations can be written as follows:

$$\begin{array}{lcrcr}
n & = & n_b & + & n_{cl} \\
p & = & p_b & + & p_{cl} \\
n^{LT} & = & \varepsilon_b^{LT} n_b & + & \varepsilon_{cl}^{LT} n_{cl} \\
p^{LT} & = & \alpha_6 \varepsilon_b^{LT} p_b & + & \alpha_4 \varepsilon_{cl}^{LT} p_{cl} \\
n^{p_{\mathrm{T}}^{\mathrm{rel}}} & = & \varepsilon_b^{p_{\mathrm{T}}^{\mathrm{rel}}} n_b & + & \varepsilon_{cl}^{p_{\mathrm{T}}^{\mathrm{rel}}} n_{cl} \\
p^{p_{\mathrm{T}}^{\mathrm{rel}}} & = & \alpha_5 \varepsilon_b^{p_{\mathrm{T}}^{\mathrm{rel}}} p_b & + & \alpha_3 \varepsilon_{cl}^{p_{\mathrm{T}}^{\mathrm{rel}}} p_{cl} \\
n^{LT, p_{\mathrm{T}}^{\mathrm{rel}}} & = & \alpha_1 \varepsilon_b^{LT} \varepsilon_b^{p_{\mathrm{T}}^{\mathrm{rel}}} n_b & + & \alpha_2 \varepsilon_{cl}^{LT} \varepsilon_{cl}^{p_{\mathrm{T}}^{\mathrm{rel}}} n_{cl} \\
p^{LT, p_{\mathrm{T}}^{\mathrm{rel}}} & = & \alpha_7 \alpha_6 \alpha_5 \varepsilon_b^{LT} \varepsilon_b^{p_{\mathrm{T}}^{\mathrm{rel}}} p_b & + & \alpha_8 \alpha_4 \alpha_3 \varepsilon_{cl}^{LT} \varepsilon_{cl}^{p_{\mathrm{T}}^{\mathrm{rel}}} p_{cl}
\end{array} \tag{5.8}$$

In these equations, the superscripts LT and $p_{\mathrm{T}}^{\mathrm{rel}}$ denote the lifetime tagging criterion and muon tagging criterion, respectively. The n in the equations denotes the event count in the full sample of jets containing at least one muon, the p denotes the event count in a subset of the n, which is formed by applying the third selection criterion, the application of an opposite lifetime b-tagged jet, which enriches it with the b-fraction.

The 8 unknowns of the system are the two flavor composition of the two samples, n_b, n_{cl}, p_b, p_{cl}, and the two efficiencies for each of the two tagging algorithms, $\varepsilon_b^{LT}, \varepsilon_{cl}^{LT}, \varepsilon_b^{p_{\mathrm{T}}^{\mathrm{rel}}}, \varepsilon_{cl}^{p_{\mathrm{T}}^{\mathrm{rel}}}$. These 8 quantities can be related by the 8 equations shown in Eq. 5.8 to 8 observable quantities that also involve coefficients, the α_i, extracted from QCD Monte Carlo simulation, that measure the violation of the assumptions that the tagging efficiency of each tagger is the same on both samples and that the two tagging algorithms are uncorrelated. The *correlation factors*

$\alpha_i, i = 1, \ldots, 8$, are defined as:

$$\begin{aligned}
\alpha_1 &= \varepsilon_b^{LT,p_{\mathrm{T}}^{\mathrm{rel}},n} / (\varepsilon_b^{LT,n} \varepsilon_b^{p_{\mathrm{T}}^{\mathrm{rel}},n}) & \alpha_2 &= \varepsilon_{cl}^{LT,p_{\mathrm{T}}^{\mathrm{rel}},n} / (\varepsilon_{cl}^{LT,n} \varepsilon_{cl}^{p_{\mathrm{T}}^{\mathrm{rel}},n}) \\
\alpha_5 &= \varepsilon_b^{p_{\mathrm{T}}^{\mathrm{rel}},p} / \varepsilon_b^{p_{\mathrm{T}}^{\mathrm{rel}},n} & \alpha_3 &= \varepsilon_{cl}^{p_{\mathrm{T}}^{\mathrm{rel}},p} / \varepsilon_{cl}^{p_{\mathrm{T}}^{\mathrm{rel}},n} \\
\alpha_6 &= \varepsilon_b^{LT,p} / \varepsilon_b^{LT,n} & \alpha_4 &= \varepsilon_{cl}^{LT,p} / \varepsilon_{cl}^{LT,n} \\
\alpha_7 &= \varepsilon_b^{LT,p_{\mathrm{T}}^{\mathrm{rel}},p} / (\varepsilon_b^{LT,p} \varepsilon_b^{p_{\mathrm{T}}^{\mathrm{rel}},p}) & \alpha_8 &= \varepsilon_{cl}^{LT,p_{\mathrm{T}}^{\mathrm{rel}},p} / (\varepsilon_{cl}^{LT,p} \varepsilon_{cl}^{p_{\mathrm{T}}^{\mathrm{rel}},p})
\end{aligned} \tag{5.9}$$

A lack of correlation between two criteria thus implies that the related correlation factors are equal to unity. The correlation factors are inferred from a mixture of data and simulated samples, as described in Section 5.5.

5.4 System8 Solution

As is evident from Eq. 5.8, the system of equations is *nonlinear*, and its solution is not entirely trivial; in fact, no general analytic solution is known.

The system of equations is solved using a χ^2 minimization:

$$\chi^2 = \sum_{i=1}^{8} (n_i - \mu_i)^2 / \sigma_i^2, \tag{5.10}$$

where n_i and μ_i represent the observed and expected event counts in event category i, respectively, and only Poisson statistical uncertainties are included in σ_i, *i.e.*, $\sigma_i = \sqrt{n_i}$ (data statistics are large enough that this is not a limitation). Here, the event counts are not precisely those of Eq. 5.8. Instead, the computation uses the statistically independent (disjoint) event counts, the events passing -or not- each combination of selection criteria, constructed from these equations. Defining the m-sample as m-sample = n-sample - p-sample we see that the following sets are disjoint:

1. The untagged events in the m-sample.

2. The events tagged exclusively with the lifetime tagger, in the m-sample.

3. The events tagged exclusively with the muon tagger, in the m-sample.

4. The events tagged by both taggers, in the m-sample.

5. The untagged events in the p-sample.

6. The events tagged exclusively with the lifetime tagger, in the p-sample.

7. The events tagged exclusively with the muon tagger, in the p-sample.

8. The events tagged by both taggers, in the p-sample

This subdivision into eight categories of disjoint events is also shown graphically in Figure 5.10.

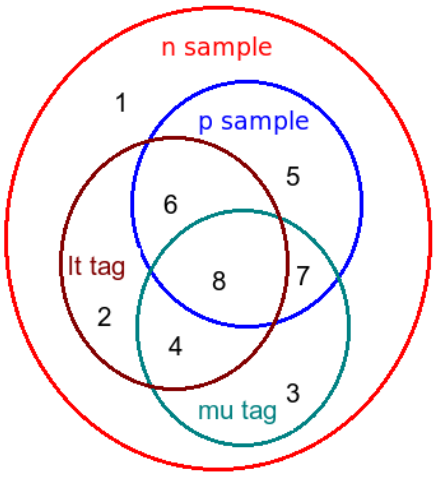

Figure 5.10: Venn diagram showing the relations between different event categories in *System8*. The set drawn in red is the n-sample. All of the other samples are subsamples of the n-sample: the p-sample (shown in blue, defined by a b-tagging cut on an away-side jet), the *Lifetime Tagged* sample (shown in brown, defined by a cut on a lifetime tag weight), and the *Muon Tagged* sample (shown in cyan, defined by a cut on a soft muon $p_{\mathrm{T}}^{\mathrm{rel}}$). None of these samples are disjoint, but it is possible to define disjoint sets, *e.g.*, lifetime-tagged events which are not muon-tagged and not in the p-sample. The numbers shown on the diagram correspond to the enumeration of the 8 disjoint categories described in Section 5.4.

The χ^2 minimization is done using `MINUIT`. Note that since zero degrees of freedom remain, the additional requirement $\chi^2 = 0$ is imposed. Multiple solutions

(χ^2 minima) exist in general. The correct solution is chosen using *a priori* knowledge, namely, that the efficiency for any of the three tagging criteria mentioned in Section 5.3 is higher for b-jets than for cl-jets.

A feature of the χ^2 minimization described above is that it allows for a straightforward computation of an associated uncertainty: χ^2 is marginalised over all "fit" parameters other than the b-jet lifetime tagging efficiency ε_b of interest, and the distance in ε_b over which χ^2 increases by one unit from its minimum is taken as its uncertainty.

The muon-jet sample is divided into four bins according to the jet p_T, where the above procedure is performed in each one them to derive the b-tagging efficiency in those bins: $20\text{GeV} < p_T^{jet} < 30\text{GeV}$, $30\text{GeV} < p_T^{jet} < 60\text{GeV}$, $60\text{GeV} < p_T^{jet} < 90\text{GeV}$ and $90\text{GeV} < p_T^{jet} < 140\text{GeV}$. More quantitatively, Figures 5.11 and 5.12 show graphically the event counts in the eight disjoint subsamples in the four jet p_T bins, for the data as well as for the b-, c-, and light-flavor samples, for the `SV0` tagger and the ones for the `JetProb` tagger are shown in Figures 5.13 and 5.14 for a working point at 3.25 and Figures 5.15 and 5.16 for a working point at 2.05.

Analytic expressions as a function of the statistically independent numbers of b and cl events are then used to determine the correlation factors, and using Gaussian error propagation also their corresponding uncertainties. In addition, the correlation factor covariance matrix V is computed, since the b and cl subsamples are statistically independent, this results in an 8×8 matrix in block-diagonal form, consisting of two 4×4 matrices for the b and cl subsamples, respectively.

The decomposition of Figure 5.10 is valid not only for the full sample, but also for subsamples of b-quark, and c-quark plus light-quark jets, constituted using Monte Carlo and (for the c, l subsample) data-derived templates. It is possible to express Eq. 5.9 in terms of predicted jet counts, coming from Monte Carlo or from the light jet data sample. In the following set of equations these expressions are provided, using the notation:

$$n_{source}^{tag\text{-}type,subsample}$$

with the following definitions:

- [*source*:] b or cl.

- [*tag-type*:] LT (lifetime tagger), $p_{\mathrm{T}}^{\mathrm{rel}}$ (muon tagger), $(LT, p_{\mathrm{T}}^{\mathrm{rel}})$ (both lifetime and muon tagger) or "none".

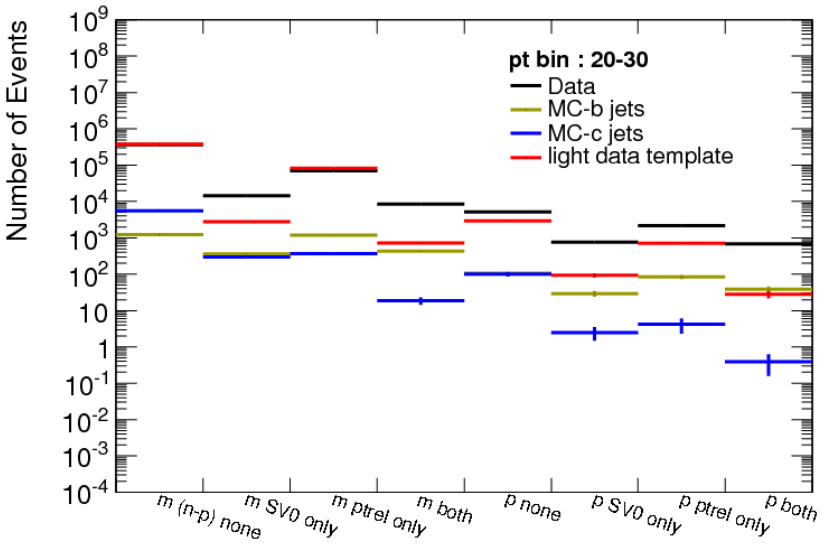

(a)

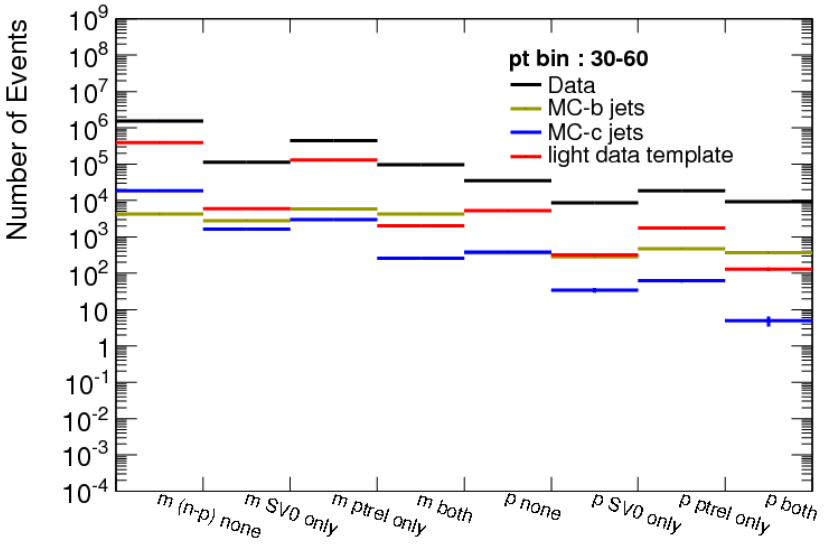

(b)

Figure 5.11: The event counts in the 8 disjoint categories (as described in Section 5.4) in two jet bins: 20 GeV $< p_T <$ 30 GeV (a) and 30 GeV $< p_T <$ 60 GeV (b), for the $w > 5.85$ working point of the SV0 tagger. Statistical uncertainties are indicated but in general are too small to be discerned.

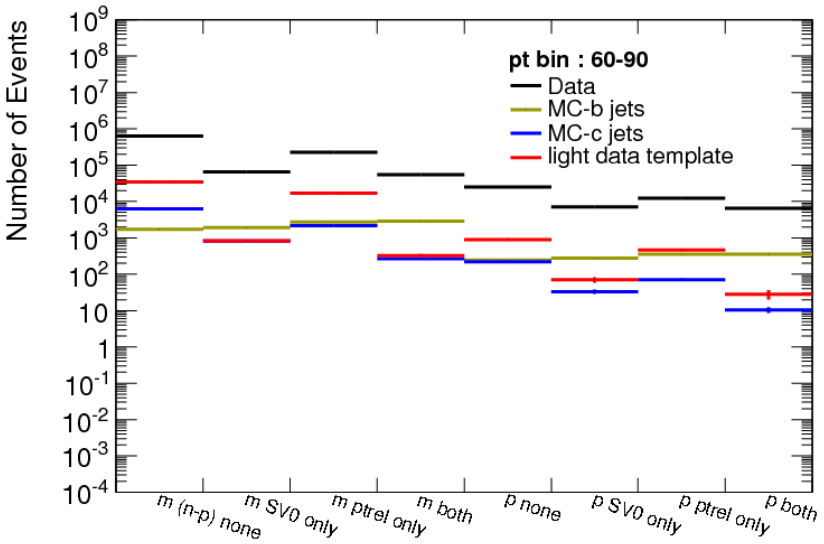

(a)

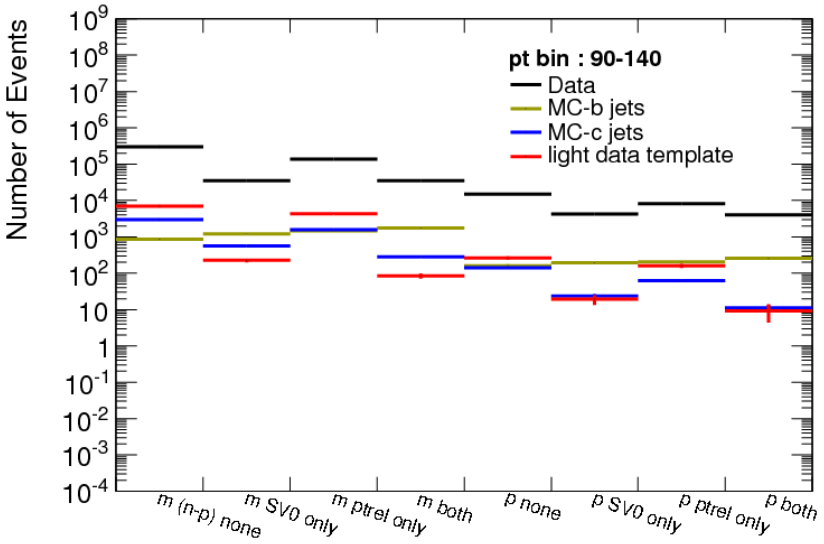

(b)

Figure 5.12: The event counts in the 8 disjoint categories (as described in Section 5.4) in two jet bins: 60 GeV $< p_T <$ 90 GeV (a) and 90 GeV $< p_T <$ 140 GeV (b), for the $w > 5.85$ working point of the SV0 tagger. Statistical uncertainties are indicated but in general are too small to be discerned.

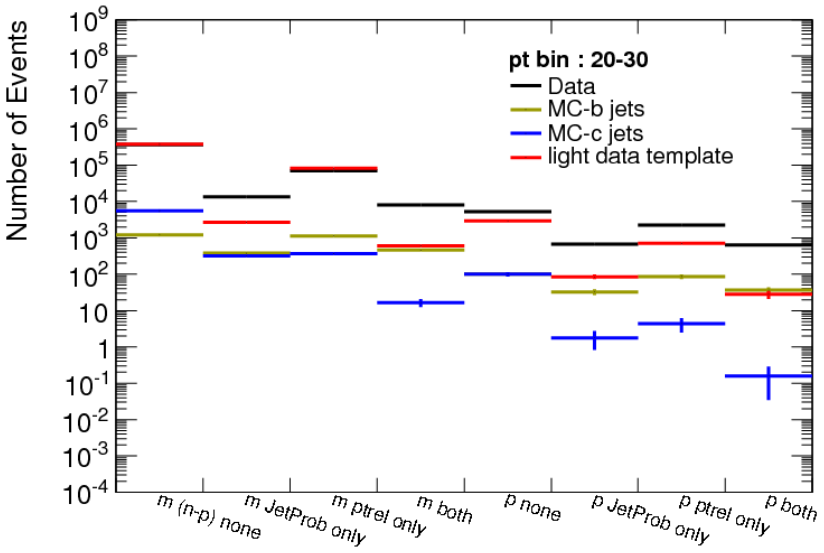

(a)

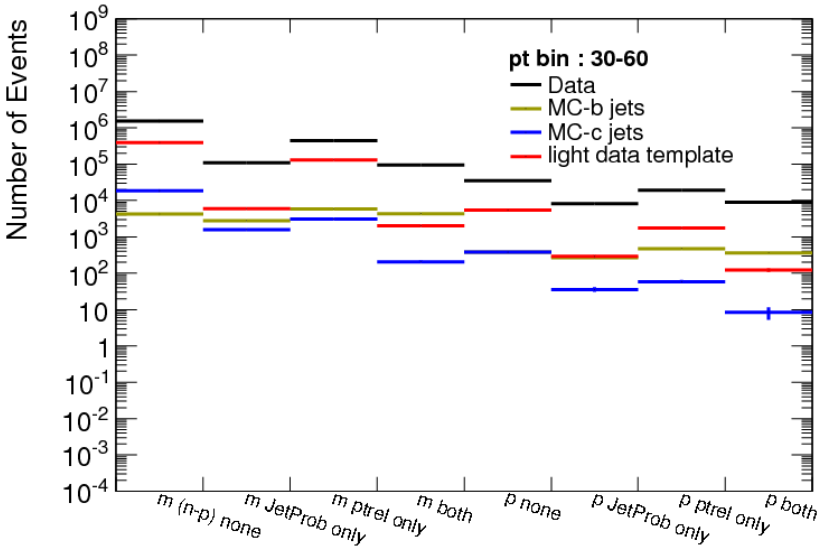

(b)

Figure 5.13: The event counts in the 8 disjoint categories (as described in Section 5.4) in two jet bins: 20 GeV $< p_T <$ 30 GeV (a) and 30 GeV $< p_T <$ 60 GeV (b), for the $w > 3.25$ working point of the `JetProb` tagger. Statistical uncertainties are indicated but in general are too small to be discerned.

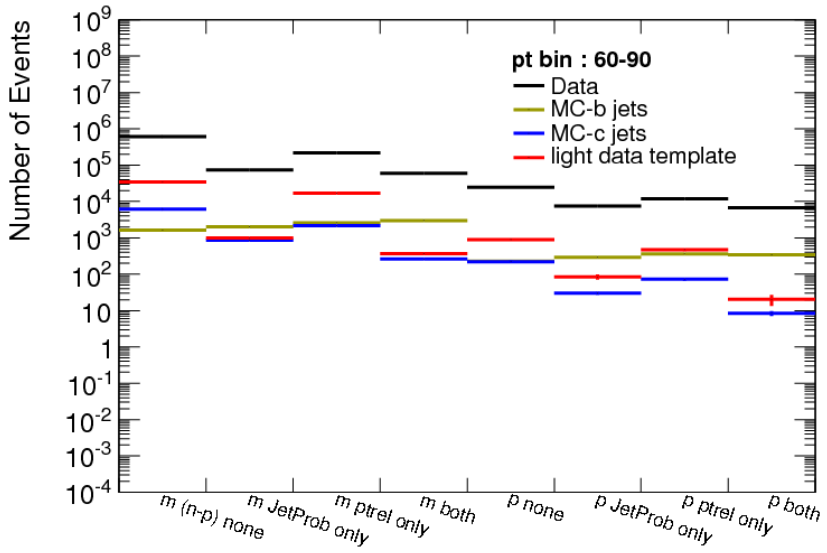

(a)

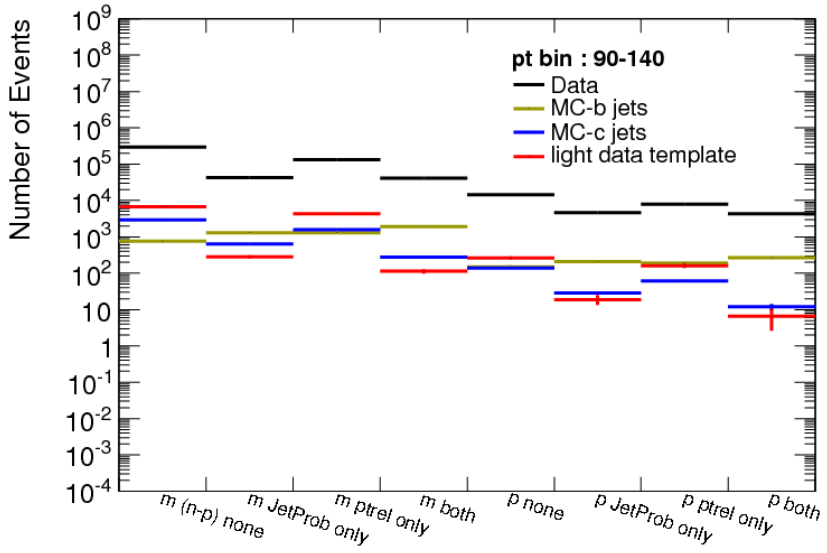

(b)

Figure 5.14: The event counts in the 8 disjoint categories (as described in Section 5.4) in two jet bins: 60 GeV $< p_T <$ 90 GeV (a) and 90 GeV $< p_T <$ 140 GeV (b), for the $w > 3.25$ working point of the `JetProb` tagger. Statistical uncertainties are indicated but in general are too small to be discerned.

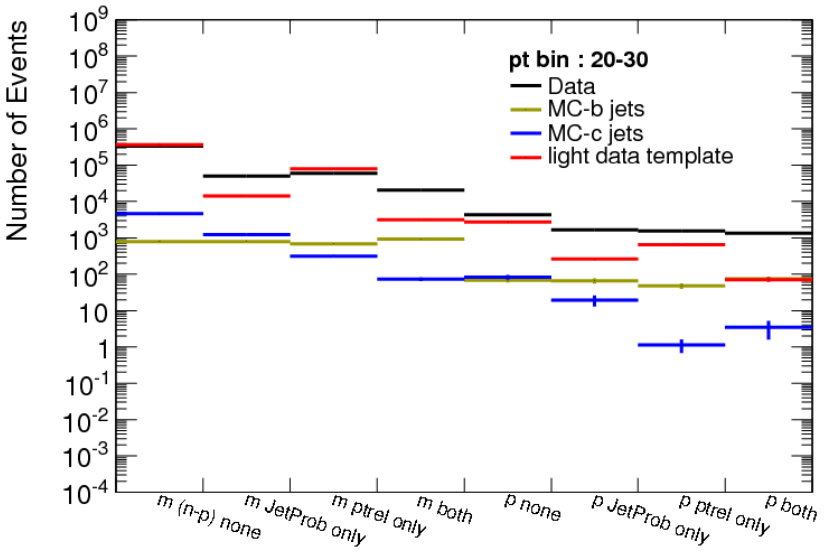

(a)

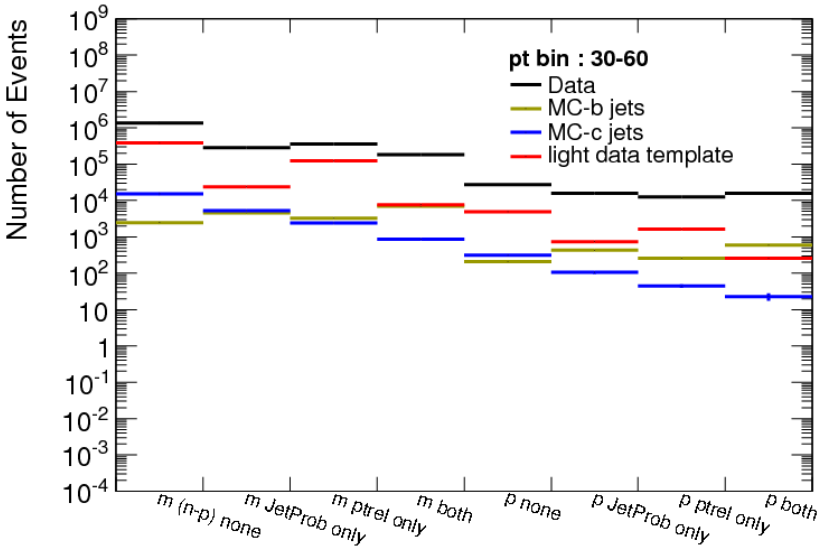

(b)

Figure 5.15: The event counts in the 8 disjoint categories (as described in Section 5.4) in two jet bins: 20 GeV $< p_T <$ 30 GeV (a) and 30 GeV $< p_T <$ 60 GeV (b), for the $w > 2.05$ working point of the `JetProb` tagger. Statistical uncertainties are indicated but in general are too small to be discerned.

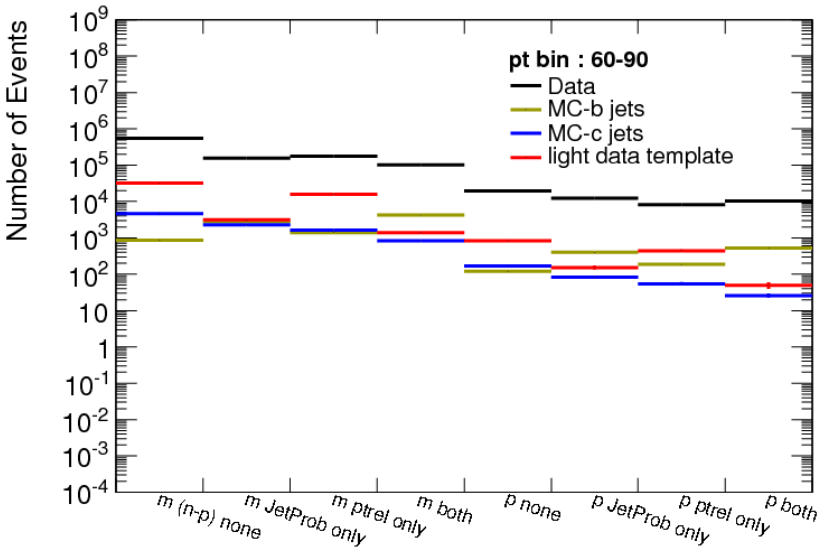

(a)

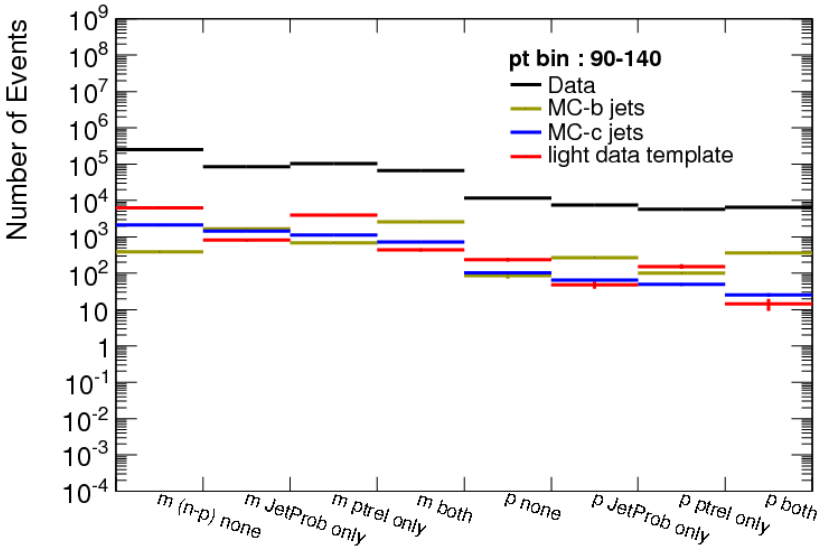

(b)

Figure 5.16: The event counts in the 8 disjoint categories (as described in Section 5.4) in two jet bins: 60 GeV $< p_T <$ 90 GeV (a) and 90 GeV $< p_T <$ 140 GeV (b), for the $w > 2.05$ working point of the `JetProb` tagger. Statistical uncertainties are indicated but in general are too small to be discerned.

- [*subsample*:] p or m (recall that the m-sample is the complement of the p sample in the n-sample).

In terms of raw event counts the expressions are the following:

$$\alpha_1 = \frac{(n_b^{(LT,p_{\mathrm{T}}^{\mathrm{rel}}),p} + n_b^{(LT,p_{\mathrm{T}}^{\mathrm{rel}}),m})}{(n_b^{LT,p} + n_b^{(LT,p_{\mathrm{T}}^{\mathrm{rel}}),p} + n_b^{LT,m} + n_b^{(LT,p_{\mathrm{T}}^{\mathrm{rel}}),m})} \cdot \frac{(n_b^{\mathrm{none},p} + n_b^{LT,p} + n_b^{p_{\mathrm{T}}^{\mathrm{rel}},p} + n_b^{(LT,p_{\mathrm{T}}^{\mathrm{rel}}),p} + n_b^{\mathrm{none},m} + n_b^{LT,m} + n_b^{p_{\mathrm{T}}^{\mathrm{rel}},m} + n_b^{(LT,p_{\mathrm{T}}^{\mathrm{rel}}),m})}{(n_b^{p_{\mathrm{T}}^{\mathrm{rel}},p} + n_b^{(LT,p_{\mathrm{T}}^{\mathrm{rel}}),p} + n_b^{p_{\mathrm{T}}^{\mathrm{rel}},m} + n_b^{(LT,p_{\mathrm{T}}^{\mathrm{rel}}),m})}$$

$$\alpha_2 = \frac{(n_{cl}^{(LT,p_{\mathrm{T}}^{\mathrm{rel}}),p} + n_{cl}^{(LT,p_{\mathrm{T}}^{\mathrm{rel}}),m})}{(n_{cl}^{LT,p} + n_{cl}^{(LT,p_{\mathrm{T}}^{\mathrm{rel}}),p} + n_{cl}^{LT,m} + n_{cl}^{(LT,p_{\mathrm{T}}^{\mathrm{rel}}),m})} \cdot \frac{(n_{cl}^{\mathrm{none},p} + n_{cl}^{LT,p} + n_{cl}^{p_{\mathrm{T}}^{\mathrm{rel}},p} + n_{cl}^{(LT,p_{\mathrm{T}}^{\mathrm{rel}}),p} + n_{cl}^{\mathrm{none},m} + n_{cl}^{LT,m} + n_{cl}^{p_{\mathrm{T}}^{\mathrm{rel}},m} + n_{cl}^{(LT,p_{\mathrm{T}}^{\mathrm{rel}}),m})}{(n_{cl}^{p_{\mathrm{T}}^{\mathrm{rel}},p} + n_{cl}^{(LT,p_{\mathrm{T}}^{\mathrm{rel}}),p} + n_{cl}^{p_{\mathrm{T}}^{\mathrm{rel}},m} + n_{cl}^{(LT,p_{\mathrm{T}}^{\mathrm{rel}}),m})}$$

$$\alpha_3 = \frac{(n_{cl}^{p_{\mathrm{T}}^{\mathrm{rel}},p} + n_{cl}^{(LT,p_{\mathrm{T}}^{\mathrm{rel}}),p})}{(n_{cl}^{\mathrm{none},p} + n_{cl}^{LT,p} + n_{cl}^{p_{\mathrm{T}}^{\mathrm{rel}},p} + n_{cl}^{(LT,p_{\mathrm{T}}^{\mathrm{rel}}),p})} \cdot \frac{(n_{cl}^{\mathrm{none},p} + n_{cl}^{LT,p} + n_{cl}^{p_{\mathrm{T}}^{\mathrm{rel}},p} + n_{cl}^{(LT,p_{\mathrm{T}}^{\mathrm{rel}}),p} + n_{cl}^{\mathrm{none},m} + n_{cl}^{LT,m} + n_{cl}^{p_{\mathrm{T}}^{\mathrm{rel}},m} + n_{cl}^{(LT,p_{\mathrm{T}}^{\mathrm{rel}}),m})}{(n_{cl}^{p_{\mathrm{T}}^{\mathrm{rel}},p} + n_{cl}^{(LT,p_{\mathrm{T}}^{\mathrm{rel}}),p} + n_{cl}^{p_{\mathrm{T}}^{\mathrm{rel}},m} + n_{cl}^{(LT,p_{\mathrm{T}}^{\mathrm{rel}}),m})}$$

$$\alpha_4 = \frac{(n_{cl}^{LT,p} + n_{cl}^{(LT,p_{\mathrm{T}}^{\mathrm{rel}}),p})}{(n_{cl}^{\mathrm{none},p} + n_{cl}^{LT,p} + n_{cl}^{p_{\mathrm{T}}^{\mathrm{rel}},p} + n_{cl}^{(LT,p_{\mathrm{T}}^{\mathrm{rel}}),p})} \cdot \frac{(n_{cl}^{\mathrm{none},p} + n_{cl}^{LT,p} + n_{cl}^{p_{\mathrm{T}}^{\mathrm{rel}},p} + n_{cl}^{(LT,p_{\mathrm{T}}^{\mathrm{rel}}),p} + n_{cl}^{\mathrm{none},m} + n_{cl}^{LT,m} + n_{cl}^{p_{\mathrm{T}}^{\mathrm{rel}},m} + n_{cl}^{(LT,p_{\mathrm{T}}^{\mathrm{rel}}),m})}{(n_{cl}^{LT,p} + n_{cl}^{(LT,p_{\mathrm{T}}^{\mathrm{rel}}),p} + n_{cl}^{LT,m} + n_{cl}^{(LT,p_{\mathrm{T}}^{\mathrm{rel}}),m})}$$

$$
\begin{aligned}
\alpha_5 &= \frac{(n_b^{p_{\mathrm{T}}^{\mathrm{rel}},p} + n_b^{(LT,p_{\mathrm{T}}^{\mathrm{rel}}),p})}{(n_b^{\mathrm{none},p} + n_b^{LT,p} + n_b^{p_{\mathrm{T}}^{\mathrm{rel}},p} + n_b^{(LT,p_{\mathrm{T}}^{\mathrm{rel}}),p})} \\
&\cdot \frac{(n_b^{\mathrm{none},p} + n_b^{LT,p} + n_b^{p_{\mathrm{T}}^{\mathrm{rel}},p} + n_b^{(LT,p_{\mathrm{T}}^{\mathrm{rel}}),p} + n_b^{\mathrm{none},m} + n_b^{LT,m} + n_b^{p_{\mathrm{T}}^{\mathrm{rel}},m} + n_b^{(LT,p_{\mathrm{T}}^{\mathrm{rel}}),m})}{(n_b^{p_{\mathrm{T}}^{\mathrm{rel}},p} + n_b^{(LT,p_{\mathrm{T}}^{\mathrm{rel}}),p} + n_b^{p_{\mathrm{T}}^{\mathrm{rel}},m} + n_b^{(LT,p_{\mathrm{T}}^{\mathrm{rel}}),m})} \\
\alpha_6 &= \frac{(n_b^{LT,p} + n_b^{(LT,p_{\mathrm{T}}^{\mathrm{rel}}),p})}{(n_b^{\mathrm{none},p} + n_b^{LT,p} + n_b^{p_{\mathrm{T}}^{\mathrm{rel}},p} + n_b^{(LT,p_{\mathrm{T}}^{\mathrm{rel}}),p})} \\
&\cdot \frac{(n_b^{\mathrm{none},p} + n_b^{LT,p} + n_b^{p_{\mathrm{T}}^{\mathrm{rel}},p} + n_b^{(LT,p_{\mathrm{T}}^{\mathrm{rel}}),p} + n_b^{\mathrm{none},m} + n_b^{LT,m} + n_b^{p_{\mathrm{T}}^{\mathrm{rel}},m} + n_b^{(LT,p_{\mathrm{T}}^{\mathrm{rel}}),m})}{(n_b^{LT,p} + n_b^{(LT,p_{\mathrm{T}}^{\mathrm{rel}}),p} + n_b^{LT,m} + n_b^{(LT,p_{\mathrm{T}}^{\mathrm{rel}}),m})}
\end{aligned}
$$

$$
\begin{aligned}
\alpha_7 &= \frac{n_b^{(LT,p_{\mathrm{T}}^{\mathrm{rel}}),p} \cdot (n_b^{\mathrm{none},p} + n_b^{LT,p} + n_b^{p_{\mathrm{T}}^{\mathrm{rel}},p} + n_b^{(LT,p_{\mathrm{T}}^{\mathrm{rel}}),p})}{(n_b^{LT,p} + n_b^{(LT,p_{\mathrm{T}}^{\mathrm{rel}}),p}) \cdot (n_b^{p_{\mathrm{T}}^{\mathrm{rel}},p} + n_b^{(LT,p_{\mathrm{T}}^{\mathrm{rel}}),p})} \\
\alpha_8 &= \frac{n_{cl}^{(LT,p_{\mathrm{T}}^{\mathrm{rel}}),p} \cdot (n_{cl}^{\mathrm{none},p} + n_{cl}^{LT,p} + n_{cl}^{p_{\mathrm{T}}^{\mathrm{rel}},p} + n_{cl}^{(LT,p_{\mathrm{T}}^{\mathrm{rel}}),p})}{(n_{cl}^{LT,p} + n_{cl}^{(LT,p_{\mathrm{T}}^{\mathrm{rel}}),p}) \cdot (n_{cl}^{p_{\mathrm{T}}^{\mathrm{rel}},p} + n_{cl}^{(LT,p_{\mathrm{T}}^{\mathrm{rel}}),p})}
\end{aligned}
\tag{5.11}
$$

System8 requires not only the values of the correlation coefficients but also their uncertainties.

The above is accounted for in the following way: each of the eight disjoint event categories (for either *b* or *cl* sources) can be thought of as a bin of an eight-bin histogram. This eight-bin histogram has an associated uncertainty. When combining either the different simulated samples (or, in the case of the *cl* source, the separate contributions of *c* and *light*), the histograms are combined by addition and the uncertainties are propagated to the final jet count prediction for each category. Then, using Eq. 5.11 the full covariance matrix for the eight correlation factors is computed using a straight forward propagation of uncertainties, which is described more fully in Ref. [79]

The required statistics to determine all correlation factors, especially those for the *cl* sample, where all tagging efficiencies are lower than for the *b* sample, with adequate precision is large, and the associated statistical uncertainties cannot be ignored. It is easy to account for these uncertainties (and their correlations) however, by allowing the correlation factors $\vec{\alpha}$ as used in *System8* to float and by adding a Gaussian constraint to the fit:

$$
\chi^2 \to \chi^{2\prime} = \chi^2 + (\vec{\alpha} - \vec{\alpha}_0)^{\mathrm{T}} V^{-1} (\vec{\alpha} - \vec{\alpha}_0), \tag{5.12}
$$

where $\vec{\alpha}_0$ represents the correlation factor estimates as obtained from the simulated samples. The fit uses the full covariance matrix for the eight correlation

factors. In order to find that covariance matrix one needs to know not only the predicted population of the sixteen categories in Eq. 5.11, but also the corresponding statistical uncertainty. Where the predictions derived simply from counting Monte Carlo events, the statistical uncertainty would be simply the square root of the number of events in each category. The system is still exactly constrained, with no remaining degrees of freedom, this does not change the central value of the solution but only affects the uncertainty. Technically, this adds 8 parameters and 8 constraints to the fit.

5.5 Data Samples and Object Selection

5.5.1 Data sample

The data sample for this calibration was collected between March and November 2010 using the jet-muon triggers. The data sample corresponds to an integrated luminosity of 35 pb^{-1}. The jet-muon triggers used were designed for b-tagging efficiency studies. These triggers, named `L2_mu4_L1JX_matched` with $X = 5, 10, 15, 30, 55$, require a jet of $p_T > X$ GeV and a muon at L1, and at L2 require the muon to satisfy $p_T > 4$ GeV and to be matched with the L1 jet within a cone radius $\Delta R = \sqrt{(\Delta\eta)^2 + (\Delta\phi)^2} < 0.4$.

Data events were required to pass the official top group's good-run list criteria among which the inner detectors, the calorimeters and the muon system are required to be fully operational.

5.5.2 Monte Carlo Simulation

The simulated QCD samples from pp collisions at $\sqrt{s} = 7$ TeV used in this b-tagging calibration study are generated with Pythia [80] using the MRST LO parton distribution functions [81]. They are referred to as "Dijet" samples. To simulate the detector response, the generated events are processed through `GEANT4` [50] simulation of the ATLAS detector, and then reconstructed as the data. The simulated geometry corresponds to a perfectly aligned detector and the majority of the disabled pixel modules and front-end chips seen in the data were masked in the simulation. The simulated samples are referred to as the JX_μ QCD samples, and they are generated in bins of non-overlapping parton transverse momenta $\hat{p_T}$ describing the "$2 \to 2$" scattering process. They are also required to have a muon with $p_T > 3$ GeV at generator level. These JX_μ samples thus contain muons from b- and c-decays, but do not fully simulate muons from in-flight decays, since pions and kaons are treated as stable particles at the generator level. Therefore, these samples are only used to measure the correlation coefficients related to b- and c-

Sample	number of events	σ (nb)	$\hat{p_T}$ range (GeV)
J0 muon-filtered QCD	4856857	$9.86 \cdot 10^6$	$8 < \hat{p_T} < 17$
J1 muon-filtered QCD	1999658	$6.78 \cdot 10^5$	$17 < \hat{p_T} < 35$
J2 muon-filtered QCD	1415615	$4.10 \cdot 10^4$	$35 < \hat{p_T} < 70$
J3 muon-filtered QCD	998507	$2.19 \cdot 10^3$	$70 < \hat{p_T} < 140$
J4 muon-filtered QCD	996145	$8.70 \cdot 10^1$	$140 < \hat{p_T} < 280$

Table 5.2: Simulated JX_μ QCD Monte Carlo samples.

jets while the correlation coefficients related to *light* flavor jets are measured from data as described in Section 5.5.3. The simulated JX_μ samples are constructed such that each of the $J0_\mu - J4_\mu$ samples cover a different jet p_T range. They are added together with event weights according to their cross-sections to form an inclusive set. Table 5.2 shows the different JX_μ with their generated number of events, cross-sections and their $\hat{p_T}$ range.

The J0 sample is dropped, since its $\hat{p_T}$ range is not of interest for this analysis[7]. Only J1, J2, J3 and J4 samples are added together to form the simulated sample used in this analysis. After the selection, these samples are further subdivided into b and cl samples based on event generator level information: if a b-quark (or anti b-quark) is found within $\Delta R < 0.3$ from the reconstructed muon jet direction, the jet is labeled as a b-jet. Similarly, if a c-quark or anti c-quark is found within $\Delta R < 0.3$, it is labeled as a c-jet; otherwise it is labeled as an l-jet. However, this last category is not useful for application of *System8*, as discussed in Section 5.5.3, so it is ignored.

5.5.3 Light-Flavor Sample

The above requirement of a muon at the generator level implies, as mentioned in the previous section, that contributions from light hadron decays (mostly $\pi \to \mu\nu$ and $K \to \mu\nu$) or other sources of particles identified as muons (notably, punch-through) are not correctly included in the simulated samples. Simulated samples without this muon requirement exist, but their statistics are too low to be used in the *System8* method. Therefore, a second data sample collected using the `L1_J5` trigger is used to provide an alternative representation of light-flavor events. Since these events do not usually contain a muon and the explicit requirement of a muon would enhance the heavy flavor component, a charged particle track in a jet is chosen randomly and treated subsequently as if it was a muon. In particular, this event is precessed as if it was a muon-jet event. The treatment of a track as a muon goes

[7]The minimum required jet p_T in data is 20 GeV.

through the following procedure:

- The probability for the track to lead to a muon observed in the muon spectrometer (which is roughly inversely proportional to the trackp_T in the barrel region but depends on other geometric details) is inferred from Pythia jet production samples, as above, but without the generator level muon requirement [82]; this procedure accounts for the in-flight decay as well as the punch-through contribution (the MC truth level information to distinguish between these contributions is not available however, the punch-through component is expected to be small). This probability is used to weight the event.

- The probability for a muon from in-flight decay to be associated with a jet depends on the jet's track multiplicity. This is accounted for using an algorithm, that retains a muon–jet association with a probability equal to the sum of its tracks' individual probabilities.

- By construction, the trigger used to collect these events does not include a muon term; and the fact that for the lower muon p_T values ($p_T \approx 4$ GeV) the above mentioned `mu4` trigger term used in the analysis sample is not fully efficient needs to be accounted for. This effect is incorporated as an additional event weight.

- The in-flight decay process leads to a neutrino, which escapes undetected and is not accounted for by the jet p_T measurement; and also the muon deposits only part of its energy in the calorimeter. These effects are corrected for in the case of the offline jet p_T measurement by means of the "semileptonic" energy correction [83] mentioned later in Section 5.5.4, but the lower p_T (and consequently, the slower efficiency turn-on) as measured at trigger level is not accounted for. This is thought to affect the jet p_T spectrum only marginally. In addition, if the decay occurs close to the interaction point, the momentum measurement is that of the muon; but if the decay occurs towards the outer radius of the ID or in the calorimeter, the momentum measured is that of the decaying hadron. While both situations occur in reality, the track weighting procedure effectively only accounts for the latter situation; this causes a slight difference between the semileptonic energy corrections as made in the two situations.

The sample thus obtained needs to be combined with the charm sample. The relative normalization is again inferred from simulated QCD samples without a generator level muon requirement, leading to a charm fraction in the combined sample of approximately 30%, with a mild dependence on jet p_T.

5.5.4 Object and Event Selection

A set of cuts is applied to data and simulated events in order to form the *System*8 main sample, the *n*-sample:

- The data events should pass the GRL criteria where all of the ATLAS sub-detectors are fully operational.

- The data and simulated events should have a reconstructed primary vertex with at least ten associated tracks.

- The data and simulated events should pass the muon-jet trigger requirement. Data events are required to pass at least one of the `L2_mu4_L1JX_matched` with $X = 5, 10, 15, 30, 55$. The simulated events are required to pass the `L2_mu4_L1J5_matched` trigger, and the data events used for measuring the *light*-related alphas are required to pass the `L1_J5` trigger.

- The data and simulated events should have at least one reconstructed jet associated with a reconstructed muon within a cone radius $\Delta R < 0.4$.

To form the *p*-sample, the muon-jet selected in the *n*-sample is required to have an opposite *b*-tagged jet with the `IP3D+SV1` tagger, described in Section 5.1.1, weight larger than 4 corresponding to $\approx 60\%$ *b*-tagging efficiency as measured on simulated $t\bar{t}$ events.

The jets selected in this analysis are reconstructed using the AntiKt4H1TopoJets algorithm described in Chapter 4 Section 4.4.2. A jet is defined as bad and then rejected if it fulfills any of the following requirements:

- $|t_{\text{jet}}| > 25$ ns where t_{jet} is the jet "time";

- the energy fraction deposited in the electromagnetic calorimeter, f_{EM}, and the fraction Q of cells with a pulse shape differing significantly from the predicted one satisfy $f_{\mathrm{EM}} < 0.95$ and $Q > 0.8$;

- the energy fraction deposited in the HEC, f_{HEC}, and the number of (energy ordered) cells accounting for 90% of the jet energy, n_{90}, satisfy $f_{\mathrm{HEC}} > 0.8$ and $n_{90} < 6$;

- $f_{\mathrm{HEC}} > 0.5$ and $Q_{\mathrm{HEC}} > 0.5$;

- $f_{\mathrm{EM}} < 0.05$;

- the maximum energy fraction in one calorimeter layer, f_{max}, satisfies $f_{\mathrm{max}} > 0.99$, and $|\eta_{\mathrm{jet}}| < 2$;

- or the ratio of the p_T sum of the jet's associated charged-particle tracks and its calibrated p_T, f_{CH}, satisfies $f_{\mathrm{CH}} < 0.02$, along with $f_{\mathrm{EM}} > 0.98$ and for $|\eta_{\mathrm{jet}}| < 2$.

The remaining jets are required to have:

- $20 < p_T^{jet}(EM+JES) < 140$ GeV.

- $|\eta| < 2.5$.

- at least one associated track in a cone ΔR(jet,track)< 0.2.

The jet energy scale used is the standard one calibrated at the EM scale, described in Chapter 4 Section 4.4.4. It is corrected for the muon and neutrino produced in the semileptonic decays [83] of b- or c-quarks: direct decays, $b \to \mu X$, and cascade decays, $b \to c \to \mu X$ (see Figure 5.17).

The decay of a b-quark almost always produces a c-quark, which then usually decays to a d-quark with a virtual W decaying into a muon and a neutrino $\approx 10\%$

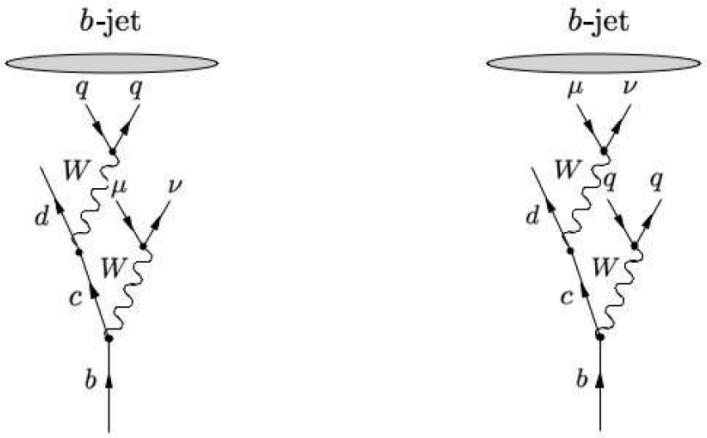

Figure 5.17: Diagrams describing the semileptonic decay of b-jet from a b and a c–quark. On the left the process $b \to \mu X$ and on the right $b \to c \to \mu X$.

of the time. As a result, a b-jet is accompanied by a neutrino and a muon or by two neutrinos and two muons. The neutrino carries away a fraction of the original parton energy, introducing a systematic underestimation of the $p_T$of the corresponding jet. The magnitude of this effect is $\approx 10\%$ [83]. The jet energy scale can be corrected through a parameterization of the energy carried by the neutrino.

The muons associated to the jets are reconstructed using the Combined STACO algorithm described in Chapter 4 Section 4.3.1. They are required to have:

- $p_T > 4$ GeV.
- $|\eta| < 2.5$.
- the transverse impact parameter $|d_0|$ measured with respect to the primary vertex smaller than 2 mm.
- the longitudinal impact parameter measured with respect to the primary vertex multiplied by $\sin\theta$: $|\Delta z \sin\theta|$, smaller than 2 mm.

- The χ^2 of the track fit divided by the number of degrees of freedom in the ID, smaller than three : $\chi^2/N_{\mathrm{DF}} < 3$.

- at least 7 hits in the silicon tracking detectors (including both pixel and SCT detectors).

- at least 2 pixel hits.

- at least 4 hits in the SCT.

- no explicit cut on the number of TRT hits on the tracks is applied. However, most tracks within its acceptance $|\eta| < 2$ do have a successful extension into the TRT and the corresponding improved momentum resolution.

If more than one muon satisfies these criteria, only the highest p_T muon is considered in the following.

5.5.5 Reweighting

The p_T spectrum of jets with muon satisfying the above criteria is shown in Figure 5.18 (a). As on can see, this spectrum differs in Monte Carlo and in data. In these plots, the relative normalization of the *b* and *cl* contributions is fixed to the result from the *System8* fit, specifically using the `JetProb` $w > 2.05$ working point. The pseudorapidity distribution of the *light*-flavor templates also does not have the expected shape (see Figure 5.19). As shown in Figure 5.22, the distribution of the number of primary vertices differs between data and the Monte Carlo. This distribution depends on instantaneous luminosity conditions, and no attempt is made to simulate the evolution of these conditions during data taking. The distribution is also different for the data-driven sample used to derive light-quark templates (an ingredient to the computation of the correlation factors). The reason for this difference is that the sample is collected with a jet trigger, `L1J5`, which is prescaled differently from the `L1JX_mu4_matched` triggers used to collect muon-jet events in data, and thus also has a different instantaneous luminosity profile.

All of these differences are corrected by reweighting the events used to obtain the contribution of each source (charm, light, bottom) to each of the eight different tagging categories. In the case of the primary vertex multiplicity distributions, the

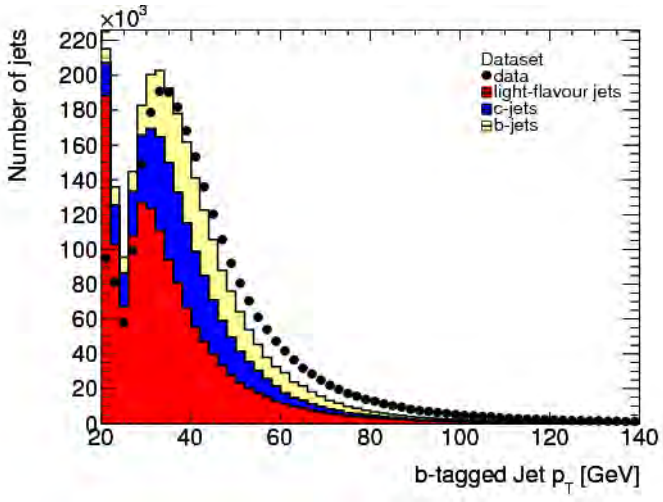

(a)

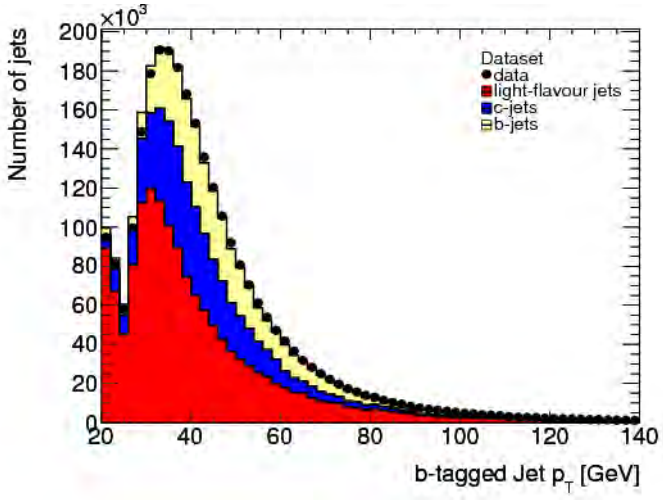

(b)

Figure 5.18: These plots show the jet p_T distribution in Data and Monte Carlo. The distribution before reweighting is shown in (a), and after the reweighting (b), the b and c-jet filtered Monte Carlo are rescaled such that the full distribution (b and c from Monte Carlo, supplemented by the *light*-flavor contribution obtained from the sample described in Section 5.5.3) matches the data.

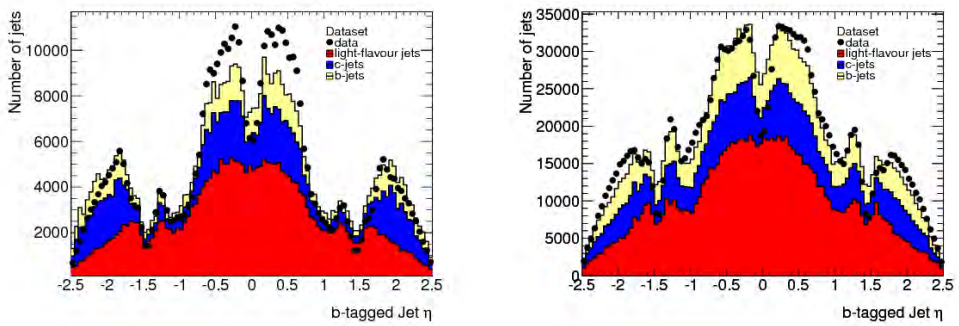

(a) (b)

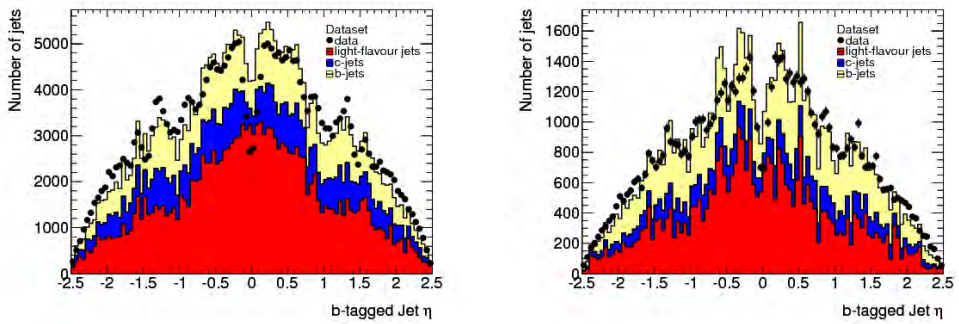

(c) (d)

Figure 5.19: In these plots one observes contributions to the η distribution from various sources (data and Monte Carlo) in the four jet p_T bins: 60 GeV $< p_T <$ 90 GeV (a), 90 GeV $< p_T <$ 140 GeV (b), 60 GeV $< p_T <$ 90 GeV (c) and 90 GeV $< p_T <$ 140 GeV (d). The distribution in data possesses a structure which reveals cracks in the muon system. It can also be seen using tag-and-probe in J/ψ events, as shown in Figure 5.21. Muon chamber acceptance is modeled in the light quark templates (red plot) but with a certain level of smoothing.

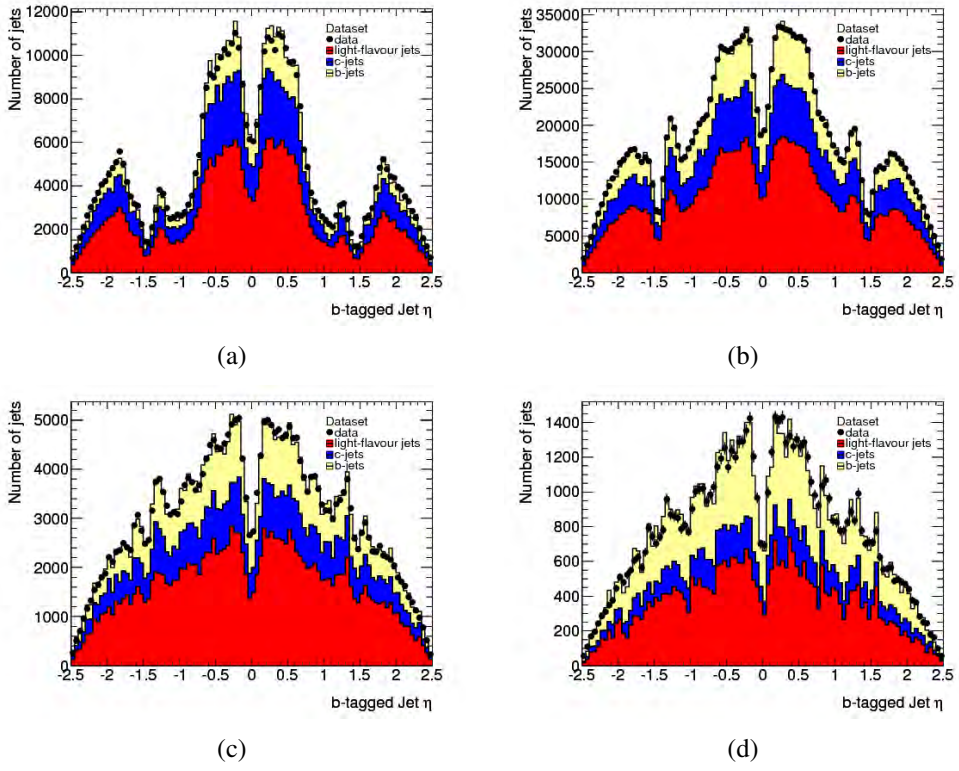

Figure 5.20: These plots present a reweighting of the η distributions shown in Figure 5.19 in the four jet p_T bins: 60 GeV $< p_T <$ 90 GeV (a), 90 GeV $< p_T <$ 140 GeV (b), 60 GeV $< p_T <$ 90 GeV (c) and 90 GeV $< p_T <$ 140 GeV (d). The *light*-jet η distribution (red) is taken from data, and is reweighted according to the expectation that its η distribution should match that of the full data sample. After this reweighting, *b*- and *c*-jets from Monte Carlo are reweighted so that the total η distributions of these samples combined with the light sample match the distribution in the data.

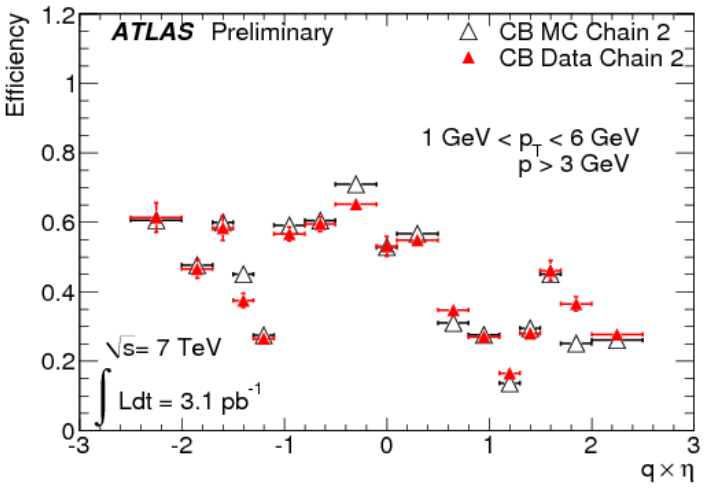

(a)

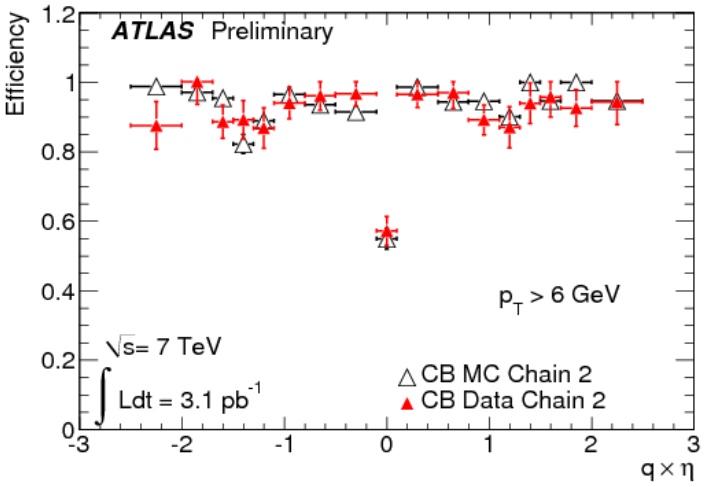

(b)

Figure 5.21: Measured muon reconstruction efficiencies versus $q \times \eta$, for a muon p_T between 1 and 6 GeV (a) and a muon p_T larger than 6 GeV (b), using 3.1 pb^{-1} of the 2010 LHC data. Taken from Ref. [84].

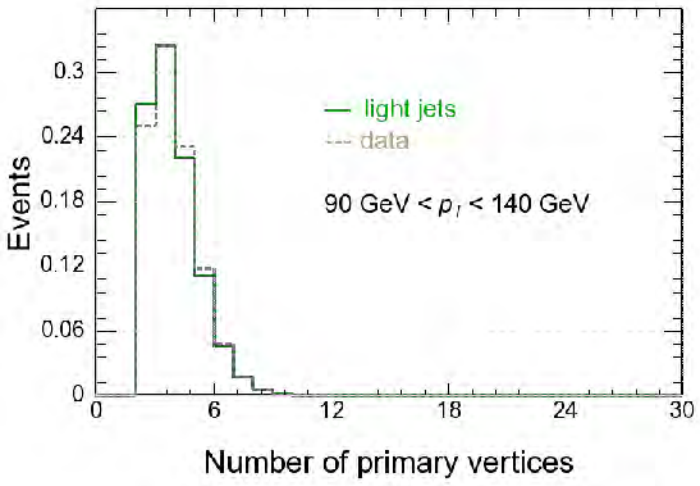

(a)

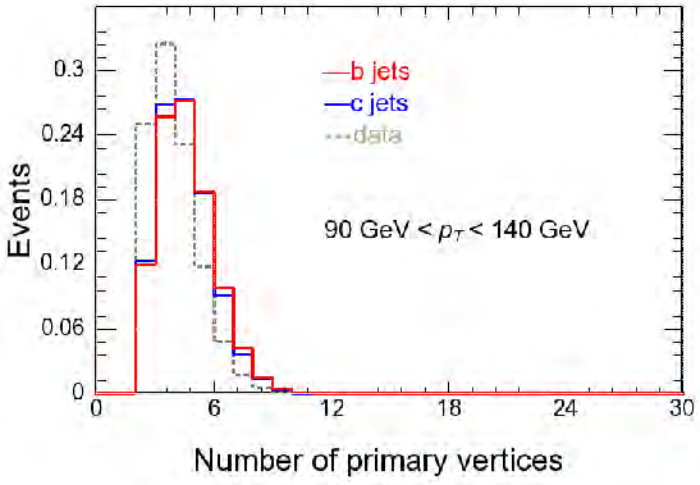

(b)

Figure 5.22: Number of primary vertices in data and in the light quark data sample (a) and in muon-filtered Monte Carlo (b) for a jet p_T between 90 and 140 GeV. The Monte Carlo differs from the data because the luminosity profile is not simulated. The data-driven light quark templates differ from data because the event sample was collected using a different trigger, and thus has different prescale factors.

reweighting is applied to both the light quark data sample and the heavy quark Monte Carlo.

5.6 *System*8 Results

The b-tagging efficiency has been measured for jets in four p_T bins: 20 GeV $< p_T <$ 30 GeV, 30 GeV $< p_T <$ 60 GeV, 60 GeV $< p_T <$ 90 GeV, and 90 GeV $< p_T <$ 140 GeV; and for several lifetime taggers and operating points, including those intended as benchmark points for the physics analyses.

The jet energy scale used for the above binning adds the muon momentum and an average correction for the undetected neutrino in the assumed semileptonic decay as already discussed in Section 5.5.4.

As mentioned in Section 5.3, the correlation factors are mostly determined on simulated samples. This gives a straightforward way to determine the correlation factors, by applying the selections to the simulated b and cl samples. Similarly to the procedure described in Section 5.4, the computation of the associated uncertainties proceeds by subdividing the simulated b and cl samples into their 8 statistically independent (disjoint) subsamples.

One complication originates from the binning of the simulated samples. These samples have been generated in different $\hat{p}_{\mathrm{T}}$ bins, as detailed in Section 5.5.2. The baseline approach, followed in this thesis, was to assign weights to events from the different `Jx` samples so as to reproduce a $\hat{p}_{\mathrm{T}}$ distribution without further binning. However, this procedure leads to large correlation factor uncertainties, due to the fact that the few events from the lower-$\hat{p}_{\mathrm{T}}$ bins passing the selection criteria carry very large weights.

Figures 5.23 and 5.24 show the efficiency results of the `SV0` and the `JetProb` algorithms respectively in the four jet p_T bins, for three values of the $p_{\mathrm{T}}^{\mathrm{rel}}$ cut. Two uncertainties are shown for each measurement:

- the data-only statistical uncertainty (error bars in black);
- the combined statistical uncertainty from data statistics and the limited statistics of the samples used to construct the correlation factors (colored bands). Here, the contribution from the latter is computed following Eq. 5.12.

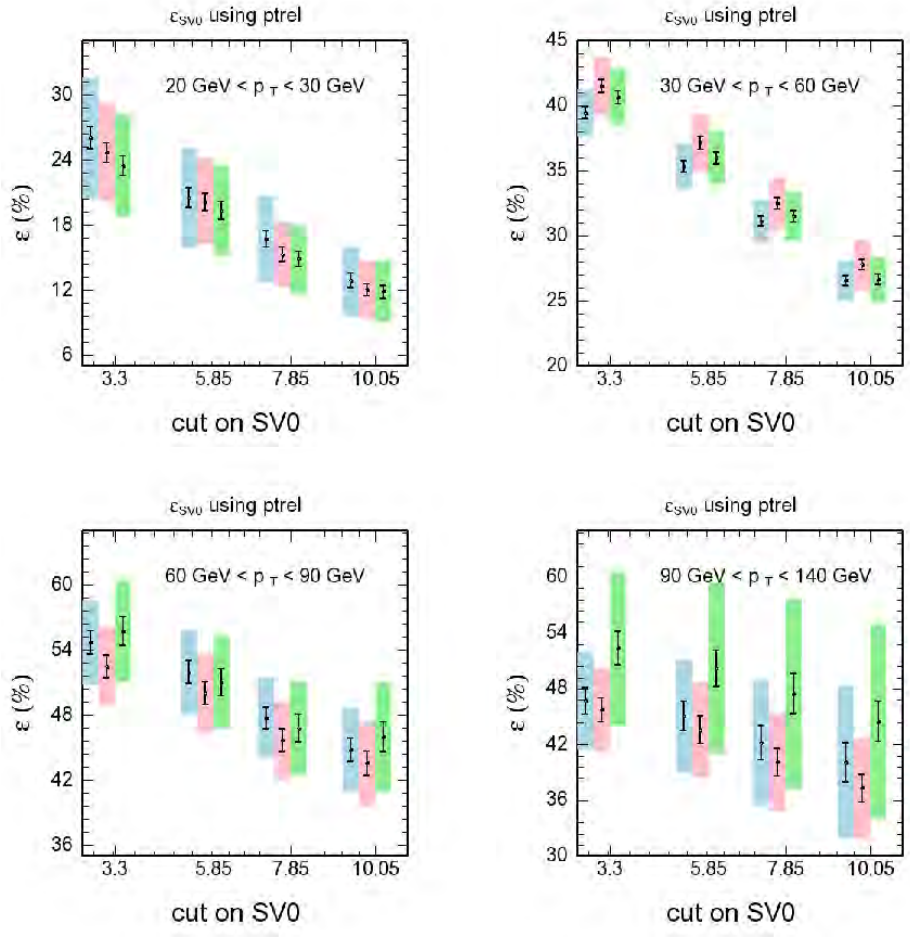

Figure 5.23: Efficiency of the SV0 algorithm determined with *System8* versus different SV0 working points for four different p_T bins. Colored bands represent the total statistical error bars determined. Different colors indicate different cuts on $p_{\mathrm{T}}^{\mathrm{rel}}$. Blue: $p_{\mathrm{T}}^{\mathrm{rel}} > 600$ MeV. Red: $p_{\mathrm{T}}^{\mathrm{rel}} > 700$ MeV. Green: $p_{\mathrm{T}}^{\mathrm{rel}} > 800$ MeV. The small error bars indicate the statistical errors due to the data statistics only, and the larger error bars indicate the contribution from data and the 8 correlation coefficients statistics.

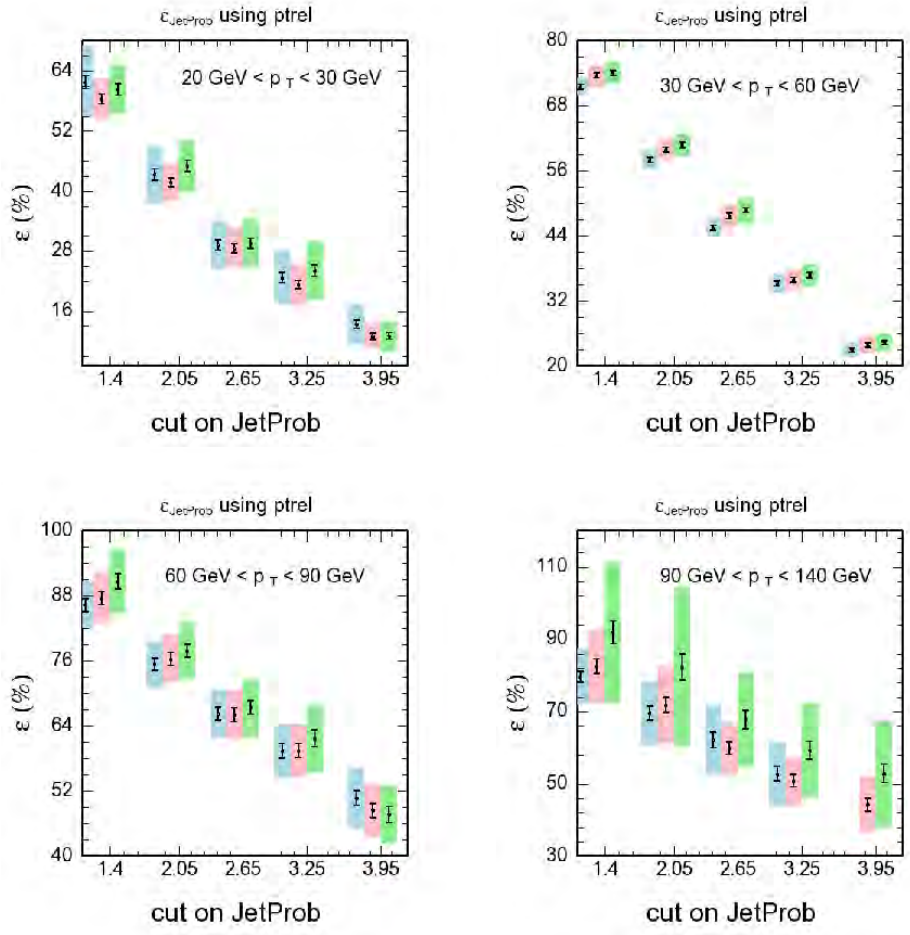

Figure 5.24: Efficiency of the `JetProb` algorithm determined with *System8* versus different `JetProb` working points for four different p_T bins. Colored bands represent the total statistical error bars determined. Different colors indicate different cuts on $p_{\mathrm{T}}^{\mathrm{rel}}$. Blue: $p_{\mathrm{T}}^{\mathrm{rel}} > 600$ MeV. Red: $p_{\mathrm{T}}^{\mathrm{rel}} > 700$ MeV. Green: $p_{\mathrm{T}}^{\mathrm{rel}} > 800$ MeV. The small error bars indicate the statistical errors due to the data statistics only, and the larger error bars indicate the contribution from data and the 8 correlation coefficients statistics.

5.7 Systematic Uncertainties

The contributions to the uncertainties on the correlation factors (which are the only source of systematic errors on the resulting tagging efficiency) are discussed below in some detail. The systematic errors are computed for each working point, within each p_T bin, and for each of the taggers we considered here (`SV0` and `JetProb`). The systematic errors for several working points are shown in Tables 5.3, 5.4, and 5.5. The tables present both the total systematic error and the individual systematic errors. The total systematic uncertainty is computed as the quadratic sum of all of the individual components.

One simplifying assumption is made in the calculation of systematic uncertainties: it is assumed that for the *b*-jet contributions, there are no correlations between the soft muon tagging criterion and the opposite-jet tagging requirement, leading to $\alpha_5 = 1$ and $\alpha_7/\alpha_1 = 1$, and hence only to 6 additional unknowns and constraints, as opposed to the 8 used for the extraction of the main results. This assumption is very nearly (up to a few percent) borne out by explicit evaluation using simulated *b* samples, and is instrumental in improving the *System8* convergence properties. The same assumption cannot be made for the *cl* sample, as the opposite-jet tagging requirement enhances the charm fraction in this sample; therefore in case of any difference in $p_{\mathrm{T}}^{\mathrm{rel}}$ distribution for the light-flavor and charm subsamples, the opposite-jet tagging requirement will result in a modification of the combined $p_{\mathrm{T}}^{\mathrm{rel}}$ spectrum. This correlation depends on the assumed charm fraction in the *cl* sample, which is not a priori known.

5.7.1 $p_{\mathrm{T}}^{\mathrm{rel}}$ Cut Variation

The nominal $p_{\mathrm{T}}^{\mathrm{rel}}$ cut applied for the application of *System8* is 700 MeV, as mentioned in Section 5.3. Due to the specific shapes of the *b*- and *cl*-sample $p_{\mathrm{T}}^{\mathrm{rel}}$ distributions, the sample composition depends on the $p_{\mathrm{T}}^{\mathrm{rel}}$ cut value used. As a consequence, the lack of dependence of the *System8* result on this cut value constitutes a stringent test of the method.

As mentioned in Section 5.6, Figures 5.23 and 5.24 show the results for different values of the $p_{\mathrm{T}}^{\mathrm{rel}}$ cut (600 and 800 MeV). The larger difference between the results using either of the above two extreme values and those using the central value is considered as a systematic uncertainty and presented in Tables 5.3, 5.4, and 5.5.

5.7.2 Muon Jet Angular Resolution

The computation of the $p_{\mathrm{T}}^{\mathrm{rel}}$ variable uses the (calorimeter) jet and muon momentum vectors, and is therefore sensitive to the resolutions of these objects' momen-

tum and direction (and in principle also the calorimeter jet energy scale). Since the largest dependence is on the muon momentum and on the directions, and since the muon can be assumed to be well measured, the calorimeter jet angular resolution in particular is investigated; and more precisely, the potential *difference* in angular resolution between data and simulation.

The systematic uncertainty related to the muon-jet angular resolution relies on the study performed in the context of the $p_{\mathrm{T}}^{\mathrm{rel}}$ calibration method [85]. In this study, as a measure for this angular resolution, a comparison is made between the distribution of opening angles between (calorimeter) jets and the momentum obtained by adding the momenta of their associated tracks in data and the corresponding distribution in simulated events. Conservatively, the larger width of the distribution in data is attributed to a difference between data and calorimeter angular resolutions, and consequently the calorimeter jet directions in simulated events are smeared by 10 mrad. The effect of this change on the correlation factors is not considered directly; rather, the modified correlation factors (and correspondingly modified covariance matrix) are used to extract an alternate b-jet tagging efficiency. Systematic uncertainties due to the muon-jet angular resolution are presented in Tables 5.3, 5.4, and 5.5.

5.7.3 B-Hadron Decay Modeling

In the simulated events used for this study, B and charmed hadron decays are implemented using PYTHIA's decay model. While this model incorporates a large body of knowledge of heavy flavor decays, this does not guarantee a perfect modeling. Following the corresponding study carried out in the context of the $p_{\mathrm{T}}^{\mathrm{rel}}$ method, the distribution of the momentum[8] p^* of muons in the rest frame of decaying B hadrons is varied using a reweighting function obtained as the ratio of measured p^* spectrum from two different experiments, DELPHI [86], and BaBar [87]. The two spectra are compared in Figure 5.25. Systematic errors due to this variation are presented in Tables 5.3, 5.4, and 5.5.

In addition, the B hadron semileptonic branching fractions are known with an uncertainty of 2 to 5%: $B(b \to \ell^- \bar{\nu}_\ell X) = (10.69 \pm 0.22)\%$ and $B(b \to c \to \ell^+ \nu_\ell X, \bar{c} \to \ell^- \bar{\nu}_\ell X) = (9.62 \pm 0.53)\%$ [88]. The uncertainty on the ratio of 1.110 ± 0.065 is used to enhance or suppress the cascade decay component relative to the direct decay component in the simulated semileptonic decays. The resulting systematic uncertainty are presented in Tables 5.3, 5.4, and 5.5.

[8] p^* is the momentum of the muon computed in the rest frame of the decaying b-hadron.

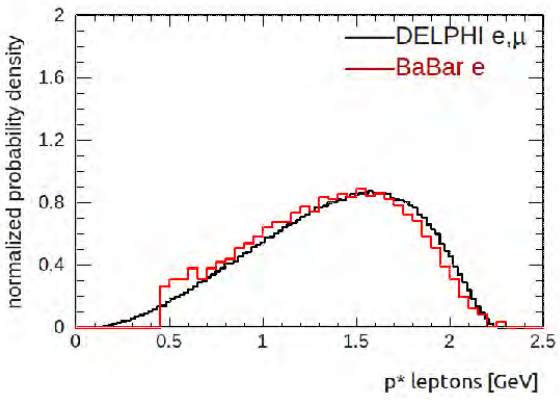

Figure 5.25: Comparison between the lepton p^* spectrum from B hadron decays in DELPHI (black, using both electrons and muons) and BaBar (red, restricted to electrons).

5.7.4 Gluon Splitting

The implicit assumption in determining the performance of b-jet tagging algorithms as a function of *jet* (kinematic or other) variables is that this performance does not depend on other details. However, final-state $g \to b\bar{b}$ splitting may result in a pair of $b\bar{b}$ quarks that are sufficiently collimated that their respective B hadrons are associated with the same reconstructed jet. Such effects would affect both the $p_{\mathrm{T}}^{\mathrm{rel}}$ distribution (since the reconstructed jet direction will not be as a good approximation of an individual B hadron flight direction) and the lifetime properties (since the B hadrons will on average have lower p_T than the B hadron resulting from the fragmentation of a single b quark in a jet of similar p_T). To assess the systematic uncertainty on the average b-jet tagging efficiency, the fraction of $g \to b\bar{b}$ events of $\approx 4\%$ found in the simulated events is either doubled or set to zero. An event is considered to come from gluon splitting if it contains a quark and an antiquark with $\Delta R < 0.8$. Systematic errors due to this variation are presented in Tables 5.3, 5.4, and 5.5.

5.7.5 b-Fragmentation Fractions

The most common ground-state b-flavored hadrons produced in proton-proton collisions are B^0, B^+, B_s^0, and Λ_b^0 (charge conjugation implied). The production fractions for each of these species (called the fragmentation fraction, denoted f_d, f_u, f_s and f_Λ, the latter implying actually *all* species of b-flavored baryon) have been measured both at LEP and at the TeVatron. Older world-average values

dominated by LEP (PDG 2006 [89]) give:

$$f_u = f_d = 39.8 \pm 1.2\%, \quad f_s = 10.3 \pm 1.4\%, \quad f_{\Lambda_b} = 10.0 \pm 2.0\%. \tag{5.13}$$

Relatively recent (2008) TeVatron results (from CDF [90]) are

$$\begin{aligned} f_u/f_d &= 1.054 \pm 0.018(\text{stat.})^{+0.025}_{-0.045}(\text{syst.}) \pm 0.082(\text{branching frct.}) \\ f_s/(f_u+f_d) &= 0.160 \pm 0.005(\text{stat.})^{+0.011}_{-0.010}(\text{syst.})^{+0.057}_{-0.034}(\text{branching frct.}) \\ f_{\Lambda_b}/(f_u+f_d) &= 0.281 \pm 0.012(\text{stat.})^{+0.058}_{-0.056}(\text{syst.})^{+0.127}_{-0.086}(\text{branching frct.}) \end{aligned}$$

with central values of:

$$f_u = 36\%, \quad f_d = 34\%, \quad f_s = 11\%, \quad f_{\Lambda_b} = 20\%. \tag{5.14}$$

The most significant difference between the two sets of measurements is the higher values of baryon production from the TeVatron measurements; nearly twice the older world average values. This has a potential effect on the correlation factors, since the baryons could have a different muon spectrum and lifetime (thus b-tagging rates) than mesons; in other words the correlations between the two algorithms could be different in Monte Carlo and in data. The ATLAS Monte Carlo simulation has the following fractions:

$$f_u = 42\%, \quad f_d = 42\%, \quad f_s = 8.6\%, \quad f_{\Lambda_b} = 7.8\%. \tag{5.15}$$

To evaluate the systematic errors related to the knowledge of the b-fragmentation fractions, a reweighting on all of the events so that the distribution of hadron species in each of the four categories matches the measured TeVatron numbers is applied. Results are presented in Tables 5.3, 5.4, and 5.5.

5.7.6 b-Fragmentation Function

To investigate the impact of fragmentation on tagging efficiency, one ideally would change the b-hadron fraction x_E, i.e. the fraction of the b-quark energy carried onto the b-hadron. As with other variables, the hadron faction x_E could be varied by reweighting. However, the value of x_E generated for each event is not stored in the generator output and cannot be recovered from other stored information. Instead we reweight on the fraction x defined as the fraction of truth-jet energy carried by the b-hadron, in Monte Carlo. We change this fraction by 5% by reweighting the histogram of x_E shown in Figure 5.26. The systematic error related to this change is presented in Tables 5.3, 5.4, and 5.5.

	SV0 operating point 5.85 - jet p_T bins (GeV)			
Source	20 - 30	30 - 60	60 - 90	90 - 140
p_T^{rel} cut variation	0.008	0.018	0.019	0.066
Cascade Decay Fraction	<0.001	<0.001	0.001	0.001
b-fragmentation fractions	0.001	0.012	0.006	0.006
b-fragmentation functions	0.007	0.009	0.003	0.029
Gluon splitting	0.0089	0.002	0.003	0.001
p^* distribution	0.002	<0.001	0.002	<0.001
Charm fraction	<0.001	0.005	0.014	0.028
Angular resolution	0.006	0.007	0.009	0.011
Correlation factor statistics	0.039	0.021	0.035	0.049
Total	0.042	0.033	0.044	0.093

Table 5.3: Table of systematic errors for SV0 at an operating point of 5.85

5.7.7 Charm Fraction

As mentioned in Section 5.5.3, the composition of the *cl* sample used for the construction of the correlation factors is taken from simulation. However, the relative normalization of charm and light-flavor events is sensitive to theoretical (charm production cross section) as well as experimental (modeling of the light-flavor sample) issues. To estimate the effect on the *System8* results, the charm fraction in the *cl* sample was varied from its predicted value (0.33, 0.31, 0.28, and 0.25, decreasing with jet p_T) to extreme values of 0.15 and 0.8. The systematic errors related to the charm fraction variation are presented in Tables 5.3, 5.4, and 5.5.

5.8 Final Results Including Systematic Errors

Final b-tagging efficiency results for JetProb and SV0 are shown for a variety of working points in Figure 5.28 and Figure 5.27. Two sets of error bars are shown for each point: the smaller error bar contains only the statistical error due to the data only, and the larger error band takes into account also all systematic errors, including the systematic error due to the limited statistics of the Monte Carlo. There are strong reasons to believe that the systematic errors shown in these plots are dominated by the limited statistics of the Monte Carlo used in deriving the errors. Specifically, by comparing Figure 5.23 with Figure 5.27, or alternately Figure 5.24 with Figure 5.28, one can notice that the systematic errors are particularly small when the error from Monte Carlo statistics is small.

Figure 5.29 shows the efficiency determination using *System8* for both taggers

	JetProb operating point 2.05 - jet p_T bins (GeV)			
Source	20 - 30	30 - 60	60 - 90	90 - 140
p_T^{rel} cut variation	0.032	0.019	0.015	0.106
Cascade Decay Fraction	<0.001	<0.001	<0.001	0.001
b-fragmentation fractions	0.008	0.009	0.006	0.009
b-fragmentation functions	0.019	0.004	0.003	0.010
Gluon splitting	0.001	0.002	0.003	0.001
p^* distribution	0.004	<0.001	<0.001	0.002
Charm fraction	0.003	0.005	0.028	0.056
Angular resolution	0.005	0.006	0.012	0.010
Correlation factor statistics	0.039	0.019	0.044	0.105
Total	0.055	0.030	0.056	0.160

Table 5.4: Table of systematic errors for JetProb at an operating point of 2.05

	JetProb operating point 3.25 - jet p_T bins (GeV)			
Source	20 - 30	30 - 60	60 - 90	90 - 140
p_T^{rel} cut variation	0.028	0.008	0.023	0.085
Cascade Decay Fraction	0.002	<0.001	<0.001	<0.001
b-fragmentation fractions	0.002	0.005	0.007	0.006
b-fragmentation functions	0.020	0.006	0.001	0.038
Gluon splitting	0.008	0.003	0.003	0.002
p^* distribution	0.001	0.002	0.005	<0.001
Charm fraction	<0.001	0.004	0.020	0.029
Angular resolution	0.001	0.005	0.012	0.011
Correlation factor statistics	0.041	0.019	0.049	0.066
Total	0.054	0.023	0.059	0.118

Table 5.5: Table of systematic errors for JetProb at an operating point of 3.25

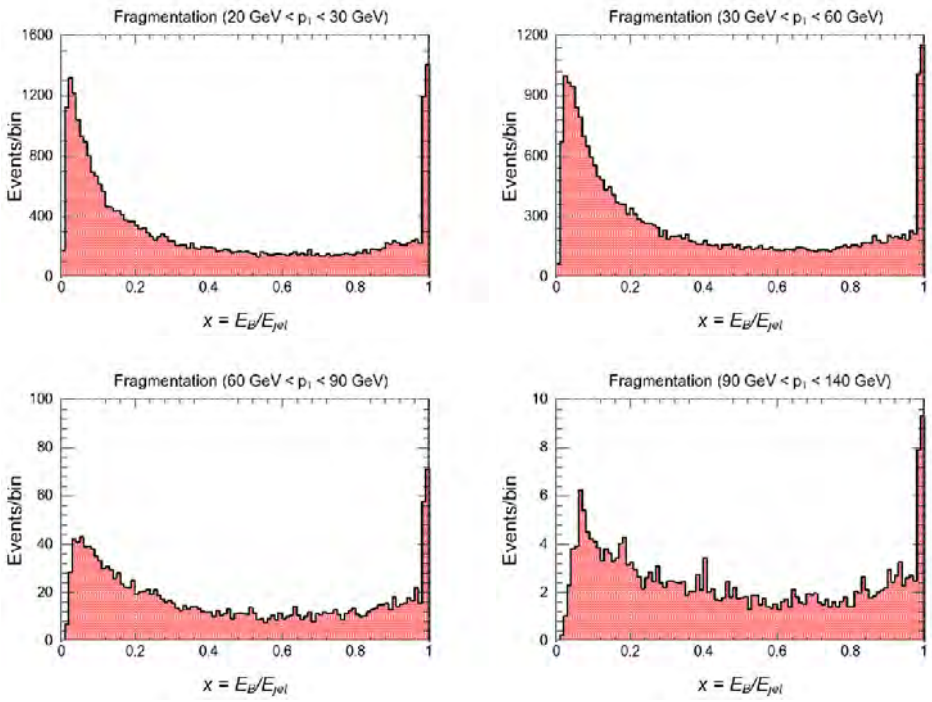

Figure 5.26: Distribution of x_E for b hadrons in Monte Carlo within each of the four jet p_T bins.

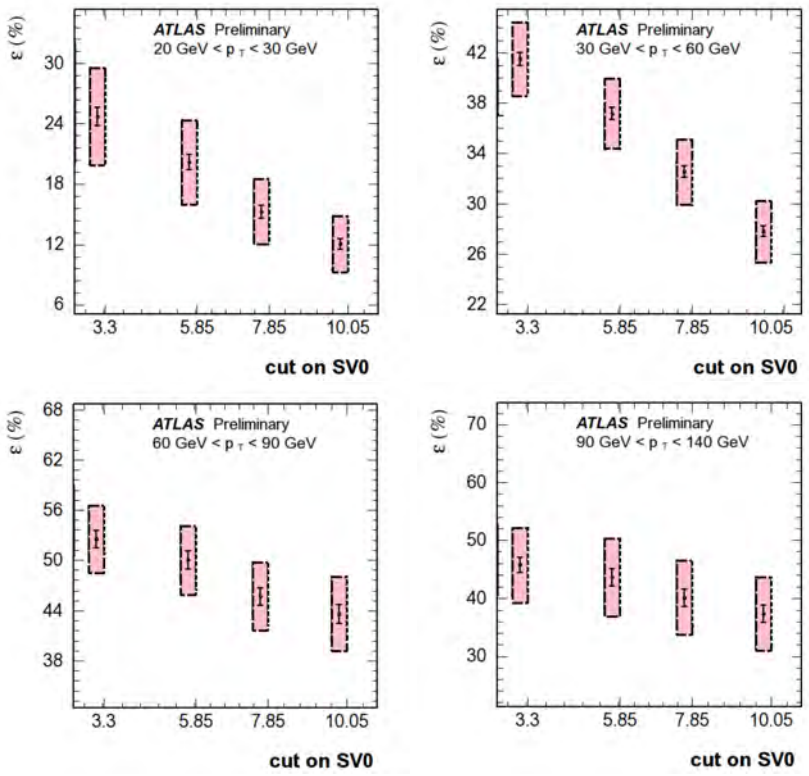

Figure 5.27: Efficiency of the SV0 algorithm determined with *System8* for four different p_T bins for the default $p_{\mathrm{T}}^{\mathrm{rel}}$ cut ($p_{\mathrm{T}}^{\mathrm{rel}} > 0.7$ GeV). Colored bands represent error bars. In these plots, the small error bar indicates the statistical error while the larger error bar indicates total error, including systematic errors.

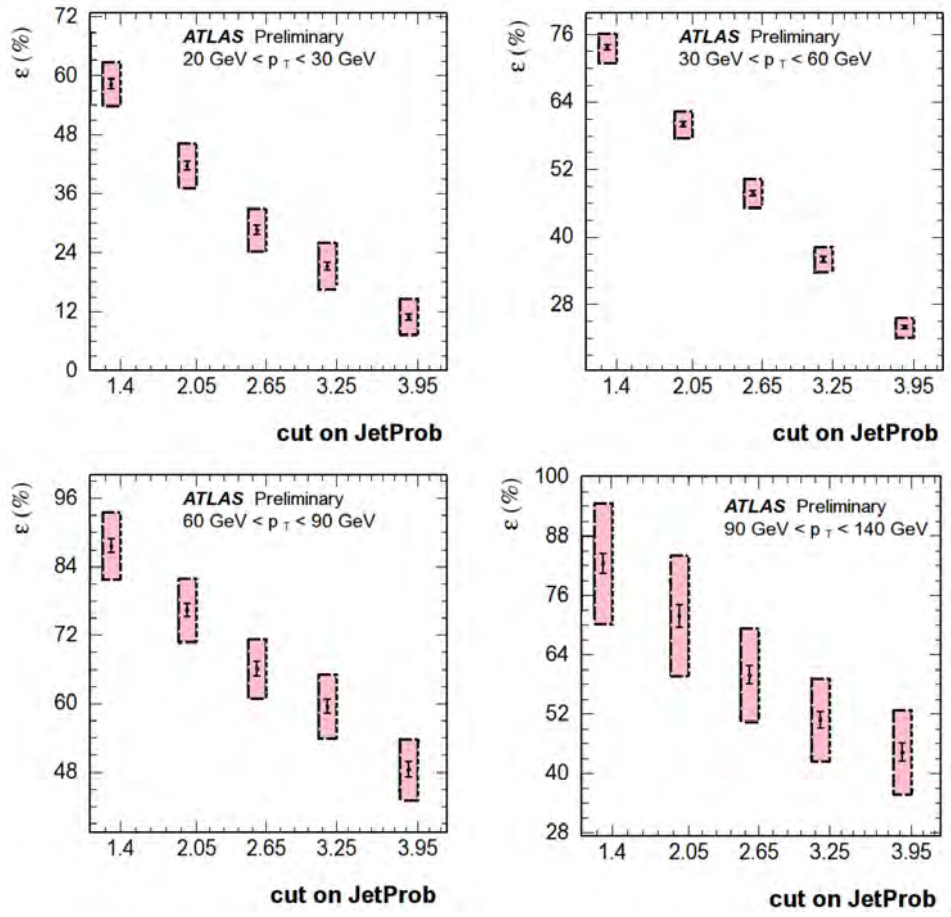

Figure 5.28: Efficiency of the `JetProb` algorithm determined with *System8* for four different p_T bins for the default $p_{\mathrm{T}}^{\mathrm{rel}}$ cut ($p_{\mathrm{T}}^{\mathrm{rel}} > 0.7$ GeV). Colored bands represent error bars. In these plots, the small error bar indicates the statistical error while the larger error bar indicates total error, including systematic errors.

at all of the benchmark points designated by the ATLAS Flavor Tagging group, compared to results of the $p_{\mathrm{T}}^{\mathrm{rel}}$ analysis [85]. The agreement between the *System8* and the $p_{\mathrm{T}}^{\mathrm{rel}}$ method is very good in each of the jet p_T bins. Scale factors are shown in Figure 5.30, where they are also compared to those obtained in the $p_{\mathrm{T}}^{\mathrm{rel}}$ analysis.

5.9 Conclusion

For the first time, *System8* has been applied to ATLAS muon+jet data to extract the *b*-tagging efficiencies and *b*-tagging data-to-Monte-Carlo scale factors. The method yields results which are in a very good agreement with the $p_{\mathrm{T}}^{\mathrm{rel}}$ calibration [75].

Results from the analysis in a form appropriate for use in physics analysis, for three taggers and operating points are shown in Table 5.6.

		Jet p_T [GeV]			
Tagger	Operating point	20–30	30–60	60–90	90–140
SV0	5.85	$0.81 \pm 0.04 \pm 0.17$	$0.90 \pm 0.01 \pm 0.08$	$0.96 \pm 0.02 \pm 0.08$	$0.77 \pm 0.03 \pm 0.17$
JetProb	3.25	$0.80 \pm 0.04 \pm 0.20$	$0.86 \pm 0.01 \pm 0.06$	$1.10 \pm 0.03 \pm 0.11$	$0.83 \pm 0.03 \pm 0.19$
JetProb	2.05	$0.77 \pm 0.02 \pm 0.10$	$0.89 \pm 0.009 \pm 0.05$	$1.01 \pm 0.02 \pm 0.07$	$0.90 \pm 0.03 \pm 0.20$

Table 5.6: The *b*-tagging efficiency scale factors from the *System8* method in bins of jet p_T, with both statistical and systematic uncertainties.

This analysis on the 2010 data served as a useful cross-check to the $p_{\mathrm{T}}^{\mathrm{rel}}$ analysis, which has already been widely used in ATLAS physics analyses. On 2011 data, *System8* provided the *b*-tagging calibration with minimal dependence on inputs from Monte Carlo. Its results were combined together with the $p_{\mathrm{T}}^{\mathrm{rel}}$ results and they have been used by all physics analyses using *b*-tagging. The limited Monte Carlo statistics still severely limit the precision of the measurement and the ability to evaluate systematic uncertainties, to such an extent that most of the uncertainties are dominated by Monte Carlo statistics. Figure 5.31 shows a combination for the *b*-tagging data-to-MC scale factors measured by p_T^{rel} and $System8$ for the MV1 tagging algorithm at a 70% *b*-tagging efficiency operating point, on the full 2011 ATLAS data set. This combination has been used by the physics analyses as well as in the $t\bar{t}$ analysis in this thesis, described in Chapter 6.

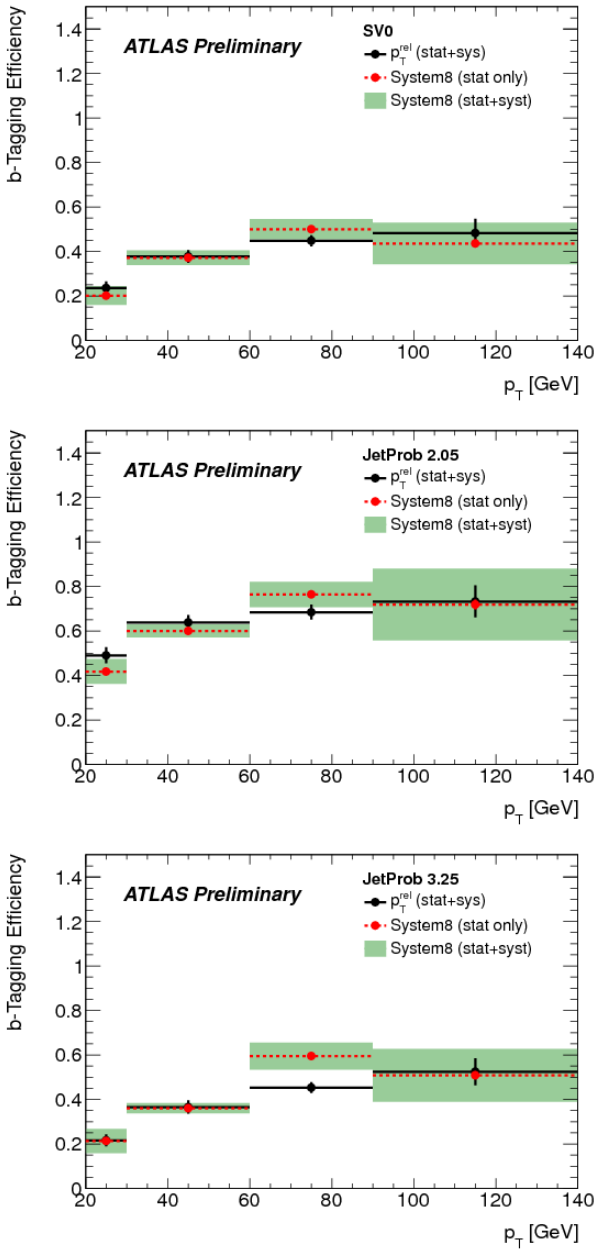

Figure 5.29: Final *b*-tagging efficiencies extracted from the *System8* method and comparison with results from the $p_{\mathrm{T}}^{\mathrm{rel}}$ analysis, for the `SV0` (top) and `JetProb` 2.05 (middle) and 3.25 (bottom) working points.

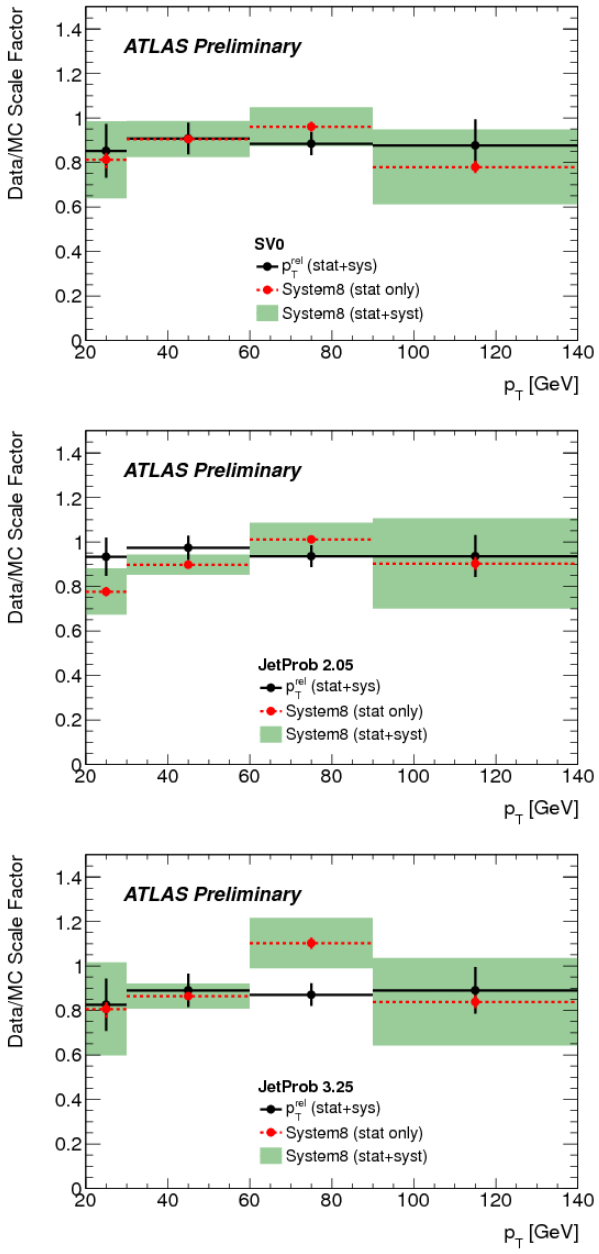

Figure 5.30: Final *b*-tagging data-to-Monte-Carlo scale factors extracted from the *System8* method and comparison with results from the $p_{\mathrm{T}}^{\mathrm{rel}}$ analysis, for the `SV0` (top) and `JetProb` 2.05 (middle) and 3.25 (bottom) working points.

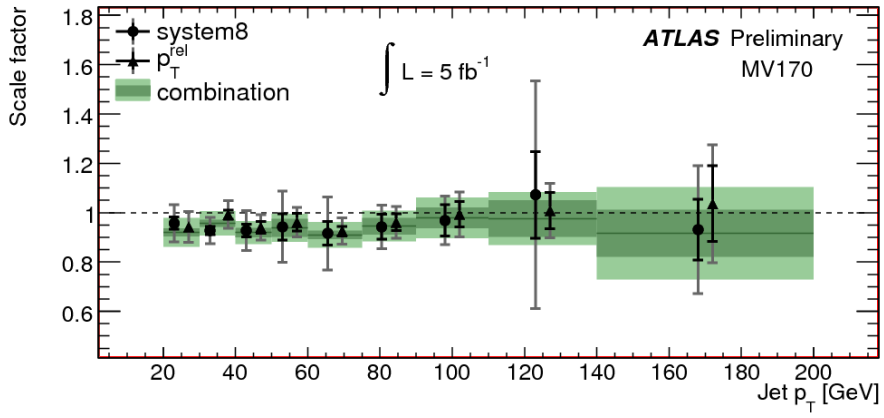

Figure 5.31: The data-to-simulation scale factor for the MV1 tagging algorithm at 70% efficiency, obtained by combining the p_T^{rel} and *System*8 results on the 2011 ATLAS data. The dark green bands represent the statistical uncertainty of the combined scale factor while the light green bands show the total uncertainty. The data points showing the p_T^{rel} and *System*8 measurements have been separated a little along the x-axis to make the plot more readable.

Chapter 6

Top Quark Pair Differential Cross Sections in the Semileptonic Channel

This Chapter presents the $t\bar{t}$ differential cross section performed on the data sample collected in 2011 with the ATLAS detector.

The top quark decays almost 100% of the time into a W boson and a b-quark. The decay products of a $t\bar{t}$ event is then $W^+bW^-\bar{b}$. As discussed in the Chapter 1, depending on the decays of the $W^{\pm}$, there are three decay channels for a $t\bar{t}$ event, namely the all-hadronic channel, the semileptonic channel and the di-lepton channel. In the analysis presented in this Chapter, the semileptonic channel with a final state $b\bar{b}l\bar{\nu}_l q\bar{q}^{'}$ is considered for the measurement of the differential cross section. This channel is considered to be the "golden channel" for $t\bar{t}$ physics and precision measurements. It is a compromise between the high QCD multi-jets background for the all-hadronic channel, and the high missing transverse energy for the di-lepton channel. The l denotes only the charged leptons of the first two generations (electron or muon) and ν_l refers to their associated neutrinos. Events with τ lepton are not considered because they are difficult to reconstruct experimentally, and their acceptance for τ decays to electrons and muons is small.

The inclusive $t\bar{t}$ production cross section has been measured at the center of mass energy of $\sqrt{s} = 7$ TeV by the ATLAS and CMS collaborations with increasing precision [91] in all decay channels using data collected in 2010 and 2011. The unprecedentedly large number of available $t\bar{t}$ events (tens of thousands) opens the door to detailed investigations of the properties of top quark production in terms of characteristic variables of the $t\bar{t}$ system. The work presented in this Chapter focuses on two observables of the $t\bar{t}$ system: the invariant mass ($M_{t\bar{t}}$) and the rapidity ($y_{t\bar{t}}$). The mass of the $t\bar{t}$ system is sensitive to new couplings/particles

beyond the SM as s-channel resonances can modify the shape of the differential production cross section in different ways depending on their spin and color properties [92]. Recent measurements of the $t\bar{t}$ asymmetry in proton-antiproton collisions at $\sqrt{s} = 1.96$ TeV have been carried out by the CDF and the DØ experiments at the Fermilab TeVatron [93, 94]. Significant inclusive asymmetries are observed in the laboratory and $t\bar{t}$ rest frame, and are consistent with CP conservation under interchange of t and $\bar{t}$. In the $t\bar{t}$ rest frame, the asymmetry increases with the $t\bar{t}$ rapidity difference, $\Delta(y)$, and with the invariant mass $M_{t\bar{t}}$ of the $t\bar{t}$ system. The asymmetry is found to be most significant at large $\Delta(y)$ and $M_{t\bar{t}}$. For $M_{t\bar{t}} > 450$ GeV/c^2, the parton-level asymmetry in the $t\bar{t}$ rest frame is $A^{t\bar{t}} = 0.475 \pm 0.114$ [95] compared to a next-to-leading order QCD prediction of 0.088 ± 0.013. A number of theoretical papers suggest interesting new physics mechanisms including axigluons, diquarks, new weak bosons, and extra-dimensions that can all produce forward-backward $t\bar{t}$ asymmetries. One proposed model [96] for example, guided by the requirement of reproducing the desired level of asymmetry, assumes the existance of two new heavy quarks, t' and b', with charges $+2/3$ and $-1/3$ respectively. These new heavy quarks have rather strong flavor interactions with the top quark and some flavor changing coupling with the up and down quarks through Yukawa couplings to charged and neutral scalar particles. The new physics can interfer with the leading order QCD process $q\bar{q} \rightarrow g \rightarrow t\bar{t}$. This interference can generate a significant forward backward asymmetry in the $t\bar{t}$ production with a dependence on the invariant mass $M_{t\bar{t}}$ of the $t\bar{t}$ system as well as the Δy.

In this chapter, the object selection as well as the event selection are detailed. The $t\bar{t}$ events reconstruction is then described along with the treatment of the different backgrounds, as well as the systematic uncertainties. The unfolding procedure and the combination between the muon and the electron channels are then presented followed by the results of the measurement performed on the complete 4.71 fb^{-1} data sample of 2011 ATLAS.

6.1 Data and Simulated Samples

The data used for the measurement of the $t\bar{t}$ differential cross section was collected in 2011 with the ATLAS detector exposed to proton-proton collisions provided by the LHC and corresponds to an integrated luminosity of approximately[1] $4.7 fb^{-1}$. The full dataset is divided into different periods, listed in Table 6.1, which are characterized by different conditions of the LHC operation. In particular the pile-up conditions increased a lot during the data taking periods L and M. The data was

[1] After applying Good Run List (GRL) selection.

Period	Integrated Luminosity [pb^{-1}]
B	17
D	179
E	50
F	152
G	560
H	278
I	399
J	232.9
K	660.2
L	1568
M	1121

Table 6.1: Data periods and their luminosity for the 2011 ATLAS data taking before GRL selection.

Period	Electron Trigger
B-H	EF-e20-medium
I-K	EF-e22-medium
L-M	EF-e22vh-medium1

Table 6.2: Single electron triggers used in the 2011 ATLAS data taking.

collected using single muon and single electron triggers, listed in Table 6.2 and Table 6.3 for the electron channel and the muon channel respectively. The trigger conditions changed during the data taking to cope with the increased pile-up. The trigger will be described with more details in Section 6.2.

The simulated samples use the full simulation of the ATLAS detector based on GEANT4 [97]. The simulation of pile-up events was taken directly from data distributions and weighted at the correct level for the 2011 data.
The simulated samples used in this analysis are the $t\bar{t}$ non all-hadronic signal and the different backgrounds; namely the single top production, the W+jets, the

Period	Muon Trigger
B-I	EF-mu18
J-M	EF-mu18-medium

Table 6.3: Single muon triggers used in the 2011 ATLAS data taking.

Z+jets and the di-boson events. The QCD multi-jets background component is estimated from data events, and thus it has no corresponding simulated sample. The background treatment and estimation is detailed in Section 6.5. The different simulated MC samples used, their cross section and the number of generated events as well as the name of the generator programs used are listed in Tables 6.4 and 6.5.

The $t\bar{t}$ signal sample is simulated using the MC@NLO [98] generator with weighted events [2] using the MSTW2008 90% NNLO parton distribution functions sets [99] incorporating PDF+α_S uncertainties according to the MSTW prescription [3] [101]. The $t\bar{t}$ cross section is normalized to the approximate NNLO prediction of 166.8 pb, evaluated for a top mass of 172.5 GeV and obtained using HATHOR 1.2 [102] tool. The parton shower and the underlying events are added using the HERWIG [103] and JIMMY [104] generators with ATLAS AUET2B LO and ATLAS CTEQ6L1 tunes [105]. For the $t\bar{t}$ initial and final state radiation studies, two samples produced with ACERMC [106] and PYTHIA generators are used with initial and final state parameters set to a range of values compatible with the current experimental data, using MRST LO, LHA [99] parton distribution functions. The s-channel and the Wt-channel MC samples of the single top are also produced using the MC@NLO+HERWIG/JIMMY generators and normalized to the approximate NNLO cross section predictions of 4.63 pb [107] and 15.74 pb [108] respectively. The t-channel generated with MC@NLO has been found to have major problems with additional unphysical jets from the HERWIG shower, therefore, the samples used in this analysis are generated using ACERMC+PYTHIA with MRST LO, LHAPDF.

The vector boson production ($W + jets$ and $Z + jets$) is simulated using ALPGEN [104] interfaced to HERWIG and JIMMY generators. For both the matrix element calculations and the parton shower evolution the CTEQ6.1 parton distribution function is used. The corresponding AUET1 HERWIG and JIMMY tune [105] to the ATLAS data are also used. The MLM matching is applied inclusively for the $W+$ five partons production and exclusively for the lower multiplicity sub-samples. The additional partons produced in the matrix element as a part of the event generation can be either light partons ($W+$jets and $\gamma/Z+$jets) or heavy quarks ($W+c+$jets, $W+c\bar{c}+$jets, $W+b\bar{b}+$jets, $Z+c\bar{c}+$jets and $Z+b\bar{b}+$jets). The inclusive W and γ/Z production samples are obtained from the full set of the parton multiplicity sub-samples belonging to the same production process including both the light and heavy quark + jets processes. The heavy flavor overlap removal is applied in order to remove the double counting of the heavy quark production.

[2] Each event has a weight of +1 or -1. Only the sum the weighted events is a physical quantity.

[3] Cross checked with the NLO+NNLL calculation of Cacciari et al. [100].

Data Sample	Generator	Cross-Section (pb)	Generated Events
Signal			
$t\bar{t}$	MC@NLO	79.01	14 983 835
Single Top			
t-channel ($e\nu$)	ACERMC	8.06	999 295
t-channel ($\mu\nu$)	ACERMC	8.06	999 948
t-channel ($\tau\nu$)	ACERMC	8.05	998 995
s-channel ($e\nu$)	MC@NLO	0.47	299 948
s-channel ($\mu\nu$)	MC@NLO	0.47	300 000
s-channel ($\tau\nu$)	MC@NLO	0.47	299 899
Wt-channel	MC@NLO	14.59	900 000
Z+jets			
$Z \rightarrow ee$+0 parton	Alpgen + Herwig,Jimmy	668.32	6 618 284
$Z \rightarrow ee$+1 parton	Alpgen + Herwig,Jimmy	134.36	1 334 897
$Z \rightarrow ee$+2 parton	Alpgen + Herwig,Jimmy	40.54	809 999
$Z \rightarrow ee$+3 parton	Alpgen + Herwig,Jimmy	11.16	220 000
$Z \rightarrow ee$+4 parton	Alpgen + Herwig,Jimmy	2.88	60 000
$Z \rightarrow ee$+5 parton	Alpgen + Herwig,Jimmy	0.83	20 000
$Z \rightarrow \mu\mu$+0 parton	Alpgen + Herwig,Jimmy	668.68	6 615 230
$Z \rightarrow \mu\mu$+1 parton	Alpgen + Herwig,Jimmy	134.14	1 334 296
$Z \rightarrow \mu\mu$+2 parton	Alpgen + Herwig,Jimmy	40.33	404 947
$Z \rightarrow \mu\mu$+3 parton	Alpgen + Herwig,Jimmy	11.19	110 000
$Z \rightarrow \mu\mu$+4 parton	Alpgen + Herwig,Jimmy	2.75	30 000
$Z \rightarrow \mu\mu$+5 parton	Alpgen + Herwig,Jimmy	0.77	10 000
$Z \rightarrow \tau\tau$+0 parton	Alpgen + Herwig,Jimmy	668.40	10 613 179
$Z \rightarrow \tau\tau$+1 parton	Alpgen + Herwig,Jimmy	134.81	3 334 137
$Z \rightarrow \tau\tau$+2 parton	Alpgen + Herwig,Jimmy	40.36	1 004 847
$Z \rightarrow \tau\tau$+3 parton	Alpgen + Herwig,Jimmy	11.25	509 847
$Z \rightarrow \tau\tau$+4 parton	Alpgen + Herwig,Jimmy	2.79	144 999
$Z \rightarrow \tau\tau$+5 parton	Alpgen + Herwig,Jimmy	0.77	45 000
$Z + bb$+0 parton	Alpgen + Herwig,Jimmy	6.57	150 000
$Z + bb$+1 parton	Alpgen + Herwig,Jimmy	2.48	100 000
$Z + bb$+2 parton	Alpgen + Herwig,Jimmy	0.89	40 000
$Z + bb$+3 parton	Alpgen + Herwig,Jimmy	0.39	10 000
Di-boson			
WW	Herwig	11.50	2 489 244
WZ	Herwig	3.46	999 896
ZZ	Herwig	0.97	249 999

Table 6.4: Summary table of the Monte Carlo samples used in the analysis, the generators, their cross-sections and their generated events, for the $t\bar{t}$ signal, the single top, the Z+jets and the di-boson backgrounds.

Data Sample	Generator	Cross-Section (pb)	Generated Events
W+jets			
$W \to e\nu$+0 parton	Alpgen + Herwig,Jimmy	6930.50	3 458 883
$W \to e\nu$+1 parton	Alpgen + Herwig,Jimmy	1305.30	2 499 645
$W \to e\nu$+2 parton	Alpgen + Herwig,Jimmy	378.13	3 768 632
$W \to e\nu$+3 parton	Alpgen + Herwig,Jimmy	101.86	1 008 947
$W \to e\nu$+4 parton	Alpgen + Herwig,Jimmy	25.68	250 000
$W \to e\nu$+5 parton	Alpgen + Herwig,Jimmy	6.88	69 999
$W \to \mu\nu$+0 parton	Alpgen + Herwig,Jimmy	6932.40	3 462 942
$W \to \mu\nu$+1 parton	Alpgen + Herwig,Jimmy	1305.90	2 498 593
$W \to \mu\nu$+2 parton	Alpgen + Herwig,Jimmy	378.07	3 758 737
$W \to \mu\nu$+3 parton	Alpgen + Herwig,Jimmy	101.85	1 008 446
$W \to \mu\nu$+4 parton	Alpgen + Herwig,Jimmy	25.72	254 950
$W \to \mu\nu$+5 parton	Alpgen + Herwig,Jimmy	7.00	70 000
$W \to \tau\nu$+0 parton	Alpgen + Herwig,Jimmy	6931.8	3 418 296
$W \to \tau\nu$+1 parton	Alpgen + Herwig,Jimmy	1304.90	2 499 194
$W \to \tau\nu$+2 parton	Alpgen + Herwig,Jimmy	377.93	3 750 986
$W \to \tau\nu$+3 parton	Alpgen + Herwig,Jimmy	101.96	1 009 946
$W \to \tau\nu$+4 parton	Alpgen + Herwig,Jimmy	25.71	249 998
$W \to \tau\nu$+5 parton	Alpgen + Herwig,Jimmy	7.00	65 000
$W + bb$+0 parton	Alpgen + Herwig,Jimmy	47.35	474 997
$W + bb$+1 parton	Alpgen + Herwig,Jimmy	35.76	205 000
$W + bb$+2 parton	Alpgen + Herwig,Jimmy	17.33	174 499
$W + bb$+3 parton	Alpgen + Herwig,Jimmy	7.61	69 999
$W + c$+0 parton	Alpgen + Herwig,Jimmy	644.4	6 427 837
$W + c$+1 parton	Alpgen + Herwig,Jimmy	205.0	2 069 646
$W + c$+2 parton	Alpgen + Herwig,Jimmy	50.8	519 998
$W + c$+3 parton	Alpgen + Herwig,Jimmy	11.4	115 000
$W + c$+4 parton	Alpgen + Herwig,Jimmy	2.8	30 000
$W + cc$+0 parton	Alpgen + Herwig,Jimmy	127.5	1 274 846
$W + cc$+1 parton	Alpgen + Herwig,Jimmy	104.7	1 049 847
$W + cc$+2 parton	Alpgen + Herwig,Jimmy	52.08	524 947
$W + cc$+3 parton	Alpgen + Herwig,Jimmy	16.9	170 000

Table 6.5: Summary table of the Monte Carlo samples used in the analysis, the generators, their cross-sections and their generated events, for the W+jets background.

Due to the use of the heavy flavor overlap removal, the phase-space populated by the heavy quarks produced in association with the vector bosons should preferably not be limited by imposing the phase-space cuts. While using no phase space cuts is feasible for the associated heavy quark pair production, a minimum transverse momentum cut of 10 GeV had to be introduced for the $W+c$ samples due to the large production cross section of this process. The production cross sections of all of the ALPGEN and HERWIG samples are normalized to the corresponding NNLO cross section prediction [109].The diboson samples (WW, ZZ, WZ) are generated using LO generator with lowest multiplicity final state, HERWIG standalone. The K-factors(1.48 for WW, 1.30 for WZ, 1.60 for ZZ) are obtained using the NLO cross section prediction [109].

6.2 Trigger

In both the electron and muon channels, the single lepton triggers which ran unprescaled in the 2011 data taking, are required. The 2011 LHC data set is divided into 11 periods of data taking, as listed in Table 6.1 labeled from B to M, where the last two periods, period L and period M, represent almost half of the 2011 data sample. Subsequently, a three-level trigger decision is required based on the lepton signatures, and designed to cope with the increase in luminosity of the LHC operations and the corresponding evolution of the number of in-time and out-of-time pile-up events.

- In the electron channel, both data and simulation are required to pass an EF trigger. For data, EF_e20_medium is required for $\approx 36\%$ of the whole dataset (up to period K), EF_e22_medium is required for $\approx 13\%$ of the dataset (period K) and the one of the two triggers : EF_e22vh_medium1 or EF_e45_medium1 for the rest of the dataset (periods L and M). Corresponding similar luminosity percentages are required to pass the previous triggers for the simulated events. Each one of these triggers require electromagnetic cluster at level-1 trigger to have a transverse energy above a threshold, listed in Table 6.6. At level-2, there are some requirements on the shower shape, and the electromagnetic cluster must match with an inner detector track. At the event filter (EF) level, the electron must have an E_T larger than a threshold also listed in Table 6.6.

- In the muon channel, also both data and simulation are required to pass the third level trigger. For data, EF_mu18 is required to be fired for $\approx 31\%$ of

Trigger	Level-1 E_T threshold (GeV)	EF E_T threshold(GeV)
EF_e20_medium	14	20
EF_e22_medium	16	22
EF_e22vh_medium1	16	22
EF_e45_medium1	30	45

Table 6.6: The single electron trigger used in this thesis with their E_T thresholds at the L1 and the EF trigger levels.

the 2011 dataset (up to period J), and EF_mu18_medium for the rest. Similar luminosity fractions in the simulated events are also required to pass the EF_mu18 and the EF_mu18_medium triggers. The EF_mu18 trigger chain requires the events to have L1_MU10 trigger which require a muon with p_T greater than 10 GeV at Level-1. At level-2, it requires the muon to be combined with an inner detector track. And last, at the EF level, it requires the muon to have a p_T greater than 18 GeV. The EF_mu18_medium trigger requires the muon to have a p_T greater than 11 GeV at level-1. At level-2, it requires the muon to be matched with an ID track too, but to have passed also a set of quality cuts for the muon, called the "medium" cuts. At the EF level, it also requires the muon to have a p_T greater than 18 GeV.

6.3 Object Selection

The $t\bar{t}$ signature in the "lepton+jets" channel includes a muon or an electron, two b-jets, two *light*-jets and missing transverse energy E_T^{miss} which is sensitive to momentum imbalance in the transverse plane indicating the presence of escaping neutrinos. In this section, the different criteria used in the analysis to define the selected objects are detailed. For the object reconstruction and selection, the official recommendation of the ATLAS Top Reconstruction Group is followed.

6.3.1 Muons

Muon candidates are reconstructed using the official ATLAS muon identification algorithm in the inner detector and the muon spectrometer detailed in Chapter 4 Section 4.3, and the combination is performed using the MuId algorithm described in Chapter 4 Section 4.3.1. Some additional specific requirements are applied to reject muons coming from heavy and light flavor decays (such as $b-$ and

$c-$hadron decays and π and K decays in flight). Muon candidates are required to fulfill the following requirements:

- p_T >20 GeV
- $|\eta|$ <2.5
- be separated from the closest jet by $\Delta R(\mu$, closest reconstructed jet) >0.4
- have a calorimeter isolation cut $<$ 4 GeV and have track isolation $<$ 2.5 GeV. Track isolation is defined as the sum of track transverse momenta in a cone of ΔR = 0.3, excluding the p_T of the muon track, while calorimeter isolation is defined as the energy deposition in the calorimeter within a cone of $\Delta R = 0.2$, excluding the energy deposited directly along the muon track.
- additional track hit requirements are:
  - at least one expected hit in the B-layer of the pixel detector
  - at least two hits in the pixel detector
  - at least seven hits in the SCT detector
  - less than three holes in the pixel and SCT detectors
  - at least five hits in the TRT detector

Muons satisfying the above criteria are used in the analysis sample and are referred to as tight, while muons with a looser isolation cut are used for the QCD multi-jets background determination described in Section 6.5. In this case, all requirements except the cuts on calorimeter and track isolation have to be fulfilled and the muons are referred to as loose. Data to simulation identification and reconstruction scale factors are applied to the reconstructed muons in Monte Carlo samples as described in Chapter 4 Section 4.3.2, to correct the basic reconstruction efficiency in the simulation. The nominal acceptance of the muon selection in the analysis is determined from simulation after the scale factors corrections have been applied. The uncertainties of such corrections are used to derive systematic uncertainties on the muon acceptance. The identification of the muon candidate is also performed at the trigger level, and thus a trigger data to simulation scale factor is also applied. The trigger efficiency is measured for the full EF_mu18 and EF_mu18_medium (muon trigger event requirement, more details in Section 6.4) chain with the requirement for the trigger object to match the muon probe. The efficiency is expressed with respect to the number of offline reconstructed muons that pass all the top-specific requirements listed above. The resulting trigger scale factors are η and ϕ dependent (averaged over p_T) with values around unity. Additionally, a muon momentum smearing is applied to correct for the differences

between data and simulation seen in the mean and the width of the muon momentum distribution.

6.3.2 Electrons

The electron candidates are identified using the official ATLAS tight identification algorithm discussed in Chapter 4 Section 4.2. This tight electron identification has an overall efficiency of 75%. During the first periods of data taking, the calorimeters were affected with dead front end boards (including dead optical links), dead high voltage regions and masked cells in the cluster core (dead cells, high noise cells, pathological sporadic noise cells). In particular about 42% of the total 2011 collected luminosity was affected by an additional acceptance loss: six front end boards (FEBs) in the EM Liquid Argon calorimeter were unreadable due to a problem with their controller board. The affected area covered a rectangular region in $\eta - \phi$ space corresponding to η [0.0, 1.45] and ϕ [0.788, 0.592]. To reproduce the data conditions, electrons with clusters falling in the affected region are rejected in a fraction of the simulated events corresponding to the fraction of the integrated luminosity collected with the acceptance loss. In addition, the electron candidates, in both data and simulation, are required to fulfill the following criteria:

- transverse energy $E_T^{cluster}/cosh(\eta_{track}) > 25$ GeV
- $|\eta_{cluster}| < 2.47$
    - excluding $1.37 < |\eta_{cluster}| < 1.52$ that corresponds to the transition region between barrel and endcap calorimeters
- an absolute transverse energy isolation Etcone20 @ 90% and an absolute transverse momentum isolation Ptcone30 @ 90% where Etcone20 and Ptcone30 stand for the leakage and pile-up corrected energies in a cone of $\Delta R = 0.2$ (for Etcone20) and $\Delta R = 0.3$ (for Ptcone30) centered around the electron, excluding the energy of the electron itself.
- be separated from the closest jet by $\Delta R_{e,jet} > 0.4$ since the electron scale factors were derived for $\Delta R_{e,jet} > 0.4$.
    - This cut is required after applying the jet-electron overlap removal where the jet is removed if found within a $\Delta R_{jet,e} < 0.2$.

Electrons meeting these requirements are used in the analysis. Looser electrons are used to estimate the QCD background. They differ from the tight ones by the isolation requirements, as it will be discussed in Section 6.5. Data to simulation

identification and reconstruction scale factors are applied to the selected electrons as described in Chapter 4 Section 4.2. Electron trigger scale factors are applied to the reconstructed electrons in MC too and they are measured using the unbiased electron in $Z \rightarrow ee$ and $W \rightarrow e\nu$ and are found to be in the plateau for $E_T > 25$ GeV. Measurements of the electron energy scale and resolution, in a kinematic range comparable to that of electrons in top events, is derived from the measurement of the $Z \rightarrow ee$ invariant mass distribution [110]. The energy scale is corrected in data as a function of the electron η cluster and systematic uncertainties are within $\pm 1\%$ to 1.5% for the $|\eta_{clus}| < 2.5$ range, dominated by uncertainties from the detector material and the presampler energy scale, but also include the event selection, pile-up, and hardware modeling. Thus, a correction to the energy of electrons in data is applied, including statistical and systematic uncertainties, and a smearing to the energy of electrons in the simulated events is applied with the relevant uncertainties.

6.3.3 Jets

Jets are reconstructed using the Anti-k_t jet clustering algorithm with a cone of $\Delta R = 0.4$ as described in Chapter 4 Section 4.4.2. Jet energy scale calibration factors as a function of p_T and η are applied to restore the full hadronic energy scale after passing through non-compensating calorimeters [72]. For such calibration, a simulated sample of inclusive QCD jet events was used with a level of pile-up corresponding to an average of eight interactions per bunch crossing and 75 ns bunch spacing within the bunch train. By default a pile-up correction is not included. A correction is applied to the jet position with respect to the primary vertex (or the beam spot if no primary vertex is found). The jet candidates are required to pass quality criteria in order to be used in the analysis. They must have:

- $p_{T,(EM+JES)} > 25$ GeV
- $|\eta_{(EM+JES)}| < 2.5$
- no overlap with an accepted electron. Jets are discarded if found in a cone of $\Delta R < 0.2$ with an electron
- a jet vertex fraction of $|JVF| > 0.75$. This cut is applied in order to reduce the effect of pile-up[4]

The jets passing these requirements are used for the $t\bar{t}$ event reconstruction. The

[4]The jet vertex fraction (JVF) quantifies the fraction of track transverse momentum associated to a jet from the hard-scattering interaction.

jets are also required to pass a set of criteria to identify the so-called "loose bad" jets. These jets are not associated to in-time real energy deposits in the calorimeters. They stem from various sources like hardware problems in the calorimeter, the LHC beam conditions, and the atmospheric muon-ray induced showers. The requirements for jets are applied to data and simulation. Whenever a "loose bad" jet is found, the whole event is rejected.

After selecting the jets in the event, the MV1 tagger, described in Chapter 5 Section 5.1.1, is applied to identify the *b*-tagged jets. A cut on the MV1 weight, corresponding to a ≈70% *b*-tagging efficiency and a *light*-jet rejection factor of ≈100, is applied, and thus, the corresponding data to simulation scale factors are also applied.

6.3.4 Missing Transverse Energy

The missing transverse energy definition used is MET_RefFinal_em_tight, described in Chapter 4 Section 4.5.1. E_T^{miss} is calculated using Eqs. 6.1 and 6.2.

$$E_{x,y}^{miss} = E_{x,y}^{miss,e} + E_{x,y}^{miss,jets} + E_{x,y}^{miss,softjets} + E_{x,y}^{miss,\mu} + E_{x,y}^{miss,CellOut} \tag{6.1}$$

$$E_T^{miss} = \sqrt{(E_x^{miss})^2 + (E_y^{miss})^2} \tag{6.2}$$

The most significant sources of uncertainty related to the E_T^{miss} come from the scale and resolution of the objects, the description of the pile-up events, and the impact of hardware failures [111]. Each of the objects in the E_T^{miss} calculation has an uncertainty related to the scale of resolution of the energy/p_T of the object. For the electrons, high p_T jets and muons, the uncertainties on the scale and resolution from the objects are propagated into the E_T^{miss} assuming a 100% correlation between the uncertainty on the objects and the E_T^{miss}. For the high p_T jets, the E_T^{miss} uncertainty also takes into account the jet efficiency uncertainty by reducing the jet contribution to the E_T^{miss} to the EM scale and properly includes the transition between EM and the hadronic scale at the $p_T = 20$ GeV boundary. For the SoftJet and CellOut terms, the main uncertainty comes from the energy scale of the topological clusters which is estimated in [111]. Therefore, the SoftJet and CellOut terms are scaled by their total uncertainty, ± 10.5% and ± 13.2% respectively, assuming a 100% correlation.

6.4 $t\bar{t}$ Event Selection

The event signature for the "lepton+jets" channel of a $t\bar{t}$ pair is four energetic jets, a lepton with large transverse momentum and a large transverse momentum im-

balance from the undetected neutrino coming from the W boson leptonic decay. Extra jets may appear in the event due to initial or final state radiations. To enhance the purity of the sample, jets from heavy flavor decays are *b*-tagged using the MV1 tagger.

The different event selection cuts are detailed in the following.

- The data events are required to pass the Top Good Run List criteria, which exclude data with bad quality and require all sub-detectors to be fully operational.

- A three level trigger for both electron and muon channels is required, detailed in Section 6.2.

- To suppress non collision backgrounds, the data and simulated events are required to have a well-defined and reconstructed primary vertex with at least five associated tracks. The tracks must have a $p_T > 0.4$ GeV.

- Events with Liquid Argon noise burst are discarded in data and simulated events, as discussed in Section 6.3.2.

- Events must have exactly one identified and isolated lepton, as defined in Section 6.3. This requirement insures an orthogonality between the lepton+jets and the di-lepton channels. The lepton is matched to the trigger that fired the event.

- The leptons and jets must not overlap:

    - Jets can be reconstructed as electrons. If a jet is found to be in a cone of $\Delta R_{jet,e} < 0.2$ with an electron, the jet is removed and not considered in the analysis.

    - Muons inside jets are mostly from semi-leptonic heavy flavor decays and thus are not isolated. A muon is removed from the event if it overlaps with any jet with $p_T > 20$ GeV and $|JVF| < 0.75$ within $\Delta R < 0.4$.

- Electrons and muons cannot overlap: an event is rejected if the electron and muon share an inner detector track.

- Events with at least one "loose bad" jet, discussed in Section 6.3.3, with p_T >20 GeV are rejected.

- Events must have a large missing transverse energy:
  - In the electron channel : $E_T^{miss} > 30$ GeV.
  - In the muon channel : $E_T^{miss} > 20$ GeV.

- A cut on the transverse mass of the leptonic W, $m_T(W)$ is required. The transverse mass $m_T(W)$ is defined as : $m_T(W) = \sqrt{2p_T^l p_T^\nu (1-\cos(\phi^l - \phi^\nu))}$, where p_T^l and ϕ^l are the transverse momentum of the lepton and it's azimuthal angle, and p_T^ν and ϕ^ν are the transverse momentum and the azimuthal angle of the neutrino, which are determined from the x and y components of the E_T^{miss} vector and the resulting azimuthal angle.
  - In the electron channel : $m_T(W) > 30$ GeV.
  - In the muon channel : $m_T(W) + E_T^{miss} > 60$ GeV.

- Events must have at least four well reconstructed jets, as defined in Section 6.3.3, with $p_T > 25$ GeV.

- Events must have at least one b-tagged jet with the MV1 tagger for an expected b-tagging efficiency of 70%.

The distribution of the jet multiplicity after all selection cuts listed above, with the exception of the cut on the number of jets and the number of b-tagged jets is shown in Fig. 6.1 for both muon and electron channels. The distribution of the lepton transverse momentum and its pseudorapidity are shown in Fig. 6.2 for both muon and electron channels, after all selection cuts were applied. The distributions of the E_T^{miss} as well as its x and y components are shown in Fig. 6.3, after all selection cuts were applied.

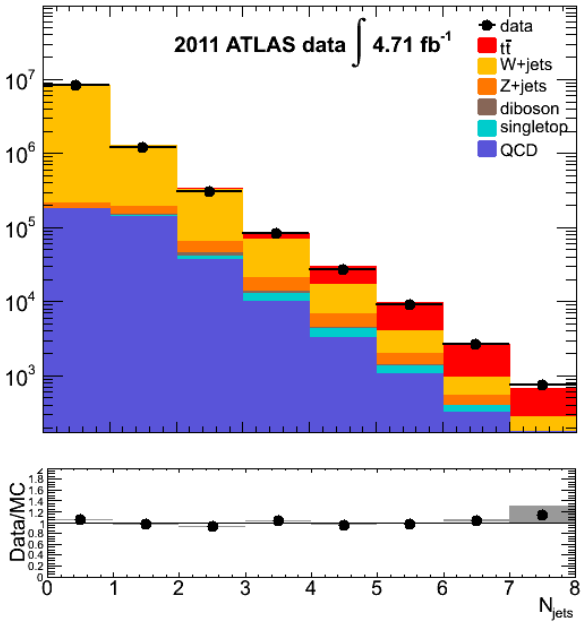

(a)

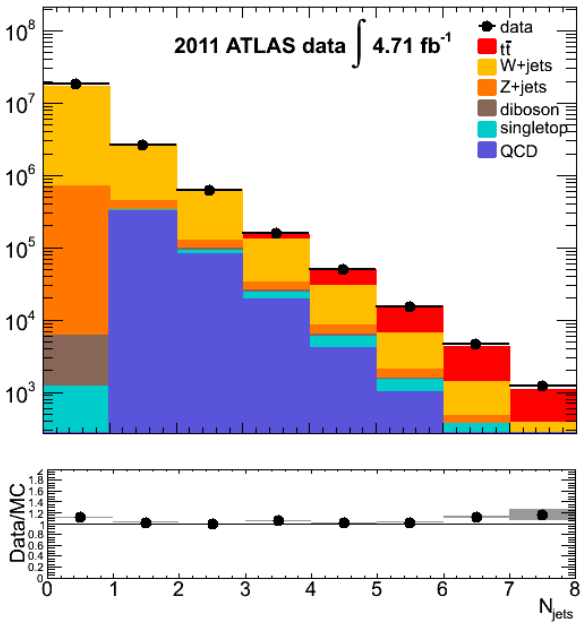

(b)

Figure 6.1: Distributions of jet multiplicity in electron (a) and the muon (b) channels. All event selection cuts outlined in Section 6.4 are applied, except the requirements on jet multiplicity and the number of *b*-tagged jets.

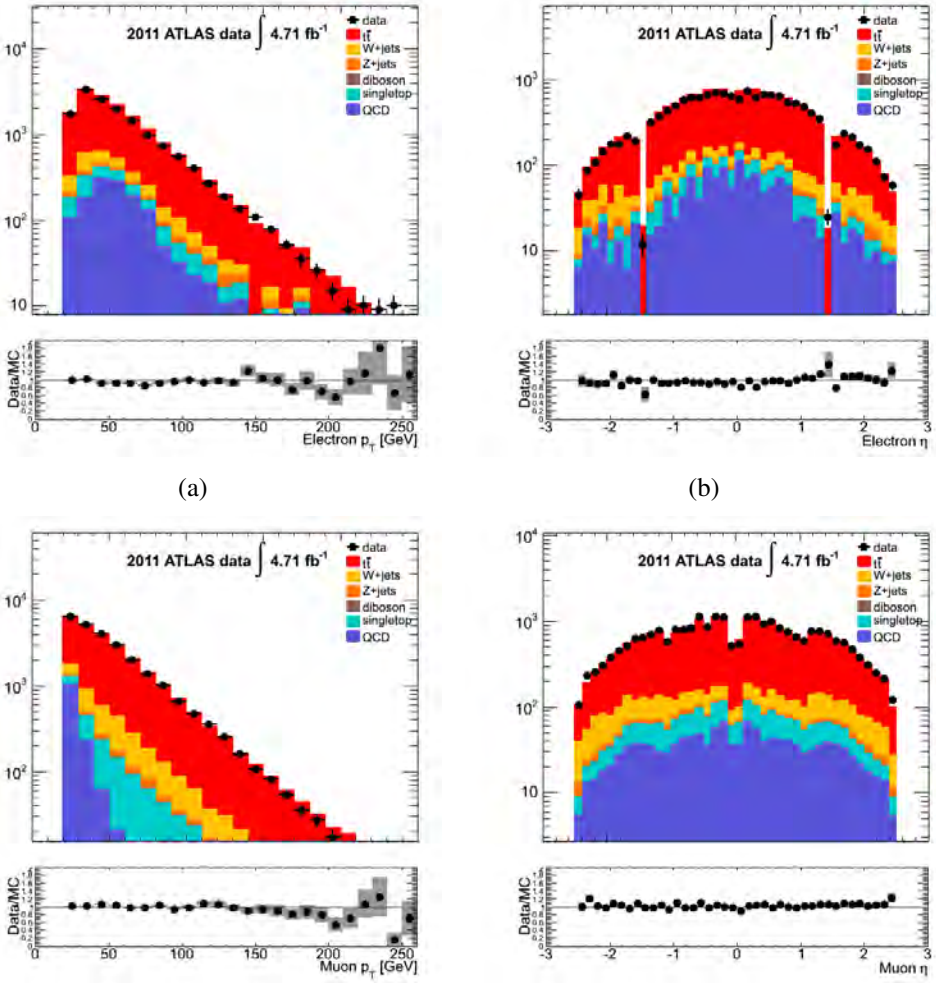

(a) (b)

(c) (d)

Figure 6.2: Distributions of the electron p_T (a) and the electron η (b), as well as the muon p_T (c) and the muon η (d) after all selection cuts. The data to simulation ratio is shown at the bottom of each plot.

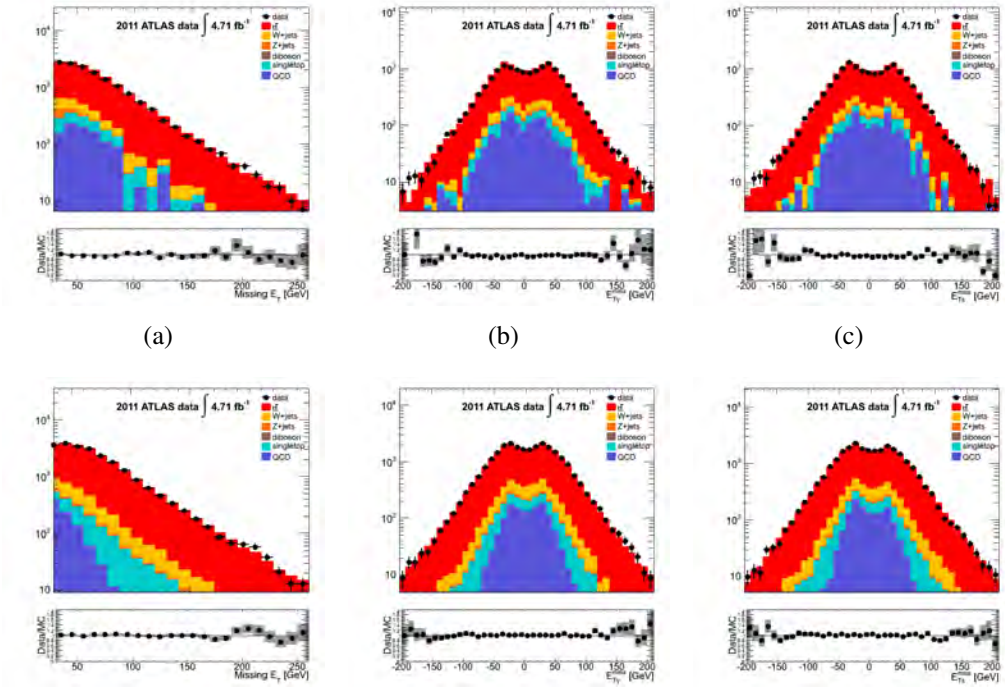

(a) (b) (c)

(d) (e) (f)

Figure 6.3: Distributions of the E_T^{miss} (a), $E_{T,x}^{miss}$ (b) and $E_{T,y}^{miss}$ (c) in the electron channel after all event selection cuts. The same distributions are also shown for the muon channel: (d), (e) and (f).

6.5 Background

Non $t\bar{t}$ processes which result in a final state similar to the lepton+jets channel are backgrounds and must be removed from the data sample. The main expected physics background in the selected lepton+jets sample described above is the W+jets, which can give rise to the same signature in the final state as the $t\bar{t}$ signal. The second main expected background is the QCD multi-jets events. This background, with multi-jets in its final state, contributes to the lepton+jets selected sample if there's an important missing transverse energy and at least one misidentified jet, reconstructed as a lepton, so-called "fake lepton". Fake leptons can also originate from non-prompt leptons from semi-leptonic decays of bottom or charm hadrons. The estimation of the W+jets and the QCD multi-jets backgrounds are detailed in Sections 6.5.1 and 6.5.2 respectively.

There are other backgrounds of electroweak nature: the single top quark, the diboson events (WW, WZ and ZZ) as well as the Z+jets production with $Z \to l^+l^-$ ($l = \tau, \mu, e$). These backgrounds are estimated using simulated samples described in Section 6.1.

6.5.1 W+Jets Background Estimation

The W+jets background is estimated using the combination of the ALPGEN samples described in Section 6.1. However, the overall normalization and the heavy flavor (HF) composition are not accurately known in simulation, hence a combination of MC and data driven corrections are applied to establish the background estimation. The charge asymmetry method is used to extract the overall normalization. The method exploits the asymmetrical cross sections for positively and negatively charged prompt leptons from W-boson decays and it is described in Section 6.5.1.1. The method used to extract the flavor scale factors that are applied to the W+jet Monte Carlo events (Wbb+jets, Wcc+jets, Wc+jets, and W+jets) is described in Section 6.5.1.2. The normalization and flavor scale factors, described in the following sections, are determined simultaneously. The total W+jet scale factors for each flavor component are the product of the overall W+jet scale factors and the flavor specific scale factors.

6.5.1.1 W+Jets Normalization

At the LHC, there is an overall charge asymmetry in the production of W bosons, with and without associated jets, due to relative differences in the quark and anti-quark parton distribution functions. Positively charged W-bosons can be produced from parton level processes such as $u\bar{d} \to W^+$ and $c\bar{s} \to W^+$ and depend upon

products of PDFs such as $u(x1)\bar{d}(x2)$. On the other hand, the production of W^--bosons from, for example, $d\bar{u} \rightarrow W^-$ depends upon the $d(x1)\bar{u}(x2)$ PDF products. As a proton contains more u than d valence quarks, one expects these PDF products to be different, hence there is a charge asymmetry.
Although the overall normalization is not well known from theoretical considerations, the ratio of W^+ to W^- can be determined with higher precision and can be used as a normalization constraint. Since signal and other background contributions are approximately charge symmetric, one can write:

$$N_{W^+} + N_{W^-} = \frac{N_{W^+}^{MC} + N_{W^-}^{MC}}{N_{W^+}^{MC} - N_{W^-}^{MC}}(D^+ - D^-) = \left(\frac{r_{MC}+1}{r_{MC}-1}\right)(D^+ - D^-) \tag{6.3}$$

where $D^+(D^-)$ are the total number of events selected in data with a positively (negatively) charged lepton, and $r_{MC} = \frac{\sigma(pp\rightarrow W^+)}{\sigma(pp\rightarrow W^-)}$. This normalization factor is measured as a function of jet multiplicity bins.

6.5.1.2 W+Heavy Flavor Normalization

In data, the W+jet events are obtained after subtracting the QCD events and all non-W+jets MC contributions, like the following:

$$N_W = N_{data} - N_{QCD} - N_{MC}^{non-W} \tag{6.4}$$

where the contribution of QCD (N_{QCD}) events is estimated as described in Section 6.5.2, using a data-driven method and the other background events are estimated using MC samples (N_{MC}^{non-W}). The background processes estimated using MC are Z+jet, single top, $t\bar{t}$, and diboson processes, which are normalized to their theory predictions. For each jet bin i the relation between the tagged and pretagged number of events is the following:

$$N_i^{W,tag} = N_i^{W,pretag}\left(F_{bb,i}P_{bb,i} + F_{cc,i}P_{cc,i} + F_{c,i}P_{c,i} + F_{light,i}P_{light,i}\right) \tag{6.5}$$

The quantities F_{bb}, F_{cc}, F_c and F_{light} represent the flavor fractions of the N_{bb} , N_{cc} , N_c and N_{light} events respectively, in the pretag sample, i.e. before applying the b-tagging requirement. The b-tagging probability for each W+jet flavor-type is denoted by $P_{xx,i}$ (with $xx = bb, cc, c, light$), separately for each jet bin i and is taken from MC simulation. On top of this an important constraint, for each separate jet bin, the flavor fractions sum to unity:

$$F_{bb,i} + F_{cc,i} + F_{c,i} + F_{light,i} = 1 \tag{6.6}$$

In Eq. 6.6, one can replace $F_{cc,i}$ by $k_{bb-to-cc}F_{bb,i}$ where $k_{bb-to-cc}$ stands for the ratio between the cc and the bb fractions taken from MC. Thus, for a 2-jet bin,

Eq. 6.6 becomes:

$$F_{bb,2} + k_{bb-to-cc}F_{bb,2} + F_{c,2} + F_{light,2} = 1 \tag{6.7}$$

and Eq. 6.5 is re-written as:

$$N_2^{W^\pm,tag} = N_2^{W^\pm,pretag}\left(F_{bb,2}P_{bb,2} + k_{bb-to-cc}F_{bb,2}P_{cc,2} + F_{c,2}P_{c,2} + F_{light,2}P_{light,2}\right) \tag{6.8}$$

The use of charge asymmetry is denoted with $\pm$ which means that the data is split into two sub-samples with negative and positive prompt lepton respectively. The fractions F_{bb}, F_c and F_{light} are then determined by the requirement that the number of tagged events in MC should be equal to the one in data, separately for events with positive and negative lepton, and, the requirement that all fractions add up to unity. With these fractions, the overall normalization is re-determined and this procedure is iterated until no significant change is observed. Finally, the flavor scale factors ($K_{xx,i}$) are defined as the ratio between the flavor fractions in data to those in the MC simulation:

$$K_{xx,i} = \frac{F_{xx,i}^{data}}{F_{xx,i}^{MC}} \tag{6.9}$$

The low jet multiplicity bin is dominated by W+jet production. The two jet bin is hence used to produce a set of K-factors between what is measured in data and what is seen in the Monte Carlo prediction. If the scale factors were the same in all jet multiplicity bins, one could simply use the set of scale factors derived from the 2 jet bin to apply them to higher jet multiplicity bins. However, this is not the case and hence the scale factors are renormalized to unity on a jet bin multiplicity basis.

6.5.2 QCD Multi-Jets Background Estimation

The QCD multi-jets background is estimated using a data driven method called the "Matrix Method" [112]. This method uses two lepton samples for each channel, one with looser selection with respect to the other, then measures the fraction of real (ε_{real}) and fake (ε_{fake}) loose leptons that pass the tight selection. The number of events which contain one loose lepton can be written as:

$$N^{loose} = N_{real}^{loose} + N_{fake}^{loose} \tag{6.10}$$

where N_{real}^{loose} and N_{fake}^{loose} are the number of events containing *real* and $fake$ leptons that pass the loose lepton selection. After applying the tight lepton criteria on the loose lepton sample, the number of events with tight leptons can be written as:

$$N^{tight} = \varepsilon_{real}N_{real}^{loose} + \varepsilon_{fake}N_{fake}^{loose} \tag{6.11}$$

where ε_{real} and ε_{fake} stand for the efficiency for real and fake loose leptons to pass the tight criteria. They are defined as:

$$\varepsilon_{real} = \frac{N_{real}^{tight}}{N_{real}^{loose}} \text{ and } \varepsilon_{fake} = \frac{N_{fake}^{tight}}{N_{fake}^{loose}} \tag{6.12}$$

Therefor, the number of events with fake leptons passing the tight selection can be expressed as :

$$N_{fake}^{tight} = \frac{\varepsilon_{fake}}{\varepsilon_{real} - \varepsilon_{fake}}(N^{loose}\varepsilon_{real} - N^{tight}) \tag{6.13}$$

ε_{real} and ε_{fake} should be significantly different so that the measurement can be done. ε_{real} is measured using the tag and probe method on Z boson decays to two leptons. The ε_{fake} is measured from control regions of di-jet events, where the contribution of fake leptons is significantly higher.

For the muon channel, the estimation of the QCD background is performed with two slightly different Matrix Methods [113]. For both methods, the loose sample is selected with the normal $t\bar{t}$ event selection described in Section 6.4, except for the muon isolation requirements. The tight selection is the same as the $t\bar{t}$ event selection. For the first method, called Matrix Method A, the signal efficiencies are determined with the tag and probe $Z \to \mu\mu$ method by selecting prompt muons from the Z decay, while for the second method, called Matrix Method B, the signal efficiency is simply derived from the Monte-Carlo samples of the physics processes producing prompt isolated muons. For the fake efficiency measurement, the first method estimates it from data in a low transverse W mass region with an inverted triangular cut: $m_T(W) < 20$ GeV and $m_T(W) + E_T^{miss} < 60$ GeV. While for the Matrix Method B, the fake efficiency is extrapolated from the ratio between loose and tight muons (the loose-to-tight efficiency) with high d_0 significance using the data sample. By counting the tight and loose muons with[5] d_0^{sign} larger than a given threshold x, a loose-to-tight efficiency function can be defined as : $\varepsilon(x) = \frac{\Sigma d_0^{sign} > x N^{tight}}{\Sigma d_0^{sign} > x N^{loose}}$.

For the electron channel, the QCD multi-jets background is estimated using one Matrix Method, where the loose sample is obtained by relaxing the isolation requirements for the electrons: the calorimeter and the track isolation cut is required to be less than 6 GeV instead of 90% value, after correcting for energy deposits from pile-up interactions. The real efficiencies are derived from the tag

[5]The impact parameter has already been defined in Chapter 5 and it is shown in Fig. 5.2.

Cut	$t\bar{t}$	Single top	W+jets	Z+jets	Diboson	QCD	Total	Data
Pretag Sample	19318	1399	12478	2885	236	4029	40345	39486
MV1tag Sample	16619	1117	2015	450	47	2021	22269	21300
$L > -52$	12345	626	947	223	25	1335	15501	14611

Table 6.7: Data and background yields after selection cuts before and after applying the MV1 *b*-tagging requirement, in the electron channel. The likelihood cut is described in Section 6.6.

Cut	$t\bar{t}$ *l*+jets	Single top	W+jets	Z+jets	Diboson	QCD	Total	Data
Pretag Sample	31948	2342	26603	2624	387	5603	69507	68109
MV1tag Sample	27467	1867	4043	444	76	2117	36014	36522
$L > -52$	20465	1047	1930	221	42	1331	24135	25382

Table 6.8: Data and background yields after selection cuts before and after the MV1 *b*-tagging requirement, in the muon channel. The likelihood cut is described in Section 6.6.

and probe method with a data sample of $Z \rightarrow ee$. The fake efficiencies are estimated in a sample with at least one jet ($p_T > 25$ GeV) and exactly one loose lepton. In order to enhance the sample in QCD jets, the fake efficiencies are measured in a control region with $E_T^{miss} < 20$ GeV.

In both channels contributions from W+jets and Z+jets backgrounds in the control region, estimated using Monte Carlo simulation, are subtracted. Control plots sensitive to the QCD background (the transverse W mass cut have been relaxed) are shown in Figure 6.4.

Given the event selection criteria outlined in Section 6.4 as well as the background treatment discussed in this section, the cut flow for the inclusive number of selected data events and the number of expected events are shown in Table 6.7 for the electron channel, and in Table 6.8 for the muon channel. The pretagged sample is the sample before the *b*-tagging requirement, while the MV1 tag sample is after applying it. The cut $L > -52$ is described in Section 6.6.

6.6 $t\bar{t}$ Event Reconstruction

Once the preselection is performed, each event contains exactly one isolated lepton with $E_T > 25$ GeV for the electrons and $p_T > 20$ GeV for the muons, at least four jets with $p_T > 25$ GeV among which at least one reconstructed *b*-tagged jet and high missing transverse energy. To reconstruct a $t\bar{t}$ system, an algorithm KL-

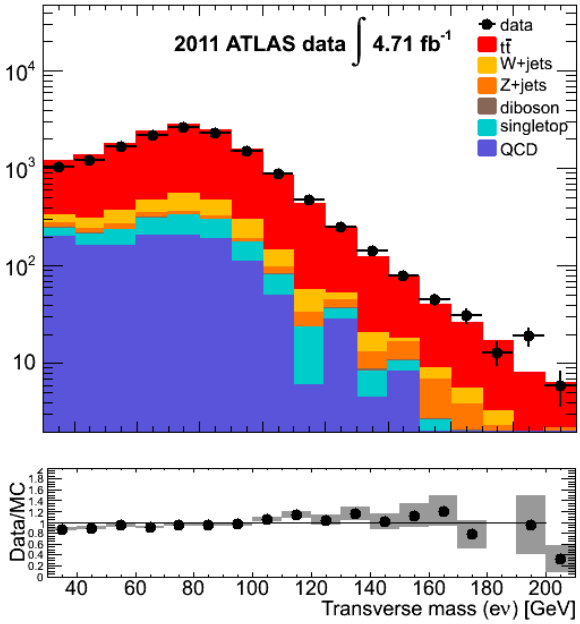

(a)

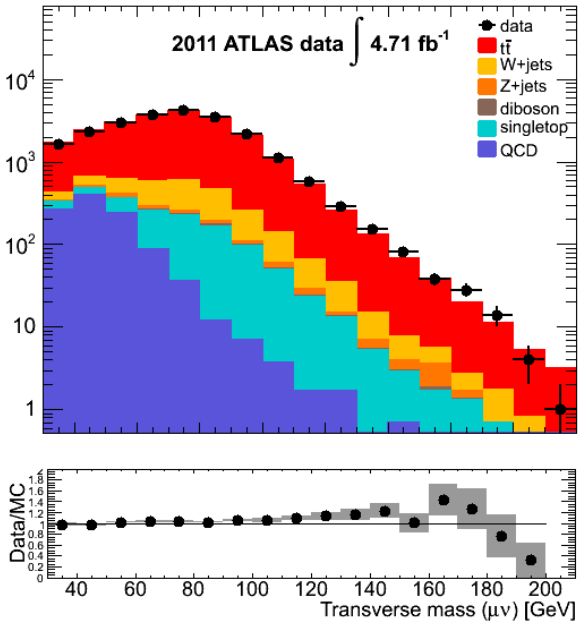

(b)

Figure 6.4: Transverse mass of the W boson leptonically decaying, after the preselection for the electron channel (a) and for the muon channel (b). These distributions have been made without applying the cut on the $m_T(W)$.

Fitter [114] is used. KLFitter performs a kinematical likelihood fit to relate the observed objects to parton level predictions from Monte Carlo signal in a leading-order picture. The likelihood is the product of a model-derived factor times a detector related one. The model derived factor consists of four Breit-Wigner distributions for the two top quark and the two W boson masses from the $t\bar{t}$ decay, expressed as function of the four momenta of the final state of six-particle system. The detector-related factor is a set of transfer functions (TFs) representing the conditional probability to obtain a measured value for the energies of four jets (two b-jets and two $light$-jets), the energy of the lepton and the transverse x and y components of the neutrino, given their true values. The transfer functions (TF) are derived from the $t\bar{t}$ simulated MC@NLO signal samples based on reconstructed objects that are uniquely matched to their parent partons in a ΔR cone of 0.3. They are parameterized by double-Gaussian functions and they are obtained for energies and angles of light jets and b-jets, the energy of the charged lepton, and the two components of the E_T^{miss}. The unconstrained z component of the neutrino momentum is a free parameter in the fit. The likelihood is defined as follows:

$$\begin{aligned} L \;=\; & BW(\hat{E}_{jet,1},\hat{E}_{jet,2}|m_W\Gamma_W).BW(\hat{E}_l,\hat{E}_\nu|m_W\Gamma_W). \\ & BW(\hat{E}_{jet,1},\hat{E}_{jet,2},\hat{E}_{jet,3}|m_{top}^{reco}\Gamma_{top}).BW(\hat{E}_l,\hat{E}_\nu,\hat{E}_{jet,4}|m_{top}^{reco}\Gamma_{top}). \\ & TF(\hat{E}_x^{miss}|\hat{p}_{x,\nu}).TF(\hat{E}_y^{miss}|\hat{p}_{y,\nu}).TF(\hat{E}_l|\hat{p}_l). \\ & \prod_{i=1}^{4} TF(E_{jet,i}|\hat{E}_{jet,i}).\prod_{i=1}^{4} TF(\eta_{jet,i}|\hat{\eta}_{jet,i}). \\ & \prod_{i=1}^{4} TF(\phi_{jet,i}|\hat{\phi}_{jet,i}).\delta(b-tagged\,jet|b-quark) \end{aligned} \tag{6.14}$$

The parton level objects are labeled with a hat like for example $\hat{E}_{jet,i}$. m_W is the known W boson mass, and m_{top}^{reco} is the estimator for the top-quark mass, i.e. the result, per event, of maximizing this kinematical likelihood. The kinematical likelihood exploits the known values of m_W (80.4 GeV) and Γ_W (2.1 GeV) to constrain the reconstructed leptonic and hadronic W boson masses using Breit-Wigner (BW) distributions. Similarly, the reconstructed leptonic and hadronic top-quark masses are constrained to be identical, and the width of the corresponding BW distribution is identified with the predicted Γ_{top} corresponding to $m_{top} = 172.5$ GeV. The inclusion of the b-tagging information as a delta function restricts the number of permutations investigated per event. It improves the ability to select the correct jet permutation.

For each possible assignment of the four jets to their partonic origin hypothesis, a maximum likelihood value is derived. If the event contains more than four jets, the assignment is done among the five jets with the highest transverse

momentum. The distributions of the p_T and η of all the selected jets from the reconstructed $t\bar{t}$ events are shown in Fig. 6.5 and 6.6 for the muon and the electron channels respectively.

The probability of each four-jet combination is weighted with the product of four factors: each factor corresponds to the b-tagging efficiency, if the jet is b-tagged, or inefficiency in the opposite case, for one of the jets given its p_T and η. The efficiencies and rejection rate correspond to the MV1 b-tagging working point being used in the analysis which corresponds to a 70% b-tagging efficiency. The combinations where one or two b-tagged jets are assigned to light-quarks have reduced, but non zero, probability. Events with more than two b-tagged jets are kept and treated like the following: each jet combination is assigned a likelihood times the b-tagging related weighting factor. The distribution of the number of b-tagged jets per event is shown in Fig. 6.7 for the electron and the muon channel.

The jet assignment with the largest maximum likelihood value is retained to estimate the momenta of the $t\bar{t}$ decay products. The top quarks four momentum is then obtained by summing the four momenta of the assigned estimates of their decay products: the b-quark and the two $light$-jets from the hadronic top quark, then the lepton, the neutrino and the b-quark from the leptonic top quark. The $t\bar{t}$ four-momentum is obtained by summing the two reconstructed top quarks four momenta: the values of $M_{t\bar{t}}$ and $y_{t\bar{t}}$ are obtained according to the standard definitions in relativistic kinematics. The $t\bar{t}$ event reconstruction with the KLFitter algorithm has a 100% efficiency, i.e. no events are removed by the fit. Since no events are removed by the fit, the sample still contains non-correctly reconstructed $t\bar{t}$ events that will make the unfolding of the detector effects difficult. A cut on the $t\bar{t}$ likelihood fit is applied to enhance the fraction of correctly reconstructed $t\bar{t}$ events. This cut is supported by the good modeling of the likelihood shown in Fig. 6.8.

The cut is applied at $L > -52$. Simulations clearly show that this cut rejects a distinct region where a large fraction of the events are badly reconstructed as one can see in Fig. 6.9. Fig. 6.9 shows a two dimensional histogram of the reconstructed $t\bar{t}$ mass versus the KLFitter likelihood function, when the reconstructed $t\bar{t}$ mass using the KLFitter algorithm lies within 50% of the generated $t\bar{t}$ mass (electron channel Fig. 6.9 (a) and muon channel Fig. 6.9 (c)), and when the the reconstructed $t\bar{t}$ mass lies more than 50% away from the generated $t\bar{t}$ mass (electron channel Fig. 6.9 (b) and the muon channel Fig. 6.9 (d)). One can clearly see that when cutting on the $L > -52$, one discards most of the reconstructed $t\bar{t}$ events, when the reconstructed $t\bar{t}$ mass lies more than 50% away from the generated $t\bar{t}$ mass.

The final $t\bar{t}$ mass ($M_{t\bar{t}}$) and rapidity ($y_{t\bar{t}}$) distributions before background subtraction and unfolding are shown in Fig. 6.10 and Fig. 6.11. The binning choice and optimization are described in Section 6.7.1.

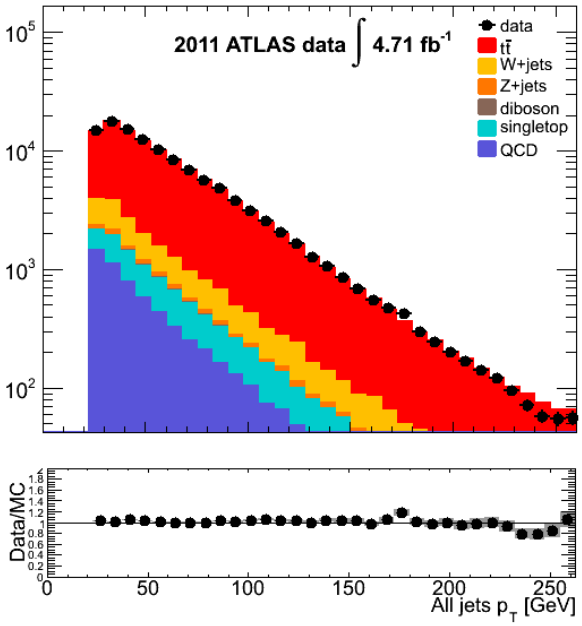

(a)

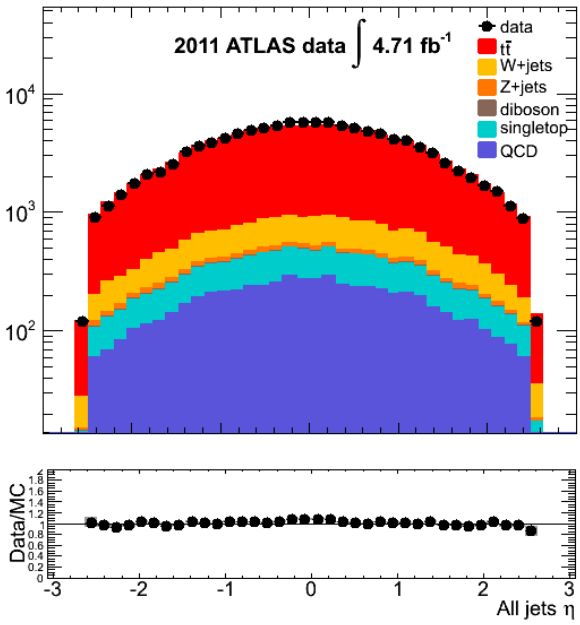

(b)

Figure 6.5: Distributions of the transverse momentum (a) and the pseudorapidity (b) of all the jets after the selection in the muon channel. The data to simulation ratio is shown at the bottom of each plot.

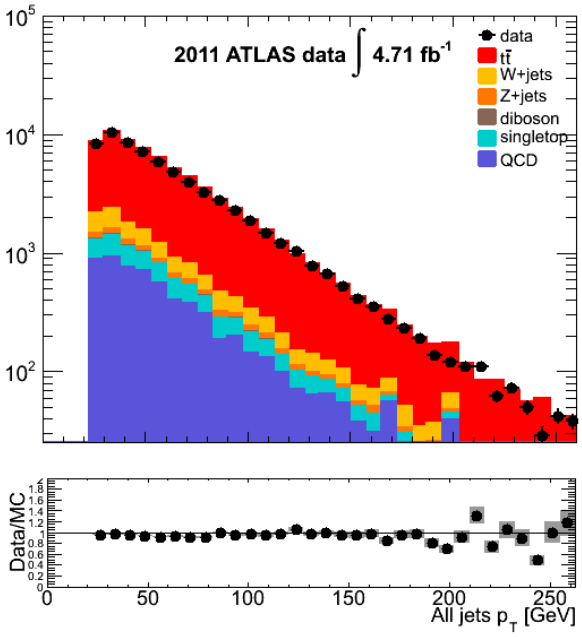

(a)

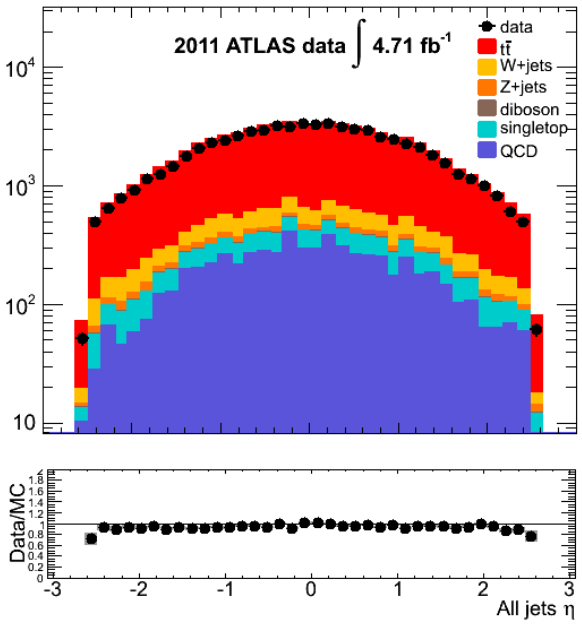

(b)

Figure 6.6: Distributions of the transverse momentum (a) and the pseudorapidity (b) of all the jets after the selection in the electron channel. The data to simulation ratio is shown at the bottom of each plot.

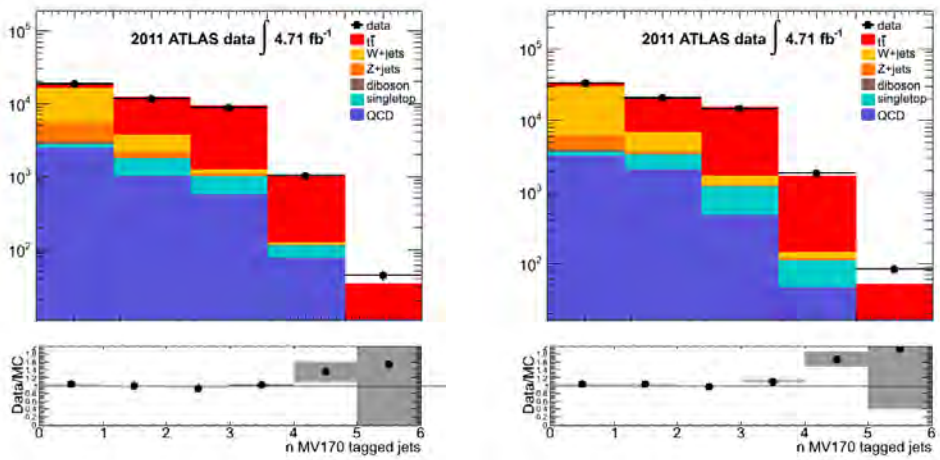

(a) (b)

Figure 6.7: Number of *b*-tagged jets per event in the electron channel (a) and the muon channel (b), after all event selection cuts were applied except the requirement on the number of *b*-tagged jets. The last two bins suffer from low MC statistics, hence the large statistical error bars.

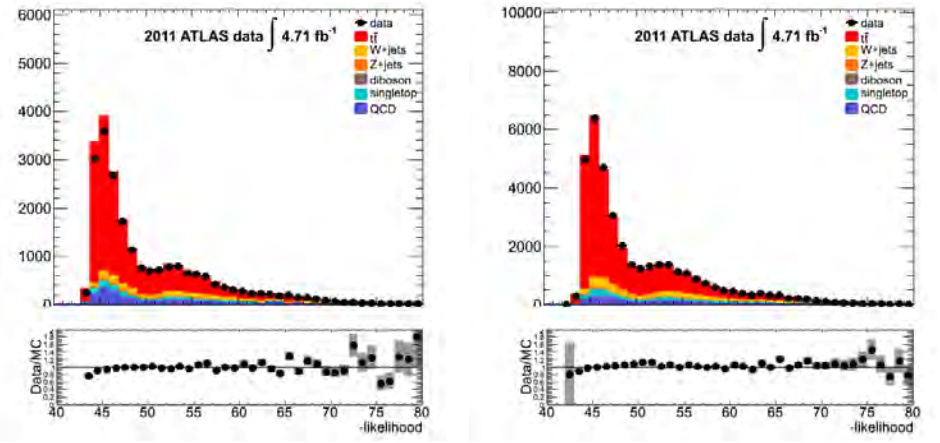

(a) (b)

Figure 6.8: Distribution of -log(likelihood) in the electron channel (a) and the muon channel (b).

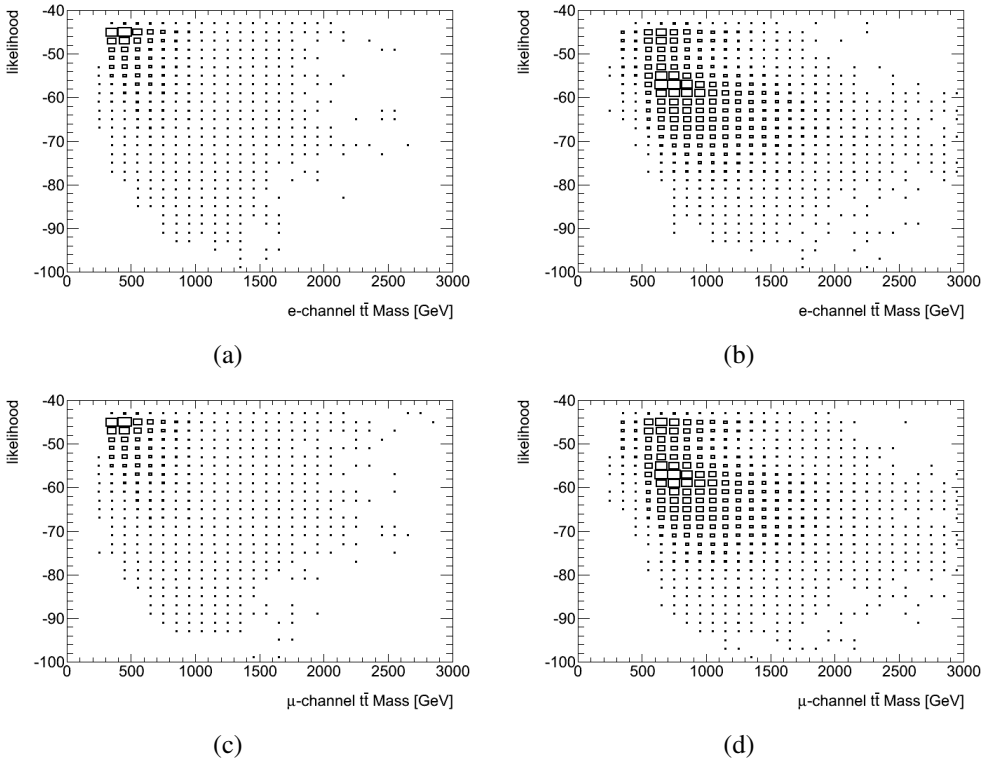

Figure 6.9: Likelihood from kinematic fitting for simulated $t\bar{t}$ events with reconstructed $t\bar{t}$ mass, $M_{t\bar{t}}$, lying within 50% of the generated $t\bar{t}$ mass as a function of the generated $t\bar{t}$ mass selected in the electron channel (a) and the muon channel (c). The same correlation is shown for simulated $t\bar{t}$ events selected in the electron channel (b) and the muon channel (d) with reconstructed $t\bar{t}$ mass lying more than 50% away from the generated $t\bar{t}$ mass.

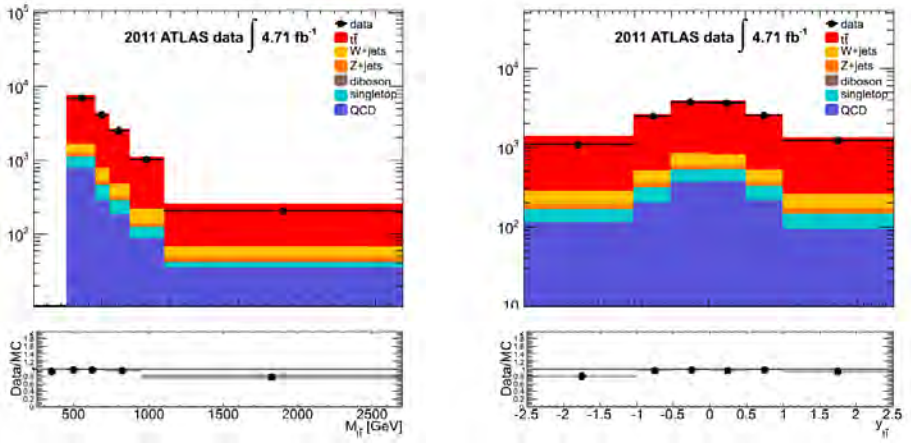

(a) (b)

Figure 6.10: Distribution of the $t\bar{t}$ mass, $M_{t\bar{t}}$ (a) and the $t\bar{t}$ rapidity, $y_{t\bar{t}}$ (b) in the electron channel, after applying all selection cuts including the cut on the likelihood, before any background subtraction or unfolding.

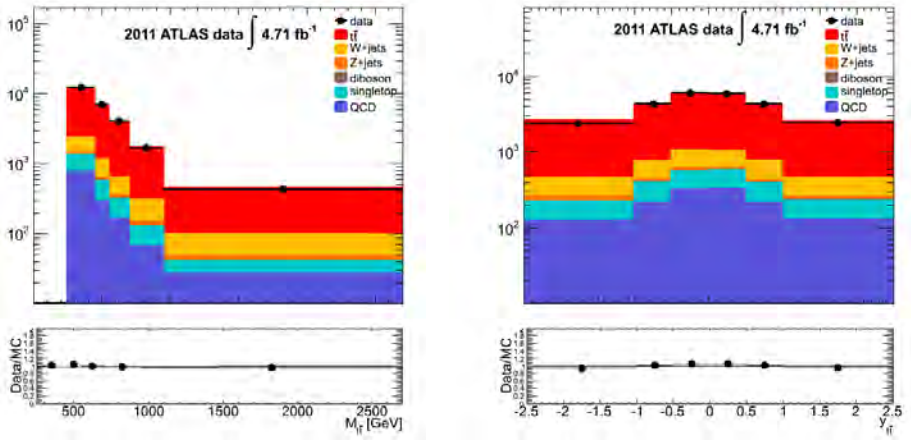

(a) (b)

Figure 6.11: Distribution of the $t\bar{t}$ mass, $M_{t\bar{t}}$ (a) and the $t\bar{t}$ rapidity, $y_{t\bar{t}}$ (b) in the muon channel, after applying all selection cuts including the cut on the likelihood, before any background subtraction or unfolding.

6.7 Cross Section Unfolding

The reconstruction of the $t\bar{t}$ system described in Section 6.6, achieves high resolution by constraining the kinematics of the final state to the kinematics of the lepton+jets decay of the $t\bar{t}$ pair. While a higher resolution on $M_{t\bar{t}}$ leads to stricter limits on physics beyond the SM, it is important to not over-constrain the system with an algorithm that makes every input look like the SM.

It is also important to consider the interpretation of results. In general the raw $M_{t\bar{t}}$ distribution that is obtained from the four momentum of the physics objects in the event is detector-dependent in the sense that the resolution of objects is detector-specific. Especially if a significant distortion of the expected $M_{t\bar{t}}$ spectrum is found, a detector-dependent $M_{t\bar{t}}$ spectrum will be very difficult to interpret theoretically. Fig. 6.12 shows a 2-dimensional histogram of $M_{t\bar{t}}^{true}$ versus the reconstructed $M_{t\bar{t}}$ as defined in Section 6.6. Generally values of $M_{t\bar{t}}$ correspond to values near $M_{t\bar{t}}^{true}$, but there is also significant spread. For example, if a resonance is found in the region of $M_{t\bar{t}} = 600$ GeV/c^2, it could be coming from values of $M_{t\bar{t}}^{true}$ from 400 to 950 GeV/c^2. The quality of jet reconstruction and missing energy reconstruction in particular determine the degree of migration from $M_{t\bar{t}}^{true}$ to $M_{t\bar{t}}$, and those quantities are detector-dependent. The challenge of $M_{t\bar{t}}$ reconstruction is to balance the need for a meaningful partonic-level measurement with the desire to maintain sensitivity to physics beyond the SM. This is the importance of the unfolding which corrects the $M_{t\bar{t}}$ distribution to $M_{t\bar{t}}^{true}$, so the results can be easily compared to SM predictions and theoretical predictions for various beyond the SM physics processes. The unfolding technique used in this analysis is described in Section 6.7.1.

6.7.1 Unfolding Technique

The cross section measured in a bin i is defined as follows:

$$\sigma_{t\bar{t}}^{i} = \frac{N_{obs}^{i} - N_{BG}^{i}}{BR \cdot A^{i} \cdot L} \tag{6.15}$$

where N_{obs}^{i} is the total number of observed events in data that pass all selection cuts, N_{BG}^{i} is the expected number of background events estimated from simulation or from data as described in Section 6.5, BR is the non all hadronic branching fraction ($BR(t\bar{t} \rightarrow l + jets) = 0.543$ [88]), A^{i} is the acceptance for the electron or the muon channel to non all hadronic events and L is the total integrated luminosity which is 4.71 fb^{-1} after the GRL selection. The underlying binned true cross section distributions $\sigma_{t\bar{t}}^{j}$ are obtained from the reconstructed events using an unfolding technique that corrects for detector effects. The unfolding uses a response matrix R_{ij} derived from $t\bar{t}$ simulations, which maps the binned true events to the

binned reconstructed events. The kinematic properties of the generated $t\bar{t}$ partons in simulated $t\bar{t}$ events define the "true" properties of the $t\bar{t}$ events. In its simplest form the unfolding equation can be written as:

$$N^i_{obs} = R_{ij} \cdot \sigma^j_{t\bar{t}} \cdot L + N^i_{BG} = M_{ij} \cdot A_j \cdot BR\sigma^j_{t\bar{t}} \cdot L + N^i_{BG} \tag{6.16}$$

The underlying binned true cross section is determined by solving the equation 6.16:

$$\sigma^j_{t\bar{t}} = \frac{M^{-1}_{ij}(N^i_{obs} - N^i_{BG})}{BR \cdot A_j \cdot L} \tag{6.17}$$

where M^{-1}_{ij} is the inverted migration matrix. M^{-1}_{ij} is calculated from: $M^{-1}_{ij} \cdot M_{ij} = I$ where I is the identity matrix. The migration matrices in the electron and the muon channel are shown in Fig. 6.12 for the $t\bar{t}$ mass and in Fig. 6.13 for the $t\bar{t}$ rapidity. The inverted migration matrices in the electron and the muon channel are shown in Fig. 6.14 for the $t\bar{t}$ mass and in Fig. 6.15 for the $t\bar{t}$ rapidity. The acceptance to non all hadronic $t\bar{t}$ events for the electron and muon channels are shown in Fig. 6.16 for the $t\bar{t}$ mass and in Fig. 6.17 for the $t\bar{t}$ rapidity.

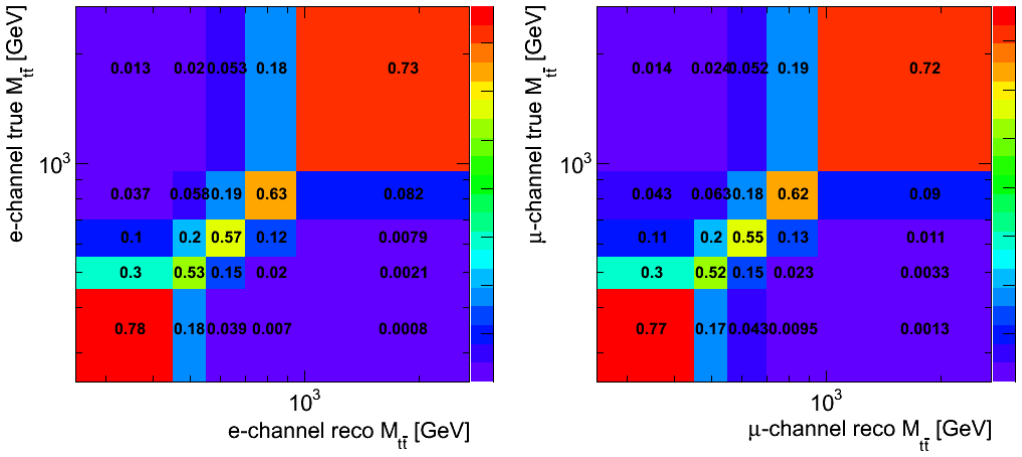

(a) (b)

Figure 6.12: Migration matrices for the $M_{t\bar{t}}$ in the electron (a) and the muon (b) channels, determined from simulated non-hadronic $t\bar{t}$ events passing all e + jets and muon + jets selection cuts. The unit is probability for true events migrating to reconstructed events.

The bin size has been optimized using pseudo-experiments with only simulated events including systematic uncertainties. The optimization strategy has been to chose as small bin size as possible without substantially deteriorate the total uncertainty. This effectively means keeping about 68% of the events in the

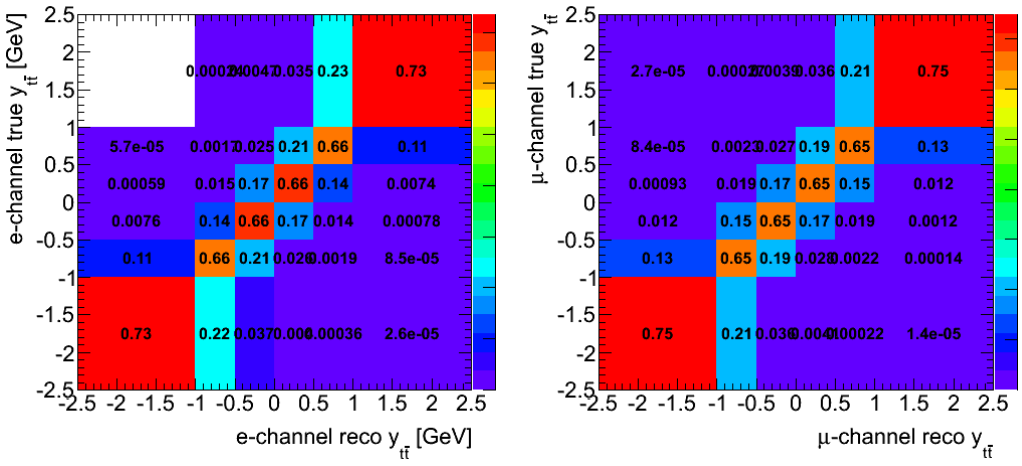

(a) (b)

Figure 6.13: Migration matrices for the $y_{t\bar{t}}$ in the electron (a) and the muon (b) channels, determined from simulated non-hadronic $t\bar{t}$ events passing all e + jets and muon + jets selection cuts. The unit is probability for true events migrating to reconstructed events.

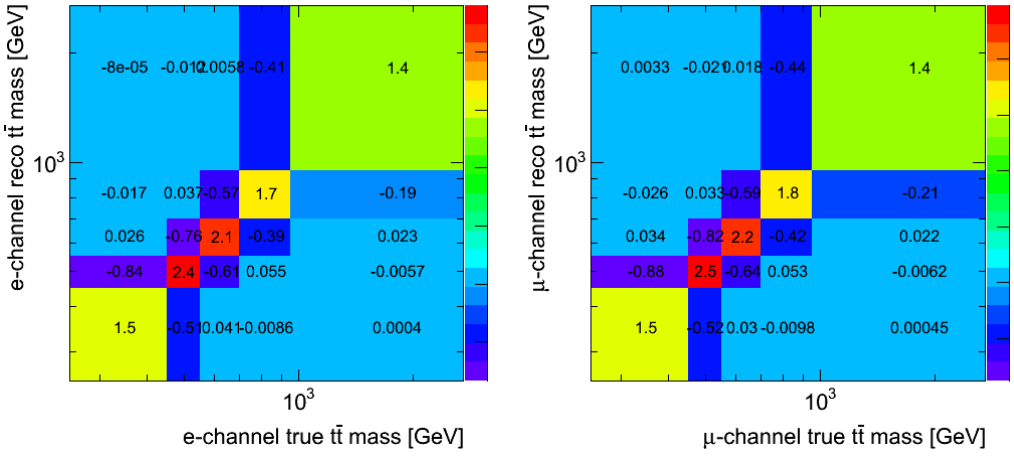

(a) (b)

Figure 6.14: Inverted Migration matrices for the $M_{t\bar{t}}$ in the electron (a) and the muon (b) channels, determined from simulated non-hadronic $t\bar{t}$ events passing all e + jets and muon + jets selection cuts. The unit is migration weight for reconstructed events to unfold back to true events.

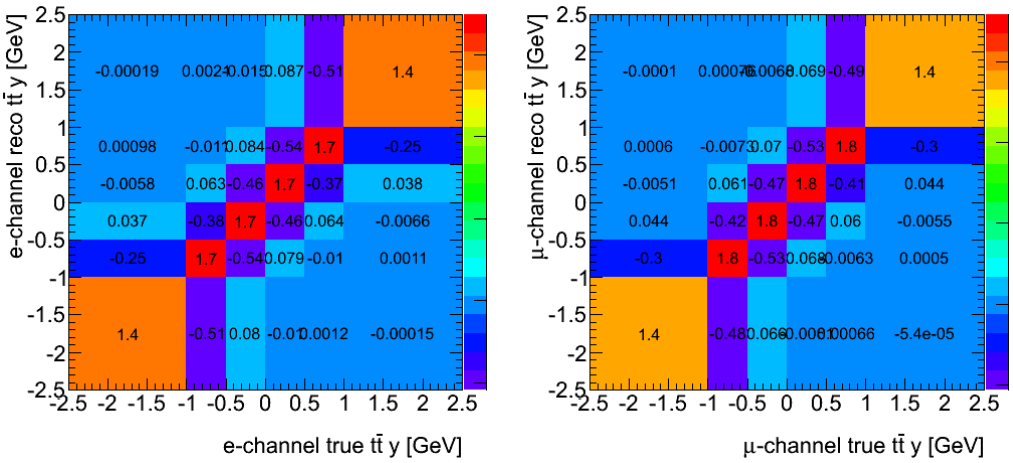

(a) (b)

Figure 6.15: Inverted Migration matrices for the $y_{t\bar{t}}$ in the electron (a) and the muon (b) channels, determined from simulated non-hadronic $t\bar{t}$ events passing all e + jets and muon + jets selection cuts. The unit is migration weight for reconstructed events to unfold back to true events.

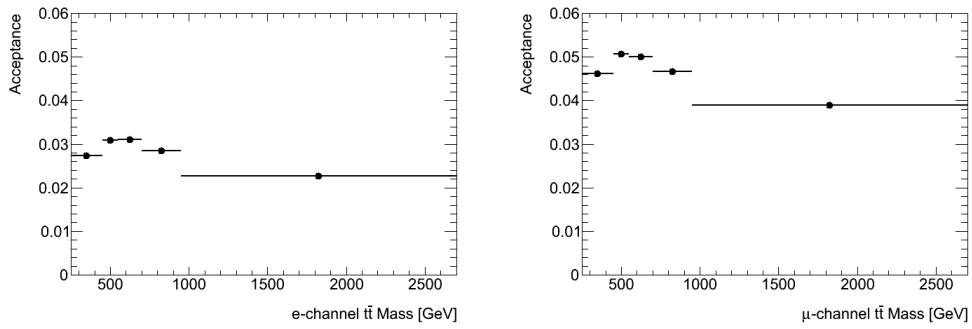

(a) (b)

Figure 6.16: Signal acceptance estimated from simulated non-hadronic $t\bar{t}$ events passing all electron + jets (a) and muon + jets (b) selection cuts binned as a function of generated $M_{t\bar{t},gen}$.

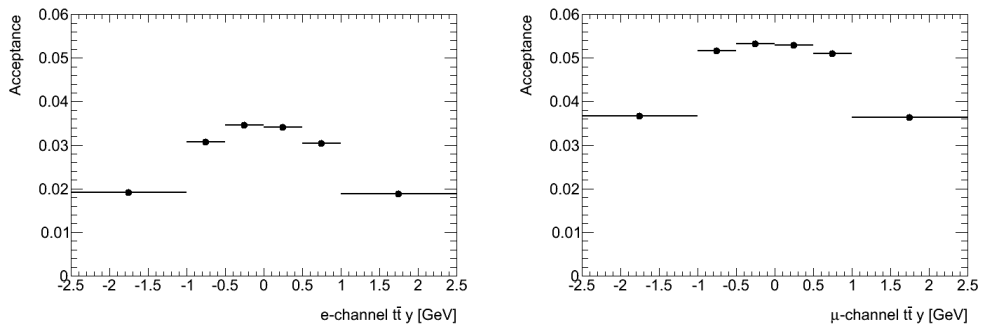

(a) (b)

Figure 6.17: Signal acceptance estimated from simulated non-hadronic $t\bar{t}$ events passing all electron + jets (a) and muon + jets (b) selection cuts binned as a function of generated $y_{t\bar{t},gen}$.

diagonal of the migration matrix. To evaluate the performance of the unfolding procedure, and to estimate the correlated uncertainties, the conceptual equation 6.17 has been extended to the following form to allow detailed studies using pseudo-experiments:

$$\sigma^{j}_{t\bar{t}}(d_k) = \frac{M^{-1}_{ij}(d_k)[P_0(N^{i}_{obs}) - N^{i}_{BG}]}{BR \cdot A_j(d_k) \cdot L(d_k)} \tag{6.18}$$

where $Po()$ is the Poisson process, and d_k are systematic sources normalized to the unit of one sigma drawn from a Gaussian distribution. The different systematic sources are detailed in Section 6.8. A cross section estimate is extracted for a given variable, $M_{t\bar{t},gen}$ or $y_{t\bar{t},gen}$ from each pseudo-experiment. The median of the results from the pseudo-experiments and their 68% interval provide the cross section estimate and its uncertainty. Data is treated in the same manner as simulated events. The parametric dependence on d_k in M^{-1}_{ij}, and other functions, is approximated using the first linear term in the Taylor expansion, treating positive and negative derivate estimates separately. Folding followed by unfolding closure tests on simulated events is evaluated by setting all $d_k = 0$ and checking the deviation of the unfolded cross section to the known true cross section input used for the detector simulation folding. Tables 6.9 and 6.10 show the unfolded cross sections on simulated events using equation 6.18 when setting d_k to 0. The integrated cross section is also derived by using equations 6.17 and 6.18 for the one bin case consisting of all the events passing the selection cuts. Such measurement is performed for both data and for the pseudo-experiments that are used to assess systematic uncertainties. Tables 6.11 and 6.12 show the true cross section as reported by the generator in each bin of the $t\bar{t}$ mass and rapidity respectively. The

two Tables, 6.13 and 6.14, show the average difference in % between the measured unfolded cross section in simulation and the true cross section as reported by the generator, for the $M_{t\bar{t}}$ and $y_{t\bar{t}}$ respectively.

$M_{t\bar{t}}$ [GeV]	$d\sigma/dM_{t\bar{t}}$[fb/GeV] (e+jets)	$d\sigma/dM_{t\bar{t}}$[fb/GeV] (μ+jets)
250 - 450	399^{+9}_{-10}	400^{+8}_{-8}
450 - 550	488^{+21}_{-20}	483^{+16}_{-16}
550 - 700	170^{+10}_{-9}	172^{+8}_{-8}
700 - 950	41^{+4}_{-3}	40^{+3}_{-3}
950 - 2700	$1.4^{+0.2}_{-0.2}$	$1.4^{+0.2}_{-0.2}$

Table 6.9: Extracted cross sections from simulated events in each bin of the $t\bar{t}$ mass, using pseudo experiments including folding with full detector simulation, followed by the unfolding procedure, to be compared to the true cross sections in Table 6.11. The integrated cross section is measured in the same way as the differential measurement but contracted down to one bin over the whole range of mass. It is found to be 166.5 $\pm$ 3.295 pb in the electron channel and 166.6 $\pm$ 2.635 pb in the muon channel.

6.7.2 Channel Combination

The unfolded cross sections from the electron and the muon channels, are combined using a weighted mean which includes the full covariance matrix between the two channels [115]. Since the covariance matrix is used in the weighting, it means that the estimate is a best linear unbiased estimator (BLUE) of the cross section. Thus this combination is a linear function of the data, unbiased, and has the smallest variance among all unbiased linear estimators. The covariance matrix is measured in simulated events using the same pseudo experiment setup outlined in the previous section and derived from equation 6.18.

6.8 Systematic Uncertainties

Systematic uncertainties arise from uncertainties in the Monte Carlo modeling of the $M_{t\bar{t}}$ and the $y_{t\bar{t}}$ shape in signal and background, modeling of the acceptance, the estimation of the data sample composition and the uncertainty on the integrated luminosity of the data sample. For each systematic effect, the complete

y	$d\sigma/dy$[pb] (e+jets)	$d\sigma/dy$[pb] (μ+jets)
-2 - -1	$15^{+0.7}_{-0.7}$	$16^{+0.5}_{-0.5}$
-1 - - 0.5	53.0^{+2}_{-2}	53^{+2}_{-2}
-0.5 - 0	68^{+3}_{-3}	68^{+2}_{-2}
0 - 0.5	68^{+3}_{-3}	68^{+2}_{-2}
0.5 - 1	53^{+2}_{-3}	53^{+2}_{-2}
1 - 2	15^{+1}_{-1}	16^{+1}_{-1}

Table 6.10: Extracted cross sections from simulated events in each bin of the $t\bar{t}$ rapidity, using pseudo experiments including folding with full detector simulation, followed by the unfolding procedure, to be compared to the true cross sections in Table 6.12. The integrated cross section is measured in the same way as the differential measurement but contracted down to one bin over the whole range of rapidity. It is found to be 166.9 $\pm$ 2.991 pb in the electron channel and 167 $\pm$ 2.297 pb in the muon channel.

$M_{t\bar{t}}$ [GeV]	$d\sigma/dM_{t\bar{t}}$[fb/GeV] (e+jets)	$d\ sigma/dM_{t\bar{t}}$[fb/GeV] (μ+jets)
250 - 450	$405.60^{+0.04}_{-0.04}$	$405.60^{+0.05}_{-0.05}$
450 - 550	$464.81^{+0.05}_{-0.05}$	$464.81^{+0.07}_{-0.07}$
550 - 700	$175.23^{+0.03}_{-0.03}$	$175.23^{+0.03}_{-0.03}$
700 - 950	$41.47^{+0.01}_{-0.01}$	$41.47^{+0.01}_{-0.01}$
950 - 2700	$1.434^{+0.001}_{-0.001}$	$1.434^{+0.001}_{-0.001}$

Table 6.11: True $t\bar{t}$ cross sections in each bin of the mass as reported by the generator. The integrated cross section is 166.7 $\pm$ 0.013 pb

analysis is re-run with the variation considered to estimate the one standard deviation (σ) change in each bin of the variable of interest due to the specific effect. A new background-subtracted distribution for the $M_{t\bar{t}}$ and the $y_{t\bar{t}}$ is derived corresponding to such deviation after re-running the full analysis from the selection to the reconstruction with the kinematic fitter. The varied distributions are obtained for the upward and downward variation of the variable of interest for each effect and for each of the two leptonic channels separately. If the direction of the variation is not defined (as in the case of the estimate resulting from the difference of

y	$d\sigma/dy$[pb] (e+jets)	$d\sigma/dy$[pb] (μ+jets)
-2 - -1	$15^{+0.002}_{-0.002}$	$15^{+0.003}_{-0.003}$
-1 - -0.5	$53^{+0.01}_{-0.01}$	$53^{+0.01}_{-0.01}$
-0.5 - 0	$68^{+0.01}_{-0.01}$	$68^{+0.01}_{-0.01}$
0 - 0.5	$68^{+0.01}_{-0.01}$	$68^{+0.01}_{-0.01}$
0.5 - 1	$53^{+0.01}_{-0.01}$	$53^{+0.01}_{-0.01}$
1 - 2	$15^{+0.002}_{-0.002}$	$15^{+0.003}_{-0.003}$

Table 6.12: True $t\bar{t}$ cross sections in each bin of the rapidity as reported by the generator. The integrated cross section is 166.8 $\pm$ 0.013 pb.

$M_{t\bar{t}}$ [GeV]	Average difference [%] (e+jets)	Average difference [%] (μ+jets)
250 - 450	-1.8$\pm$ 0.053	-1.3$\pm$ 0.043
450 - 550	5$\pm$ 0.1	3.8$\pm$ 0.079
550 - 700	-3.1$\pm$ 0.12	-1.7$\pm$ 0.1
700 - 950	-1.8$\pm$ 0.18	-3.1$\pm$ 0.15
950 - 2700	-5.8$\pm$ 0.36	-4.2$\pm$ 0.29

Table 6.13: Cross section bias observed in the pseudo-experiments closure test for $M_{t\bar{t}}$. This table shows the average difference between the measured and the true result. For each bin i of $M_{t\bar{t}}$, the average difference in % is given by: $xsec_{t\bar{t}}^{measured,i} - xsec_{t\bar{t}}^{true,i}/xsec_{t\bar{t}}^{true,i}$.

$y_{t\bar{t}}$	Average difference [%] (e+jets)	Average difference [%] (μ+jets)
-2 - -1	0.93$\pm$ 0.11	1.9$\pm$ 0.079
-1 - -0.5	0.019$\pm$ 0.1	-0.73$\pm$ 0.079
-0.5 - 0	-0.56$\pm$ 0.088	0.14$\pm$ 0.071
0 - 0.5	0.033$\pm$ 0.088	-0.34$\pm$ 0.072
0.5 - 1	-0.19$\pm$ 0.1	-0.66$\pm$ 0.081
1 - 2	0.75$\pm$ 0.11	1.2$\pm$ 0.079

Table 6.14: Cross section bias observed in the pseudo-experiments closure test for $y_{t\bar{t}}$. This table shows the average difference between the measured and the true result. For each bin i of $y_{t\bar{t}}$, the average difference in % is given by: $xsec_{t\bar{t}}^{measured,i} - xsec_{t\bar{t}}^{true,i}/xsec_{t\bar{t}}^{true,i}$.

two models), the estimated variation is symmetrized, i.e. considered as having the same size in both the upward and the downward direction. The baseline distribution and the distributions of the estimated standard deviations are the input to the pseudo-experiment calculation (detailed in Section 6.7) that performs unfolding

and efficiency correction so as to include correlations and permit combination of the electron and the muon channels. The different estimates are assumed to be uncorrelated with each other unless specified.

6.8.1 Signal and Background Modeling

1. Signal modeling:
   The $t\bar{t}$ samples for the nominal use are generated with MC@NLO as mentioned in Section 6.1. Systematic shifts are obtained by comparing predictions from MC@NLO and POWHEG [116]. The MC@NLO generator uses a careful elaboration of the NLO results, that has to match certain features of the Shower Monte Carlo (SMC) program. The SMC programs contain a large library of SM and BSM cross sections, models for hadron formation and they can handle unstable particle decays.They dress the hard event with QCD radiation that enhances the cross section in the soft or collinear limit. Hence, the name shower. For the MC@NLO generator, the approximate SMC implementation of the NLO corrections is subtracted to the exact NLO result in order to avoid double counting and it correctly accounts for hard emissions at NLO. While in POWHEG, POsitive Weight Hardest Emission Generator, the generation of the hardest emission is performed first, with NLO accuracy, independently from the subsequent shower. Therefore, it generates events with positive weights only, contrary to the MC@NLO generator, and it can easily be interfaced with any SMC program such as HERWIG, PYTHIA, SHERPA, etc... The SMC program interfaced with the $t\bar{t}$ POWHEG sample used for the determination of the systematic uncertainties in this analysis is HERWIG [103]. HERWIG is a general-purpose Monte Carlo event generator, which includes the simulation of hard lepton-lepton, lepton-hadron and hadron-hadron scattering and soft hadron-hadron collisions. It uses the parton-shower approach for initial- and final-state QCD radiation, including color coherence effects and azimuthal correlations both within and between jets.

2. Parton showering:
   The effect of parton shower modeling is estimated by comparing two POWHEG samples interfaced to HERWIG and PYTHIA [80], respectively. PYTHIA shares many common features with HERWIG, but they also have some significant differences, in particular in the treatment of the non-perturbative processes. PYTHIA and HERWIG are slightly different also in the description of the hard sub-process. In particular, in photoproduction events PYTHIA uses the Weiszacker and Williams [117] approximation to gener-

ate the spectrum of the photons radiated from the incoming lepton, whereas HERWIG uses the equivalent photon approximation. They also differ in the scale of the hard scattering.

3. ISR/FSR:
   Gluons radiated by the initial quarks or gluons and/or the final state $t\bar{t}$ pair produce extra jets in the event not from top decay. Allowing greater than 4 jets in the event selection is a more or less a reason to be less sensitive to the effects of final state radiation (FSR) w.r.t. the initial state radiation (ISR), but jets due to ISR that are incorrectly attributed to the $t\bar{t}$ pair alter the shape of the $M_{t\bar{t}}$ and $y_{t\bar{t}}$ distributions and the acceptance in each bin. The amount of ISR and FSR are tunable parameters in the Monte Carlo simulation. Two ACERMC [106] samples interfaced with PYTHIA are generated with less or more parton shower (ps) activity as discussed in Section 6.1. The systematic uncertainty is taken as half of the difference between the sample with less ps activity and the one with more ps.

4. PDF sets:
   In deep-inelastic scattering and hard proton-proton high-energy collisions, the scattering proceeds via the partonic constituents of the hadron. To predict the rates of the various processes a set of universal parton distribution functions, PDFs, is required. The PDFs describe the distribution of the p-p momentum among the constituent quarks and gluons. They carry uncertainties due to the uncertainties associated with the underlying experimental measurements used to calculate the PDFs. The default $t\bar{t}$ sample used in the analysis is generated using the MSTW2008 90% NNLO as mentioned in Section 6.1. The impact of the choice of the PDFs in simulation is studied by re-weighting $t\bar{t}$ events with three different NLO PDF sets (CTEQ66, MSTW2008NLO68CL and NNPDF20) and taking the the maximal spread of the variations from the nominal values.

5. QCD multijet processes:
   The QCD background is estimated using the data driven method discussed in Section 6.5.2. The normalization is varied within a 50% uncertainty in the pre-tagged and the tagged sample in the electron channel, and within 20% uncertainty in the pre-tagged and the tagged sample in the muon channel. An additional systematic uncertainty is assigned on the shape and it's done by varying the estimation within its uncertainty (i.e. the resulting statistical

and systematical uncertainty of the Matrix Method) for both channels.

6. W+jets processes:
   The normalization of W+jets processes is estimated from auxiliary measurements using the asymmetric production of positively and negatively charged W bosons in W+jets events. Scaling factors correcting the fraction of heavy flavor contributions in simulated W+jets samples are also estimated from collision data and their uncertainty is considered. The different contributions to the overall uncertainty are considered to produce variations of the measured distributions. In addition systematic uncertainties on the shape of W+jets distributions are based on the observed differences when changing the factorization scale from fixed to $\sqrt{m^2(W)+p_T^2(W)}$, and changing the parton matching scale from 15 GeV to 10 GeV.

7. Z+jets processes:
   The uncertainty in the normalization for the inclusive sample requiring four or more jets is 48% as propagated from the Berends-Giele-scaling [118].

8. Single top processes:
   For a total single top cross section of 84.93 pb, an additional uncertainty is applied: 3.43% for an upper deviation and 2.69% for a lower deviation. As mentioned in Section 6.1, the single top sample in the s-, Wt, and t-channels are generated with a cross section of $4.63^{+0.19}_{-0.17}$ pb [107], $15.74^{+1.06}_{-1.08}$ pb [108] and $64.57^{+2.71}_{-2.01}$ pb [119] respectively. The square root of the sum of the upper and the lower uncertainties divided by the total single top cross section gives the systematic deviation inputs.

9. Diboson processes:
   To derive the varied distribution, the normalization of the diboson processes is varied within 5% uncertainty [120].

6.8.2 Detector Modeling

1. Lepton reconstruction:
   The mis-modeling of muon and electron trigger, reconstruction and selection efficiencies in simulations are corrected for by scale factors derived from $Z \to \mu\mu$, $Z \to ee$ and $W \to e\nu$ efficiency measurements in data. These

scale factors are obtained as functions of the lepton kinematics (p_T and η). Scale factors are varied within their uncertainties to obtain the variation of the variable of interest representing the systematic uncertainty.

2. Lepton momentum scale and resolution:
   The $Z \to \mu\mu$ and $Z \to ee$ processes are used to measure the lepton momentum scale and resolution. Correction factors and associated uncertainties are derived to match the simulation to observed distributions in collision data. The correction factors are varied within their uncertainties to obtain the estimated shift in the variable of interest that represent the systematic uncertainties. The systematic errors resulting from scale and resolution uncertainty are considered uncorrelated.

3. Jet energy scale:
   The jet energy scale is derived using single particle response, test-beam data and 7 TeV LHC collision data and simulation. It varies as function of the jet p_T and η. Jet energies are varied within their error to obtain the corresponding systematic uncertainties. The b-jet energy scale is included in total jet energy scale calculation.

4. Jet energy resolution:
   The jet energy resolution is measured with the di-jet balance and the bisector techniques [121]. It was shown to agree between data and simulation within its uncertainties. The Monte Carlo simulation describes the jet energy resolution measured in data within 14 % for jets with p_T values between 20 and 80 GeV in the rapidity range $|y| < 2.8$. No correction to simulated events is applied for resolution effects on jets. The uncertainty is used for systematic studies by smearing the jet p_T within the uncertainty of the jet p_T resolution.

5. Jet reconstruction efficiency:
   The calorimeter jet reconstruction efficiency [121] is derived relative to jets reconstructed from charged tracks in the inner detector system, using a tag and probe technique. The reconstruction efficiency was defined as the fraction of probe track-jets matched to a calorimeter jet. Data agree with simulation within 1.1%. No default correction is applied. The observed uncertainty on the agreement between data and simulation is used randomly to drop a fraction of jets in simulation consistent with that uncertainty range.

The resulting varied distribution provide the estimate of the systematic uncertainty.

6. *b*-tagging:
   The b-tagging efficiencies and mistag rates for the MV1 tagger were measured in data, and the data to Monte Carlo scale factors used in this analysis are results of the combination of the $System8$ and the p_T^{rel} methods described in Sections 5.2.2 and 5.2.1 respectively. Each jet has an efficiency or inefficiency scale factor depending on whether it was *b*-tagged by the MV1 algorithm or not. The event has a *b*-tagging weight which is the product of a series of the tagging [122]/mistagging [123] efficiencies and inefficiencies. The scale factors are varied within their uncertainties to asses the resulting systematic uncertainty on the measurements. The efficiency and inefficiency scale factors variations are applied simultaneously in the opposite directions for the *b*-jets, *c*-jets and $light$-jets separately. The variations of *b*-tagging efficiencies and mistag rates are considered uncorrelated. The resulting variation in the variable of interest provide the systematic uncertainty.

7. Missing transverse energy:
   The uncertainties from the energy scale and resolution corrections on leptons and jets are propagated into the calculation of the missing transverse energy. Additional uncertainties are added from contributions of calorimeter cells not associated to any jets (CELLOUT) and soft jets (7 GeV$< p_T <$ 20 GeV). They all concur to provide the varied distribution to assess the systematic effect.

8. Luminosity:
   Luminosity is varied within its uncertainty on the measured value from Van der Meer scans (about 3.9%.) to estimate the variation.

9. MC statistics:
   A final systematic error taken into account is due to the limited statistics in the MC samples used in this analysis.

6.9 Results

To reduce the impact of correlated systematic uncertainties only relative differential cross sections are reported. The relative cross section is the differential cross

section normalized to the integrated cross section. The relative differential cross section results are listed in Table 6.15 as a function of $M_{t\bar{t}}$ and in Table 6.16 as a function of $y_{t\bar{t}}$. Both electron and muon channels results and their combination are shown. The measurements are reported with their full uncertainty combining statistical and systematic errors. They are compared to the unfolded simulation and to the true cross section computed from the MC@NLO generator as shown in Fig. 6.18 for $M_{t\bar{t}}$ and in 6.19 for $y_{t\bar{t}}$. The relative differential cross sections are also compared to NLO prediction from MCFM [124] for the two variables; approximate NNLO predictions from [125] are included for $M_{t\bar{t}}$, shown in Fig. 6.20 and Fig. 6.21. Theory uncertainty bands include uncertainties on parton distribution functions (at 68% confidence level) and on factorization and renormalization scales, summed in quadrature.

	$d\sigma/(\sigma_{t\bar{t}}dM_{t\bar{t}})$ [GeV^{-1}]		
$M_{t\bar{t}}$ [GeV]	e+jets	μ+jets	l+jets
250 - 450	$2.343^{+0.145}_{-0.13}$	$2.578^{+0.15}_{-0.11}$	$2.491^{+0.13}_{-0.099}$
450 - 550	$2.951^{+0.260}_{-0.25}$	$2.701^{+0.17}_{-0.22}$	$2.798^{+0.15}_{-0.19}$
550 - 700	$1.097^{+0.133}_{-0.11}$	$0.985^{+0.12}_{-0.087}$	$1.023^{+0.10}_{-0.075}$
700 - 950	$0.2401^{+0.040}_{-0.034}$	$0.218^{+0.031}_{-0.028}$	$0.2265^{+0.025}_{-0.023}$
950 - 2700	$0.0028^{+0.0025}_{-0.002}$	$0.006^{+0.0025}_{-0.002}$	$0.005^{+0.002}_{-0.002}$

Table 6.15: Relative differential cross section as function of $M_{t\bar{t}}$ measured in the e+jets, μ+jets channels and their combination.

	$d\sigma/(\sigma_{t\bar{t}}dy_{t\bar{t}})$		
y	e+jets	μ+jets	l+jets
-2 - -1	$0.10^{+1.7}_{-1.8}$	$0.12^{+2.1}_{-2.1}$	$0.11^{+1.9}_{-2.0}$
-1 - -0.5	$0.60^{+9.7}_{-10.05}$	$0.54^{+8.6}_{-9.08}$	$0.57^{+9.2}_{-9.73}$
-0.5 - 0	$0.70^{+11.84}_{-11.8}$	$0.77^{+12.47}_{-12.39}$	$0.73^{+12.04}_{-12.3}$
0 - 0.5	$0.014^{+0.02}_{-0.009}$	$0.012^{+0.02}_{-0.008}$	$0.013^{+0.02}_{-0.008}$
0.5 - 1	$0.5852^{+9.389}_{-9.747}$	$0.5576^{+8.86}_{-9.158}$	$0.569^{+9.151}_{-9.57}$
1 - 2	$0.1437^{+2.376}_{-2.42}$	$0.1407^{+2.328}_{-2.419}$	$0.1423^{+2.391}_{-2.364}$

Table 6.16: Relative differential cross section as function of $y_{t\bar{t}}$ measured in the e+jets, μ+jets channels and their combination.

The total and the break down of the uncertainties on the electron+jets and the muon+jets relative $t\bar{t}$ differential cross sections and their combination in the 5 $M_{t\bar{t}}$ bins are presented in Tables 6.17, 6.18 and 6.19 respectively. Tables 6.20, 6.21

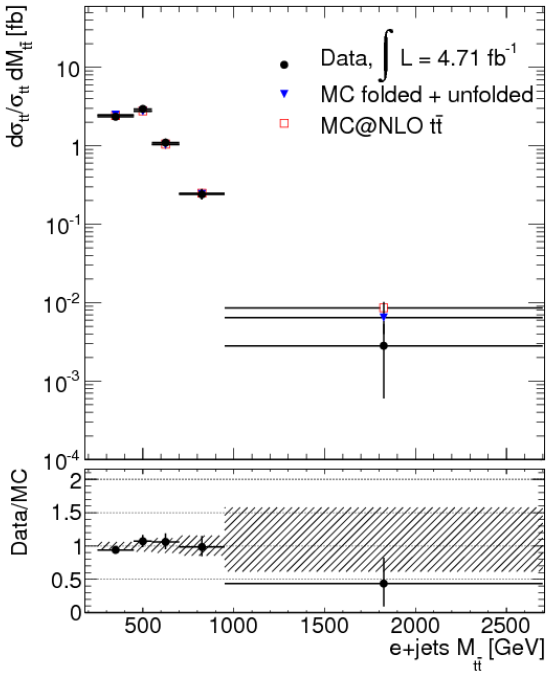

(a)

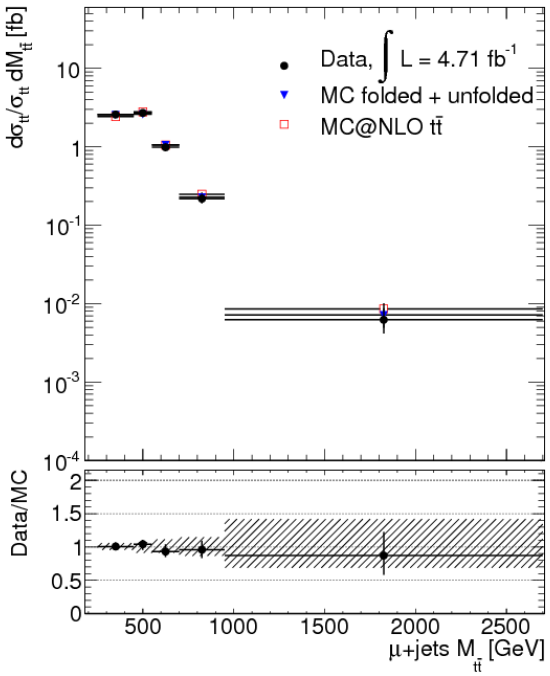

(b)

Figure 6.18: Relative cross sections measured in data as a function of $M_{t\bar{t}}$, in the electron (a) and the muon (b) channels, compared to the folded and unfolded cross sections measured from simulation and the true cross sections as computed from the MC@NLO generator.

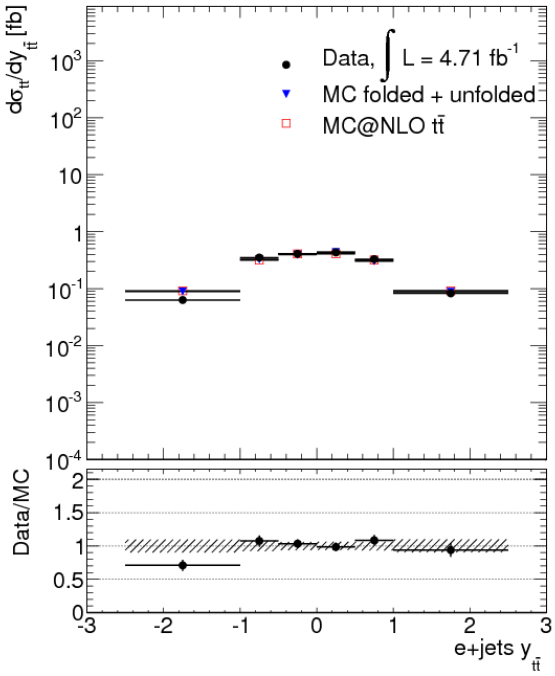

(a)

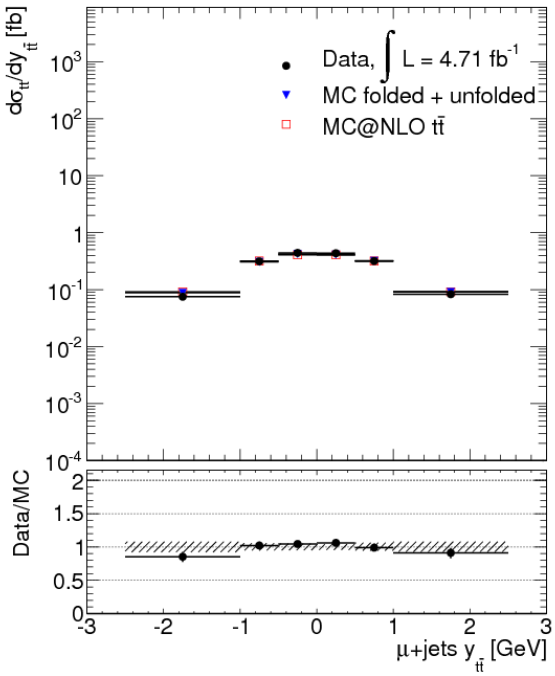

(b)

Figure 6.19: Relative cross sections measured in data as a function of $y_{t\bar{t}}$, in the electron (a) and the muon (b) channels, compared to the folded and unfolded cross sections measured from simulation and the true cross sections as computed from the MC@NLO generator.

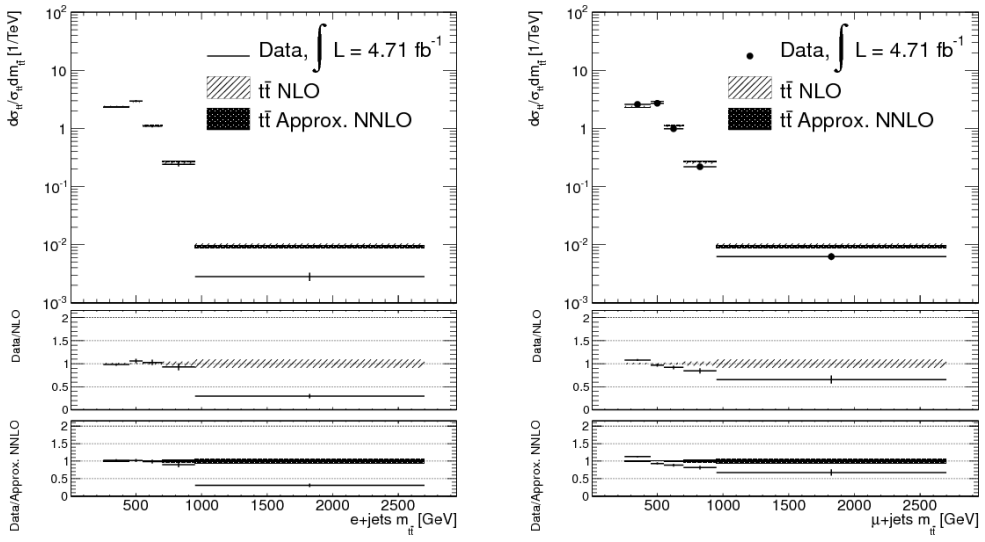

(a) (b)

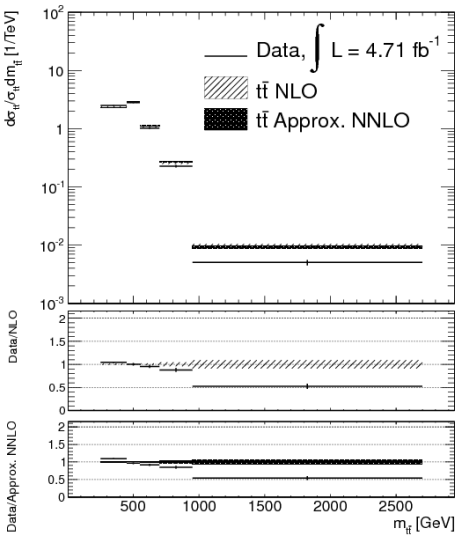

(c)

Figure 6.20: Relative differential cross section as function of $M_{t\bar{t}}$ measured in the e+jets channel (a), μ+jets channel (b) and their combination 6.20(c). The results are compared with the NLO prediction from MCFM [124] and the approximate NNLO prediction from [125].

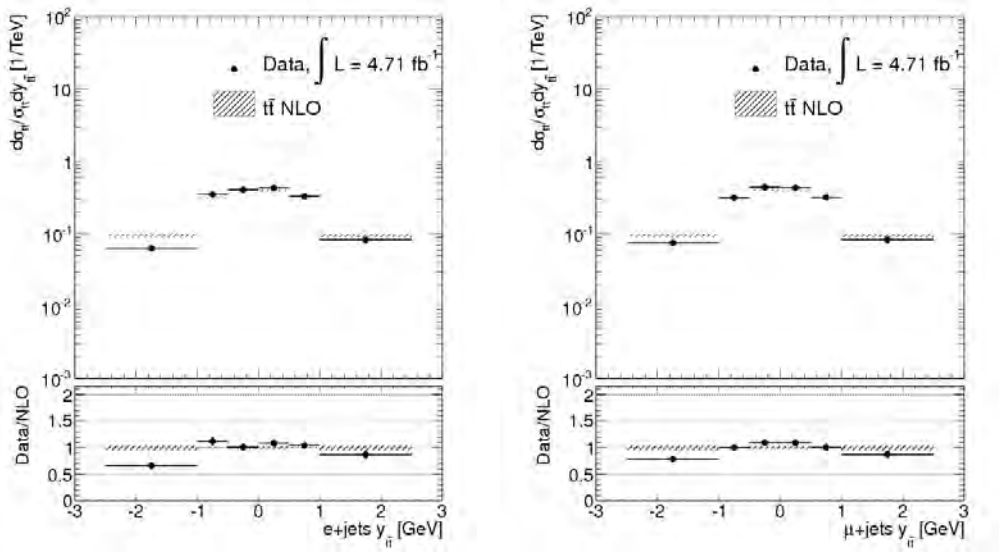

(a)

(b)

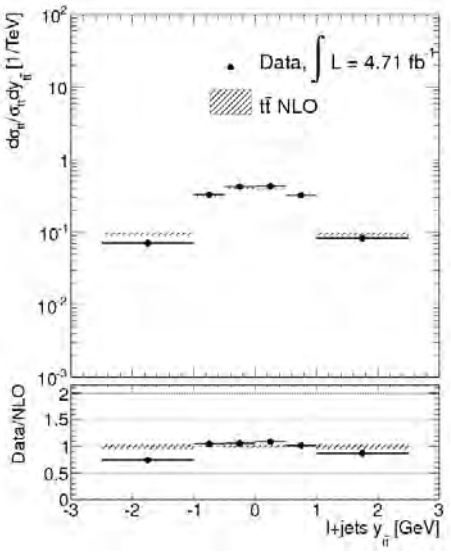

(c)

Figure 6.21: Relative differential cross section as function of $y_{t\bar{t}}$ measured in the e+jets channel (a), μ+jets channel (b) and their combination (c). The results are compared with the NLO prediction from MCFM [124].

and 6.22 show these uncertainties for the 6 $y_{t\bar{t}}$ bins. The assessment of the impact of a given systematic effect is obtained by running pseudo-experiments as described in Section 6.7. Pseudo-experiments are first generated by incorporating signal Poissonian fluctuations and then by adding only fluctuations related to the systematic effect under consideration. The difference between the corresponding uncertainties is taken as a measure of the uncertainty associated to the considered systematic effect. For each systematic error, two thousand pseudo-experiments are used to extract the cross section values.

	$dM_{t\bar{t}}$				
$d\sigma_{t\bar{t}}/(\sigma_{t\bar{t}}dM)$	250-450	450-550	550-700	700-950	950-2700
Total[%]	6.19 / -5.64	8.82 / -8.37	12.15 / -10.15	16.86 / -13.97	88.95 / -78.72
Stat. only[%]	2.87 / -2.88	4.98 / -4.63	5.67 / -5.75	8.99 / -8.78	50.98 / -44.92
Syst. only[%]	5.48 / -4.85	7.28 / -6.97	10.75 / -8.36	14.27 / -10.87	72.89 / -64.65
Luminosity[%]	1.57 / -0.87	2.45 / -2.92	3.51 / -3.12	5.45 / -5.36	16.58 / -34.20
JES[%]	1.18 / -0.43	2.88 / -2.61	2.95 / -3.49	3.88 / -3.66	18.58 / -41.69
JVF[%]	1.15 / -1.15	0.78 / -0.51	1.74 / -1.85	3.43 / -3.52	21.16 / -24.72
JER[%]	1.97 / -0.77	4.50 / -2.87	0.88 / -1.98	1.11 / -2.72	13.45 / -46.10
JRE[%]	1.37 / -1.46	3.70 / -1.59	0.60 / -3.68	4.79 / -6.15	9.80 / -27.92
BTAG[%]	2.64 / -0.41	3.54 / -1.99	1.91 / -3.47	3.10 / -2.45	25.26 / -31.03
LSF[%]	0.75 / -1.96	3.23 / -1.79	1.88 / -1.05	1.11 / -3.77	28.84 / -29.30
QCD[%]	2.99 / -3.23	5.50 / -3.91	2.64 / -0.37	0.63 / -6.02	29.89 / -45.00
PDF[%]	0.67 / -0.94	1.15 / -0.87	3.95 / -2.95	3.69 / -3.25	6.79 / -16.30
PS[%]	3.62 / -3.41	4.48 / -4.81	6.33 / -6.15	8.38 / -8.14	44.18 / -41.66
GEN[%]	1.08 / -1.69	4.89 / -4.74	8.17 / -5.86	5.88 / -5.14	42.60 / -48.50
ISR/FSR[%]	0.06 / -0.06	0.03 / -0.03	0.13 / -0.13	0.09 / -0.09	0.06 / -0.06
PILE-UP[%]	1.68 / -1.84	2.82 / -2.74	2.87 / -1.57	1.13 / -0.47	32.80 / -36.62
W[%]	1.76 / -1.14	4.00 / -2.80	1.71 / -2.25	2.41 / -4.91	12.30 / -40.20
CELLOUT[%]	0.59 / -1.27	1.21 / -3.49	1.81 / -1.89	4.28 / -4.82	13.03 / -34.00
XS[%]	2.71 / -1.38	3.04 / -2.71	2.98 / -3.65	5.72 / -6.05	5.65 / -28.83
MC stat.[%]	2.96 / -1.94	5.05 / -3.61	6.03 / -6.25	13.33 / -9.77	60.83 / -32.18

Table 6.17: Uncertainties on $d\sigma_{t\bar{t}}/(\sigma_{t\bar{t}}dM_{t\bar{t}})$ in the e+jets channel

6.10 Conclusion

This chapter presents a complete measurement of the $t\bar{t}$ differential cross section using a dataset of 4.7 fb^{-1} which corresponds to the full 2011 ATLAS data. The relative differential cross section for $t\bar{t}$ production is measured as a function of two variables of the $t\bar{t}$ system: $M_{t\bar{t}}$ and $y_{t\bar{t}}$. The background subtracted, detector-unfolded values of $d\sigma_{t\bar{t}}/(\sigma_{t\bar{t}}dM_{t\bar{t}})$ and $d\sigma_{t\bar{t}}/(\sigma_{t\bar{t}}dy_{t\bar{t}})$ are reported. The measurements are dominated by systematic effects. The dominant systematic uncertainty for the differential cross section as function of the $t\bar{t}$ mass in the elec-

	$dM_{t\bar{t}}$				
$d\sigma_{t\bar{t}}/(\sigma_{t\bar{t}}dM)$	250-450	450-550	550-700	700-950	950-2700
Total[%]	5.88 / -4.40	6.33 / -8.21	11.81 / -8.85	14.20 / -13.03	40.38 / -32.93
Stat. only[%]	1.82 / -1.90	3.91 / -3.64	5.01 / -4.33	7.20 / -7.16	16.28 / -16.45
Syst. only[%]	5.59 / -3.97	4.97 / -7.35	10.70 / -7.71	12.25 / -10.89	36.95 / -28.53
Luminosity[%]	1.00 / -1.62	2.20 / -0.65	2.42 / -3.35	2.85 / -3.63	6.51 / -6.34
JES[%]	0.84 / -0.59	1.71 / -3.56	3.88 / -1.62	3.03 / -0.95	9.52 / -10.88
JVF[%]	2.42 / -0.68	2.48 / -2.71	4.09 / -2.08	4.22 / -2.41	14.03 / -4.46
JER[%]	3.56 / -2.03	1.50 / -4.36	5.29 / -3.75	2.15 / -3.42	19.15 / -7.23
JRE[%]	0.85 / -1.29	2.78 / -2.49	2.31 / -1.33	3.60 / -3.54	11.31 / -7.94
BTAG[%]	1.09 / -0.80	2.32 / -2.61	3.56 / -2.67	4.91 / -1.72	5.55 / -10.72
LSF[%]	0.57 / -1.60	3.02 / -1.00	1.95 / -1.72	3.89 / -2.82	17.07 / -3.00
QCD[%]	1.50 / -1.23	1.65 / -3.26	3.97 / -3.01	3.06 / -1.14	11.73 / -2.64
PDF[%]	1.41 / -0.33	2.41 / -0.89	2.23 / -1.37	3.67 / -1.86	14.41 / -5.72
PS[%]	3.05 / -2.46	4.24 / -4.51	4.57 / -4.55	8.25 / -7.73	16.50 / -16.64
GEN[%]	2.37 / -0.08	2.44 / -5.46	9.76 / -6.33	7.12 / -4.72	16.58 / -14.26
ISR/FSR[%]	0.10 / -0.10	-0.09 / 0.09	0.12 / -0.12	0.04 / -0.04	0.08 / -0.08
PILE-UP[%]	1.22 / -1.06	3.55 / -3.07	4.40 / -2.09	2.57 / -1.02	7.89 / -5.86
W[%]	1.81 / -1.28	2.54 / -2.83	2.63 / -3.21	4.97 / -3.47	11.71 / -5.29
CELLOUT[%]	0.60 / -1.68	2.80 / -1.29	3.72 / -2.42	1.84 / -2.49	19.21 / -4.59
XS[%]	0.89 / -1.21	2.52 / -0.38	1.79 / -3.07	2.56 / -0.74	18.63 / -11.12
MC stat.[%]	2.69 / -0.64	1.58 / -3.45	5.31 / -4.72	11.11 / -8.71	31.91 / -19.84

Table 6.18: Uncertainties on $d\sigma_{t\bar{t}}/(\sigma_{t\bar{t}}dM_{t\bar{t}})$ in the μ+jets channel

tron+jets and the muon+jets channels is the MC statistics, especially in the last bin ($950 < M_{t\bar{t}} < 2700$ GeV). The parton shower systematic is also a dominant one as well as the MC generators for the $t\bar{t}$ signal modeling.
As for the differential cross section as function of the $t\bar{t}$ rapidity, the dominant systematic uncertainty is also the MC statistics, especially in the first and the last two bins ($-2 < y_{t\bar{t}} < -1$ and $1 < y_{t\bar{t}} < 2$). The ISR/FSR uncertainty on the $t\bar{t}$ signal modeling is also a dominant systematic especially in the second and the fifth bins ($-1 < y_{t\bar{t}} < -0.5$ and $0.5 < y_{t\bar{t}} < 1$). The results are compared to theoretical calculation for the NLO predictions for the $t\bar{t}$ mass and rapidity, as well as the approximate NNLO in the case of the $t\bar{t}$ mass. No significant deviations from the SM expectations is observed.

The first ATLAS measurement of the $t\bar{t}$ relative differential cross section was performed using the first 2.05 fb^{-1} of the 2011 data, and this measurement was submitted to European Physical Journal C [115]. The analysis in this thesis is an updated version of this measurement, using the full 2011 ATLAS data. This measurement presents an improvement in the total systematic error, as shown in Table 6.23 for the $t\bar{t}$ mass and in Table 6.24 for the $t\bar{t}$ rapidity, more specifically, in the b-tagging. The b-tagging algorithm used in this update is the MV1 tag-

	$dM_{t\bar{t}}$				
$d\sigma_{t\bar{t}}/(\sigma_{t\bar{t}}dM)$	250-450	450-550	550-700	700-950	950-2700
Total[%]	5.33 / -3.99	5.59 / -7.10	10.09 / -7.41	11.39 / -10.53	38.69 / -34.52
Stat. only[%]	1.54 / -1.54	2.93 / -2.90	3.68 / -3.46	5.40 / -5.52	17.32 / -16.30
Syst. only[%]	5.11 / -3.68	4.76 / -6.48	9.39 / -6.55	10.03 / -8.96	34.59 / -30.42
Luminosity[%]	1.47 / -1.24	0.94 / -0.42	1.81 / -2.23	3.90 / -2.14	8.53 / -3.37
JES[%]	2.05 / -0.78	0.56 / -2.77	1.86 / -1.39	4.17 / -3.76	8.58 / -13.97
JVF[%]	1.81 / -0.96	0.36 / -1.68	2.48 / -1.49	1.20 / -1.81	12.18 / -11.05
JER[%]	3.13 / -2.00	1.66 / -3.97	1.94 / -2.99	0.63 / -3.49	4.57 / -4.28
JRE[%]	1.03 / -0.67	0.18 / -2.53	2.05 / -0.66	2.41 / -1.90	7.00 / -8.09
BTAG[%]	1.94 / -0.94	1.39 / -2.40	2.39 / -1.44	3.31 / -3.60	12.23 / -7.38
LSF[%]	0.87 / -0.58	0.57 / -2.52	0.10 / -1.68	1.49 / -1.83	14.29 / -1.93
QCD[%]	1.44 / -1.54	2.45 / -3.55	0.91 / -1.49	3.84 / -2.30	13.18 / -4.68
PDF[%]	1.84 / -0.67	1.19 / -1.01	1.10 / -2.35	3.32 / -1.89	9.09 / -7.12
PS[%]	2.89 / -2.04	3.21 / -3.52	3.76 / -3.81	6.00 / -6.20	16.87 / -16.42
GEN[%]	2.18 / -1.17	2.40 / -5.13	8.76 / -5.38	5.88 / -4.68	16.26 / -15.46
ISR/FSR[%]	0.17 / -0.17	-0.05 / 0.05	0.16 / -0.16	0.04 / -0.04	0.06 / -0.06
PILE-UP[%]	1.99 / -1.44	1.85 / -2.25	1.75 / -1.25	1.78 / -1.47	6.82 / -4.46
W[%]	2.01 / -0.89	0.52 / -3.12	2.32 / -0.91	2.12 / -2.94	6.34 / -6.83
CELLOUT[%]	1.23 / -1.01	1.82 / -2.23	2.30 / -1.13	3.52 / -1.86	3.17 / -15.19
XS[%]	2.07 / -0.83	1.35 / -1.47	3.47 / -0.51	2.06 / -2.60	14.62 / -4.50
MC stat.[%]	2.07 / -1.49	1.57 / -3.59	1.36 / -3.81	8.96 / -6.84	26.01 / -18.95

Table 6.19: Uncertainties on $d\sigma_{t\bar{t}}/(\sigma_{t\bar{t}}dM_{t\bar{t}})$ in the combined l+jets channel

ger, described in Chapter 5 Section 5.1.1, which is more powerful, in terms of *light*-jets rejection with respect to the one used in the 2.05 fb^{-1} measurement, the `JetFitterCombNN`, as shown in Figure 5.6. The *b*-tagging data-to-MC scale factors used in this analysis are the result of the combination between the $p_{\mathrm{T}}^{\mathrm{rel}}$ and the *System*8 measurements, which reduced the systematic error, while for the 2.05 fb^{-1} measurement, the *b*-tagging scale factors were obtained from the$p_{\mathrm{T}}^{\mathrm{rel}}$ method only since the combination was not available at that time. However, these results, presented in this thesis, are not ATLAS final results. These results present the status of the analysis as it is until June 2012.

The CMS collaboration has also measured the $t\bar{t}$ differential cross section using a dataset recorded in 2011 corresponding to an integrated luminosity of 1.14 fb^{-1} [126]. Good agreement is found with predictions from different QCD models.
Previous measurement of the $t\bar{t}$ differential cross section were done at the CDF experiment using 2.5 fb^{-1} of proton-antiproton collisions with an energy at a center-of-mass of 1.96 TeV [127]. The result was found to be consistent with the standard model expectation.

	$dy_{t\bar{t}}$					
$d\sigma_{t\bar{t}}/(\sigma_{t\bar{t}}dy)$	-2 - -1	-1 - -0.5	-0.5 - 0	0 - 0.5	0.5 - 1	1 - 2
Total[%]	11.6 / -11.8	7.8 / -7.7	6.2 / -6.2	6.7 / -6.2	7.6 / -6.8	11.1 / -10.8
Stat. only[%]	7.2 / -6.8	4.3 / -4.5	4.1 / -4.0	3.7 / -4.1	4.7 / -4.5	5.8 / -5.9
Syst. only[%]	9.1 / -9.6	6.5 / -6.3	4.7 / -4.8	5.6 / -4.6	5.9 / -5.0	9.5 / -9.1
Luminosity[%]	2.3 / -3.8	1.4 / -1.2	1.5 / -1.2	1.3 / -1.4	1.8 / -2.1	2.2 / -4.3
JES[%]	1.6 / -4.0	0.6 / -2.3	2.6 / -2.3	2.9 / -1.5	2.0 / -1.7	3.3 / -4.2
JVF[%]	2.4 / -2.5	2.4 / -1.8	0.5 / -1.8	0.6 / -1.7	2.4 / -1.2	1.9 / -1.8
JER[%]	3.1 / -4.3	2.1 / -1.4	1.7 / -1.1	3.2 / -2.2	2.8 / -1.3	4.6 / -3.4
JRE[%]	2.8 / -3.8	1.3 / -1.7	0.6 / -1.7	0.7 / -1.0	2.7 / -1.9	3.9 / -1.8
BTAG[%]	2.6 / -2.6	3.3 / -1.6	1.8 / -0.3	1.4 / -1.5	2.3 / -2.3	3.3 / -3.5
LSF[%]	5.0 / -1.7	2.7 / -1.3	1.5 / -1.1	1.3 / -1.1	1.9 / -1.3	2.8 / -3.3
QCD[%]	1.6 / -3.9	1.4 / -2.8	0.8 / -0.8	1.4 / -1.6	1.4 / -1.8	2.6 / -2.6
PDF[%]	4.7 / -2.0	1.6 / -1.3	1.4 / -1.2	1.9 / -1.0	2.1 / -1.1	2.2 / -4.1
PS[%]	3.3 / -1.9	2.2 / -3.1	1.8 / -1.6	2.9 / -1.8	3.1 / -1.6	1.8 / -4.8
GEN[%]	2.2 / -3.0	3.3 / -3.2	3.0 / -2.2	1.8 / -2.1	3.3 / -2.2	2.8 / -3.6
ISR/FSR[%]	2.07 / -2.07	-4.9 / 4.9	-1.7 / 1.7	2.0 / -2.0	-2.6 / 2.6	-1.2 / 1.2
PILE-UP[%]	4.5 / -3.6	2.3 / -1.9	1.7 / -0.3	1.3 / -1.5	1.2 / -0.7	0.9 / -2.1
W[%]	3.5 / -0.9	2.9 / -2.8	0.9 / -1.0	2.2 / -1.6	1.6 / -0.6	2.5 / -5.0
CELLOUT[%]	1.1 / -3.0	3.2 / -2.8	1.7 / -1.3	1.8 / -1.8	2.9 / -1.0	2.0 / -4.5
XS[%]	5.5 / -2.0	1.2 / -2.4	1.4 / -1.3	0.5 / -1.1	1.2 / -1.8	1.1 / -2.0
MC stat.[%]	8.0 / -7.2	4.8 / -5.1	3.9 / -3.0	4.0 / -3.2	5.2 / -4.7	8.9 / -8.2

Table 6.20: Uncertainties on $d\sigma_{t\bar{t}}/(\sigma_{t\bar{t}}dy)$ in the electron+jets channel

	$dy_{t\bar{t}}$					
$d\sigma_{t\bar{t}}/(\sigma_{t\bar{t}}dy)$	-2 - -1	-1 - -0.5	-0.5 - 0	0 - 0.5	0.5 - 1	1 - 2
Total[%]	8.5 / -9.0	5.6 / -5.3	5.0 / -4.6	4.2 / -4.3	6.1 / -5.4	7.7 / -8.9
Stat. only[%]	4.2 / -4.0	3.5 / -3.5	3.1 / -3.1	3.0 / -2.9	3.6 / -3.6	3.9 / -3.7
Syst. only[%]	7.5 / -8.1	4.3 / -3.9	3.9 / -3.4	2.9 / -3.2	4.9 / -4.0	6.7 / -8.1
Luminosity[%]	2.0 / -1.5	1.5 / -1.1	1.2 / -1.3	0.8 / -1.0	1.1 / -1.8	2.8 / -4.1
JES[%]	2.2 / -4.0	1.4 / -2.0	2.0 / -1.0	1.7 / -1.1	2.6 / -1.1	1.1 / -5.4
JVF[%]	2.8 / -0.3	2.1 / -1.2	1.6 / -1.1	1.9 / -1.0	1.3 / -2.1	2.1 / -2.5
JER[%]	1.8 / -2.0	2.2 / -0.4	1.2 / -1.7	0.6 / -1.6	2.4 / -1.7	1.6 / -4.3
JRE[%]	2.3 / -0.6	2.1 / -0.7	0.9 / -1.7	0.4 / -0.9	1.4 / -2.2	2.2 / -2.0
BTAG[%]	4.6 / -2.5	1.7 / -1.0	1.1 / -1.2	1.6 / -0.7	0.6 / -1.2	2.9 / -3.3
LSF[%]	0.3 / -1.3	1.7 / -1.8	1.4 / -1.0	1.0 / -2.0	2.3 / -0.6	2.6 / -4.1
QCD[%]	3.3 / -0.7	1.5 / -1.8	1.5 / -1.9	1.4 / -1.3	1.4 / -1.4	3.9 / -2.6
PDF[%]	2.9 / -2.6	0.8 / -1.0	0.6 / -0.5	1.9 / -0.6	1.0 / -0.7	3.3 / -2.8
PS[%]	2.1 / -2.6	0.3 / -1.0	1.6 / -0.7	0.4 / -0.9	1.9 / -1.8	2.1 / -4.4
GEN[%]	1.4 / -4.4	1.1 / -1.5	1.8 / -1.7	1.1 / -0.6	2.5 / -1.1	2.8 / -3.0
ISR/FSR[%]	1.5 / -1.5	3.6 / -3.6	2.6 / -2.6	3.1 / -3.1	-5.3 / 5.3	-1.1 / 1.1
PILE-UP[%]	2.5 / -4.2	1.1 / -1.4	0.4 / -1.3	0.9 / -1.5	1.0 / -0.9	2.8 / -2.8
W[%]	2.6 / -2.9	1.0 / -0.6	1.4 / -1.2	1.8 / -0.7	1.9 / -2.6	3.3 / -2.9
CELLOUT[%]	4.1 / -1.3	0.9 / -0.9	1.3 / -0.5	1.0 / -0.8	0.5 / -0.3	4.1 / -3.1
XS[%]	3.6 / -1.3	0.7 / -0.9	1.5 / -2.0	2.0 / -1.4	2.0 / -1.5	3.2 / -3.7
MC stat.[%]	4.9 / -5.8	3.6 / -3.5	3.0 / -2.7	2.9 / -3.0	3.9 / -3.5	5.5 / -6.0

Table 6.21: Uncertainties on $d\sigma_{t\bar{t}}/(\sigma_{t\bar{t}}dy)$ in the muon+jets channel

	$dy_{t\bar{t}}$					
$d\sigma_{t\bar{t}}/(\sigma_{t\bar{t}}dy)$	-2 - -1	-1 - -0.5	-0.5 - 0	0 - 0.5	0.5 - 1	1 - 2
Total[%]	7.3 / -7.8	4.5 / -4.7	3.8 / -3.7	3.9 / -3.4	4.8 / -4.4	6.9 / -7.0
Stat. only[%]	3.6 / -3.4	2.8 / -2.8	2.4 / -2.3	2.4 / -2.4	2.8 / -2.7	3.2 / -3.2
Syst. only[%]	6.4 / -7.1	3.5 / -3.8	2.9 / -2.9	3.0 / -2.4	3.9 / -3.4	6.1 / -6.2
Luminosity[%]	0.4 / -1.5	1.5 / -1.1	0.3 / -0.6	1.5 / -0.5	1.1 / -1.2	2.3 / -1.0
JES[%]	2.2 / -4.2	0.6 / -1.4	1.4 / -1.6	1.9 / -1.6	2.4 / -1.5	2.4 / -3.7
JVF[%]	2.8 / -1.2	2.1 / -1.4	1.2 / -0.8	0.9 / -1.3	1.0 / -1.5	0.9 / -0.2
JER[%]	1.1 / -1.3	0.2 / -1.6	0.9 / -1.0	1.5 / -1.1	2.3 / -1.6	1.2 / -2.7
JRE[%]	2.5 / -1.7	0.6 / -1.9	0.4 / -1.3	2.0 / -1.6	1.6 / -0.7	1.6 / -1.7
BTAG[%]	2.2 / -0.7	0.8 / -1.3	0.4 / -1.3	1.8 / -1.1	1.1 / -1.1	2.3 / -1.2
LSF[%]	1.5 / -2.6	1.2 / -1.3	1.3 / -0.7	0.9 / -0.7	1.5 / -0.5	2.0 / -1.0
QCD[%]	2.5 / -1.9	0.3 / -0.6	0.5 / -0.6	1.5 / -1.1	1.4 / -0.8	2.5 / -1.2
PDF[%]	2.9 / -1.8	1.7 / -1.0	1.4 / -1.1	0.2 / -1.3	0.5 / -1.7	1.5 / -2.1
PS[%]	0.4 / -2.3	1.5 / -2.5	1.2 / -1.1	1.3 / -0.8	1.1 / -1.6	1.6 / -1.6
GEN[%]	1.8 / -3.2	1.1 / -1.4	1.4 / -1.3	1.5 / -0.5	1.9 / -1.6	1.5 / -1.1
ISR/FSR[%]	-2.05 / 2.05	4.6 / -4.6	-0.1 / 0.1	0.9 / -0.9	4.5 / -4.5	1.6 / -1.6
PILE-UP[%]	3.8 / -2.1	1.8 / -1.6	0.4 / -1.0	1.6 / -0.8	2.0 / -0.7	1.4 / -0.4
W[%]	3.1 / -2.9	1.5 / -0.9	1.6 / -1.4	0.9 / -1.0	1.0 / -0.9	1.3 / -2.0
CELLOUT[%]	3.1 / -1.7	1.0 / -1.1	0.6 / -0.8	1.8 / -1.2	1.2 / -1.7	2.8 / -1.1
XS[%]	2.5 / -2.2	1.0 / -1.8	0.9 / -1.0	0.8 / -1.5	1.3 / -0.6	2.5 / -0.8
MC stat.[%]	3.8 / -4.7	2.7 / -2.9	2.3 / -2.3	2.6 / -1.8	3.1 / -3.2	4.9 / -4.1

Table 6.22: Uncertainties on $d\sigma_{t\bar{t}}/(\sigma_{t\bar{t}}dy)$ in the l+jets channel

	$dM_{t\bar{t}}$ Syst. error only[%]				
$d\sigma_{t\bar{t}}/(\sigma_{t\bar{t}}dM)$	250-450	450-550	550-700	700-950	950-2700
2.05 fb^{-1} of 2011 data	14/-14	14/-15	8/-8	16/-14	32/-37
Full 2011 data	5.11 / -3.68	4.76 / -6.48	9.39 / -6.55	10.03 / -8.96	34.59 / -30.42

Table 6.23: Systematic uncertainty on $d\sigma_{t\bar{t}}/(\sigma_{t\bar{t}}dM_{t\bar{t}})$ in the l+jets channel using the full 2011 data sample in comparison with the one using only the first 2.05 fb^{-1} of the 2011 data.

	$dy_{t\bar{t}}$ Syst. error only[%]					
$d\sigma_{t\bar{t}}/(\sigma_{t\bar{t}}dy)$	-2 - -1	-1 - -0.5	-0.5 - 0	0 - 0.5	0.5 - 1	1 - 2
2.05 fb^{-1} of 2011 data	10/-9	5/-5	4/-3	4/-4	4/-3	7/-7
Full 2011 data	6.4 / -7.1	3.5 / -3.8	2.9 / -2.9	3.0 / -2.4	3.9 / -3.4	6.1 / -6.2

Table 6.24: Systematic uncertainty on $d\sigma_{t\bar{t}}/(\sigma_{t\bar{t}}dy)$ in the l+jets channel using the full 2011 data sample in comparison with the one using only the first 2.05 fb^{-1} of the 2011 data.

Conclusion

The ATLAS detector at the Large Hadron Collider at CERN, Geneva, Switzerland, has been successfully commissioned during the last years. The LHC opened up a new energy frontier by colliding two proton beams with unprecedented center-of-mass energy of 7 TeV in 2010-2011 and 8 TeV in 2012. First physics measurements testing the Standard Model of elementary particle physics were successfully carried out. During my three years as a PhD student from October 2009 till September 2012, I had the opportunity to work on two different analysis which involve all the reconstructed physics objects. In these analyses, I carried out the first measurement of the b-tagging efficiency with 2010 data using the *System*8 method, which became one of the ATLAS standard methods and, subsequently I carried out also the first measurement of the $t\bar{t}$ differential cross section which was performed on the first half of the 2011 data and turned out into a publication submitted to the arXiv and to EPJC journal. I present an update of this measurement in this thesis, using the full 2011 data sample.

During the first part of my thesis, I worked on commissioning and developing the *System*8 method, a data driven method which is used to calibrate the b-tagging algorithms with data. I had the opportunity to analyze the first 7 TeV LHC collisions with the ATLAS detector, by using the muon-jet triggers, selecting events containing muon-jets, and preparing the samples for the b-tagging efficiency measurement. The b-tagging efficiency is a key ingredient to all physics analysis that involve b-jet signature, hence its importance. *System*8 consists of a non-linear system of 8 equations, where no general analytic solution is known. The system is solved using a minimization of a χ^2 using MINUIT. The correlation factors for b and c jets are determined from simulation while the ones for the *light*-jets are determined from data. The full covariance matrix of the correlation factors is computed and used in the fit to allow a proper propagation of the statistical errors on these correlation factors. The measurement of the b-tagging efficiency using the *System*8 method was performed on the full 2010 ATLAS data sample, on two different *early* b-tagging algorithms: `JetProb` and `SV0`. In the beginning, this measurement came as a cross check for the b-tagging efficiency results provided

by the p_T^{rel} method on the 2010 data. But since 2011 data, the results of these two methods are combined to improve the b-tagging efficiency measurements and the combined results with their scale factors are then communicated to the physics analyses groups.

During the second half of my thesis, I had the opportunity to analyze a larger sample of data, almost 5 fb^{-1}, to perform the measurement of the $t\bar{t}$ differential cross section as function of the $t\bar{t}$ mass and the $t\bar{t}$ rapidity. I carried out this measurement by selecting $t\bar{t}$ event candidates with exactly one lepton, electron or muon, at least four jets with high energy and a large missing transverse energy. This selection gave me the opportunity to familiarize with the different reconstructed physics objects using the ATLAS detector. I estimated the different backgrounds using the standard recommendation of the ATLAS experiment and also reconstructed the $t\bar{t}$ system using the KLFitter algorithm, which is widely used within the ATLAS collaboration. I applied the unfolding using the inverted matrix method and performed closure tests on simulations which ended with a very good agreement with the Monte Carlo truth. The measurement on data was done with the full estimation of the different systematic uncertainties. The results agree with NLO predictions and approximately NNLO predictions. No significant deviation from the SM expectations are observed. No resonance nor a distortion in the $t\bar{t}$ differential cross section as function of the $t\bar{t}$ mass spectrum has been observed.

Bibliography

[1] S.L. Glashow, *Partial symmetries of weak interactions*, Nucl. Phys. 22 579-588 (1961) .

[2] S. Weinberg, *A model of Leptons*, Phys. Rev. Let. 19 1264-1266 (1967) .

[3] A.Salam, N. Svartholm, *Elementary Particle Physics:Relativistic Groups and Analyticity* , Eight Nobel Symposium. Stockholm : Almquvist and Wiksell. p367 (1968) .

[4] The ATLAS Collaboration, *Observation of a new particle in the search for the Standard Model Higgs boson with the ATLAS detector at the LHC*, CERN-PH-EP-2012-218 arXiv:1207.7214v1 [hep-ex].

[5] The CMS Collaboration, *Observation of a new boson at a mass of 125 GeV with the CMS experiment at the LHC*, arXiv:1207.7235 CERN-PH-EP-2012-220.

[6] J. Beringer et al. [Particle Data Group], *The Review of Particle Physics*, PR D86 (2012) no. 010001, .

[7] K. G. Wilson, *Confinement of Quarks*, Phys. Rev. D10, 2445 (1974) 151 .

[8] M. Gell-Mann, *Quarks*, 11th Internationale Universitatswochen fur Kernphysik, Schladming, Austria, 21 Feb - 4 Mar 1972, pp.733-61 .

[9] G. Zweig, *An $SU(3)$ model for strong interaction symmetry and its breaking*, Developments in the Quark Theory of Hadrons, pp.22-101 .

[10] R. P. Feynman, *Very high-energy collisions of hadrons*, Phys. Rev. Lett. **23**, 1415 (1969).

[11] M.A. Peskin, D.V. Schroder, *An introduction to quantum field theory*, 1995.

[12] Yang, Chen-Ning et Mills, Robert L., *Conservation of isotopic gauge invariance*, Phys. Rev.,96, 191-195, 1954.

[13] P. Watkins, *Story of the W and Z.*, Cambridge University Press. p. 70. ISBN 978-0-521-31875-4 (1986).

[14] J. Goldstone, A. Salam, and S. Weinberg, *Broken Symmetries*, Phys. Rev.127, 965 (1962).

[15] P. W. Higgs, *Broken Symmetries and the Masses of Gauge Bosons*, Phys. Rev.Lett. 13, 508 (1964).

[16] F. Englert and R. Brout, *Broken Symmetry and the Mass of Gauge Vector Mesons*, Phys. Rev. Lett. 13, 321 (1964).

[17] Amsler, C. et al. , *Review of Particle Physics*, Physics Letters B 667 (2008).

[18] N. Cabibbo, *Unitary Symmetry and Leptonic Decays* , Phys. Rev. Lett. 10,531 (1963).

[19] M. Kobayashi and T. Maskawa, *CP Violation in the Renormalizable Theory of Weak Interaction* , Prog. Theor. Phys. 49, 652 (1973).

[20] F. Abe et al., *The CDF Collaboration* , Phys. Rev. Lett. 74 (1995) 2626 [arXiv:hep-ex/9503002].

[21] S. Abachi et al, *The D0 Collaboration* , Phys. Rev. Lett. 74 (1995) 2632 [arXiv:hep-ex/9503003].

[22] N. Kidonakis and R. Vogt, *The theoretical top quark cross section at the Tevatron and the LHC*, Physical Review D, May 30, 2008 .

[23] Michal Czakon, Alexander Mitov , *NNLO corrections to top-pair production at hadron colliders: the all-fermionic scattering channels*, arXiv:1207.0236 [hep-ph].

[24] The CDF Collaboration, *Observation of Single Top-Quark Production* , Phys. Rev. Lett. 103, 092002 (2009).

[25] The D0 Collaboration, *Observation of Single Top-Quark Production* , Phys. Rev. Lett. 103, 092001 (2009).

[26] The ATLAS Collaboration, *Observation of t Channel Single Top-Quark Production in pp Collisions at* $\sqrt{s} = 7$ *TeV with the ATLAS detector* , (ATLAS-CONF-2011-088) .

[27] The CMS Collaboration, *Measurement of the single-top t-channel cross section in pp collisions at* $\sqrt{s} = 7$ *TeV*, (CMS-PAS-TOP-10-008) .

[28] H. Xing Zhu, J. Wang, J. Zhang, *Factorization and Resummation for Single Top Production at both Tevatron and LHC with SCET*, arXiv:1010.4509v2 [hep-ph] 25 Oct 2010, arXiv1006.0681.

[29] The ATLAS Collaboration , *Evidence for the associated production of a W boson and a top quark in ATLAS at* $\sqrt{s} = 7$ *TeV* , Phys. Lett. B 716 (2012) 142-159.

[30] The CMS Collaboration , *Evidence for associated production of a single top quark and W boson in pp collisions at 7 TeV*, arXiv:1209.3489 .

[31] The ATLAS Collaboration, *Expected Performance of the ATLAS Experiment – Detector, Trigger and Physics*, CERN-OPEN-2008-020, arXiv:0901.0512 [hep-ex], 2009.

[32] The ATLAS Collaboration, *Search for s-channel Single Top-Quark Production in pp Collisions at* $\sqrt{s} = 7$ *7 TeV*, (ATLAS-CONF-2011-118).

[33] The ATLAS Collaboration, *Summary Plot of Vector-Boson and Top Production Cross-Sections in Proton-Proton Collisions at* $\sqrt{s} = 7$ *7 TeV at ATLAS*, https://twiki.cern.ch/twiki/bin/view/AtlasPublic/CombinedSummaryPlots.

[34] C. Amsler et al., , Physics Letters B667, 1 (2008).

[35] The Tevatron Electroweak Working Group, , arxiv:1107.5255v3 (2011).

[36] The ATLAS and CMS Collaborations, *Combination of ATLAS and CMS results on the mass of the top quark using up to 4.9* fb^{-1} *of data*, (ATLAS-CONF-2012-095) (CMS PAS TOP-12-001).

[37] The ATLAS Collaboration , *Observation of spin correlation in ttbar events from pp collisions at* $\sqrt{s} = 7$ *TeV using the ATLAS detector* , Phys. Rev. Lett. 108, 212001 (2012).

[38]

[39] D. Chang, W. F. Chang and E. Ma, *Phys. Rev. D 59 (1999) 091503* , [arXiv:hep-ph/9810531].

[40] The D0 Collaboration, *Phys. Rev. Lett. 98 (2007) 041801*, [arXiv:hep-ex/0608044].

[41] The CDF Collaboration, *Finding the charge of the top quark in the dilepton channel*, arXiv:0707.1339 [hep-ex].

[42] The ATLAS Collaboration, *Measurement of the top quark charge in pp collisions at $\sqrt{s} = 7$ TeV in the ATLAS experiment* , ATLAS-CONF-2011-141.

[43] C. T. Hill and E. H. Simmons, *Phys. Rept. 381 (2003) 235*, [Erratum-ibid. 390 (2004) 553] [arXiv:hep-ph/0203079].

[44] C. T. Hill and S. J. Parke, *Phys. Rev. D 49*, (1994) 4454 [arXiv:hep-ph/9312324].

[45] N. Arkani-Hamed, A. G. Cohen and H. Georgi, *Phys. Lett. B 513 (2001) 232*, [arXiv:hep-ph/0105239].

[46] N. Arkani-Hamed, S. Dimopoulos and G. R. Dvali, *The Hierarchy problem and new dimensions at a millimeter*, Phys. Lett. B 429 (1998) 263 [arXiv:hep-ph/9803315].

[47] L. Randall and R. Sundrum, *An Alternative to Compactification*, Phys. Rev. Lett. 83 (1999) 4690 [arXiv:hep-th/9906064].

[48] K. Agashe, A. Delgado, M. J. May and R. Sundrum, , JHEP 0308 (2003) 050 [arXiv:hep-ph/0308036].

[49] A. L. Fitzpatrick, J. Kaplan, L. Randall and L. T. Wang, , JHEP 0709 (2007) 013 [arXiv:hep-ph/0701150].

[50] O. Bruning et al., *LHC Design Report*, Tech. Rep. CERN-2004-003.

[51] The ALICE Collaboration, *The ALICE Experiment at the CERN Large Hadron Collider*, JINST **3** (2008) S08002.

[52] The ATLAS Collaboration, *The ATLAS Experiment at the CERN Large Hadron Collider*, JINST **3** (2008) S08003.

[53] The CMS Collaboration, *The CMS Experiment at the CERN Large Hadron Collider*, JINST **3** (2008) S08004.

[54] The LHCb Collaboration, *The LHCb Experiment at the CERN Large Hadron Collider*, JINST **3** (2008) S08005.

[55] The ATLAS Collaboration, *ATLAS Inner detector: technical design report. 1 and 2*, Tech. Rep. CERN-LHCC-97-016,7, CERN, 1997.

[56] The ATLAS Collaboration, *ATLAS pixel detector electronics and sensors*, JINST **3** (2008) P07007.

[57] A.Ahmad et al., *The silicon microstrip sensors of the ATLAS SemiConductor Tracker*, Nucl. Instrum. Meth. **1** (2007) A578.

[58] The ATLAS Collaboration, *Particle Identification Performance of the ATLAS Transition Radiation Tracker*, ATLAS-CONF-2011-128 (2011).

[59] D. Attree et al., *The evaporative cooling system for the ATLAS inner detector*, JINST **1** (2008) P07008.

[60] The ATLAS Collaboration, *ATLAS Muon Spectrometer: TechnicalDesign Report*, Tech. Rep. CERN-LHCC-97-022, CERN, 1997.

[61] The ATLAS Collaboration, *The ATLAS Trigger Monitoring and Operations in proton-proton collisions* , ATL-DAQ-PUB-2010-003 .

[62] The ATLAS Collaboration, *ATLAS Computing: TechnicalDesign Report*, Tech. Rep. CERN-LHCC-2005-022, CERN, 2005.

[63] P.F.Akesson et al, *ATLAS Tacking Event Data Model,*, ATLAS Note ATL-SOFT-PUB-2006-004(2006).

[64] A. Salzburger, S. Todorova and M. Wolter, *The ATLAS Tracking Geometry Description*, ATLAS Note ATL-SOFT-PUB-2007-004 (2007).

[65] A. Salzburger, *The ATLAS Track Extrapolation Package*, ATLAS Note ATL-SOFT-PUB-2007-005(2007).

[66] The ATLAS Collaboration, *Expected electron performance in the ATLAS experiment*, ATL-PHYS-PUB-2011-006, 2011.

[67] The ATLAS Collaboration, *Supporting Document for egamma Paper: Electron efficiency measurements using ATLAS 2010 data at sqrt(s) = 7 TeV*, ATLAS Note ATL-COM-PHYS-2011-322, 2011.

[68] R. Fruehwirth, *Comp. Phys. Comm. 100*, Eur. Phys. J (1997) no. C45, 35.

[69] V. Kartvelishvili, *Electron bremsstrahlung recovery in ATLAS*, Nucl. Phys. B. **172** (1997) 208.

[70] The ATLAS Collaboration, *Determination of the muon reconstruction efficiency in ATLAS at the Z resonance in proton-proton collisons at* $\sqrt{s} = 7$ *TeV*, Tech. Rep. ATLAS-CONF-2011-008, CERN, 2011.

[71] M. Cacciari, G.P. Salam, and G. Soyez, *The anti-k_t jet clustering algorithm*, JHEP **04** (2008) 063.

[72] The ATLAS Collaboration, *Jet energy scale and its systematic uncertainty in proton-proton collisions at $\sqrt{s} = 7$ TeV in ATLAS 2010 data*, Tech. Rep. ATLAS-CONF-2011-032, CERN, Geneva, 2011.

[73] The ATLAS Collaboration, *Reconstruction and Calibration of Missing Transverse Energy and Performance in Z and W events in ATLAS Proton-Proton Collisions at $\sqrt{s}$ =7 TeV*, Tech. Rep. ATLAS-CONF-2011-080, CERN, 2011.

[74] The ATLAS Collaboration, *Impact parameter-based b-tagging algorithms in the 7 TeV collision data with the ATLAS detector: the TrackCounting and JetProb algorithms*, ATLAS Note ATLAS-CONF-2010-041.

[75] The ATLAS Collaboration, *Calibrating the b-Tag Efficiency and Mistag Rate in 35 pb^{-1} of Data with the ATLAS Detector*, Tech. Rep. ATLAS-CONF-2011-089, CERN, 2011.

[76] The ATLAS Collaboration, *Performance of the ATLAS Secondary Vertex b-tagging Algorithm in 7 TeV Collision Data,*, ATLAS Note ATLAS-CONF-2010-042.

[77] The ATLAS Collaboration, *Commissioning of the ATLAS high-performance b-tagging algorithms in the 7 TeV collision data*, Tech. Rep. ATLAS-CONF-2011-102, CERN, 2011.

[78] V.M. Abazov *et al.* [D0 Collaboration], *b-Jet Identification in the D0 Experiment*, Nucl. Instrum. Meth. **A620** (2010) 490–517.

[79] J. Boudreau *et al.*, *Measuring the b-tagging Efficiency with the System 8 Method Using Soft Muons*, ATLAS Note ATLAS-COM-PHYS-2010-764.

[80] T. Sjostrand, S. Mrenna and P. Skands, *PYTHIA 6.4 Physics and Manual*, JHEP **05** (2006) 026.

[81] A. Sherstnev et al.,, *Parton Distributions for LO Generators,*, Eur. Phys. J. C **55** (2008) S08003.

[82] The ATLAS Collaboration, *Measurement of the b-jet production cross section using muons in jets with ATLAS in pp Collisions at $\sqrt{s}$ =7 TeV*, ATLAS-CONF-2011-057, 2011.

[83] D. Lopez Mateos, E.W. Hughes, and A. Schwartzman, *Jet Energy Scale Correction to Semileptonic b-jets from Missing Neutrino Energy*, ATL-PHYS-INT-2008-047, 2008.

[84] The ATLAS Collaboration, *A Measurement of the ATLAS muon reconstruction efficiency using J/ψ decays*, ATLAS-CONF-2011-021.

[85] S. Aoun *et al.*, *Calibration of b-Jet Tagging Efficiency using the $p_{\mathrm{T}}^{\mathrm{rel}}$ Method*, ATLAS Note ATL-COM-PHYS-2011-043, 2011.

[86] J. Abdallah *et al.* [DELPHI Collaboration], *Determination of heavy quark non-perturbative parameters from spectral moments in semileptonic B decays*, Eur. Phys. J (2006) no. C45, 35.

[87] The BaBar Collaboration, *Measurement of the electron energy spectrum and its moments in inclusive $B \to Xe\nu$ decays*, Phys. Rev. D 69 (2004).

[88] K. Nakamura *et al.* [Particle Data Group], *The Review of Particle Physics*, J. Phys. (2010) no. G37, 075021.

[89] W.-M. Yao et al. , *(Particle Data Group)*, J. Phys. G 33, 1 (2006) no. 010001, .

[90] The CDF Collaboration, *Relative B Hadron Fragmentation Fractions* , Phys. Rev. D77, 072003 (2008).

[91] L. Fiorini for ATLAS and CMS collaborations, *Top-Quark Physics Results From LHC,contribution to LCWS11, proceedings*, ATLAS-PHYS-PROC-2012-029 , arXiv:1201.5844v1[hep-ex] (September 2011).

[92] R. Frederix and F. Maltoni, *Top pair invariant mass distribution: a window on new physics*, JHEP, (2009) arXiv:0712.2355 [hep-ph] .

[93] T. Aaltonen et al. (CDF Collaboration), , Phys. Rev. Lett.101, 202001 (2008).

[94] V. M. Abazov et al. (D0 Collaboration), , Phys. Rev. Lett.100, 142002 (2008).

[95] T. Aaltonen et al. (CDF Collaboration), *Evidence for a Mass Dependent Forward-Backward Asymmetry in Top Quark Pair Production* , arXiv:1101.0034v1 [hep-ex].

[96] Hooman Davoudiasl, Thomas McElmurry, Amarjit Soni , *Top Pair Forward-Backward Asymmetry from Loops of New Strongly Coupled Quarks*, arXiv:1108.1173v2 [hep-ph].

[97] S. Agostinelli et al., *GEANT4 - A Simulation Toolkit*, Nucl. Instr. and Meth. A506 (2003) 250 .

[98] S. Frixione and B.R. Webber, *Matching NLO QCD computations and parton shower simulations*, JHEP 0206 (2002) 029, hep-ph/0204244.

[99] A.D. Martin et al., *Parton distributions for the LHC*, Eur.Phys.J.C63:189-285,(2009).

[100] M. Cacciari et al., *Top-pair production at hadron colliders with next-to-next-to-leading logarithmic soft-gluon resummation*, arXiv:1111.5869v2 [hep-ph] (2012) .

[101] A.D. Martin et al., *Uncertainties on α_S in global PDF analyses and implications for predicted hadronic cross sections*, Eur.Phys.J.C64:653-680,(2009).

[102] M. Aliev et al., *HATHOR: HAdronic Top and Heavy quarks crOss section calculatoR*, Comput.Phys. Commun. 182 (2011) 1034-1046, arXiv:1007.1327[hep-ph].

[103] G. Corcella et al., *HERWIG 6: An Event generator for hadron emission reactions with interfering gluons (including supersymmetric processes)*, JHEP 0101 (2001) 010, hep-ph/00113.

[104] J. M. Butterworth et al., *Multiparton interactions in photoproduction at HERA*, Z. Phys. C72 (1996) 637-646, arXiv:hep-ph/9601371.

[105] The ATLAS Collaboration, *First tuning of HERWIG/JIMMY to ATLAS data*, ATL-PHYS-PUB-2010-014, 2010.

[106] B.P. Kersevan and E. Richter-Was, *The Monte Carlo event generator AcerMC version 2.0 with interfaces to PYTHIA 6.2 and HERWIG 6.5*, (2004) , hep-ph/0405247.

[107] Phys. Rev. D 81, 054028 (2010).

[108] Phys. Rev. D 82, 054018 (2010).

[109] The ATLAS Collaboration, *Single Boson and Diboson Production Cross Sections in pp Collisions at sqrts = 7 TeV*, ATL-COM-PHYS-2010-695, 2010.

[110] M. Agustoni et al., *Electron energy scale in-situ calibration and performance*, ATL-COM-PHYS-2011-263 (2011).

[111] A. Canepa et al., *Missing Transverse Energy for Top Physics analyses with early ATLAS data at* $\sqrt{s}$ *=7 TeV*, ATL-COM-PHYS-2010-821, CERN, Geneva, Oct, 2010.

[112] K. Becker et al., *Mis-identified lepton backgrounds in top quark p1 air production studies for EPS 2011 analyses*, ATL-COM-PHYS-2011-768, 2011.

[113] B. Acharya et al., *Object selection and calibration, background 1 estimations and MC samples for the Winter 2012 Top Quark analyses with 2011 data*, ATL-COM-PHYS-2012-224, 2012.

[114] The ATLAS Collaboration, *Measurement of the Top-Quark Mass using the Template Method in pp Collisions at* $\sqrt{s}$ *= 7 TeV with the ATLAS detector*, ATLAS-CONF-2011-033 (2011).

[115] The ATLAS Collaboration, *Measurements of top quark pair relative differential cross-sections with ATLAS in pp collisions at* $\sqrt{(s)}$ *=7 TeV*, arXiv:1207.5644v1 [hep-ex].

[116] P. Nason et al., *A new method for combining NLO QCD with shower Monte Carlo algorithms*, JHEP 11 (2004) 040, arXiv:hep-ph/0409146 (2004).

[117] C.F. Weizsaecker, E.J. Williams, , Z. Phys., 88, 612 ,Phys. Rev., 45, 729 (1934), .

[118] F. A. Berends, H. Kuijf, B. Tausk, and W. T. Giele, *On the Production of a W and Jets at HadronColliders* , Nucl. Phys. B357 (1991) 32-6 .

[119] Phys. Rev. D 83, 091503(R) (2011).

[120] The ATLAS Collaboration, *Single Boson and Diboson Production Cross Sections in pp Collisions at* $\sqrt{s}$ *= 7 TeV* , ATLAS-COM-2010-695 (2010) .

[121] The ATLAS Collaboration, *Jet energy resolution and selection efficiency relative to track jets from in-situ techniques with the ATLAS Detector Using Proton-Proton Collisions at a Center of Mass Energy* $\sqrt{s}$ *= 7 TeV* , ATLAS-CONF-2010-054 (2010) .

[122] The ATLAS Collaboration, *Measurement of the b-tag Efficiency in a Sample of Jets Containing Muons with 5 fb^{-1} of Data from the ATLAS Detector*, ATLAS-CONF-2012-043 (2012) .

[123] The ATLAS Collaboration, *Measurement of the Mistag Rate of b-tagging algorithms with 5 fb^{-1} of Data Collected by the ATLAS Detector*, ATLAS-CONF-2012-040 (2012) .

[124] MCFM - Monte Carlo for FeMtobarn processes, http://mcfm.fnal.gov/.

[125] V. Ahrens et al., *Renormalization-Group Improved Predictions for Top-Quark Pair Production at Hadron Colliders*, JHEP 09 (2010) 097, arxiv:1003.5827 .

[126] The CMS Collaboration, *Measurement of Top Quark Pair Differential Cross Sections at sqrt(s) = 7 TeV*, CMS-PAS-TOP-11-013.

[127] The CDF Collaboration, *First Measurement of the tt-bar Differential Cross Section $d\sigma/dM_{t\bar{t}}$ in pp-bar Collisions at sqrt s= 1.96 TeV*, Phys. Rev. Lett. 102 222003 (2009). Fermilab-Pub-09-079-E.